A MEASUREMENT OF THE RATIO OF NEUTRAL CURRENT TO CHARGED CURRENT DEEP INELASTIC MUON NEUTRINO SCATTERING INTERACTIONS IN A FINE-GRAINED NEUTRINO DETECTOR AT FNAL

By

George John Perkins

A DISSERTATION

Submitted to
Michigan State University
in partial fulfillment of the requirements
for the degree of

DOCTOR OF PHILOSOPHY

Department of Physics and Astronomy

1992

ABSTRACT

A Measurement of the Ratio of Neutral Current to Charged Current Deep Inelastic Muon Neutrino Scattering Interactions in a Fine-grained Neutrino Detector at FNAL

By

George John Perkins

R_ν, the ratio of neutral current to charged current deep inelastic ν_μ-nucleon scattering interactions was measured in the Lab C fine-grained neutrino detector at the Fermi National Accelerator Laboratory. With a hadronic shower energy cut of 10 GeV, $R_\nu = 0.304 \pm 0.006$. With a hadronic shower energy cut of 60 GeV, $R_\nu = 0.304 \pm 0.008$.

Contents

List of Figures

List of Tables

Introduction

The Standard Model of elementary particle physics incorporates a set of Electroweak forces. These include the familiar Electromagnetic forces, mediated by massless photons, and the Weak forces responsible for nuclear decay, which are mediated by the W^+, W^-, and Z^0 intermediate vector bosons. A fundamental part of the theoretical description of these forces and their relationship to one another is the view that they are mixtures of a pair of even more fundamental forces, mediated by massless bosons. The mixing between these primordial forces which produces the Electroweak forces observed in the present-day universe is described by the Standard Model, but its actual behavior is not predicted quantitatively in any detail.

A convenient measure of this mixing is found in the quantity referred to as the *weak mixing angle*, or "Weinberg angle", designated $\sin^2\theta_W$, which relates the strengths of the charge-changing weak force to the non-charge-changing electromagnetic and weak forces and the masses of the mediating bosons. It is customary to use $\sin^2\theta_W$ as a standard measurement, as it has no units to keep track of and appears in that form in some of the relevant equations.

One method of determining the effects of the various constituents of the Electroweak set of forces in such a way as to tell which is which is by using neutrino deep inelastic scattering as a probe. One of the side effects of this method, however, is that experimentalists must deal with the other type of force which comes into play when ripping nucleons apart: the Strong Nuclear Force, which is described by the theory of Quantum Chromodynamics. The details of the processes involved in neutrino DIS are important, and are not well known, especially in the case of relatively low energy transfer to the disrupted nucleon during the course of the interaction. This imposes a limit on just how well we can determine the relationship between the Electroweak constituent forces. It also indicates that experiments with a predominance of high energy transfer interactions will better avoid the theoretical uncertainties involved with separating out the QCD influences from the Electroweak force-moderated behavior which is being studied.

The present experiment used the QT neutrino beam at FNAL and the Lab C neutrino detector to gather a data set which includes a large sample of relatively-high energy transfer events in order to determine $\sin^2\theta_W$ with a minimum of dependence on specific models of the QCD influence on the DIS process.

The subject of this dissertation is the measurement of the physical quantity used in determining $\sin^2\theta_W$ by means of neutrino-nucleon deep inelastic scattering, the ratio

$$R_\nu \equiv \frac{\#\text{ of neutral current }\nu_\mu\text{ DIS interactions}}{\#\text{ of charged current }\nu_\mu\text{ DIS interactions}}.$$

Several topics related to this measurement will be discussed.

- The physics of ν_μ DIS leading to the relation of R_ν to $\sin^2\theta_W$ will be the central topic of Chapter 1.

- Chapter 2 will cover the usual methods for measuring R_ν experimentally, and will describe the neutrino beamline at Fermilab which provided the neutrinos for this experiment.

- Chapter 3 will describe the experimental apparatus at FNAL Lab C which was used to detect the neutrino interactions.

- In Chapter 4, the analysis procedure used to characterize these detected neutrino interactions will be presented.
- A discussion of the final extraction of R_ν from the data set and the Monte Carlo simulation which made acceptance corrections possible will be the focus of Chapter 5.
- The Appendices will present a more detailed description of certain items mentioned in the course of the main discussion.

Chapter 1

The Physics of $\sin^2\theta_W$ and R_ν

1.1 The Standard Model

1.1.1 Overview

The present picture of the fundamental structure and operating principles of Nature is that of 4-space point interactions between pointlike elementary particles: matter constituents and force mediators, which have the following basic properties.

- Elementary matter constituents obey Fermi-Dirac statistics and differ from each other in the manner in which they couple to the different force mediators — these differences are described by various *quantum numbers.*

- Elementary force mediators obey Bose-Einstein statistics and transfer energy and momentum; they may also change certain particles' quantum numbers or redistribute them between the particles involved in an interaction.

The interactions themselves are described using field theory. Many of the characteristics described by particles' quantum numbers are associated with their interactions' space-time transformation properties and the conservation rules obeyed by the interacting fields.

1.1.2 Description of Elementary Particles

There are two main types of elementary particles, leptons and quarks.

Leptons have the following properties.

- They interact with gravitational and electroweak forces.
- There are three *generations* of leptons which appear to differ from one another only in mass.
- Within each generation there is a massive charged particle and a neutrino, which is treated as massless in the basic Standard Model[1].
- For each lepton, there is a corresponding anti-lepton.
- If leptons in a generation are assigned a quantum number $L_{generation} = +1$ and anti-leptons are assigned $L_{generation} = -1$, then all interactions involving leptons and anti-leptons will conserve $L_{generation}$.
- The charged leptons interact with all forms of electroweak fields, while the neutrinos interact only with the weak forces.
- The spin-vector of a neutrino is parallel to its velocity vector, but points in the opposite direction (*i.e.,* neutrinos are longitudinally polarized with $J_z = -\frac{1}{2}$).

---

[1] There are extensions of the Standard Model which do take into account the possible effects of neutrino mass; these effects will be considered as negligible in this dissertation.

- The spin-vector of an anti-neutrino is parallel to its velocity vector, and points in the same direction (*i.e.,* anti-neutrinos are longitudinally polarized with $J_z = +\frac{1}{2}$).
- Spin-vectors of charged leptons may have both longitudinal and transverse components; the weak forces couple to the longitudinal polarization components.

A list of the leptons and some of their individual properties may be found in Table 1.1.

Quarks have the following properties.

- They interact with all forces.
- There are three *generations* of quarks including two *flavors* each for a total of 6 flavors, called up, down, charm, strange, top & bottom.
- For each quark, there is a corresponding anti-quark.
- Flavor is conserved in all interactions except the charged current weak interaction.
- Quarks carry electric charge and baryon number as outlined in table 1.2, and also a *color* charge (one of three states, often represented as *red, green,*and *blue*); each of these quantities is conserved in all interactions.
- They make up hadronic matter of two basic types:
  - mesons (quark + anti-quark) and
  - baryons (three quarks or anti-quarks).

A list of the quarks and some of their individual properties may be found in Table 1.2.

Table 1.1: Lepton Properties

	LEPTONS		ANTI-LEPTONS		
Name	Symbol	Charge (e)	Symbol	Charge (e)	Mass (GeV/c^2)
electron	e^-	-1	e^+	$+1$	0.000511
electron neutrino	ν_e	0	$\overline{\nu}_e$	0	0
muon	μ^-	-1	μ^+	$+1$	0.10566
muon neutrino	ν_μ	0	$\overline{\nu}_\mu$	0	0
tau	τ^-	-1	τ^+	$+1$	1.784
tau neutrino	ν_τ	0	$\overline{\nu}_\tau$	0	0

Table 1.2: Quark Properties

	Quarks (Baryon# =+1/3)		Anti-Quarks (Baryon# =–1/3)		
Flavor Name	Symbol	Charge (e)	Symbol	Charge (e)	Bare mass (GeV/c^2)
down	d	$-1/3$	$\overline{d}$	$+1/3$	$\approx .007$
up	u	$+2/3$	$\overline{u}$	$-2/3$	$\approx .004$
strange	s	$-1/3$	$\overline{s}$	$+1/3$	$\approx .15$
charm	c	$+2/3$	$\overline{c}$	$-2/3$	≈ 1.1
bottom	b	$-1/3$	$\overline{b}$	$+1/3$	≈ 4.2
top	t	$+2/3$	$\overline{t}$	$-2/3$	> 92

1.1.3 Elementary forces and force-mediating particles

The Standard Model ignores one of the four fundamental forces observed in nature and describes the unification of two of the others.

Gravity is transmitted by spin-2 vector bosons called *gravitons*; all particles with mass interact with it directly while massless particles are influenced by effect on spacetime geometry; the link between the two types of influence is not yet well-understood (there is no satisfactory quantum theory of gravity which ties in with general relativity formulation). *It is not dealt with in the Standard Model at all, as the strength of gravitational interaction with a single elementary particle is vanishingly small, especially with respect to the strength of the other forces (*$\lesssim 10^{-38}$ *of the EM force).*

Strong nuclear force holds nucleons together in ordinary matter; very strong, but effectively limited in range, this is a side-effect of the forces carried by massless *gluons* which bind the nucleons themselves together. These gluon-mediated forces are described by the theory of Quantum Chromodynamics, and involve the transfer of *color charge* from quark to quark.

Weak nuclear force is responsible for details of radioactive breakup of unstable nuclei among other interactions. This limited-range force is carried by massive spin-1 *Intermediate Vector Bosons*, the W^+ and W^-, which transfer electric charge, and the Z^0, which does not.

Electromagnetic force governs familiar phenomena (radio, visible light, compass needles, most chemical reactions, etc.) mediated by massless spin-1 vector bosons called *photons* (symbolized by γ; the electromagnetic potential field is called A_μ).

Weinberg[1], Salam[2] and Glashow[3] showed that the latter two forces can be considered special cases of a single force (called *Electroweak*) and the photon is related to the other Vector Bosons, if the governing equations are written and solved in a consistent way. This representation can lead to insights into the underlying physics processes when extrapolated to conditions not generally found in the current observable universe. This dissertation concerns the measurement of $\sin^2\theta_W$, one of the parameters governing the relationship between these forces whose value is used by the Standard Model, but not predicted by it.

1.1.4 The Electroweak forces

The cornerstone of the Electroweak unification was the determination that the normally-observed properties of the infinite-range electromagnetic forces and the very short-range ($\ll 10^{-15}$ m) weak forces may be reproduced by starting with a set of four massless fundamental vector boson fields.

- An isovector triplet $\mathbf{W}_\mu = W_\mu^{(1)}, W_\mu^{(2)}, W_\mu^{(3)}$ interacts with the "weak isospin" properties of the elementary fermions (governed by SU(2) group theory), and
- an isosinglet B_μ interacts with the "weak hypercharge" component of the elementary fermions (governed by U(1) group theory).

If $\mathbf{J}_\mu$ represents the isospin current and J_μ^Y is the hypercharge current, the Lagrangian energy density of the interaction between a fermion and these fields is

$$\mathcal{L} = g\mathbf{J}_\mu \cdot \mathbf{W}_\mu + g' J_\mu^Y B_\mu,$$

where g and g' are the current-to-field coupling factors for the two processes.

The observable vector boson fields are linear combinations of these primordial boson fields and *vice versa*. The primordial fields can be related to the observable fields[2] using these equations:

$$W_\mu^{(1)} = \frac{1}{\sqrt{2}}(W_\mu^+ + W_\mu^-), \quad W_\mu^{(2)} = \frac{-i}{\sqrt{2}}(W_\mu^+ - W_\mu^-),$$

$$W_\mu^{(3)} = \frac{gZ_\mu + g'A_\mu}{\sqrt{g^2 + g'^2}},$$

and

$$B_\mu = \frac{-g'Z_\mu + gA_\mu}{\sqrt{g^2 + g'^2}}.$$

Separating the components of the isospin and hypercharge currents to isolate the electromagnetic part one can define

$$J_\mu^\pm = J_\mu^{(1)} \pm iJ_\mu^{(2)}$$

and

$$J_\mu^{EM} = J_\mu^Y - J_\mu^{(3)}.$$

Define a *mixing angle* relating the coupling constants

$$\theta_W = \arctan(g'/g),$$

and the Lagrangian energy density can be rewritten as

$$\mathcal{L} = \frac{1}{\sqrt{2}}(J_\mu^- W_\mu^+ + J_\mu^+ W_\mu^-) + \frac{g}{\cos\theta_W}(J_\mu^{(3)} - \sin^2\theta_W J_\mu^{EM})Z_\mu + g\sin\theta_W J_\mu^{EM} A_\mu.$$

---

[2] The observable fields use the nomenclature A_μ for electromagnetic, Z_μ for weak neutral current, and $W_\mu^\pm$ for weak charged current.

The first term can be identified as the weak charged current interaction, the second as the weak neutral current interaction, and the third as the electromagnetic interaction. Considered in this way, electromagnetism is also a neutral current interaction, and standard EM theory calls the coupling e; we can now relate g and g$'$ to a known quantity by equating $e = g \sin\theta_W = g' \cos\theta_W$. The couplings of the other electroweak currents to fermion fields can then be associated with physically measurable quantities, given this relationship between the electroweak coupling constants, the electromagnetic coupling e, and the weak mixing angle, or *Weinberg angle*, θ_W.

These algebraic manipulations continue to assume massless particles. Mass is introduced to the fermions and to some of the vector bosons by the *Higgs mechanism*. This involves a representation of the fields involved in these interactions, including the *vacuum* field, in a form involving a new scalar particle called the *Higgs*:

$$\phi \rightarrow \begin{pmatrix} 0 \\ \frac{v+H}{\sqrt{2}} \end{pmatrix}$$

where v is the vacuum expectation value and H is the Higgs particle field. The benefit of adding the Higgs to the lineup of particles is that it provides for a breaking of the symmetry which maintains the primordial boson fields as effectively identical infinite-range forces. This symmetry is broken in such a way that the field theory maintains renormalizability and the appropriate gauge invariances. It also allows for the interacting fermions and fields to acquire mass (energy drawn from the primordial vacuum). The details depend on particular forms of the scalar Higgs fields used, but the mass of the photon can be set to zero, as observed, and the other observed bosons have masses which obey the relations

$$M_{W^\pm} = M_{Z^0} \cos\theta_W,$$

and in the low momentum transfer limit,

$$M_{W^\pm}^2 = \frac{e^2\sqrt{2}}{8G_F \sin^2\theta_W},$$

where G_F is the Fermi constant.

Since electroweak unification makes use of the mixing angle $\sin^2\theta_W$ in relating these physically observable quantities, there is a way to determine its value, which is *not* predicted by the theory.

1.1.5 QCD particles and forces

In addition to the $SU(2) \times U(1)$ field properties which all of the fermions in the Standard Model have, quarks also possess *color charge* and interact via eight *gluon* fields which have $SU(3)$ gauge properties. The theory describing the form of the $SU(3)$ field interactions is called Quantum Chromodynamics (QCD).

In Deep Inelastic Scattering (DIS) of neutrinos from nucleons, QCD effects are indirect. The neutrinos do not interact directly with the gluons in the nucleon as the primary interaction is entirely via the weak force. QCD plays a role, however, in determining the properties of the quark in the target nucleon with which the neutrino interacts, and the behavior of the hadronic debris left behind as a result of the interaction. A full treatment of the interaction process must take these factors into account.

A process of considerable importance to the present measurement is that of *charm production.* One of the properties of the weak charged current interactions is that they do not respect a strict division of the quarks into generations (whereas they do respect such a division amongst the leptons). The quark eigenstate with which they do interact is described by the *Cabibbo-Kobayashi-Maskawa Matrix*[4, p. III.65–67], V, relating t he mix of quark generations as "seen" by the weak interaction.

$$\text{The weak eigenstate, } \begin{pmatrix} d' \\ s' \\ b' \end{pmatrix} = V \begin{pmatrix} d \\ s \\ b \end{pmatrix}, \quad \text{the mass eigenstate, where}$$

$$\begin{aligned} V &= \begin{pmatrix} V_{ud} & V_{us} & V_{ub} \\ V_{cd} & V_{cs} & V_{cb} \\ V_{td} & V_{ts} & V_{tb} \end{pmatrix} \\ &= \begin{pmatrix} c_{12}c_{13} & s_{12}c_{13} & s_{13}e^{-i\delta_{13}} \\ -s_{12}c_{23} - c_{12}s_{23}s_{13}e^{-i\delta_{13}} & c_{12}c_{23} - s_{12}s_{23}s_{13}e^{-i\delta_{13}} & s_{23}c_{13} \\ s_{12}s_{23} - c_{12}c_{23}s_{13}e^{-i\delta_{13}} & -c_{12}s_{23} - s_{12}c_{23}s_{13}e^{-i\delta_{13}} & c_{23}c_{13} \end{pmatrix}. \end{aligned}$$

The s_{ij} and c_{ij} represent the sine and cosine of the mixing angles θ_{ij} between the i^{th} & j^{th} generations, and δ_{13} is a phase constant representing CP violation in weak interactions (if it is non-zero). If θ_{13} and θ_{23} go to zero, then θ_{12} represents the *Cabibbo angle* in the two-generation-mixing model.

Another property of weak charged current interactions is that they connect the two I_3 states in a fermion isospin doublet, such as

$$\begin{pmatrix} \nu_e \\ e^- \end{pmatrix}_L ; \ \mathit{or} \text{ for quarks, } \begin{pmatrix} u \\ d \end{pmatrix}, \begin{pmatrix} c \\ s \end{pmatrix}, \ \mathit{or} \begin{pmatrix} t \\ b \end{pmatrix}.$$

Thus, charged current weak interactions may change any quark in the upper row to any in the lower row (as written here). Starting with a nucleon state which is primarily u and d quarks, a weak interaction may produce quarks of any flavor. The more massive quarks, though, require that the interaction carry sufficient energy to produce them in the first place.

For the present measurement, the available energy range is such that there is effectively no penalty for producing strange quarks, and they are treated the same as u or d quarks in most equations. It can be shown that combinations of mass-energy threshold effects and Cabibbo-Kobayashi-Maskawa matrix elements with the available DIS interaction energies cause the expected number of bottom and top quarks to be vanishingly small. The number of produced charm quarks expected is, however, not negligible, and is dependent on the energy of the interacting neutrino and the properties of the quarks within the nucleon. These effects must be taken into account in the experimental analysis, and will be described later.

1.2 The Parton Model

Historically, in experiments investigating the structure of matter, as the energy of probes increased, each "fundamental" unit of matter was shown to consist of particles with smaller size scales. In the early days of attempting to determine if nucleons were composed of still smaller particles, these hypothetical constituent particles were named *partons* by Feynman. He and others worked out what kinematic constraints such objects would be subject to, based on a model where a probing particle conveyed an effectively infinite amount of energy to a pointlike parton inside a nucleon. This assumed high energy transfer *Parton Model* has the advantage that it corresponds to an extremely short time and distance scale. The results of the probe-parton interaction can thus be considered as virtually independent of any other ongoing processes in the nucleon which the parton may be part of, since these other processes are too far away to have any effect at such a short time scale. At sufficiently high probe energies, interactions with nucleons could be seen as approximating elastic scattering from their constituents.

The observation that the total cross section of neutrino-nucleon DIS is close to a simple linear function of the neutrino energy is evidence of such elastic scattering from partons, as it can be interpreted as a pointlike interaction cross section, which rises with available phase space, proportional to the probe energy. Subsequent investigation has indicated that the role of parton is played by the quarks and gluons.

1.2.1 Kinematics terminology

In order to make quantitative predictions about the results of deep inelastic neutrino-nucleon scattering based on this model, some terms will have to be defined. Refer to Figure 1.1 to assist in understanding these terms.

- E_ν = energy of the incoming neutrino.
- $\vec{p_\nu}$ = momentum of the incoming neutrino.
- M = mass of the nucleon.
- q = 4-vector momentum transfer from the neutrino to the parton.
- $\vec{q}$ = momentum transfer from the neutrino to the parton.
- ν = energy transferred from the incoming neutrino to the parton.

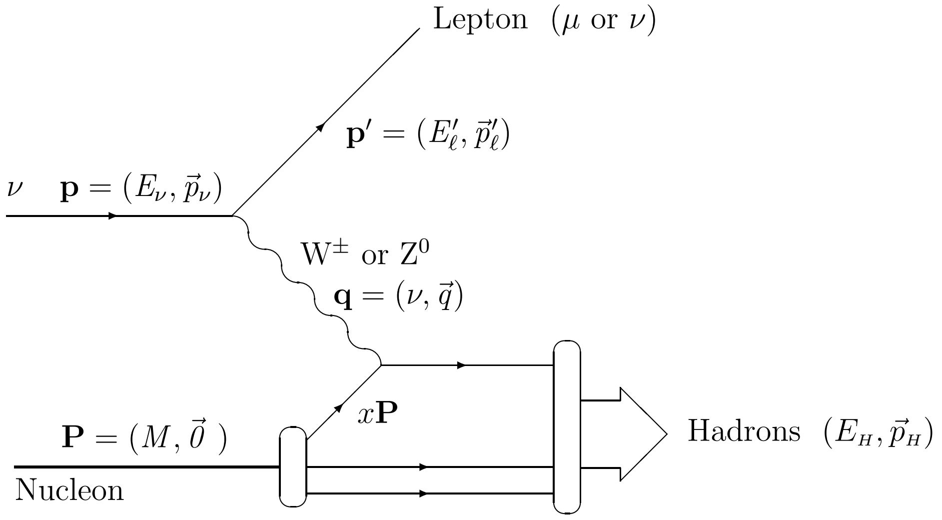

Figure 1.1: Basic Deep Inelastic Scattering

- E'_ℓ = energy of outgoing lepton ($E'_\ell = E_\nu - \nu$).
- $\vec{p_\ell}'$ = momentum of outgoing lepton.
- m'_ℓ = mass of outgoing lepton.
- θ'_ℓ = angle which the outgoing lepton's path makes relative to the path of the incoming neutrino ($\vec{p_\nu} \cdot \vec{p_\ell}' = |\vec{p_\nu}| \left|\vec{p_\ell}'\right| \cos\theta'_\ell$).
- E_H = energy of the hadronic debris shower resulting from the collision and subsequent breakup of the nucleon.
- $\vec{p_H}$ = momentum of the hadron shower.
- W = invariant mass of the final hadron state ($W = \sqrt{E_H^2 - |\vec{p_H}|^2}$).
- x = the fraction of the nucleon's momentum carried by the parton[3].

---

[3] Since in the usual frame of reference the nucleon is stationary, the fact that this fraction is independent of reference frame is relied on for this explanation of x.

- y $= \nu/E_\nu$, the fraction of the incoming neutrino's energy which is transferred to the parton.
- Q^2 $= -q^2$, the square of the 4-momentum transfer from the neutrino to the parton. Since this is a transfer via a virtual particle in the usual Lorentz frame representation with metric $[1, -1, -1, -1]$, q^2 is negative; Q^2 is often used for convenience in notation.

These are some of the more useful equations which relate these to one another:

$$x = \frac{Q^2}{2M\nu}, \qquad Q^2 = 2ME_\nu xy = 2E_\nu \left(E'_\ell - \left|\vec{p_\ell}'\right| \cos\theta'_\ell \right) - m'^2_\ell,$$

$$W^2 \;=\; M^2 + 2M\nu - Q^2 \;=\; M^2 + 2M\nu(1 - x).$$

1.2.2 Constraints on using the Parton Model

The assumed conditions of the interaction in the parton model are that ν and Q^2 are much greater than the masses of the particles involved. While these assumptions are generally close to the actual situation, experimentalists must recognize that they do not always hold true in all cases. Deviations from this *Naïve* Parton Model result from some of the following causes.

- Interactions with low ν or Q^2 are not forbidden in nature — they are just not described well by this model. Experimental cuts may be used to avoid some of this difficulty; extensions to the naïve parton model based on observed behavior may be also used to describe the actual physical interactions occuring in the $Q^2 \sim M$ region of phase space. QCD models may be of assistance in predicting the form of some of these model extensions.

- There is an assumption that the parton has no momentum or spin-polarization components orthogonal to the path of the probing neutrino (*i.e.,* there is so much momentum in the $\vec{p_\nu}$ direction of the system that any other momentum components may be safely ignored for the duration of the interaction). This is not necessarily true, and the effects of transverse momentum must be considered when it is more than a few % of the actual longitudinal momentum.

- Another case in which the $Q^2 \gg M$ condition does not strictly hold is in dealing with very massive partons, such as c and b quarks. Even when the momentum transfer is large compared with all of the other components, when such massive objects participate in the interaction, the naïve model must be adjusted to compensate for this breakdown in the basic assumed conditions.

1.3 Cross sections for neutrino and anti-neutrino deep inelastic scattering from nucleons

1.3.1 General kinematic description of the ν and $\overline{\nu}$ DIS differential cross sections

Due to kinematic constraints at the lepton and hadron interaction points, the cross section in ν and $\overline{\nu}$ deep inelastic scattering may vary with respect to observable quantities. The total cross section varies almost linearly with E_ν. The differential cross section with respect to a number of different choices of measurable quantity can be shown to vary as a function of the angle of the outgoing lepton. The dependence on θ'_ℓ is in part due to the lepton interaction. Due to kinematic constraints, it also is due to the properties of the parton at the other end of the 4-momentum transfer.

This hadronic sector θ'_ℓ-dependence is expressed in terms of *structure functions.* We can choose to differentiate the cross section (σ) over the measurable quantities Q^2 and ν, for example. The relationship between θ'_ℓ and the nucleon structure functions can be expressed for neutrino-nucleon DIS as:

$$\frac{d^2\sigma^\nu}{dQ^2 d\nu} = \frac{G_F^2 E'_\ell}{2\pi E_\nu}\left\{W_2(Q^2,\nu)\cos^2\frac{\theta'_\ell}{2} + \left[2W_1(Q^2,\nu) + \left(\tfrac{E_\nu + E'_\ell}{M}\right)W_3(Q^2,\nu)\right]\sin^2\frac{\theta'_\ell}{2}\right\}$$

where W_1, W_2, and W_3 are the structure functions of the nucleon. W_1 and W_2 may be distinguished by measuring the angular distributions of the outgoing leptons. W_3 is only found in weak interactions and covers their parity-violating components.

These structure functions are all functions of Q^2 and ν. They are related to the momentum distributions and spin-polarization states of the partons in ways that their relationships to each other can also be established. Thus, it is possible to extract details of the structure of a nucleon from simple observations of DIS interaction products.

1.3.2 The differential cross section in the Parton Model

It is customary in neutrino DIS experiments to use a set of measurable quantities different from that used in the earlier equation. It can be shown that assuming Parton Model conditions (Q^2, $\nu \to \infty$ with $Q^2/\nu =$ *constant*) and making certain substitutions of variables such as

$$MW_1 \to \textit{(parton limit)} \to F_1 \quad \text{and} \quad \nu W_2 \to \textit{(parton limit)} \to F_2,$$

the following expression is equivalent to the earlier differential cross section for neutrino and anti-neutrino deep inelastic scattering:

$$\begin{aligned}\frac{d^2\sigma^{\overset{(-)}{\nu}N}}{dx\,dy} &= \mathcal{K}E_\nu\mathcal{P}(Q^2)\left\{y^2xF_1(x,Q^2)+\left(1-y-\frac{Mxy}{2E_\nu}\right)F_2(x,Q^2)\right. \\ &\qquad\left.\pm\left(y-y^2/2\right)xF_3(x,Q^2)\right\}.\end{aligned} \tag{1.1}$$

The xF_3 term is added in ν DIS and subtracted in $\overline{\nu}$ DIS. $\mathcal{K}$ is a constant which equals G_F^2M/π. $\mathcal{P}(Q^2)$ is a *propagator* factor, used to take into account the actual mass of the vector boson carrying the momentum transfer. In ν DIS, this mediator is a virtual particle, and at actual experimentally-achieved energies, the effect of the boson mass is small.

$$\mathcal{P}(Q^2)=\frac{M^4_{(W,Z)}}{(Q^2+M^2_{(W,Z)})^2}\approx 1.$$

The dependencies on θ'_ℓ in the first equation have been absorbed into the x- and y-dependencies of the new equation.

This is the nomenclature used in this dissertation. There are other systems of nomenclature used which are equivalent to this one and which may have some advantages over it (*e.g., explicitly* separating out polarization states[5]).

1.3.3 The Significance of the Structure Functions xF_1, F_2, and xF_3

Measuring structure functions gives information about the composition and arrangement of partons within the nucleon. If quarks and gluons are identified as the partons established by DIS experiments, further information may be extracted about the nucleon environment. Neutrino DIS gives direct evidence only for the quarks' characteristics, as neither neutrinos or Intermediate Vector Bosons couple to the gluons themselves. The structure functions can be seen as functions of the electric charge, spin-polarization and momentum distributions of the various quarks and anti-quarks inside a nucleon.

1.3.4 Parton distribution functions

Each kind of parton in a nucleon has an x-dependent population distribution, $f^{nucleon}_{parton}(x)$, which can be considered as the probability of finding a parton of a particular type which carries a fraction between x and $x + dx$ of that nucleon's momentum. For example, $d^p(0.25)$ is the normalized probability of finding a d quark which carries one-fourth of a proton's momentum. Technically, these *parton distribution functions* (p.d.f.'s) are functions of Q^2 as well as of x, accounting for QCD effects and other deviations from exact *scaling* behavior (*i.e.*, the behavior which lepton-nucleon DIS displays which allows it to be described as lepton-parton *point-like elastic* scattering). For convenience, these will be written as $u^p(x), s^n(x)$, etc. A further shorthand which will be used is to leave off the nucleon-type superscript, allowing the proton p.d.f. to be the default. The neutron u and $\overline{u}$ distributions are considered to be the same as the proton d and $\overline{d}$ distributions, respectively; similarly, the neutron d and $\overline{d}$ distributions are identified with proton u and $\overline{u}$:

$$u(x) = u^p(x) = d^n(x), \qquad d(x) = d^p(x) = u^n(x)$$

$$\overline{u}(x) = \overline{u}^p(x) = \overline{d}^n(x), \qquad \overline{d}(x) = \overline{d}^p(x) = \overline{u}^n(x).$$

The other quark population distributions are considered to be the same in both protons and neutrons. Any contributions to the cross section from the presence of virtual bottom or top quarks in the nucleon are neglected (the charm quark contributions are very small, but are taken into account).

As nucleons have no net charm or strangeness, $s(x) = \overline{s}(x)$ and $c(x) = \overline{c}(x)$. The excess of $u(x)$ and $d(x)$ over their respective anti-quark distributions are termed the *valence* quark distributions. These anti-quark distributions and the fraction of the total u and d quark distributions which match them join the strange and charm quark and anti-quark as the *sea* (or *ocean*) of particles continuously emerging from and being reabsorbed by the gluon population of the nucleon, with which the neutrinos have no direct interactions.

Parton distribution functions are parameterized by theorists and fit to numerous sets of nucleon scattering data. The set of p.d.f.'s used in this study is known as HMRS-BCDMS[6].

1.3.5 Charged current structure functions

In expressing the structure functions F_2 and xF_3 for charged current neutrino and anti-neutrino DIS as functions of parton distribution functions, a pattern of their characteristics may be discerned (xF_1 will be related to F_2 in section 1.3.7).

- Neutrinos interact with the negatively charged quarks and anti-quarks in a nucleon.
- Anti-neutrinos interact with the positively charged quarks and anti-quarks in a nucleon.
- F_2 is a simple sum of the parton distribution functions of all interacting quarks and anti-quarks; and

- xF_3 is the difference between the parton distribution functions of the interacting quarks and those of the interacting anti-quarks.

These definitions form the basis of the following equations.

$$\begin{aligned}
F_2^{\nu N\to\mu^- X}(x) &= 2x\left[d^N(x)+\overline{u}^N(x)+s^N(x)+\overline{c}^N(x)\right]\\
&= 2x\left[d(x)+\overline{u}(x)+s(x)+\overline{c}(x)\right] \quad (proton)\\
&= 2x\left[u(x)+\overline{d}(x)+s(x)+\overline{c}(x)\right] \quad (neutron)
\end{aligned}$$

$$\begin{aligned}
F_2^{\overline{\nu} N\to\mu^+ X}(x) &= 2x\left[u^N(x)+\overline{d}^N(x)+c^N(x)+\overline{s}^N(x)\right]\\
&= 2x\left[u(x)+\overline{d}(x)+c(x)+\overline{s}(x)\right] \quad (proton)\\
&= 2x\left[d(x)+\overline{u}(x)+c(x)+\overline{s}(x)\right] \quad (neutron)
\end{aligned}$$

$$\begin{aligned}
xF_3^{\nu N\to\mu^- X}(x) &= 2x\left[d^N(x)-\overline{u}^N(x)+s^N(x)-\overline{c}^N(x)\right]\\
&= 2x\left[d(x)-\overline{u}(x)+s(x)-\overline{c}(x)\right] \quad (proton)\\
&= 2x\left[u(x)-\overline{d}(x)+s(x)-\overline{c}(x)\right] \quad (neutron)
\end{aligned}$$

$$\begin{aligned}
xF_3^{\overline{\nu} N\to\mu^+ X}(x) &= 2x\left[u^N(x)-\overline{d}^N(x)+c^N(x)-\overline{s}^N(x)\right]\\
&= 2x\left[u(x)-\overline{d}(x)+c(x)-\overline{s}(x)\right] \quad (proton)\\
&= 2x\left[d(x)-\overline{u}(x)+c(x)-\overline{s}(x)\right] \quad (neutron)
\end{aligned}$$

In practice, these basic definitions are modified to account for mass effects in interactions which produce charm quarks. These modifications will be discussed in section 1.3.8.

1.3.6 Neutral current structure functions

Expressing F_2 and xF_3 for neutral current neutrino and anti-neutrino DIS, it can be seen that the basic patterns established by the charged current structure functions remain. The major difference is that in neutral current weak interactions, neutrinos and anti-neutrinos both couple to all quarks and anti-quarks. The coupling constants are determined by a combination of the weak isospin's longitudinal component (I_3) and the electric charge (Q_e) of the interacting quarks rather than by their electric charges alone, as in charged current interactions. These coupling constants are also functions of $\sin^2\theta_W$:

$$\varepsilon_L^q = I_3^q - \mathrm{Q}_e^q \sin^2\theta_W, \qquad \varepsilon_R^q = -\mathrm{Q}_e^q \sin^2\theta_W.$$

Inserting the I_3 and Q_e of the quark types results in the following values:

$$\varepsilon_L^{u\,2} = \left(+\frac{1}{2} - \frac{2}{3}\sin^2\theta_W\right)^2 \qquad \varepsilon_R^{u\,2} = \left(-\frac{2}{3}\sin^2\theta_W\right)^2$$

$$\varepsilon_L^{d\,2} = \left(-\frac{1}{2} + \frac{1}{3}\sin^2\theta_W\right)^2 \qquad \varepsilon_R^{d\,2} = \left(+\frac{1}{3}\sin^2\theta_W\right)^2.$$

These have been labelled u and d, where u represents coupling to the "up-type" quarks (u, c, t) and d represents coupling to the "down-type" quarks (d, s, b). It can be seen from the definitions that $\varepsilon_{L,R}^{\overline{q}} = -\varepsilon_{L,R}^q$. Since they are used in DIS structure functions only in their squared forms, the labels hold for anti-quark interactions as well as for quark interactions.

There is no difference between the neutrino and anti-neutrino versions of the neutral current structure functions F_2 and xF_3. There is a flip in the sign of the xF_3 term when used, but otherwise the differential cross sections are the same.

The expressions for neutral current F_2 and xF_3 are as follows :

$$\begin{aligned}
F_2^{\overset{(-)}{\nu} N \rightarrow \overset{(-)}{\nu} X}(x) &= 2x\rho^2 \Big\{ \Big[\varepsilon_L^{u\,2} + \varepsilon_R^{u\,2}\Big] \cdot \Big[u^N(x) + \overline{u}^N(x) + c^N(x) + \overline{c}^N(x)\Big] + \\
&\qquad \Big[\varepsilon_L^{d\,2} + \varepsilon_R^{d\,2}\Big] \cdot \Big[d^N(x) + \overline{d}^N(x) + s^N(x) + \overline{s}^N(x)\Big] \Big\} \\
&= 2x\rho^2 \Big\{ \Big[\varepsilon_L^{u\,2} + \varepsilon_R^{u\,2}\Big] \cdot [u(x) + \overline{u}(x) + c(x) + \overline{c}(x)] + \\
&\qquad \Big[\varepsilon_L^{d\,2} + \varepsilon_R^{d\,2}\Big] \cdot \Big[d(x) + \overline{d}(x) + s(x) + \overline{s}(x)\Big] \Big\} \quad (proton) \\
&= 2x\rho^2 \Big\{ \Big[\varepsilon_L^{u\,2} + \varepsilon_R^{u\,2}\Big] \cdot \Big[d(x) + \overline{d}(x) + c(x) + \overline{c}(x)\Big] + \\
&\qquad \Big[\varepsilon_L^{d\,2} + \varepsilon_R^{d\,2}\Big] \cdot [u(x) + \overline{u}(x) + s(x) + \overline{s}(x)] \Big\} \quad (neutron)
\end{aligned}$$

$$\begin{aligned}
xF_3^{\overset{(-)}{\nu} N \rightarrow \overset{(-)}{\nu} X}(x) &= 2x\rho^2 \Big\{ \Big[\varepsilon_L^{u\,2} - \varepsilon_R^{u\,2}\Big] \cdot \Big[u^N(x) - \overline{u}^N(x) + c^N(x) - \overline{c}^N(x)\Big] + \\
&\qquad \Big[\varepsilon_L^{d\,2} - \varepsilon_R^{d\,2}\Big] \cdot \Big[d^N(x) - \overline{d}^N(x) + s^N(x) - \overline{s}^N(x)\Big] \Big\} \\
&= 2x\rho^2 \Big\{ \Big[\varepsilon_L^{u\,2} - \varepsilon_R^{u\,2}\Big] \cdot [u(x) - \overline{u}(x) + c(x) - \overline{c}(x)] + \\
&\qquad \Big[\varepsilon_L^{d\,2} - \varepsilon_R^{d\,2}\Big] \cdot \Big[d(x) - \overline{d}(x) + s(x) - \overline{s}(x)\Big] \Big\} \quad (proton) \\
&= 2x\rho^2 \Big\{ \Big[\varepsilon_L^{u\,2} - \varepsilon_R^{u\,2}\Big] \cdot \Big[d(x) - \overline{d}(x) + c(x) - \overline{c}(x)\Big] + \\
&\qquad \Big[\varepsilon_L^{d\,2} - \varepsilon_R^{d\,2}\Big] \cdot [u(x) - \overline{u}(x) + s(x) - \overline{s}(x)] \Big\} \quad (neutron)
\end{aligned}$$

The ρ^2 factors are included for generality and represent possible deviations from the isospin-charge couplings defined above. This might happen in the case of a Higgs particle which is more complicated than a simple isospin doublet. In practice, ρ^2 is set equal to 1, consistent with the simple Higgs model and with current experimental evidence.

The dependence of the neutral current structure functions upon $\sin^2\theta_W$ makes it possible to use neutrino DIS to determine its value.

1.3.7 Spin polarization, xF_1 and F_2

The nucleon structure functions can be considered to be functions of the spin-polarization states of the partons interacting with those of the virtual bosons transmitting the electroweak forces. The transverse and longitudinal polarization contributions to the cross section can be separated out and called σ_T and σ_L, respectively. Their ratio is defined as $R_L \equiv \sigma_L/\sigma_T$. If all partons are pure spin-$\frac{1}{2}$ fermions, there is no longitudinally polarized coupling in the high momentum transfer limit:

$$\lim_{\nu, Q^2 \to \infty} R_L = 0.$$

It can be shown that

$$\frac{xF_1(x,Q^2)}{F_2(x,Q^2)} = \frac{1}{2}\left(\frac{1}{1+R_L}\right)\left(1+\frac{Q^2}{\nu^2}\right),$$

which reduces to $xF_1 = F_2/2$ in the Parton Model limit (ν and $Q^2 \to \infty$ with $0 < Q^2/\nu < 2M$) with the assumption that the only partons interacting with the neutrinos are spin-$\frac{1}{2}$ quarks. This is called the *Callan-Gross relation* [7].

Since the experimentally achieved Q^2 and ν are not really infinite, the Q^2- and ν-dependence is kept. It is of most importance for high-x events with hadronic shower energies around the low E_h cut. As an example, if $Q^2 = 12$ GeV^2 and $\nu = 11$ GeV, then $x \approx 0.6$ and $\left(1 + \frac{Q^2}{\nu^2}\right) \approx 1.1$. For most experimentally observed events, this quantity is closer to 1.

In the calculated cross sections used, R_L is set to 0, but contributes to the theoretical uncertainty in the resulting measurements, as there is some evidence that R_L is probably non-zero at typical experimental interaction energies[8, 9].

1.3.8 Describing the charm production mechanism with the slow rescaling model

One of the basic assumptions of the Parton Model is that the interaction energies involved are sufficiently large that any masses which the partons might have are completely negligible. The one process which happens measurably often where this assumption is incorrect enough to matter is the production of charm quarks in charged current weak interactions.

Charm quarks ($m_c \approx 1.2 - 1.8$ GeV) are massive enough that low energy transfer neutrino interactions cannot produce them. Higher energy transfer interactions may be able to produce a charm quark, but the amount of energy going into its mass results in observable quantities for a given input energy different from those seen in events where more transferred energy was available to go into kinetic energy or the production of additional hadronic debris particles.

The method used to model this threshold effect and available-energy limitation is *slow rescaling*[10].

For that part of the cross section which represents the conversion of d or s quarks to charm quarks, the scaling variable x is replaced by ξ.

$$\xi = \frac{Q^2 + {m_c}^2}{2M\nu} = x + \frac{{m_c}^2}{2M\nu} = x\left(1 + \frac{{m_c}^2}{Q^2}\right)$$

ξ relates the Q^2 and ν of the interaction under the constraint that some of its energy goes into the charm quark mass instead of being available for the production of other hadronic shower particles or as kinetic energy. $\xi > 1$ implies that there is insufficient 4-momentum transfer in the reaction to create a charm quark at all; in this case, the cross section for this subprocess is set to zero. This is equivalent to including a factor in the subprocess cross section which is a threshold step-function, $\theta(1-\xi)$.

There is another kinematic correction term to the charm production cross section related to the behavior of the outgoing muon. The muon's energy and nucleon reference frame angle depend on the kinematic variables x and y in such a way that a correction to x for a given set of observed muon quantities must be accompanied by a correction to y. This correction is applied to the charm production subprocess in the form of a multiplicative factor:

$$T(y, x, \xi) = 1 - y + \frac{xy}{\xi}$$

This is, in effect, an extra helicity suppression factor.[4] It has little or no effect (*i.e.*, $T \approx 1$) when momentum transfer is large enough that the charm quark really does have negligible mass and transverse spin polarization. It approaches the standard $(1-y)$ helicity suppression behavior in the limit where all energy transfer goes

---

[4] *Helicity* is the normalized dot product of a particle's spin and velocity direction vectors ($\lambda = \vec{\sigma} \cdot \hat{p}/2 = \pm 1/2$). The term *helicity suppression* describes cross section factors handling cases where spin alignment determines whether an interaction takes place or not.

into creating the charm quark, which then has very little momentum and therefore a random spin polarization. Since the $W^\pm$ will only couple to one polarization state, it cannot "see" the charm quark polarization states which point in the wrong direction, and such interactions simply don't happen in the first place.

The final component of the slow rescaling prescription for dealing with charm quark production is the explicit introduction of the Cabibbo-Kobayashi-Maskawa matrix elements corresponding to the weak interaction transitions from d or s to charm. Ordinarily, the composition of the outgoing hadronic vector is irrelevant to the cross section (*e.g.,* most up quarks will interact with a W^- and produce a down quark, while some will produce a strange quark, but the final states are indistinguishable, so there is little point in separating the two cases). In this case, however, the uniqueness of the charmed final hadronic state requires that the actual parent quarks be identified and set apart from those which are not involved. The method uses the C-K-M Matrix elements known historically as the sine and cosine of the *Cabibbo angle*, θ_C (see section 1.1.5 for more information). The representation of the quark isospin doublets as "seen" by the weak interactions incorporates mixing between the d and s quarks.

$$\begin{pmatrix} u \\ d_C \end{pmatrix} = \begin{pmatrix} u \\ d\cos\theta_C + s\sin\theta_C \end{pmatrix}, \quad \begin{pmatrix} c \\ s_C \end{pmatrix} = \begin{pmatrix} c \\ s\cos\theta_C - d\sin\theta_C \end{pmatrix}$$

In the cross section, corrections for this mixing are handled by replacing the usual d, $\bar{d}$, s and $\bar{s}$ parton distribution functions in the structure functions with the appropriate linear combinations of Cabibbo-enhanced or -suppressed, charm threshold- and kinematics-corrected parton distribution functions. These substitutions are as follows (the quark distributions undergo substitution in neutrino scattering, since they are negatively charged, while the anti-quark distributions do so for anti-neutrino scattering, since they have positive charge):

$$\begin{aligned}
\overset{(-)}{d}{}^{N}(x) &\rightarrow \underbrace{\overset{(-)}{d}{}^{N}(x)\cos^2\theta_C}_{(\textit{up}\text{ quark production})} + \underbrace{\theta(1-\xi)\,T(y,x,\xi)\;\overset{(-)}{s}{}^{N}(\xi)\sin^2\theta_C}_{(\textit{charm}\text{ quark production})} \\
\overset{(-)}{s}{}^{N}(x) &\rightarrow \overbrace{\overset{(-)}{s}{}^{N}(x)\sin^2\theta_C} + \overbrace{\theta(1-\xi)\,T(y,x,\xi)\;\overset{(-)}{d}{}^{N}(\xi)\cos^2\theta_C}
\end{aligned}$$

An important characteristic to note is that an increase in energy transfer ν to the hadronic sector of a DIS interaction causes the amount of cross section correction to decrease, as at high ν, $\xi \rightarrow x$.

1.3.9 Radiative corrections

The last major deviations from the simple neutrino DIS cross section which are of major importance are the *radiative corrections*. These are caused by the influence on the total cross section of electromagnetic processes resulting primarily from the acceleration of charged particles in the course of the DIS interaction. The processes contributing most towards these deviations are described in Figure 1.2. Note that only (c) and (d) are possible in neutral current interactions, since the outgoing neutrino does not couple to the photon. The box diagram requires a larger correction than the real photon radiation diagrams; since it is excluded from neutral current interactions, this means that the radiative corrections to the NC cross section will be lower than those to the CC cross section.

In practice, the radiative corrections are determined as a function of the total cross section for an event and applied as a multiplicative factor. Llewellyn-Smith and Wheater[11, 12, 13], have calculated the correction factors $K = \sigma_{corrected}/\sigma_{initial}$ for neutrino scattering from down quarks in CC interactions:

$$K_d^{\nu\,CC} = 1 + \frac{\alpha}{\pi}\left\{\left[\ln\frac{M_{W^\pm}^2}{s_q} + \frac{9}{4}\right] - \frac{1}{9}\left[\frac{2}{3}\ln\frac{s_q}{m_d^2} + \frac{1}{6}\left(\pi^2 - \frac{19}{4}\right)\right]\right\},$$

for anti-neutrino scattering from up quarks in CC interactions:

$$K_u^{\bar{\nu}\,CC} = 1 + \frac{\alpha}{\pi}\left\{\left[\ln\frac{M_{W^\pm}^2}{s_q} + \frac{1}{2}\right] - \frac{4}{9}\left[\frac{2}{3}\ln\frac{s_q}{m_u^2} + \frac{1}{6}\left(\pi^2 - \frac{43}{4}\right)\right]\right\},$$

and for neutral current neutrino and anti-neutrino scattering from any quark:

$$K_q^{\overset{(-)}{\nu}\,NC} = 1 - \frac{\alpha}{\pi}\mathrm{Q}_q^2\left\{\sum_{\chi=L,R}\varepsilon_\chi^{q\,2}\left[\frac{2}{3}\ln\frac{s_q}{m_q^2} + \frac{1}{6}\left(\pi^2 - \frac{v_\chi^{\overset{(-)}{\nu}}}{4}\right)\right]\right\},$$

$$\text{where } \ v_L^{\nu} = v_R^{\bar{\nu}} = 19 \ \text{ and } \ v_R^{\nu} = v_L^{\bar{\nu}} = 43.$$

In these equations, $s_q = 2E_\nu xM + (xM)^2$, a measure of the momentum transfer to the particular quark in question.

These are slowly–varying functions. Uncertainties in quark masses will therefore not contribute much. The factorization makes it possible to separate the radiative corrections from the rest of the cross section information in order to report a "total" radiative correction for the integral over all events. It is best to handle radiative corrections on an event-by-event basis, though, since they may influence the observable quantities: the box diagram transfers momentum between the muon and hadronic shower, potentially altering not only the cross section for the event, but also the observed muon momentum or angle and possibly the measured hadronic shower energy. The radiation of collinear real photons by outgoing muons may also influence such measurements.

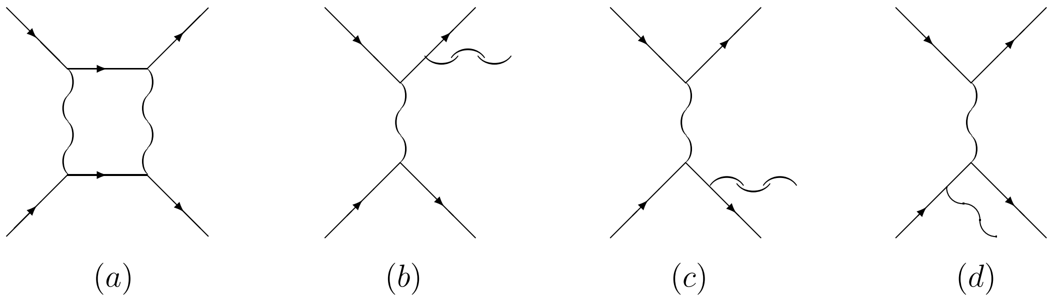

Figure 1.2: Radiative corrections: (a) Box diagram (b) Real photon radiation from outgoing muon (c) Real photon radiation from outgoing quark (d) Real photon radiation from incoming quark

Typical values for the cross section enhancement due to the radiative corrections for experimentally-achieved energies and x's are 1 to 2 per cent for charged current processes and 0.1 to 0.2 per cent for neutral current processes.

1.3.10 The isoscalar correction

In the discussion above, nucleons have been treated collectively, or when appropriate, protons and neutrons have been separately dealt with. The cross section equations can be summed over the two nucleon types in the ratio observed in a given detector, or in any other ratio desired. It is customary to do the calculations assuming an *isoscalar* target (one with equal numbers of protons and neutrons) and then to make a correction for any deviation from this "ideal" state which real detector characteristics would indicate. This is called the *isoscalar correction* to a cross section. The closer a detector is to actually having equal numbers of protons and neutrons, the smaller the isoscalar correction will be.

1.3.11 Other theoretical considerations

The chief remaining qualification to the cross section calculation process refers back to the fact that the parton distribution functions depend not only on x, but also on Q^2, separately. The details of this dependence are intimately linked to QCD calculations, and therefore to the renormalization schemes used in such theoretical approaches. The parton distribution functions used are the outcome of fits of experimental results to a theoretical framework. If the fitting procedure uses a theoretical framework different from that used by the cross section calculations in which the p.d.f.'s are used, incompatibilities may arise.

This happens to be the case with the acceptance-determining Monte Carlo used in this analysis. The basic first-order parton model neutrino DIS cross section equations were used with parton distribution functions from the HMRS-BCDMS fit to a higher order model of the cross section, tied to the $\overline{\mathrm{MS}}$ renormalization scheme. There was reasonable agreement, however, between the Monte Carlo results and the data in most measurable quantities, as shown in Appendix B. This is evidence that any deviation from the modelled cross sections due to the use of parton distribution functions not designed for them was probably insufficient to overcome resolution effects and event statistics and become significant.

1.4 Methods for finding $\sin^2\theta_W$

The measurement made and reported in this dissertation is that of R_ν, the ratio of neutral current to charged current ν_μ-nucleon deep inelastic scattering events. The primary reason for making this measurement is to use it to measure $\sin^2\theta_W$. The next sections will contain a description of how this latter measurement is possible given R_ν, and will also describe several alternative $\sin^2\theta_W$ measurement methods.

1.4.1 The R_ν method

In order to simplify the discussion, let us take the neutral current and charged current cross sections for neutrino DIS discussed in the previous section, limit them to deal only with up and down valence quarks (ignoring quarks & anti-quarks in the nucleon's "ocean"), assume the Callan-Gross relationship and isoscalarity, and then integrate over x and y. It can be shown that the *total* cross sections for NC and CC neutrino interactions under these restrictions will allow the $\sin^2\theta_W$ dependence in the $\varepsilon_{L,R}$ factors to reveal itself in the ratio

$$\mathbf{R}_{\nu\,0} \equiv \frac{\sigma^{\nu\,NC}}{\sigma^{\nu\,CC}} = \frac{1}{2} - \sin^2\theta_W + \frac{20}{27}\sin^4\theta_W.$$

Similarly, for anti-neutrinos, the ratio is

$$\mathbf{R}_{\bar{\nu}\,0} \equiv \frac{\sigma^{\bar{\nu}\,NC}}{\sigma^{\bar{\nu}\,CC}} = \frac{1}{2} - \sin^2\theta_W + \frac{20}{9}\sin^4\theta_W.$$

It happens that the expression for $\mathbf{R}_{\bar{\nu}\,0}$ is near a minimum in the neighborhood of the actual value of $\sin^2\theta_W$, so it is not a sensitive indicator for an accurate determination of that value. This relative insensitivity of $R_{\bar{\nu}}$ and $\sin^2\theta_W$ to one another is beneficial during the data analysis, since it reduces the importance of an exact knowledge of the anti-neutrino content of the data sample. $\mathbf{R}_{\nu\,0}$ *does* vary with $\sin^2\theta_W$ sufficiently sharply to enable an accurate measurement.

In practice, the full expression for the true cross section ratio

$$\mathbf{R}_\nu = \frac{\sigma^{\nu\,NC}_{total}}{\sigma^{\nu\,CC}_{total}}$$

is much more complicated, as can be seen in the previous discussion of the full cross section expressions and corrections (section 1.3). The procedure is the same in principle, however, as in the simplified case. A given value of $\sin^2\theta_W$ should yield a particular $\mathbf{R}_\nu$, determined by the total cross sections.

When cuts are made which affect the x, y and Q^2, the ratio R_ν[5] of the remaining integrated cross sections may be used. This is a function of $\sin^2\theta_W$ *and* of the cuts made. The additional dependence is also calculable, however, so R_ν may be used to determine $\sin^2\theta_W$. This is the ultimate goal of the method used in this analysis.

1.4.2 The Paschos-Wolfenstein test

The *Paschos-Wolfenstein* test measures a ratio

$$R^- \equiv \frac{\sigma^{\nu}_{NC\,total} - \sigma^{\bar\nu}_{NC\,total}}{\sigma^{\nu}_{CC\,total} - \sigma^{\bar\nu}_{CC\,total}}$$

which has the property of being relatively insensitive to the usual Parton Model uncertainties (many sources of such uncertainties are common to the neutrino and anti-neutrino interactions and so cancel in the subtractions). While R^- is appealing due to its theoretical structure, in practice it is not used due mainly to the difficulties in measuring relative neutrino and anti-neutrino fluxes in existing beam

---

[5] Note the distinction between R_ν and $\mathbf{R}_\nu$.

designs. Experimental systematic uncertainty would be large enough to make the improvement in model-dependent uncertainty pointless.

1.4.3 The Standard Model Lagrangian prediction for $M^2_{W^\pm}$

From section 2.1.4, $\sin^2\theta_W$ can be seen in a direct relationship to the mass of the $W^\pm$ bosons and some physical constants:

$$\sin^2\theta_W = \frac{e^2\sqrt{2}}{8G_F M^2_{W^\pm}}$$

This expression depends on the details of the Higgs fields used and the momentum scale of the interaction involving the $W^\pm$, and is strictly true only for low-Q^2 virtual bosons. At the energy and momentum scales of real $W^\pm$ bosons, corrections must be made to the basic relation for the effects of the propagator term in the interaction matrix element. Radiative corrections must also be considered, and in this case they represent a change of 3 to 7 %, the exact value of which depends on unresolved matters such as the top quark mass for rigorous calculational treatment. Such a measurement is also sensitive to uncertainties in the measurement of $M_{W^\pm}$.

1.4.4 The intermediate vector boson mass ratio $M_{W^\pm}/M_{Z^0}$

From section 2.1.4, the ratio of the masses $M_{W^\pm}/M_{Z^0}$ can be seen to be $\cos\theta_W$. Technically, there should also be a dependence on ρ, the neutral current coupling constant correction referred to in section 2.3.1. Taking this into account, it can be found that

$$\sin^2\theta_W = 1 - \frac{M^2_{W^\pm}}{\rho M^2_{Z^0}}.$$

Here, ρ will continue to be considered to equal one (though it may contribute to the theoretical uncertainty). This method is less sensitive to mass measurement uncertainties, since systematic errors will tend to cancel when the ratio is calculated. The chief limiting factors for this process are statistical uncertainties, which continue to decrease as more $W^{\pm}$ and Z^0 events are seen in collider experiments.

1.4.5 Other methods

A number of other particle scattering cross sections can be used to extract a value for $\sin^2\theta_W$. These include

- ν-electron scattering, which suffers from a low overall cross section and therefore, experimentally, from low event statistics;
- charged lepton-nucleon scattering, which suffer from having more complicated radiative corrections than ν-nucleon DIS, as *both* incoming particles are electrically charged; and
- Atomic transition parity violation resulting from γ-Z^0 interference, which suffers mainly from the small magnitude of such interference effects which causes the fractional uncertainty in their measurement to be large.

Chapter 2

Experimental Procedures for Measuring R_ν Using ν_μ DIS

2.1 Neutrino detectors

The basic features of neutrino-nucleon interactions put certain restrictions on neutrino detectors, which have shaped many of the decisions made as to their designs.

1. The small cross section requires a large target mass to provide a sufficiently large number of interactions to analyze for statistically significant measurements of physical quantities.

2. The interactions typically result in a combination of large numbers of hadronic particles and high-energy electromagnetic radiation. Calorimetric detector elements are needed which can measure energy deposition from such a mixture in a consistent way. For practical purposes, the target material also acts as the calorimeter medium in which the energy is deposited. Two quantities which characterize such materials are the *radiation length,* X_0 and the *hadronic interaction length,* Λ_I, which are scale constants for the exponential energy loss

of typical high-energy electrons and hadrons in matter[4, pp. III.15–17, 26–27], respectively.

3. To distinguish between neutral current and charged current events, there must be some way for the detector to signal the presence or absence of a muon amongst the other products of each interaction.

4. In order to study nucleonic structure functions, the outgoing lepton angle and momentum must be measurable in some fashion.

    - For charged current ν_μ interactions, the outgoing lepton is a muon, so some form of magnetic spectrometer is desirable.
    - For neutral current interactions, the outgoing lepton is a neutrino, which is effectively invisible. The only way to measure its properties is to be capable of making good measurements of everything *else* in the interaction. Then it is possible to determine the most likely characteristics of the unseen interaction product.

Two main classes of neutrino detector have been designed and used in the measurement of $\sin^2\theta_W$ by the R_ν method: detectors using electronic readout with nearly all-iron target/calorimeters and those with less dense target/calorimeter compositions, designed for making certain measurements where it is desirable to discriminate between electrons and hadrons in the final state. This additional requirement results in compositions approaching isoscalarity more closely than a simple iron composition, which is a side effect beneficial to the present analysis.

Since bubble chambers fail to satisfy condition #1 above, they will not be included; though they have made contributions to many areas of neutrino physics, they are of limited use for precise measurements of $\sin^2\theta_W$.

2.1.1 Iron calorimeters

CDHSW

The CERN-Dortmund-Heidelberg-Saclay-Warsaw collaboration uses a detector at CERN consisting of 21 magnetized iron toroids with 1.875 m radius and 15 cm thickness, instrumented with scintillators and drift chambers. This gives an energy sample every 8.5 radiation lengths or 0.9 hadronic interaction lengths.

CCFRR

The Chicago-Columbia-FNAL-Rochester collaboration uses a steel target calorimeter in Lab E at Fermilab with a 3.05 m square cross section instrumented with scintillation counters after every 10 cm of steel and drift chambers every 20 cm. This is an energy sample every 5.6 radiation lengths, and a detailed position measurement every 11 radiation lengths. There are just under two energy samples per hadron interaction length. (This is halved if only the drift chamber information is used). The calorimeter is followed by a spectrometer using toroidal magnets and drift chambers for muon momentum measurements.

R_ν analysis strategy: length distributions

Due to the lack of detail available in reconstructing events individually, the analysis of data from the large iron calorimeters focuses on length distributions. Each DIS event deposits energy in some number of detector elements downstream of the interaction site. Because muons are not strongly-interacting particles, they will continue to deposit energy into detector elements for a much greater distance than a hadron can before decaying, interacting with the target material or losing most of its kinetic energy via scattering. Charged current events, which produce muons, will therefore tend to have a greater measured length of energy deposition than neutral current events, which do not.

Even without very good transverse position resolution, and with longitudinal resolutions inadequate for detailed analysis of the development of shower processes, the large iron calorimeters are able to determine the simple distance from the first observed energy deposition in an event to the last. By comparing the length distributions for observed events to those predicted by models, an estimate of the relative frequency of neutral current and charged current DIS interactions may be obtained, yielding a value for R_ν.

2.1.2 Low density, nearly isoscalar calorimeters

CHARM

The CERN-Hamburg-Rome-Moscow collaboration uses a fine-grained calorimeter with instrumentation every radiation length or 0.22 hadronic interaction lengths. The target material was marble (primarily calcium carbonate) during early running and glass (primarily silicon dioxide) in more recent runs. The instrumentation consists of scintillators, proportional drift tubes and streamer tubes. The calorimeter is surrounded by a magnetized iron frame. This is followed by a toroidal iron magnetic spectrometer. Transverse position determination for interaction vertices was as good as 3 cm at high energies.

FMMF at Lab C

This is the detector used in the present analysis, and will be discussed in detail in later sections.

R_ν analysis strategy: pattern recognition

Due to the fineness of the sampling of energy deposition, the lower density fine-grained neutrino detectors have an option which is difficult for the large iron detectors to use. They can take advantage of the properties of muons in an additional way. Not only are muons more likely than hadrons to travel a great distance, but they tend to be far less affected by scattering processes and therefore travel in relatively straight paths through the detector. The increased spatial resolution of the low density detectors enables them to separate out the energy deposition due to the interaction products and then to see if a pattern characteristic of a muon track is discernable. While the muon track's length is still a good indicator of its identity, now other criteria can be determined to more accurately distinguish muons from abnormally-long hadronic showers and to identify muons which would not necessarily pass a cut made purely on the basis of energy deposition length in the detector. This identification is made on an event-by-event basis, and the numbers of events with and without muons found can be processed along with computer models of detector acceptance to determine the underlying value of R_ν.

2.2 FNAL Quadrupole Triplet neutrino beam

The neutrino exposure for the 1987-88 period used the quadrupole triplet wide-band neutrino beam installed in the N-Center line at Fermilab (*see Figure 2.1*). The Tevatron proton beam was extracted into this beamline three or four times per machine cycle at a momentum of 800 GeV/c and directed to a water-cooled beryllium target, 1 inch (2.54 cm) in diameter and 10 to 12 inches (25-30 cm) long. The beam spot on this target was designed to have a FWHM diameter of 2 mm. The target was movable, and travelled about 1.5 inches (4 cm) off the beamline axis in the intervals between neutrino spills. This allowed the protons to pass unimpeded to a dipole magnet further downstream which diverted them to the N-West beamline during part of the slow spill time periods. A typical schedule for fast and slow spill beam extraction is diagrammed in Figure 2.2.

The secondary particles (mainly pions and kaons) resulting from the collisions between the beam protons and the target material, along with any primary protons which did not interact in the target, passed through a 12-foot (3.7 m) long 6 inch (15.2 cm) square water-cooled collimator with a 3.5 inch wide by 1.5 inch high (8.9 cm x 3.8 cm) aperture which provided shielding for the beam-focusing magnetic elements downstream. The collimated beam then passed through and was focused by a series of quadrupole magnets. The design optimally focused particles with 300 GeV/c momenta, but there were no specific momentum-cutting measures taken. There was no steering of charged particles intended. From the quadrupoles, the focused beam passed into an approximately 500-meter long decay pipe. Any charged particles remaining in the beam at the end of this decay region were filtered out by an iron-and-aluminum beam dump followed by about 870 meters of concrete, metal and earth.

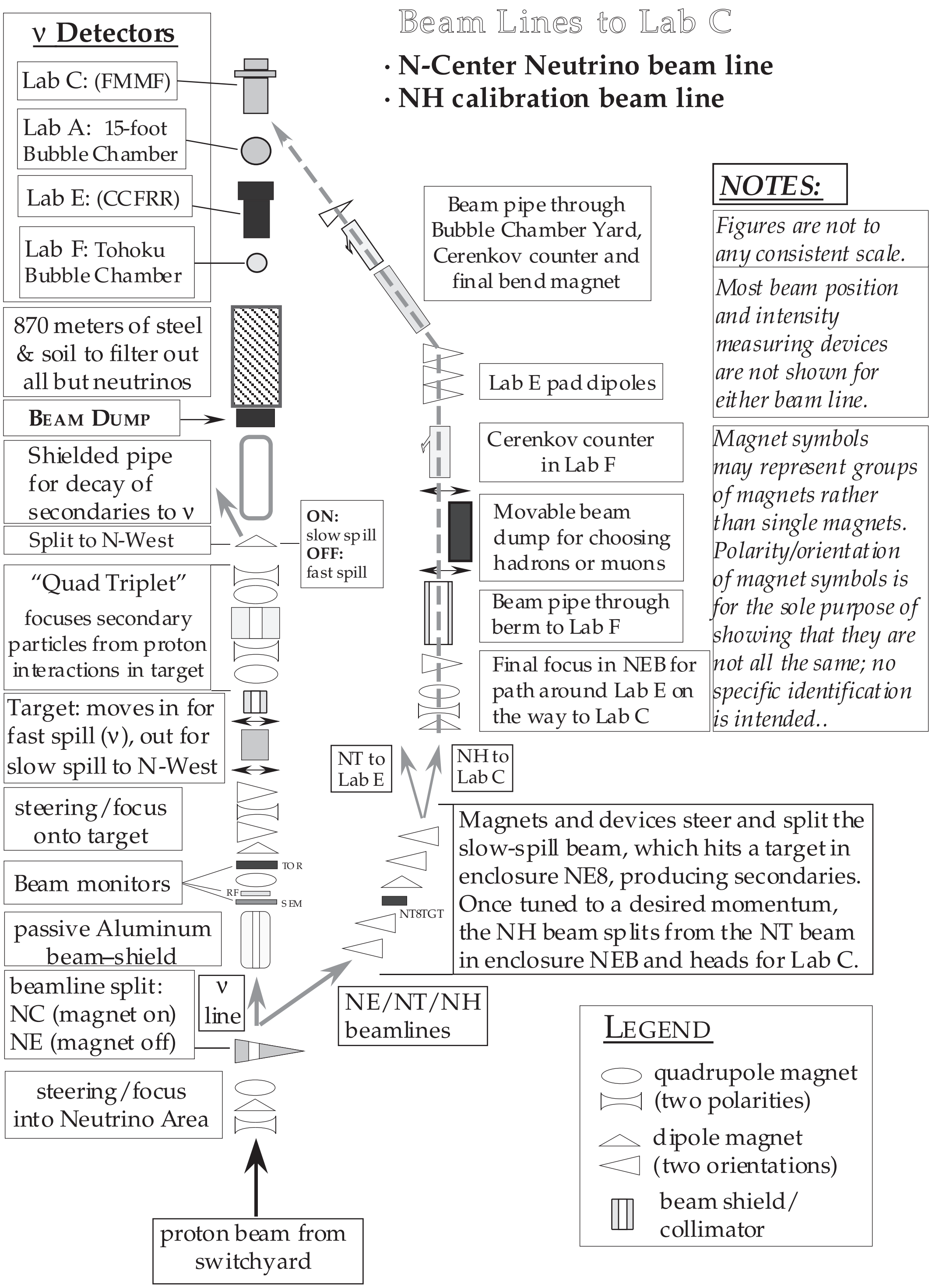

Figure 2.1: The Quadrupole Triplet Neutrino Beam Line and NH Calibration Beam Lines at FNAL

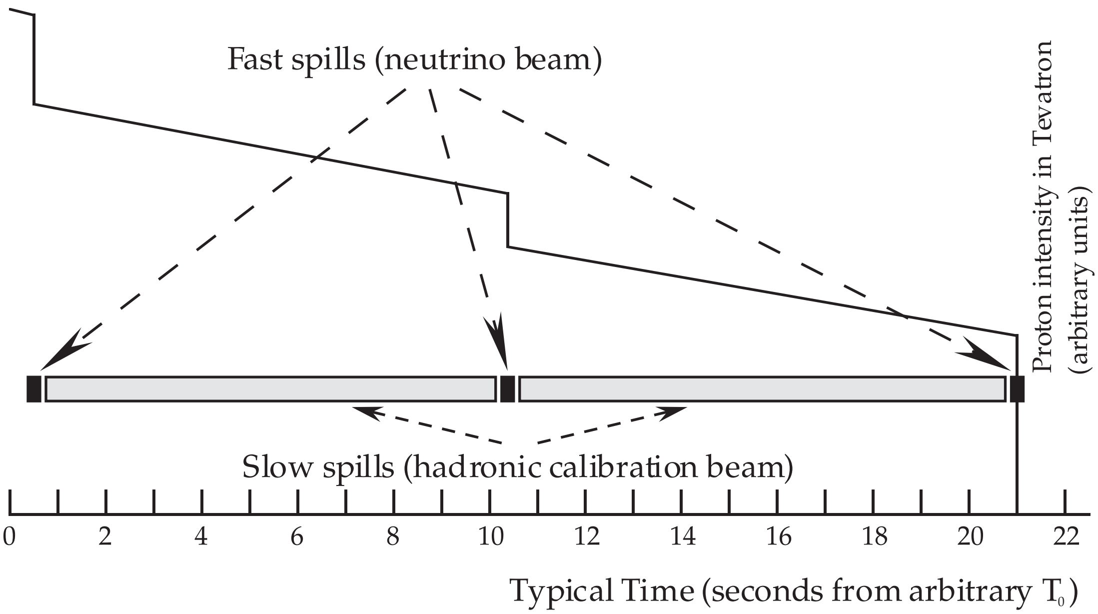

Figure 2.2: Typical schedule for fast/slow extraction to the neutrino area.

The secondary beam and decay pipe pointed towards the neutrino detector area, so neutrinos from the decays of all secondaries were centered approximately on the neutrino detectors. The neutrino beam center during the 1987-88 run was offset by about 8.3 inches (21 cm) from the centerline of the Lab C detector's toroid spectrometer. The center of the anti-neutrino component of the beam was an additional 1.5 inches (3.9 cm) further from the centerline (in nearly the same direction). The energy distribution of the neutrino and anti-neutrino flux within the fiducial volume of the Lab C detector may be seen in Figure 2.3. The radius-dependence of the neutrino energy may be seen in Figure 2.4. From this figure it can be seen that it is possible to distinguish between the types of parent particles for certain events which have sufficiently good vertex position and E_ν measurements.

Detectors of various types were placed along the path of the incoming proton beam. Wire chambers and wire *S*econdary *E*mission *M*onitors (SEMs) provided beam position information for proper beam steering. The proton flux intensity was

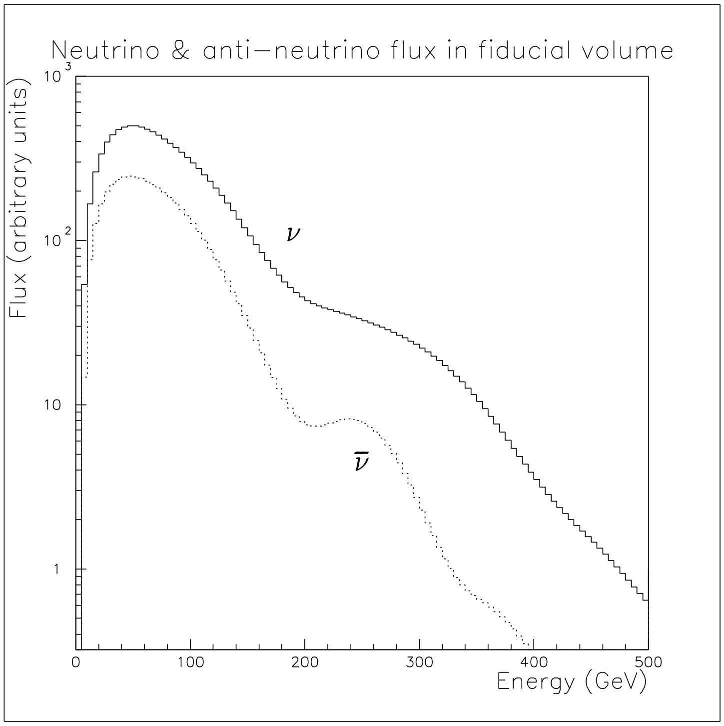

Figure 2.3: ν and $\overline{\nu}$ flux spectra in the fiducial volume of the Lab C detector

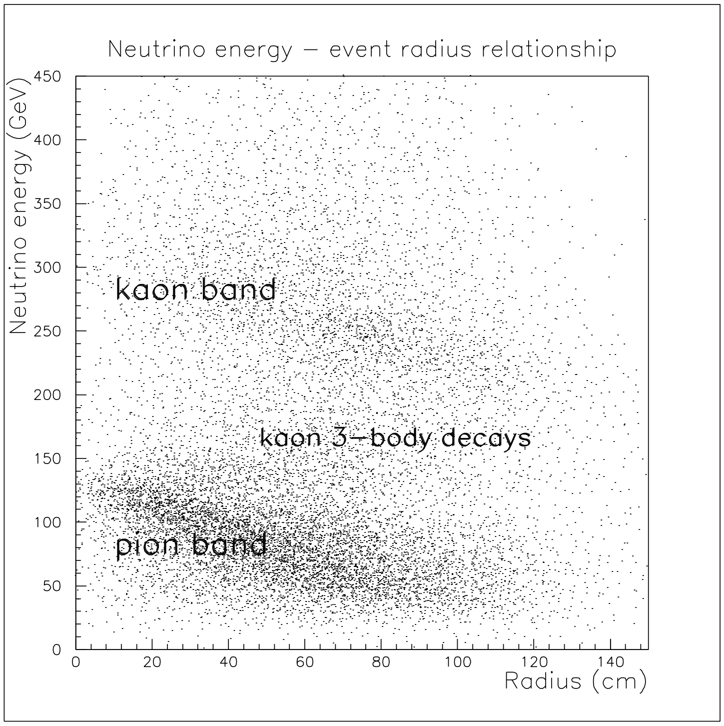

Figure 2.4: E_ν vs event radius from the ν beam center in the fiducial volume of the Lab C neutrino detector

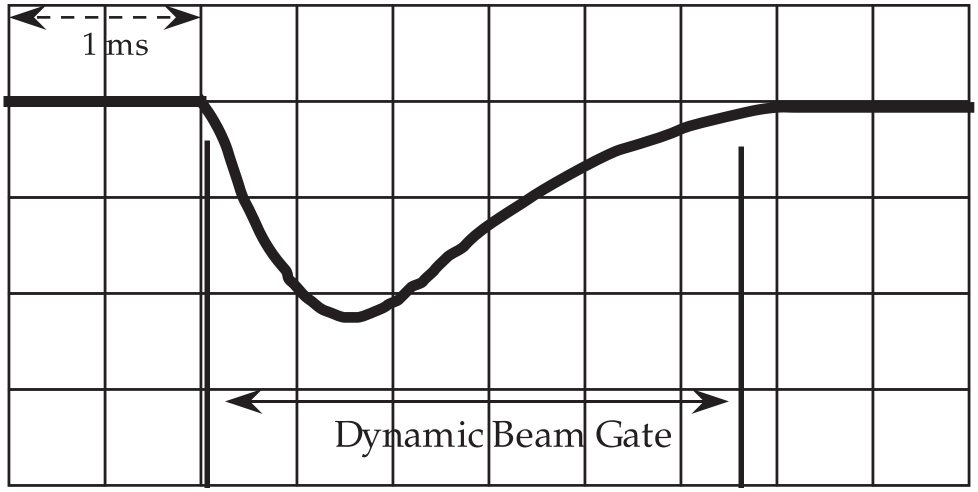

Figure 2.5: Typical Beam Toroid PBM signal used for dynamic beam gate.

measured by a Beam Toroid monitor (TOR), which also provided an internally gated signal-processed measurement called the *P*roton *B*eam *M*eter (PBM). There were also intensity readings from a tuned RF cavity and a SEM placed just upstream of the Beam Toroid.

The Beam Toroid PBM signal was discriminated and provided the *D*ynamic *B*eam *G*ate (DBG), which indicated that there was activity in the neutrino-producing proton beam. This DBG was used to enable the neutrino event triggers in the E733 detector. A fixed-time-interval gate signalled the end of the neutrino spill, at which time the pulser triggered an event if no neutrino event had induced a trigger during that spill. This fixed-time interval also acted as a backup beam gate on occasions when there were hardware problems in the DBG system. Figure 2.5 depicts a typical PBM signal and its resulting DBG.

2.3 The Calibration Beam

In order to calibrate the Lab C detector and better understand its characteristics for the study of neutrino interactions, a beamline supplied it with momentum-selected hadrons or muons during the intervals between fast neutrino beam spills. The hadrons assisted in studying

- the energy scale and resolution of the calorimeter,
- the pattern-recognition capabilities of the analysis software,
- the detector's angular resolution for hadronic showers, and
- the characteristics of such showers, particularly the production of muons from the decay of hadronic particles in the showers.

The muons assisted in studying

- the momentum resolution of the toroidal magnetic spectrometer,
- the angular resolution of muons found with the calorimeter tracking software, and
- the alignment of the detector components.

The general layout of the NH calibration beamline can be found in Figure 2.1. Protons with 800 GeV/c momenta were diverted away from the neutrino beamline for parts of the slow-spill period. They were conveyed to a target in Enclosure NE8, which they hit and interacted with, producing a spectrum of secondary particles. This spray of secondaries was focused and collimated. Those in a particular range of momenta, selected by magnet settings, proceeded down the beamline. The rest were stopped from further progress by a beam dump. The selected momentum range was further restricted by focusing quadrupole magnets and dipole magnets steering it through its path to Lab C.

The final momentum selection was achieved at the trigger level by requiring coincidence in a set of scintillator wands placed along the beam's path, with vetos from scintillator wands placed just outside the desired path. This signal, in conjunction with the usual energy deposition-sensing elements in the detector itself, provided the *test beam trigger*. Information from the scintillator wands in and around the beamline aided in tuning the beam to its maximum useful intensity while ensuring that only particles with appropriate momenta enabled the calibration event trigger. Figure 2.6 shows an example of a calibration beam hadron interacting with the detector (which is described in Chapter 3). Aside from the incoming hadronic track, this shower is a good model for the hadronic showers produced in ν_μ DIS interactions.

Table 2.1 is a list of the momentum settings chosen for the calibration beam during the 1987–88 running period. The standard angle was determined by the approach of the NH beamline to Lab C as it skirted Lab E and the 24-foot Bubble Chamber. It was 0.07 radians off the centerline of the detector. The optional added bend was provided by a set of small dipole magnets just in front of the Lab C detector, which gave the experimenters the chance to probe different sections of the detector, in answer to concerns that the calibration of the calorimeter was based on too small a sampling of the fiducial volume of the detector.

Another attempt to alleviate such concerns was the *deep trigger*, noted in Table 2.1, in which events were rejected if they deposited shower energy in the first quarter

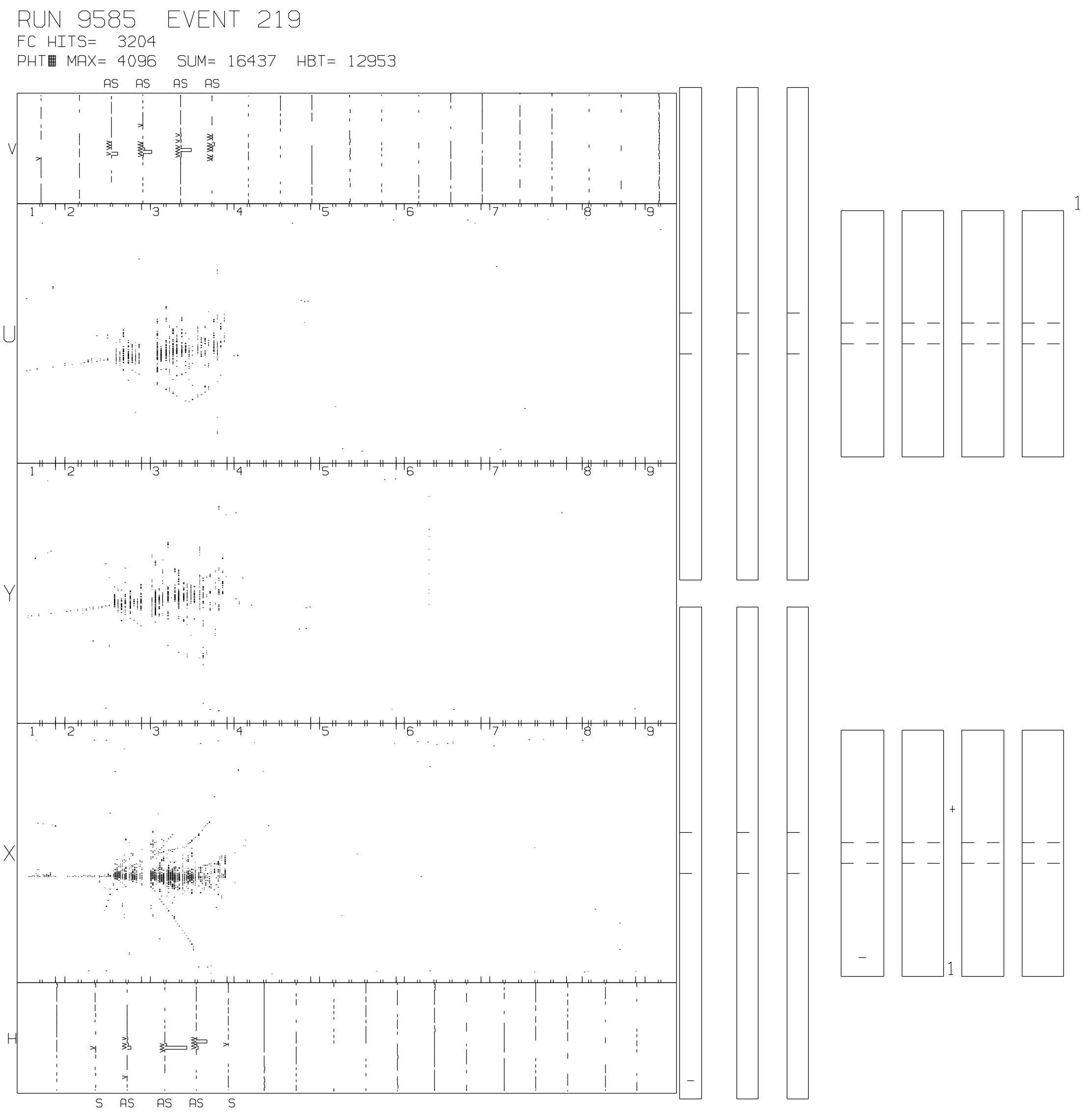

Figure 2.6: A typical calibration beam event (at 70 GeV setting).

For a description of the various detector components displayed in the above figure, see Chapter 3 (particularly Figure 3.1).

Table 2.1: A listing of calibration beam settings used in the 1987 run

Calibration beam momentum settings (GeV) *(sign denotes charge of beam particles selected)*	Std. Angle Hadrons	Deep trigger (veto 10) in some runs	Muon runs	Additional bend angles applied at front of Lab C (mrad, *nominal*)					
				Hadrons			Muons		
				Bend East	Bend Up	Bend Diag	Bend East	Bend Up	Bend Diag
+25	●			*50*					
+50	●	●	$\boxed{\mu}$	*32,50*			*25,50*	35	
+70			$\boxed{\mu}$						
+100			$\boxed{\mu}$						
+250	●								
–25	●								
–50	●				*25,35,50*				
–70	●		$\boxed{\mu}$*	*17*	*10,36*	*17E+17up*	17		*17E+17up*
–75			$\boxed{\mu}$*					*10,25*	
–100	●	●	$\boxed{\mu}$	*17*	*25*	*17E+17up*	*17,25*	*17,25*	*17E+17up*
–150	●	●	$\boxed{\mu}$	*17*	*10*		*17*	*10,17*	
–250	●	●	$\boxed{\mu}$*	*10*			*2,10*	*10*	
–325	●		$\boxed{\mu}$*	*8*			*8*		

**at these settings, no standard-angle* μ *runs were done, only extra-bend runs*

(or, sometimes, third) of the calorimeter. As hadrons are strongly interacting particles, and the calorimeter was over 22 hadronic interaction lengths long, relatively few passed this cut. Those which did, however, showered in a region of the detector rarely reached by the typical calibration beam hadron. This added to the useful calibration zone of the calorimeter.

The accuracy of the momentum selected by the beamline geometry and magnet settings could be confirmed by analysis of data from the two Čerenkov counters placed in the downstream section of the NH line. These counters operated on the principle that relativistic charged particles induce electromagnetic radiation in materials they pass through at speeds greater than that of photons progressing through the same material. This induced *Čerenkov radiation* spreads from the track of the charged particle at a characteristic angle associated with the momentum-to-mass ratio of the particle and the index of refraction of the material.

A Čerenkov counter is a long tube containing a gas (as a transparent medium with a non-unity index of refraction), a mirror (or mirrors) to focus light incident at a particular angle and photo-detectors which record the light from particles whose Čerenkov radiation is at that angle. The simple case is at the minimum angle, where Čerenkov light at wavelengths the photo-detector can register is emitted co-linearly with the charged particles' paths. Here, the momentum-to-mass ratio obeys the relationship

$$\frac{p}{m} = \sqrt{\frac{0.5}{n-1}},$$

where n is the index of refraction.

By setting the counter's mirror to capture this light, and determining the dependence of the gas's index of refraction upon the density of the gas (which in turn depends on its temperature and pressure, both measurable), one can make a good measurement of the actual momenta of the particles in a hadronic beam.

Figure 2.7 shows the changing fraction of particles whose passage was recorded by the Čerenkov counter at a particular beam setting and an approximately constant temperature, as the gas pressure was varied. In this case, one can approximate $n-1$ by a constant k (actually a parameter depending on temperature and wavelength, which are taken to be essentially constant here) times the gas pressure $\mathcal{P}$.

For a given beam momentum, the appearance of Čerenkov light as a pressure is reached signals the transition of the pressure-dependent speed of light in the gas from above to below the speed of a particle whose mass can then be measured, as

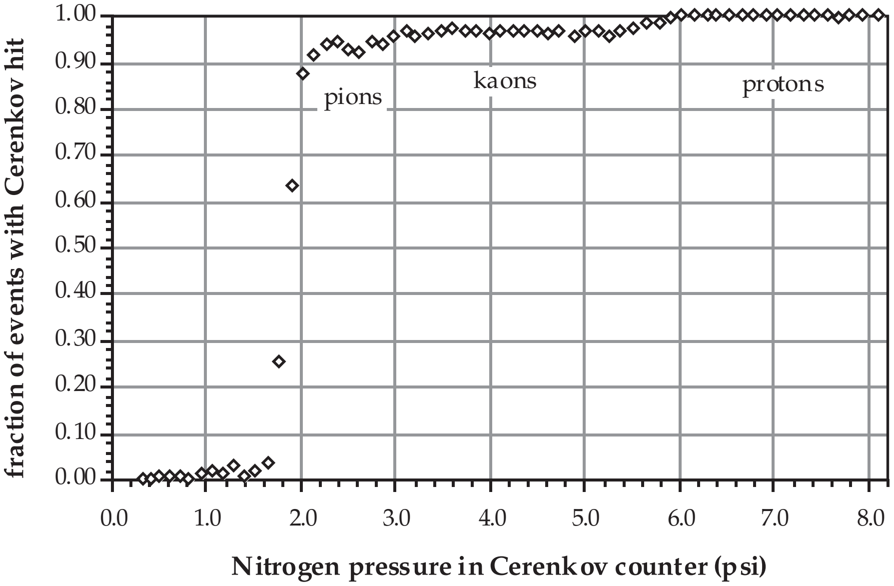

Figure 2.7: Čerenkov counter results for a sequence of nitrogen pressures with a calibration beam momentum setting of 70 GeV

it is proportional to the square root of the gas pressure at the transition point.

$$m = p_{beam}\sqrt{2k\mathcal{P}}$$

Ordinarily, one uses the known particle mass and derives the momentum from the transition points of the pressure-dependent counter-efficiency curve. The detailed shape of the transition curve can provide information on the momentum spread in the beam as well as the central momentum value.

Between this type of analysis and study of the geometry of the beamline elements and trigger-providing scintillator wands and of the magnetic field strengths of the bending magnets, precise estimates can be made of the value and distribution of the calibration beam particles' momenta at the various settings. These were used in calibrating the shower energy scale of the calorimeter, and in measuring its energy resolution. Typical calibration beam momentum spread was 4 per cent or less.

Chapter 3

The Lab C Neutrino Detector

The Lab C neutrino detector had a target/calorimeter of relatively low density material with a very fine-grained instrumentation and a muon spectrometer consisting of instrumented iron toroidal magnets. Figure 3.1 is a representation of the major components of the Lab C neutrino detector.

3.1 The Calorimeter System

3.1.1 Overall Configuration and Nomenclature

The calorimeter as a whole was a structure about 19 meters long, 5 meters wide and 6 meters tall, including the support superstructure. The active region was approximately 12 feet (3.7 m) square by 62 feet (19 m) long.

The calorimeter was constructed of simple, nearly interchangeable, independent sub-units. This is a basic glossary of the system of nomenclature which was used to describe the various functional sub-units, which may appear later in this text.

beam The fundamental construction sub-unit of the calorimeter: one of the 148

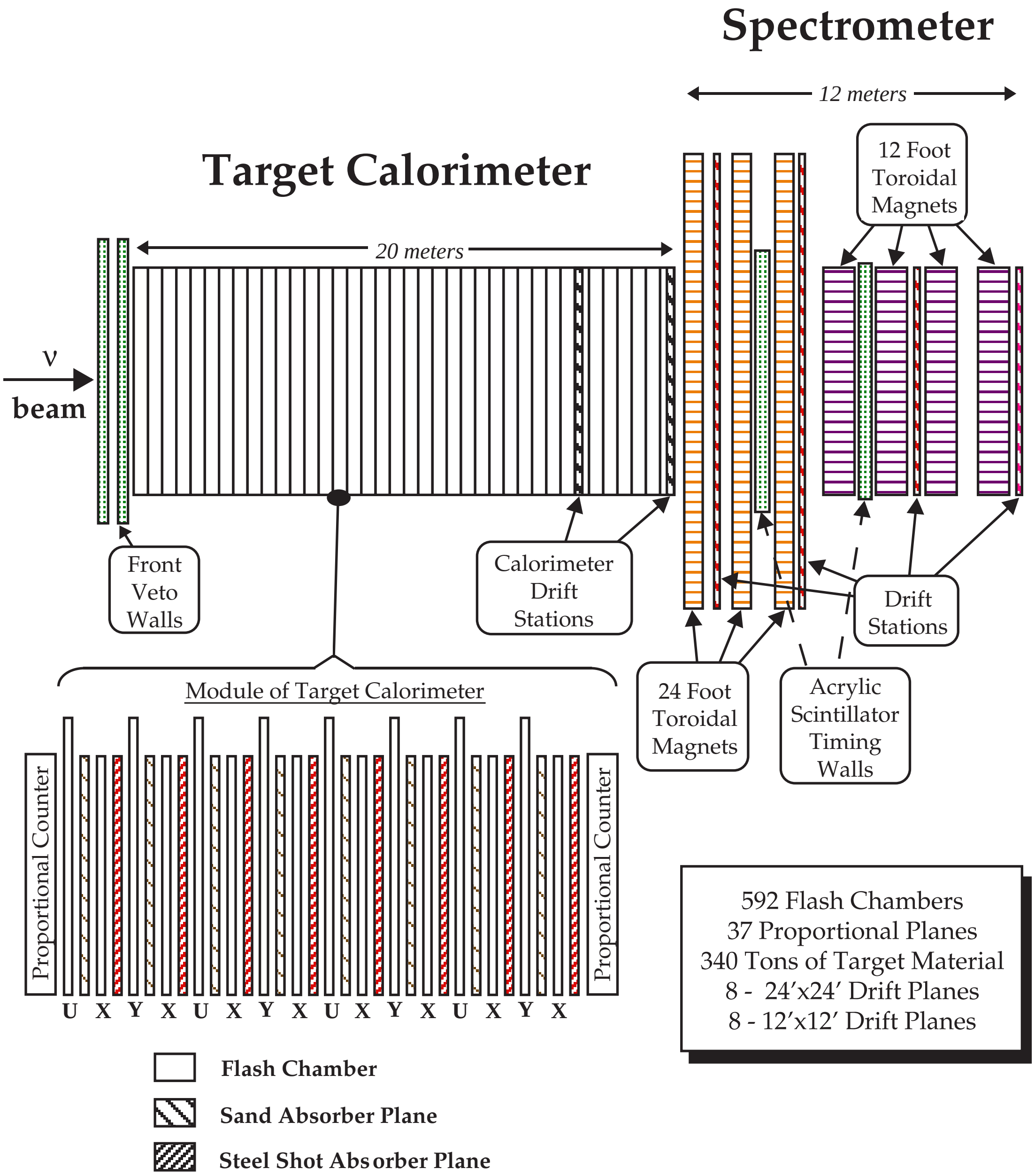

Figure 3.1: The Lab C Neutrino Detector *(this figure courtesy of Wm. G. Cobau)*

box-beams from which target material containers and flash chambers were suspended (four of each).

module The basic sub-unit of the proportional plane system and of the flash chamber high voltage system; generally consisted of four beams and one of the 37 proportional planes. There were 38 modules in the Lab C detector (the module at the downstream end was associated with a set of drift planes instead of the usual proportional plane).

bay A group of two to five modules within the detector, delineated primarily by its overall structural framework (*e.g.,* support columns and I-beams). The bay boundaries were the sites of the liquid scintillators, WIMP detectors, and calorimeter drift planes. Some of the detector subsystems (*e.g.,* flash chamber HV and readout, and proportional plane HV) were grouped by bays for maintenance convenience.

Identification of a module in the detector used either the sequential number from 1 to 38 or, more often, by the bay number and the module position within that bay (*e.g.,* module 5–4 was the fourth module in bay 5, or the 21st of the 38 modules). Similarly, beams were referred to by their position within a module (*e.g.,* the last beam in Bay 2 was labelled 2–5–4).

3.1.2 The Target Material

There were four target material containers per beam, for a total of 592. These containers were extruded Lucite panels, about $\frac{5}{8}$ inches (16 mm) thick, approximately 12 feet long by 12 feet wide (3.7 m x 3.7 m), divided transversely into cells with equal widths of approximately $\frac{5}{8}$ inch (16 mm).

Half of the target panels were filled with pure sand (SiO_2). The other 296 contained steel pellets of various sizes, with typical diameters of two millimeters. The two types of target planes were hung from the beams in the alternating order *sand, steel, sand, steel* (from upstream to downstream). The target was, therefore, a nearly homogeneous substance down to a length scale of half a beam ($\sim$ 6 cm).

3.1.3 The Flash Chambers

Flash chambers are devices in which the application of a triggered high voltage pulse to a set of electrodes generates a glow discharge in a gaseous medium between them at the locations of pre-existing ionization due to the passage of charged particles. It is possible to record the light from the discharge photographically or using optical electronics. The Lab C flash chamber readout relied instead on the electrical properties of the gas which the discharge converted to plasma. The term *flash* was used in Lab C jargon for both the glow discharge and the HV pulse which initiated it.

Flash Chamber Geometry

The flash chambers were about 12 feet (3.7 m) wide, 16 feet (4.9 m) long and $\frac{1}{5}$ inch (5 mm) thick. There were three varieties of flash chamber, which were designated U, X, and Y, based on the orientation of their flash cells.

Four flash chambers hung from each beam, interleaved with the target panels, arranged in the upstream-to-downstream order U, X, Y, X. The flash chambers' gas supply and recirculation system was subdivided at the beam level of organization.

Generally, four beams containing sixteen flash chambers made up a module.[1] The flash chamber high voltage system was subdivided at this level, with a common HV power bus for the chambers in the X-orientation of the module and another for chambers with U- or Y-orientation. The high voltage pulse triggering system lumped modules together into bays, for the most part, as did some of the subsystems involved in flash chamber readout.

Construction

The flash chambers themselves were made of 4 foot (1.22 m) wide extruded polypropylene panels with about 211 rectangular cells each measuring 0.227 inches (5.77 mm) wide by 0.165 inches (4.2 mm) thick and about 16 feet (4.9 m) long. Each flash chamber was constructed from three of these panels in one of three orientations:

- X, with cells horizontal;
- U, with cells tilted 174 mrad ($\approx 10^\circ$) from the vertical, sloping from top east to bottom west[2];
- Y, with cells tilted 174 mrad ($\approx 10^\circ$) from the vertical, sloping from top west to bottom east.

Non-instrumented panelling filled the corners of the U and Y planes, to square off the otherwise parallellogram shape and provide additional structural support. The panelling was held together with mylar tape, which also protected against

---

[1] There were two exceptions, modules 8–1 and 9–2, where two of the beams in the module had been replaced by the calorimeter drift planes, leaving only eight flash chambers and eight target planes.

[2] directions such as “west”, when they are mentioned, are relative to Fermilab’s “Site North”, which is the direction along the neutrino line from the extraction site towards Lab C, or approximately north-northeast in Earth-based coordinates.

inadvertant electrode contact through the gaps between panels. The HV electrodes were sheets of heavy aluminum foil, 5 mils (0.13 mm) thick, 3 feet (0.91 m) wide and originally 14 feet (4.3 m) long, glued to the panel surfaces with a water-based latex contact glue. The overlaps at the edges of the foil sheets were typically 3 inches (76 mm), and were sealed with conductive aluminum tape. The electrodes were trimmed to make a final 12 foot by 14 foot (3.7 m x 4.3 m) active area (including the readout region which projected out from the detector's target area). This also kept a minimum distance of about a foot (0.3 m) from the active HV area and the ends of the cells, which minimized ionization spillover between cells. The gas in this buffer zone is not subject to high electric fields, and acted to quench the plasma discharge in the activated cells before it reached the gas manifold and spread to neighboring cells not already ionized.

The flash chambers were made leak-tight by capping the ends of the polypropylene panels with gas manifolds composed of folded strips of translucent polypropylene fused to the panels by a heating process. This avoided difficulties which might have arisen from outgassing into the flash cells had adhesive bonding techniques been used. The gas was evenly distributed through the manifold by a polypropylene tube with 40 mil (1.0 mm) holes every 2 inches (50 mm) along its length, connected to the inflow/outflow tubing via plastic spigots attached to the gas manifold with teflon seals. Figure 3.2 depicts the connection of a typical flash chamber to the gas recirculation and purification system.

Gas Recirculation and Purification

The gas inflow and outflow tubes were grouped together at the beam level of organization, 12 tubes (3 tubes, one per panel, for each of four flash chambers) connected

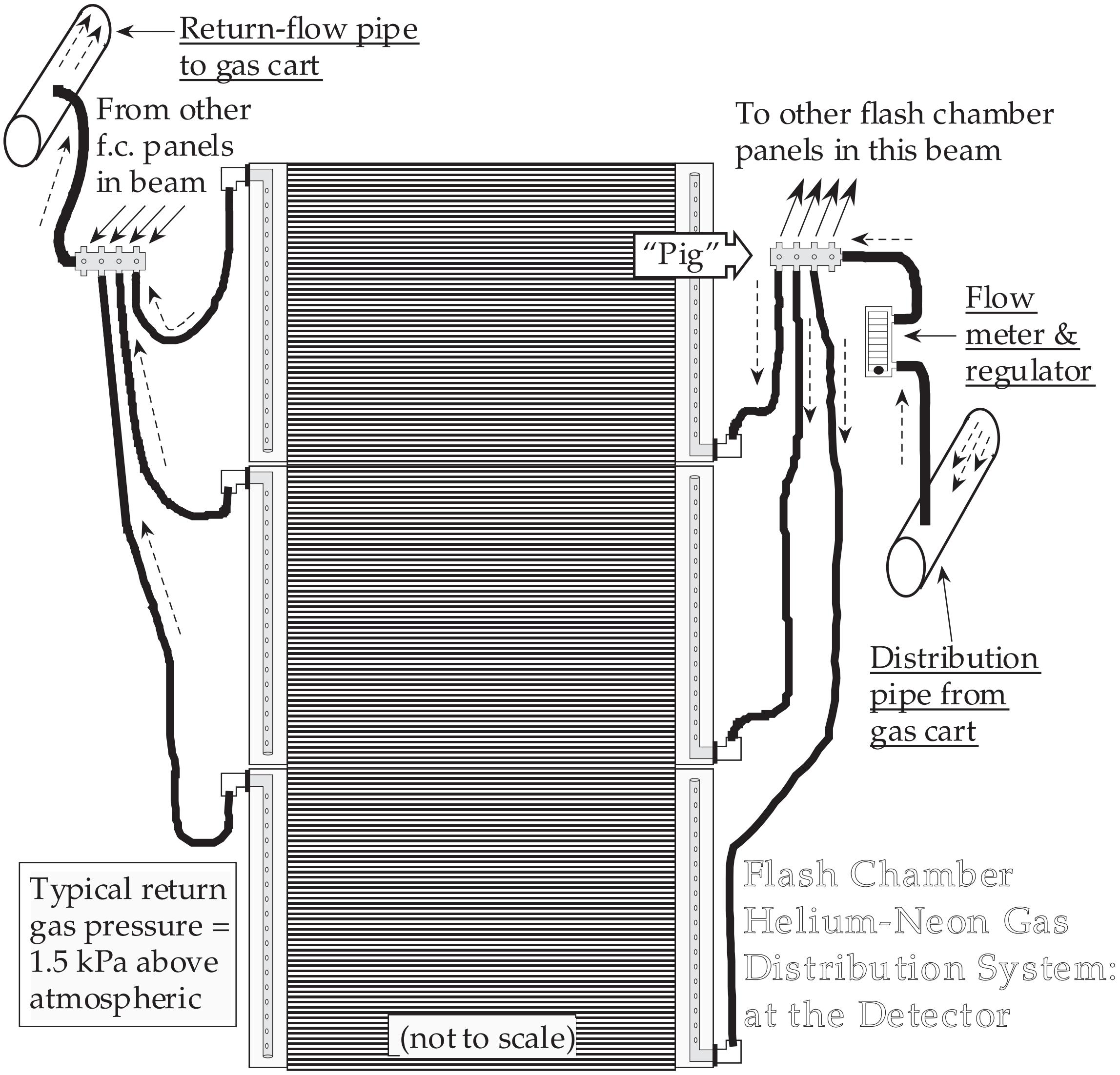

Figure 3.2: Flash Chamber Construction: Gas Recirculation System

to a brass “pig”, the other end of which was connected to the supply or return tubing of the gas recirculation system. The seals were sufficient to maintain a 12.5 kPa over-pressure of helium in a beam with a loss of no more than 0.25 kPa per 10 minutes (and most beams exceeded this specification by a wide margin). Flow rates through the beams were about 9000 cm^3 per minute, approximately two complete volume changes per hour. The usual gas overpressure of the system at the calorimeter was 1 to 1.5 KPa.

The ionization medium in the flash chambers was a purified mixture of 90 % neon and 10 % helium gas, with a very small amount of added Argon ($\approx \frac{1}{8}\%$). To maintain gas purity (and to reduce costs), this gas was recirculated via a system of polypropylene hoses and PVC pipes through the *gas cart* system, which contained filters and molecular sieves at room temperature and liquid N_2 temperature for the purpose of removing contaminants, such as water vapor, nitrogen and oxygen, from the Ne-He mixture. These contaminants could enter the system slowly through the plastic of the panels, manifolds, hoses, and seals of the detector, and via small leaks in the system. They had to be removed since they acted to absorb the ionization resulting from the initial interactions before the HV pulse could propagate it down the cells; in high enough concentrations, they could also interfere with this HV-pulse-induced ion propagation as well. A schematic for this gas cart system may be found in Figure 3.3.

High Voltage Distribution

Flash chambers, unlike proportional planes or scintillators, are only active when triggered externally. At the trigger, a high voltage pulse is produced across the electrodes on each flash chamber, which creates a strong transient electric field in

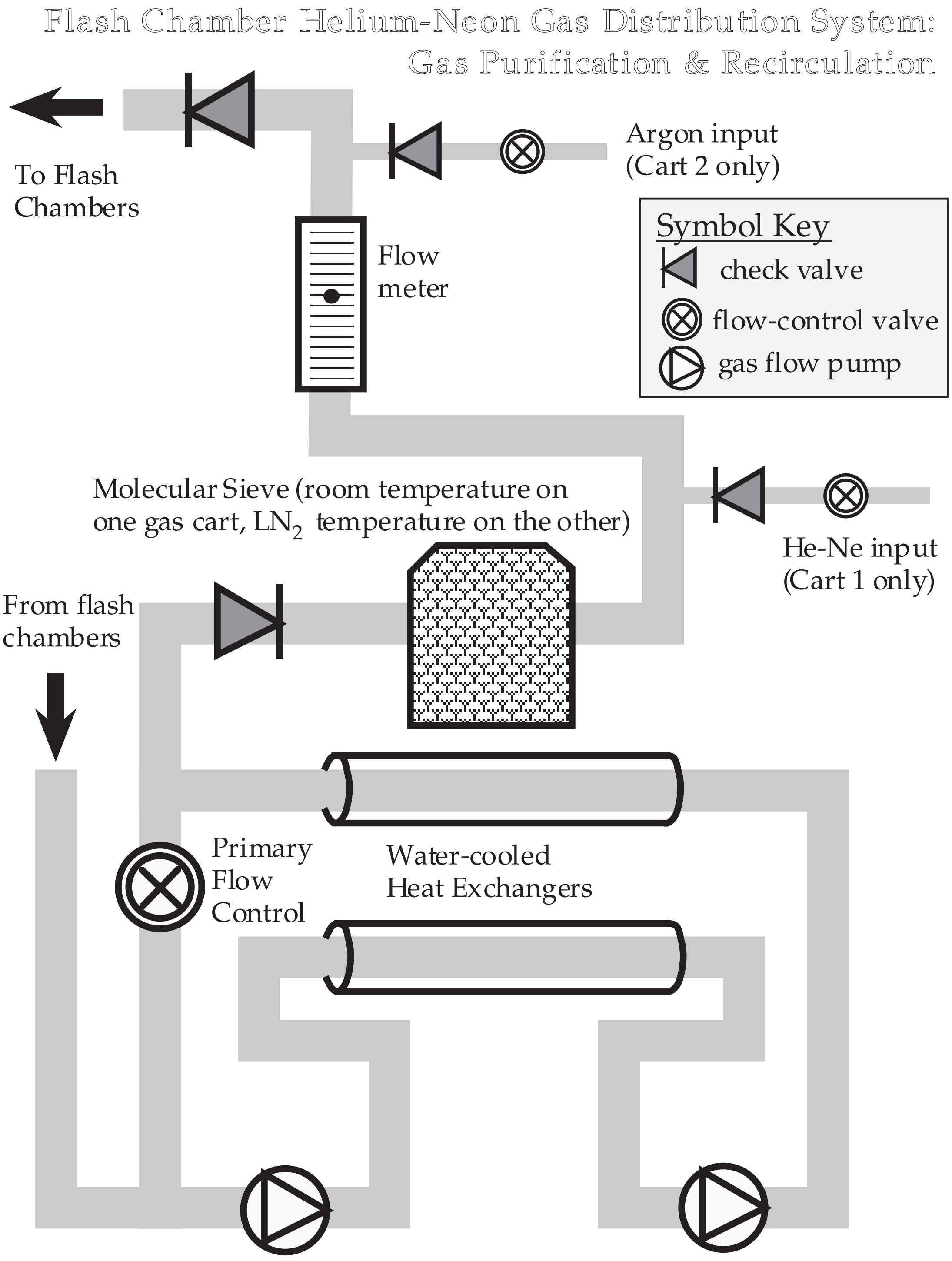

Figure 3.3: Gas Recirculation System: the Gas Carts

the cells between them. Driven by this electric field, any ions present in the Ne-He gas are accelerated, collide with other gas molecules and produce a cascade of ionization. This plasma propagates down the flash cell in both directions over the active region of the chamber, so the readout system at one end of the chamber can detect it.

This process depends on the attributes of the detector and of the generated pulse, and of the interactions between them.

- The voltage of the pulse must be sufficient to induce the required electric field for the ionization process to take place.
- The design of the system must allow the energy of the pulse to be transferred efficiently to the ionization medium without a great loss in voltage across the chamber (*i.e.,* a set of tracks on one side of the detector must not absorb so much of the pulse's energy that it is incapable of inducing a plasma discharge from the ionization trail left by a particle on the other side of the chamber).

To achieve good efficiency independent of location on each chamber, the pulse must have certain characteristics.

- The propagation speed across the chamber must be fast. If the pulse reaches full height much sooner in the region near the HV supply than on the opposite side of the detector, then ionization from two particles traversing the detector at the same time, one near the HV supply and the other far from it, will produce different results. The near particle's ionization track will still be fresh when the HV hits it, and will induce plasma propagation. The far particle's ionization track may have had time to recombine before the HV pulse reaches its position, so there will be nothing left to cause a plasma to form.

- The pulse must have a short rise time. If the high voltage pulse rises too slowly, the smaller electric fields present at the early stages of the pulse may accelerate the ions in the initial particle track quickly enough to reach the electrode before the peak voltage occurs, but not quickly enough to build up the energy needed to cause an ionization cascade and plasma formation. Alternatively, it may not reach the electrode, but may undergo recombination in the time it takes for the electric field to reach a level where it could invoke a plasma discharge.
- The pulse duration must be long enough for the plasma to propagate the length of the flash cell to the readout area.

The Lab C flash chamber high voltage system was supplied by two Hipotronic voltage supplies, one for each half of the detector, supplying each flash chamber in parallel through large HV distribution panels with branch buses for each bay and two taps per module. The standard operating point was 8500 V.

The HV pulse was provided to each chamber by a pulse forming network (PFN) of capacitors, inductors and resistors, with a characteristic impedance of 5 Ω [*see Figure 3.4*], attached to a 30 inch (76 cm) wide tongue extending from the electrodes at one edge of the chamber (the east end of the bottom edge of most X chambers and the middle of the east edge of the U and Y chambers). The high voltage was dumped into the flash chamber through a spark gap which acted as a switch, using a marine spark plug (Champion L-20 V) triggered by a thyratron pulser with a typical rise time of 10 to 15 ns. This spark gap was operated in a dry nitrogen environment, to reduce fire hazards during the spark and to avoid operational degradation due to gradual oxidation of the elements. Each spark gap was manually tuned to guarantee minimum trigger-response time; the spread in actual HV pulse initiation

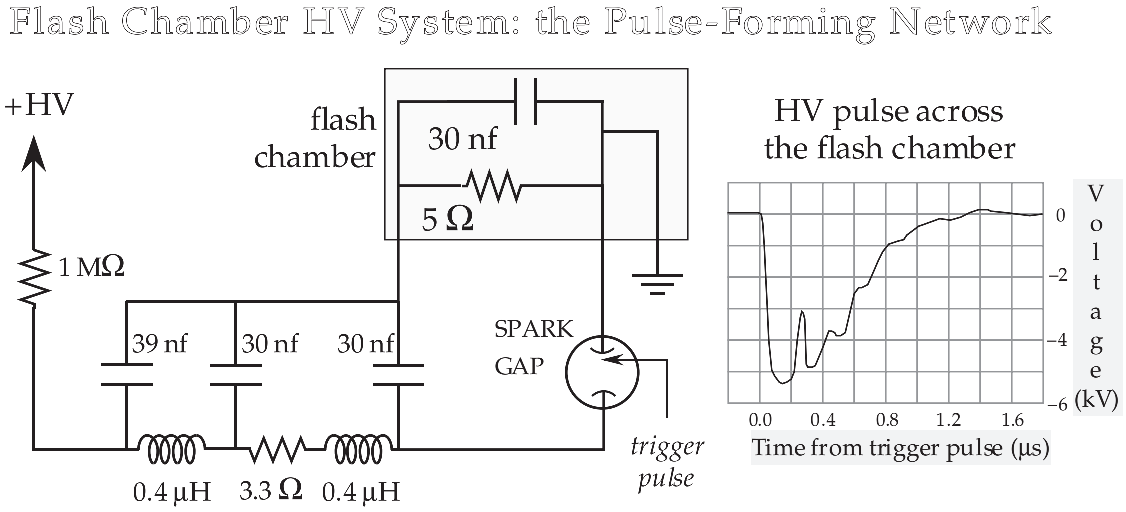

Figure 3.4: Flash chamber HV triggering system pulse-forming network (PFN). *When the spark bridged the gap, the capacitors discharged to ground through the flash chamber, producing the HV pulse.*

from chamber to chamber across the detector was typically less than 15 ns.

With this system, the pulse measured on the chamber had a peak voltage of 5 to 5.5 kV, a rise time of 50 to 60 ns, and a duration of 450 to 600 ns. Since the typical plasma transit time from one end of a cell to the other at these voltages was about 150 ns, this duration was sufficient to ensure thorough propagation of the ionization to the readout area. There were no significant variations in the HV pulse shape over the face of a flash chamber.

A current-sensing system for each of the HV power supplies acted as a safety mechanism, allowing full current draw only at the time of the trigger plus a 4.5 second re-charging period; current flow greater than $\sim$ 1 mA outside this time period tripped off the power supply, requiring a full reset of the HV system. A test mode was available which required human intervention, where the current limiter was set to $\sim$ 5 mA, used for tracking down problems causing HV trips at the standard setting. These measures were taken to reduce the probability of sustained electrical fires due to equipment faults.

Onboard Data Readout System

Figure 3.5 depicts the basic layout of the flash chamber onboard readout system. The readout area was along the edge of each flash chamber[3] extending about two feet (60 cm) in from the edge of the foil ground electrode. Copper strips 3 mm wide and 508 mm long, spaced so as to align with the flash chamber cells, were constructed using photoetched copper-clad mylar sheets and glued to the ground side of the polypropylene panels, beneath the ground electrode foil (and isolated from it by a polypropylene spacer). Each of these strips was connected to a grounded bus at the edge of the active region by a fine sense wire. Each of the strips acted as a cell-wide capacitor plate in conjunction with the high voltage electrode on the other side of the panel; the typical capacitance for each of these strip capacitors was about 3 pF.

When the HV pulse was triggered and cells containing particle-track-induced ionization were filled with a plasma, the change in the dielectric constant of the gas in the cell caused a change in the capacitance of the copper strip/high voltage electrode combination. This change in capacitance induced a current ($\sim$ 500 mA) from those copper strips belonging to the hit cells, through the sense wires, and on to the ground bus.

Current flow in copper strips which did not overlie hit cells was smaller, and mainly due to the passage of the HV pulse between the ground electrode and the hot electrode, 5 mm above and below the strip. The geometry allowed a small delay before the potential of the strip regained equilibrium with the ground electrode

---

[3] the west edge of the X chambers, the top edge of the U and Y chambers

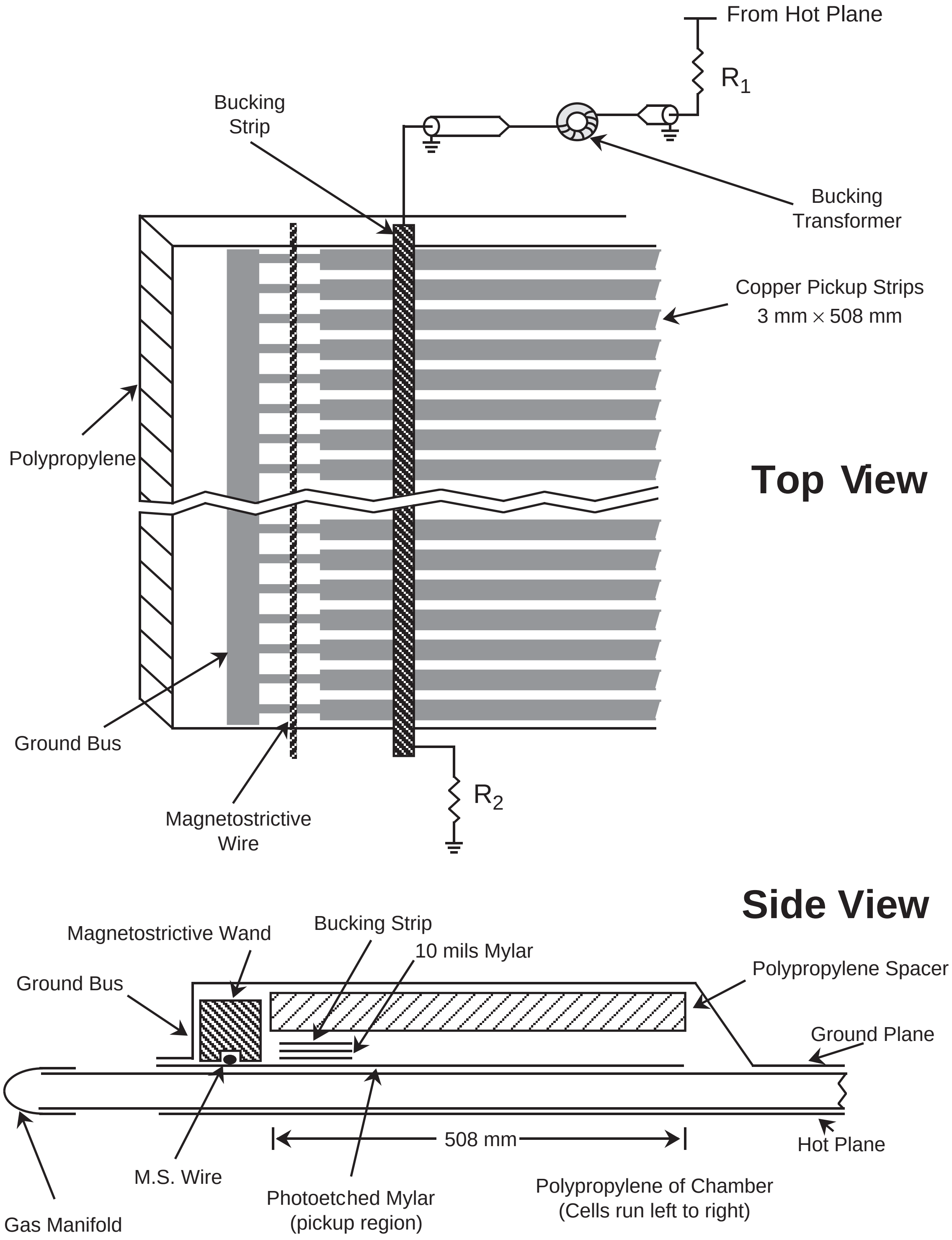

Figure 3.5: Flash Chamber Construction: Readout *(this figure courtesy of Wm. G. Cobau)*

after the HV pulse passed. This brief potential difference induced a current through the sense wires. In general, this current would be less than that induced by the plasma in a hit cell, by roughly a factor of five. To further improve on this signal-to-noise ratio, an additional device was used to reduce the current flow induced solely by the HV pulse. A two inch (5 cm) wide aluminum *bucking strip* was placed across the cells transversely, isolated from the copper strips by two layers of 10 mil (0.25 mm) Mylar, connected to the ground electrode at one end through a resistor and to the hot electrode at the other end through a resistor and a 1-to-1 inverting cable transformer. With the values of the resistors chosen appropriately, this strip delivered an opposite-polarity version of the HV pulse to the region of the copper strip capacitor plates near the sense wires. This pulse was of a magnitude sufficient to cancel the original HV pulse-induced potential drop and current flow through the sense wires, while it had no effect on the plasma-induced current flow. This increased the typical signal-to-noise ratio to 10:1 or greater.

A 5 x 12 mil (0.13 mm x 0.30 mm) Remendur 27 magnetostrictive wire was positioned perpendicularly across the flash chamber cells immediately above the sense wires. The current pulse in a sense wire is accompanied by a magnetic field of similarly limited duration. This magnetic field pulse causes the magnetostrictive wire to contract locally in the region of the sense wire. After the HV pulse, there is no magnetic field and the magnetostrictive wire relaxes. The local contraction/relaxation induces an acoustic pulse, which propagates along the magnetostrictive wire in both directions at the sound speed of the material. In this case, the sound speed was about 5000 m/s, or 5 mm ($\approx$ 1 cell) per μs. The magnetostrictive wire was held in a 10 mil (0.25 mm) deep groove in a long aluminum bar ("wand") and was isolated from it and the sense wires by a tube of teflon tape. Dry nitrogen gas continuously flowed through the teflon tube to deter oxidation or other corrosion of the magnetostrictive wire. The exterior of the wand was wrapped in a solenoidal coil, for the purpose of periodically degaussing and remagnetizing the magnetostrictive wire ("zapping"). It was found that there was an optimum magnetization for each wire which minimized dispersion and limited attenuation of the acoustic pulse on its way from the hit cell's sense wire to the ends of the magnetostrictive wire. Typical attenuation was about 20% per 6 feet (2 m). During the 1987 run, the zapper system remagnetized the wire once per accelerator cycle, during the period immediately after each final neutrino spill.

Each end of the magnetostrictive wire was encased in a small teflon sleeve wrapped with a 50-turn pickup coil of very fine (44-gauge) copper wire and anchored above a small permanent magnet. The anchoring system was designed to minimize reflections and maximize absorption of the acoustic pulse. The acoustic pulse from a hit flash cell travelled along the magnetostrictive wire and vibrating the pickup coil. This vibration of the coil through the stationary field of the permanent magnet induced a voltage between the coil leads, which were connected to a pre-amplifier with a gain of 1000 through a noise-reduction ferrite toroid. This amplified signal then left the flash chamber on its way to the readout system (see section 3.4.1).

3.1.4 The Proportional Planes

In addition to the flash chambers, the calorimeter was also instrumented with a set of 37 proportional planes, one at the downstream boundary of each module (except the last). These planes acted as the primary triggering devices for the neutrino data. They were always active during the time of the neutrino spill, and their continuous measurement of energy deposition in the detector, if any, was the key to deciding when to trigger the flash chambers and the readout systems for all of the detector components.

Construction and Organization

The active region of each proportional plane consisted of 18 segments of extruded aluminum channel (*extrusions*). Each extrusion was composed of eight identical *tubes*, with approximately 1 inch (2.54 cm) square cross sections, 12 feet (3.7 m) long. A gas-distribution manifold was welded to each end of the extrusion. The manifolds were 8-inch by 1-inch 20.3 cm x 2.54 cm) pieces of square aluminum tubing, precision drilled with eight holes to match the center-positions of the tubes in the extrusion. Each tube was threaded with a 50-micron diameter gold-plated tungsten anode wire which was soldered to brass pins at either end. These pins were inserted into and supported by the centered holes in the manifolds at either end and insulated from them by nylon sleeves. The wires were strung between the manifolds under tension, to keep them straight and of a consistent distance to the tube walls. Typical resistance for each wire was 100 Ω and the tube capacitance was 40 pF. Figure 3.6 is a depiction of the end of one basic construction unit, showing some of these features.

After they were strung, eighteen of the extrusions were placed side-by-side and secured to $\frac{1}{4}$-inch-thick (6.3 cm) aluminum plates via bolts through the gas manifolds' non-critical areas, and to an outer support framework which was hung by cables from a trolley located in a channel of UniStrut^{TM} rail attached to the detector's main structure. The trolley system allowed for rolling the proportional plane out of the detector for maintenance. Stresses from the suspension system could

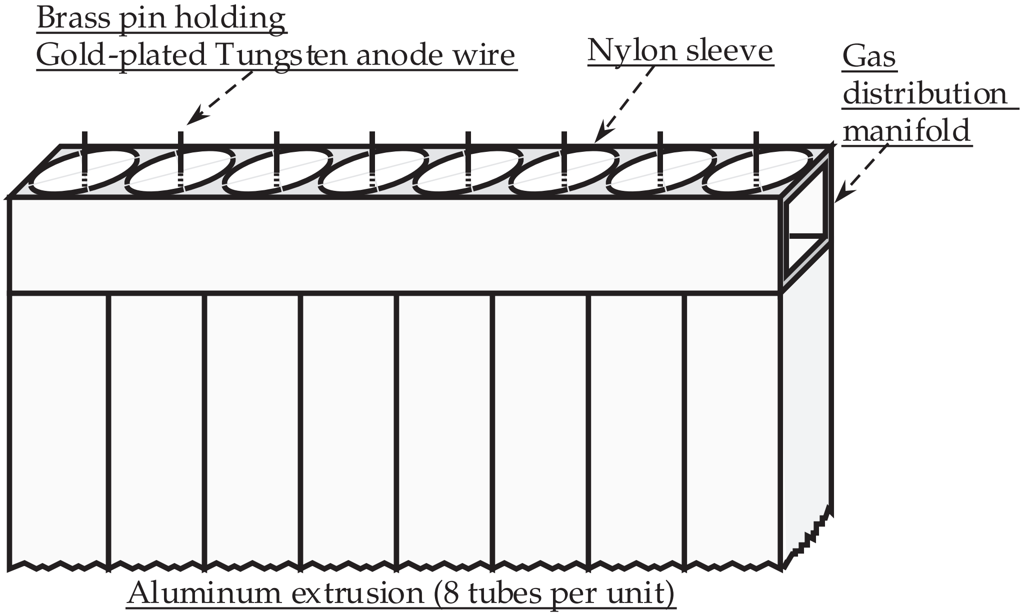

Figure 3.6: Proportional Plane Construction: basic construction unit

result in a slight bowing of the extrusions, which were minimized by a strategically placed alignment clamping mechanism, consisting of 10-mil (0.25 mm) brass shims and $\frac{1}{8}$-inch (3.2 mm) diameter steel rods (for a visual representation of the clamping mechanism, see Figure 3.7). The sagitta of clamped extrusions was $< \frac{1}{32}$-inch (0.8 mm) over the 12-foot length of the plane; this results in a very uniform distance from the anode wires to the extruded tubes' inner walls, which establishes a uniform electric field within the tube, leading to homogeneous response to the passage of ionizing radiation among all tubes in a plane.

The outer support frame also provided mounts for the on-board readout electronics, which were then shielded from electrical noise by $\frac{1}{16}$-inch-thick aluminum sheets, forming an enclosure within the framework.

This design provided a total active area of 12 feet by 12 feet (3.7 m x 3.7 m).

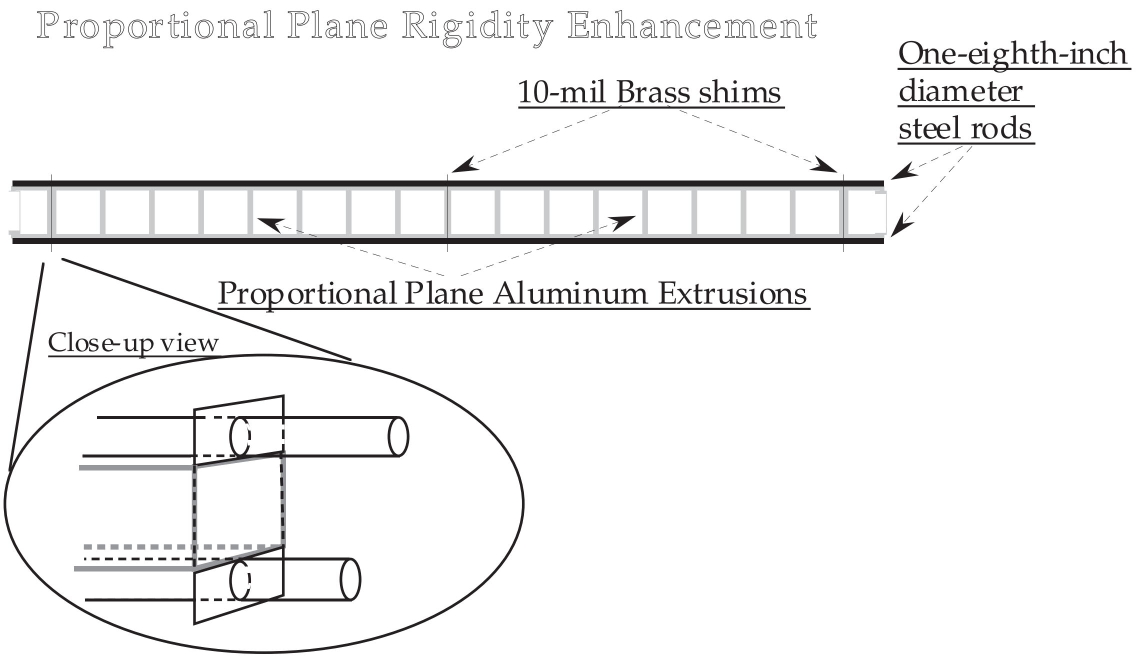

Figure 3.7: Proportional Plane Construction: Extrusion Clamping system

The orientation of the tubes was either horizontal or vertical, and the two types of planes were placed in alternating order through the calorimeter.

Gas system and gain monitoring

The ionization medium used in the proportional planes was a mixture of 90% Argon and 10% Methane (CH_4), called P-10, fed in parallel under very low overpressure to all extrusions in each plane. The gas was supplied to each plane at a flow rate of about 0.5 ft^3 ($14\ \ell^3$) per hour; since the volume of each plane was about 12 ft^3, this represented a complete exchange of gas per day. No attempt was made to recirculate this gas.

Because the P-10 gas was essentially at atmospheric pressure, its density varied with temperature and barometric pressure. Corrections to the gain and efficiency of the proportional planes could be made based on measurements of these quantities, so thermal and barometric measurements were made and put into the data structure for later analysis. Another potential source of gain variations was variance in exact composition between different batches of P-10 gas. Estimates of this effect could be made based on high-precision chemical analysis.

A system for checking these results was designed to assist in calibrating the proportional planes. At several locations on each proportional plane, Cd^{109} sources were mounted, providing 21.7 keV photons which interact in the P-10 of nearby tubes, depositing an energy roughly that of 3 or 4 traversals by minimum ionizing particles. By the time of the 1987 run, the age of the Cd^{109} sources (half-life 462 days; installed on the detector before the 1985 run) was great enough to severely limit the number of channels which could be successfully illuminated for these calibration purposes. In earlier runs, a stability had been seen in relative performance between neighboring channels; this was relied on when calibrating the 1987 run's proportional plane response characteristics.

Construction of the Electronics and HV systems

Nine amplifier cards with four channels each were mounted at the gas input end of the framework. Each amplifier channel was connected to four adjacent proportional tube wire pins. These were enclosed by noise-reducing aluminum covers, along with their signal and power supply cables. A second electrical noise-proofed aluminum enclosure at one of the corners of the plane contained some first-stage signal-processing electronics and the cable connections for transmitting information to and from the plane (see section 3.4.2).

At the brass pins on the opposite end of the anode wires from the amplifier cards, a positive high voltage was applied through 15 MΩ resistors, from HV buses, grouped by fours, just as the amplifier cards were. The resistors acted to electrically isolate adjacent wires, and also limited current draw in case of a wire's breaking and shorting to the grounded extrusion exterior. The grouping system was useful when trying to locate bad wires. The HV lines were RC-filtered inside the planes as well as being LRC-filtered externally.

3.1.5 Liquid Scintillators and WIMP Detectors

At the bay boundaries there were two types of detectors which were not used directly in the parts of the 1987 neutrino run which enter into this analysis.

After bays 1, 6, 7, and 8 were steel tanks, covering a roughly 12-foot by 12-foot (3.7 m x 3.7 m) area and about 5 inches (13 cm) thick, filled with a scintillating liquid and instrumented with photomultiplier tubes. In earlier runs, these had been placed after bays 1–8, and had played a role in vetoing triggers on events caused by interactions upstream from the calorimeter which spilled into the front of the detector. They continued to play an indirect role by providing triggers for the cosmic ray events used to track time dependent response changes in the flash chambers.

Between the 1985 and 1987 runs, the liquid scintillator tanks after bays 2 through 5 were removed and replaced by a system of acrylic plastic scintillator sheets, each about 6.6 feet long by 1 foot wide by 1 inch thick (200 cm x 31 cm x 2.5 cm), encased in a light-tight combination of materials, mounted in a UniStrut^{TM} framework and instrumented at each end with photomultiplier tubes. These were placed so as to provide about 60% coverage of a region about 2 meters square in each bay gap, in arrays such as shown in Figure 3.8. They were used for time-of-flight analyses

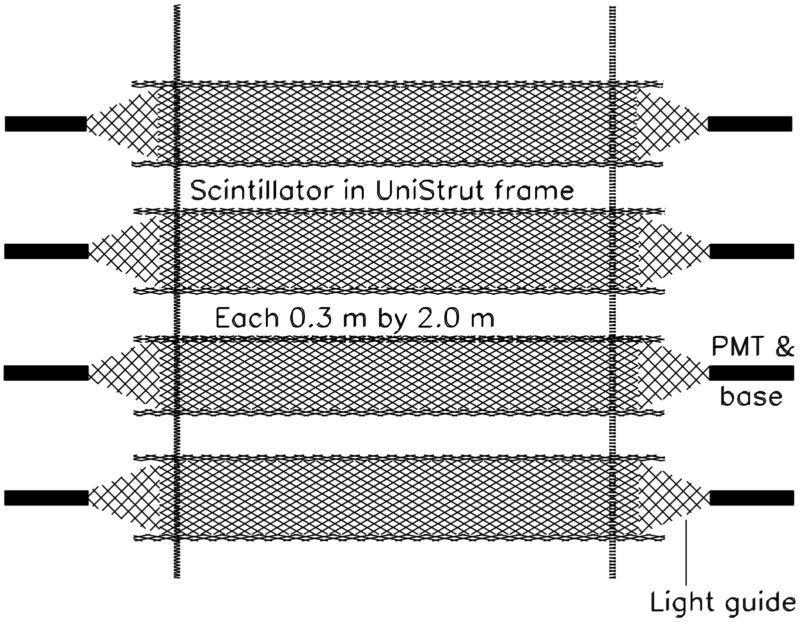

Figure 3.8: Wimp Detector Array

important to exotic particle searches (and so were dubbed the *WIMP detectors*, being sensitive to the effects of Weakly Interacting Massive Particles, should any have been present in the FNAL ν_μ beam), but were of no consequence to the determination of R_ν. They also provided information for the cosmic ray trigger used in the flash chamber response-tracking process.

3.1.6 The Bulk Properties of the Calorimeter System

The detector target was, by mass, predominantly steel and sand. The plastic and aluminum in the detector elements and target-material containers contribute an appreciable amount as well. The WIMP detectors and liquid scintillator tanks, however, are considered to be negligible in the current discussion (though some of the actual analysis software which was most sensitive to their presence was designed to take them into account when it was appropriate to do so).

From the organization of target planes and detector elements, it has been shown that the target medium was nearly homogeneous down to longitudinal length scales of six to ten centimeters. At length scales of over 90 cm (two modules), even the small contribution of the proportional planes averaged out. The characteristics of the detector were such that there was also considerable uniformity in directions transverse to the beam axis over the active area of the calorimeter. Studies of neutrino interaction vertex positions have confirmed these observations.

The target materials' mass was measured in two ways:

1. small ($\approx$ 1 ft x 1 ft) segments of the lucite containers were filled with target materials and carefully measured, and the results scaled up to the full panel size; and
2. seventeen of the 148 beams in the detector were randomly selected and weighed on a calibrated scale before and after being loaded with a full complement of filled target material containers.

There was good agreement between these two methods: the mean weights were within 0.3%, with the RMS spread in the measured weights being $\sim$3%.

This composition[14], with a mean density (including the gaseous components of the detector) of 1.35 g/cm^3, has $< Z > = 9.8$, $< A > = 20.2$, a radiation length $X_0 \approx 14$ cm, interaction length $\Lambda_I \approx 85$ cm, and critical Energy $E_c \approx 38.9$ MeV. The nucleonic composition averaged 49% protons and 51% neutrons.

The flash chambers sampled, on average, every 0.23 X_0 or 0.038 Λ_I. The proportional planes sampled once per 3.4 X_0 or 0.55 Λ_I.

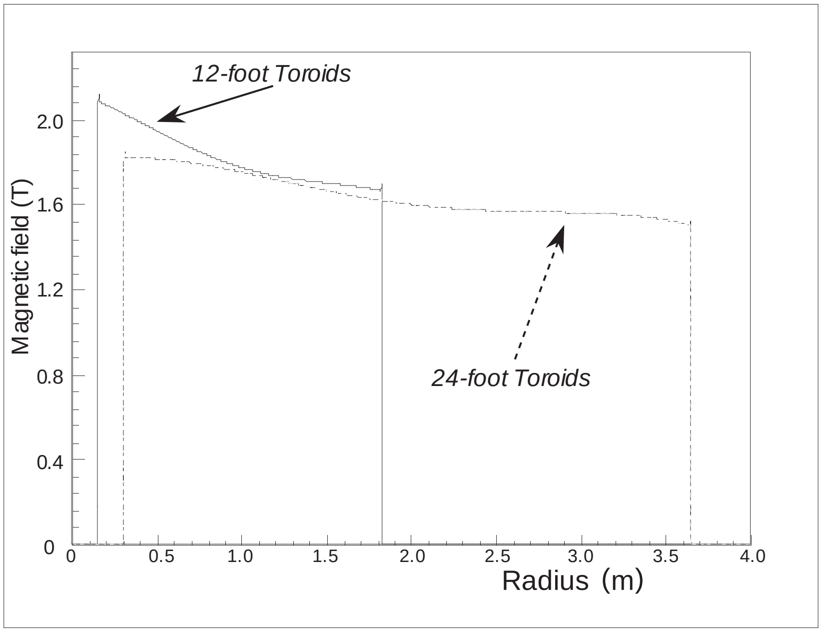

Figure 3.9: Toroid Magnetic Fields as a Function of Radius
These are the functions fitted to the muon data which were used by the muon momentum analysis and spectrometer Monte Carlo programs; they make no attempt to approximate the fringe fields outside the iron toroids, and neglect localized deviations.

3.2 The Spectrometer

3.2.1 The Toroidal Magnets

The magnetic field of the Lab C Neutrino Detector's spectrometer was provided by large iron toroids wrapped with water-cooled electric current conduits. This geometry yielded an approximately uniform solenoidal field throughout most of each toroid. With a nominal current of 800 A, typical magnetic field strengths were 1.6–2.0 Tesla, with a slow variation with radius (*see Figure 3.9*).

The three upstream toroids had a 24-foot (7.32 m) outer diameter, a two-foot (0.61 m) inner diameter and averaged 26 inches (0.65 m) in thickness. The four

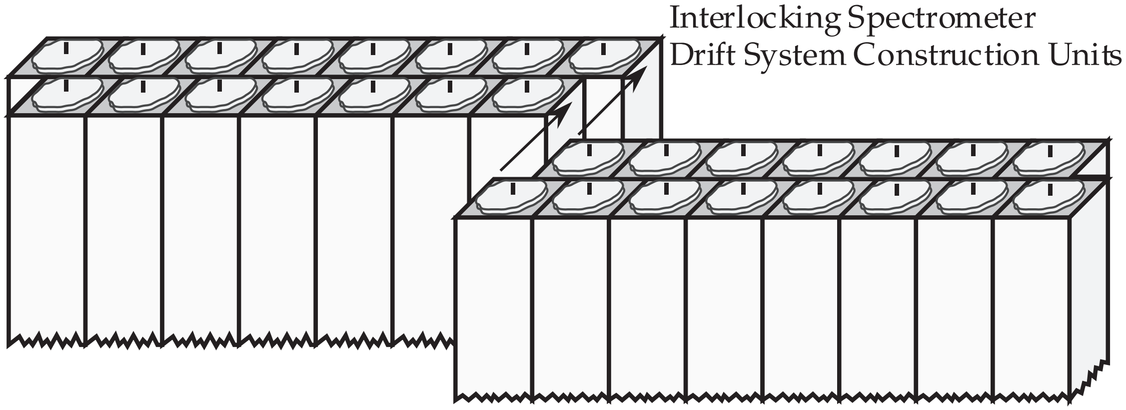

Figure 3.10: Drift Chamber construction unit

downstream toroids had 12-foot (3.66 m) outer diameters, one-foot (0.30 m) inner diameters and averaged 49.5 inches (1.26 m) in thickness. The distance travelled through the spectrometer by a typical muon exposed it to an integrated magnetic field inducing a transverse momentum of 2 to 3 GeV/c.

3.2.2 The Drift Chambers

The spectrometer was instrumented with drift chambers of construction similar to that of the proportional planes. The drift chamber system was arranged in *stations*, each consisting of two double-layered planes, one for each view (horizontal and vertical). The basic construction unit was a double layered aluminum extrusion containing one inch by one inch (2.54 cm x 2.54 cm) cells in staggered rows (*see Figure 3.10*) of the appropriate length, strung with gold-plated tungsten wires under tension (as in the proportional planes).

There were two stations of drift planes in the far downstream end of the calorimeter, in modules 8–1 and 9–2 (the latter being between the last of the calorimeter

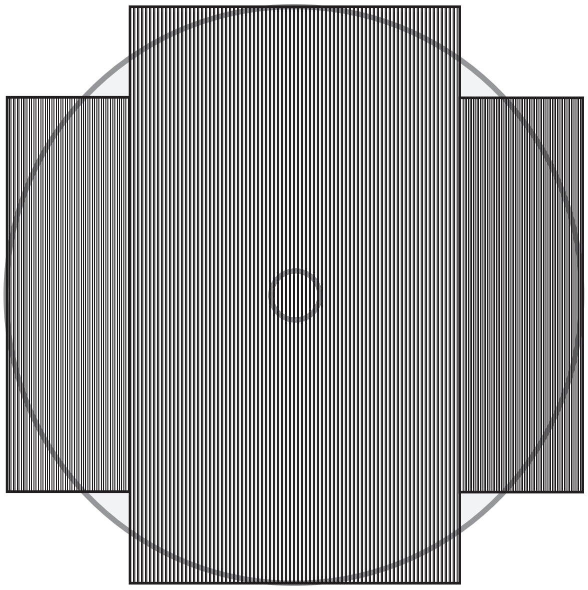

Figure 3.11: 24-foot Drift Plane coverage of magnetic field area

beams and the upstream face of the first iron toroid). Each station had two double-layered planes, 12 feet by 12 feet (3.7 m x 3.7 m).

These could be used to establish the incoming trajectory of a muon precisely, before it encountered the spectrometer magnetic field. They were therefore useful in establishing alignment parameters (with the magnets degaussed) and magnetic field measurements (with usual spectrometer field conditions). They were not used directly in the present analysis.

There were four stations of drift planes in the spectrometer, immediately downstream of odd-numbered toroids (see Figure 3.1). The two stations in the 24-foot toroid region measured about 24 feet by 24 feet (7.3 m x 7.3 m), with notches taken out of the corners where they would have extended well beyond the circular region of the toroid, as shown in Figure 3.11. The two stations in the 12-foot toroid region measured 12 feet by 12 feet (3.7 m x 3.7 m). For readout purposes, the 24-foot drift planes were subdivided into *logical planes*, which had the same number of channels as the 12-foot drift planes.

3.2.3 The Drift Timing Planes

There were timing plane arrays in the gap between the second and third 24-foot toroids (counting from upstream to downstream), and in the gap between the first and second 12-foot toroids. Their purpose was to provide a reference time for the measurement of the ionization travel time in the drift chambers, so that time-to-distance conversions could be made, yielding a spatial resolution for charged particle tracks better than the simple drift-tube width.

The array in the 24-foot toroid region provided about 16-foot by 16-foot (4.9 m x 4.9 m) coverage. The array in the 12-foot toroid region covered about 12 feet by 12 feet (3.7 m x 3.7 m). Each array consisted of two independent sub-arrays. One such sub-array is depicted in Figure 3.12.

These were made from slabs[4] of one inch (2.54 cm) thick scintillating acrylic material, surrounded at the edges by plastic wave-shifting light-pipes leading to photomultiplier tubes (RCA 8575) mounted on active bases. The slabs were mounted in a UniStrut^{TM} framework within large rectangular aluminum cases. The 12-foot sub-array cases' faces were covered and sealed with aluminum sheeting, forming a light-tight boxlike structure. The 24-foot sub-array cases's faces were similarly covered and sealed to light-tightness, but with heavy black polyurethane plastic, doubled over the edges of the case and clamped down with aluminum channeling.

---

[4] 5 ft by 8 ft (1.52 m x 2.44 m) for the timing planes in the 24-foot toroid region; 4 ft by 8 ft (1.22 m x 2.44 m) for the timing planes in the 12-foot toroid region

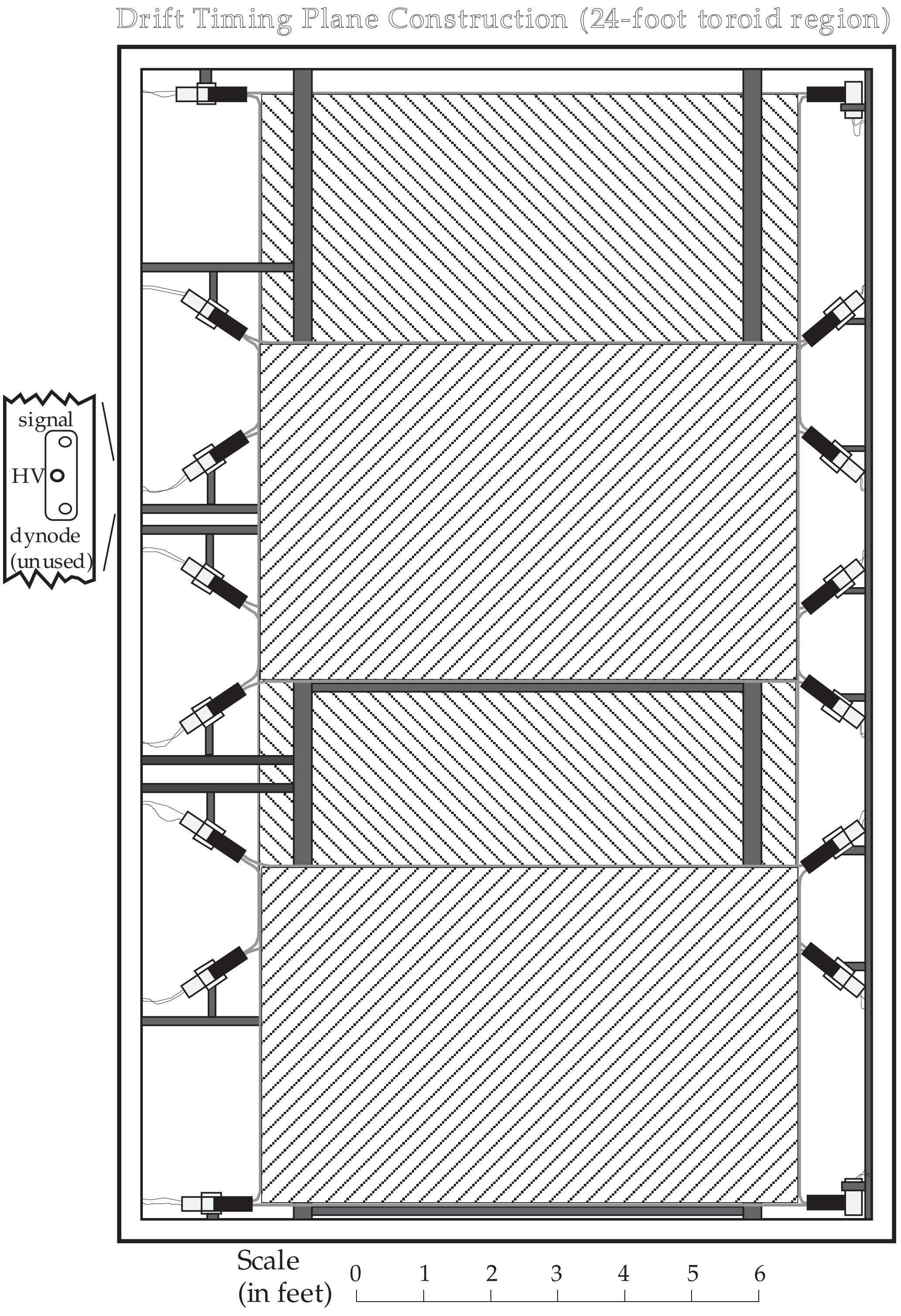

Figure 3.12: Drift Timing Plane Array and Case

Each case was attached to trolleys and suspended from horizontal I-beams. The trolleys allowed the cases to be rolled out from the toroids for maintenance. The cases had light-tight electrical feed-throughs to provide power to the photomultiplier tubes and to export their signals to the readout electronics system. The signal cables on a given array were of equal length to provide equal time delays between the photomultiplier tubes and the readout electronics.

The purpose of having two timing planes was to reduce the fraction of spurious timing plane triggers due to "skyshine". This consisted of low energy particles coming from outside the detector and associated with the neutrino beam spills. Sources included neutrino interactions outside the detector and charged particle interactions far upstream which produced long-lived daughter particles such as neutrons, which could travel through the air above the beamline long enough to reach Lab C before losing all their kinetic energy.

As acrylic scintillator is an efficient detector of low-to-medium energy neutrons, the drift timing planes had an enhanced noise rate during the beam spills. This interfered with a single timing plane's providing a signal corresponding only to the muon which the drift chambers were recording. The skyshine noise, however, was determined to come mainly from low and medium energy particles with steep trajectories. These particles, though visible in the acrylic scintillator, interacted rarely with the drift chamber materials, so the noise problem primarily affected the timing measurements, and not the event itself as seen in the drift chamber readouts.

The solution was to install an acrylic scintillator timing array in the 24-foot toroid region[5] to supplement the existing one in the 12-foot toroid region. A coincidence of

---

[5] This array had been intended originally as the veto wall, but its effectiveness was severely limited by the skyshine noise at the front of the detector.

signals between both timing arrays was required before establishing the drift time reference. This eliminated the problem, as the skyshine particles were not energetic enough in general to survive the initial interaction with the acrylic. Even the higher energy particles among them which did survive were extremely unlikely to proceed then to penetrate two meters of iron and interact with the second timing plane array. They would either interact with material along the way and lose energy, or else had been travelling at too steep a trajectory to have both timing planes in its path in the first place. A side effect of this coincidence requirement was that it virtually eliminated the previously minor noise rate from cosmic ray interactions and electronic noise in the photomultiplier tubes as well.

Since the upstream timing array was larger than the downstream, and the toroidal magnets acted (under normal operating conditions) to focus the negatively charged muons resulting from neutrino charged current interactions, the requirement of a coincidence had a minimal effect on the muon track timing plane measurements. Nearly all of the muons which hit the timing plane array in the 12-foot toroid region had to go through the other timing plane array along their way. As the efficiency for registering muon hits was better than 99% in each array (assuming the muon actually passed through the acrylic), there was a very good chance that a timing could be established for any such muon track.

3.3 Other Detector Elements

3.3.1 The Veto Wall

A *veto wall* is necessary in a neutrino detector, to avoid triggers caused by particles other than neutrinos coming into the detector from the outside. The interaction probability of neutrinos is low enough that it is especially crucial that the rate of non-neutrino events be kept as low as possible. With some sort of veto in place, the experimenters avoid wasting neutrino spill time because the detector has already triggered on some event of no interest. There were three major sources of interfering particles:

1. cosmic rays;
2. muons left over from the decays of the secondaries which produced the neutrinos; and
3. daughter particles from neutrino interactions upstream of the detector.

Cosmic ray events were not specifically vetoed. The rate of cosmic ray interactions in the detector which satisfied the trigger conditions for neutrino events was low enough that the expected number of triggers in the short time spans of the neutrino beam spills was small compared to the expected number of neutrino triggers (see section 3.6 on triggers). Cosmic ray events also have characteristic energy deposition patterns, so software analysis procedures and event-scanning by physicists could also be effective filters.

The other two kinds of external trigger sources both involved ionizing particles entering the front of the detector. The veto wall was an effective strategy for minimizing triggers from these sources, by recording the passage of such ionizing particles and preventing event triggers based on the other components' response to them.

The veto wall used in the Lab C neutrino detector was a two-plane array of 16 acrylic scintillator slabs similar to those used in the drift timing planes in the 24-foot toroid region. The veto wall slabs were, however, enclosed in individual light-tight casings and had photomultiplier tubes on only one pair of diagonally opposite corners. The slabs were arranged on UniStrut^{TM} frames, four per sub-array. The sub-arrays were suspended from trolleys hanging from I-beams, so that they could be moved around for maintenance and testing. They were arranged so that two sub-arrays hung in nearly the same plane with a minimal ($\sim$ 4–6 inch) overlap in the middle. The two planes formed in this manner generally were positioned about three feet (90 cm) apart at the front of the calorimeter. The general arrangement of this system is depicted in Figure 3.13.

The signals from the photomultiplier tubes travelled via equal-length coaxial cables to a rack of electronics modules which amplified them and then summed and discriminated the amplified signals. If there was a coincidence in the signals from both planes of acrylic scintillators, then event triggers were suppressed for $\sim$ 400 ns. The requirement of the coincidence between the two planes minimized spurious vetos from photomultiplier tube noise and skyshine particles.

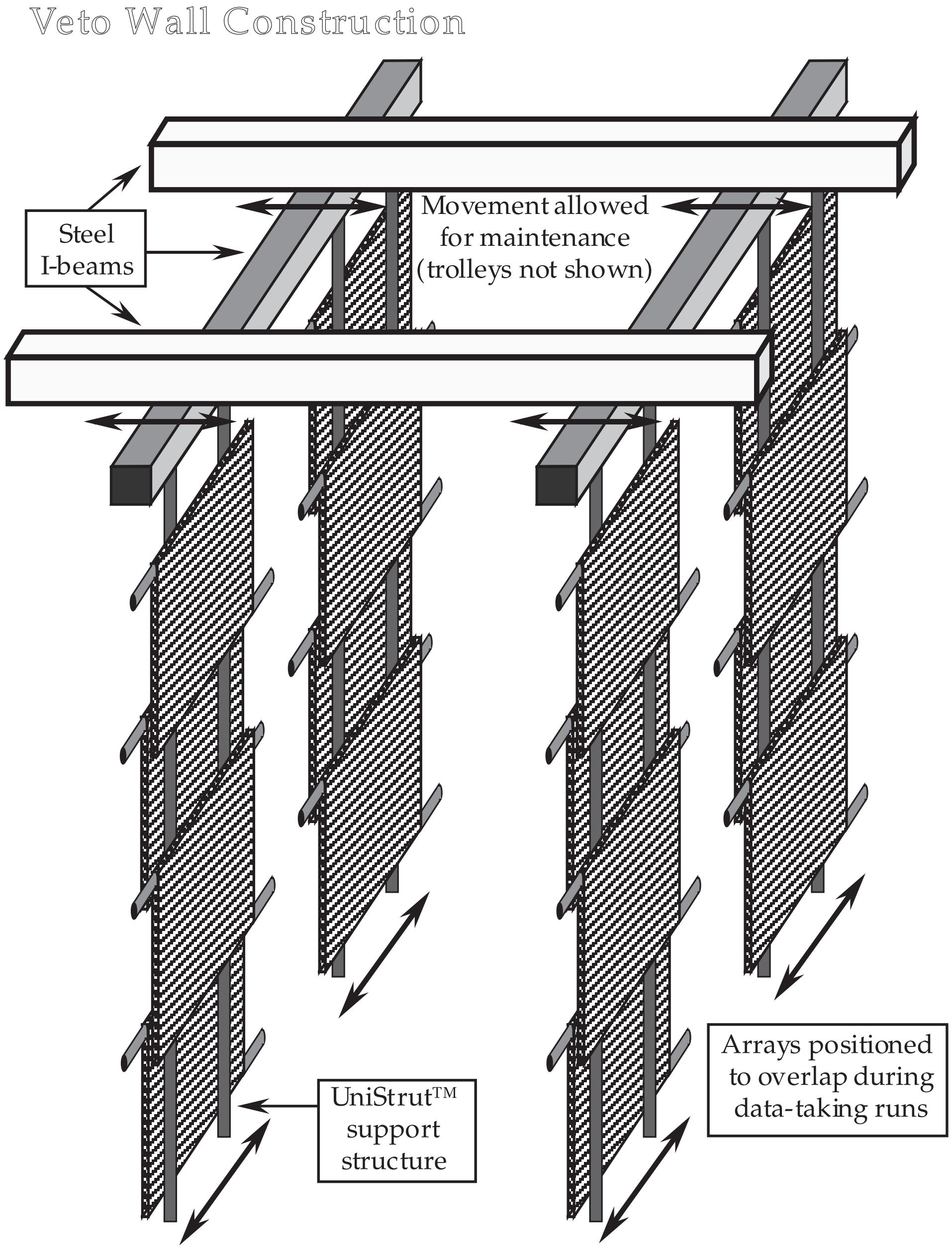

Figure 3.13: Veto Wall Construction

3.4 Calorimeter Readout

3.4.1 Flash Chamber Readout

Information from the flash chamber system was in the form of a small induced *emf* in a pickup coil, varying over time with the passage of acoustic pulses through the magnetostrictive wire. These pulses represented hit flash cells at distances from the pickup coil which could be related to their arrival times by the sound speed of the wire. The small-voltage signal was enhanced by an on-board pre-amplifier, to avoid picking up electrical noise on its way from the detector to the readout electronics outside. The quality of the signal could depend on the positioning of the pickup coil relative to the permanent magnet, so its placement was one of the parameters adjusted in the course of optimizing output signal performance.

This amplified signal (as shown in Figure 3.14) was fed into a discriminator circuit programmed with an exponentially varying threshold[6] to compensate for pulse strength attenuation along the magnetostrictive wire. Here, the discriminated signal was clocked into a 1024 x 1 memory chip at a frequency of slightly over two clock counts per microsecond. This resulted in a length-to-clock count conversion factor of 2.4037 mm per clock count. One cell-width (≈ 5.75 mm) corresponded to about 2.4 clock counts, resulting in a good distinguishability between hit cells and their neighbors, even after the digitization process. The data buffering process had additional safeguards against counting the same discriminated pulse twice in case it was long enough to extend for more than one clock count of time.

---

[6] The parameters of this threshold — overall level and rate of fall-off — were manually adjustable; every one was checked and tuned for optimal performance. In addition, the overall level could be adjusted globally by the on-line data acquisition system for testing purposes.

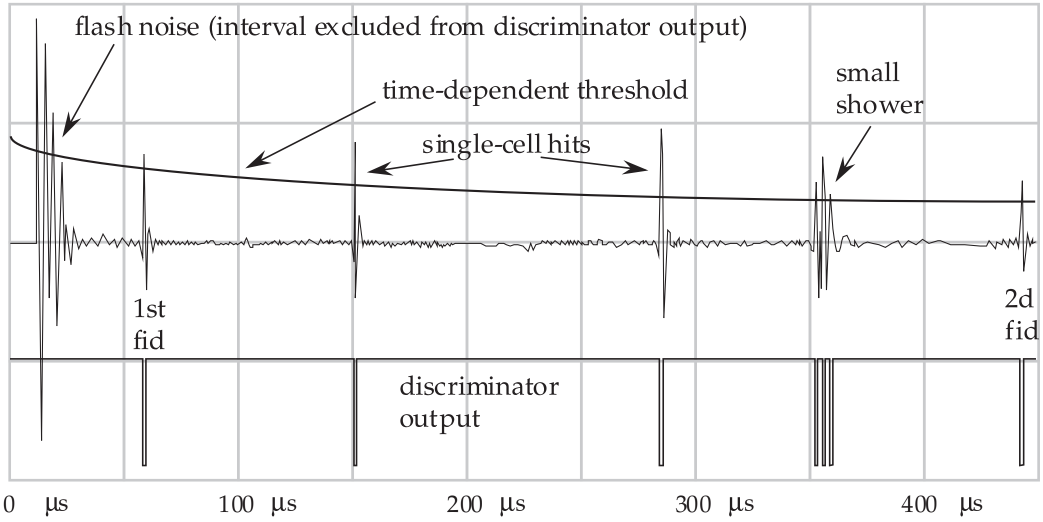

Figure 3.14: Typical Flash Chamber Output Signal

This time-to-spatial position conversion was calibrated by means of *fiducials*, thin wires passing current between the electrodes during the HV pulse independent of plasma formation, placed at the ends and middle of the active region, the positions of which could be measured in absolute spatial coordinates.

The memory boards were read out asynchronously via CAMAC to a PDP-11/45 computer. The discriminator and memory circuit for each end of the wand covered a region just over half of its length; the overlap region, where signals were recorded from both ends, was processed in the analysis software to eliminate duplicate hits.

3.4.2 On-board Proportional Plane Readout

The on-board proportional plane readout system included four kinds of electronics cards for the measurement and pre-processing of signals.

- There were 9 amplifier cards mounted on each proportional plane, each containing 4 amplifiers, each of which was capacitively coupled to a group of four proportional plane anode wires in parallel.

- On each plane there was one of each of these, which will be described later:
  - Electron Logic Board (ELB);
  - Sum & Multiplex Board (SMB); and an
  - Interface Card (IFC).

Amplifiers and initial signal output

The amplifiers attached to the anode wires of the proportional planes were charge-integrating with rise times of 180 ns and gains of 1 mv/fC (± 12% sample variation). The amplified output signal passed through a 600 ns delay line. A tap off this signal at the 250 ns point was subtracted from the undelayed signal. The resulting differential signal was called FAST-OUT and was driven via twisted pair cable to the SMB, IFC, and ELB.

A trigger signal to the plane started ADC circuitry, storing the pulse height of each amplifier. Two signals labelled B (Before) and A (After) were generated to sample and hold on capacitors the delayed amplifier output voltage at two times, normally set 400 ns apart (the maximum allowable for avoidance of electrical noise from the flash chambers). These were intended to represent the pulse heights (B) before any voltage rise due to interacting particles and (A) after reaching post-interaction levels. Their timing relative to the trigger was adjusted to ensure this representation. The difference between the capacitor voltages was called the SLOW-OUT pulse height ($\mathrm{PH}_{SLOWOUT} = V_A - V_B$). A RESET signal cleared and re-enabled this system to await further triggers.

Electron Logic Board

The ELB could be programmed to perform a number of FAST-OUT signal processing functions to generate pattern recognition-based signals for use by triggers and for event reconstruction. It also provided the hardware used for gain calibration of each amplifier channel. The operating mode was selected by applying TTL voltage levels or pulses to a number of control lines by way of the IFB, which also provided a readout of the ELB's status to a monitor (called the ELBOW) in one of the CAMAC crates in the data acquisition system.

The FAST-OUT signals from the amplifiers were terminated through 100 Ω resistance to ground at the ELB, where they were also fed into comparators. The comparators discriminated these signals at programmable threshold levels, adjustable externally in 5 mv steps from 5 to 128 mV. The comparator output was logically $TRUE$ if the input voltage was above the threshold. The threshold was generally set $\geq$15 mV, to reduce the effects of amplifier noise. The logical state of each comparator was stored in a latch, called the HITBIT, upon receiving a trigger pulse from the SMB.

The comparator outputs were processed further by the ELB. Three fast signals were constructed for potential trigger use, revealing information about the pattern of energy deposition observed in the proportional plane:

Analog Multiplicity (AM) was a signal proportional to the number of comparators registering hits. For every channel with a HITBIT, AM was increased by 50 mV.

Single (S) was the logical OR of the 36 comparator outputs. If any of the channels registered a HITBIT, then S was set.

Fat Shower Veto (FSV) was logically TRUE if the HITBIT pattern indicated a shower width greater than a programmable number of channels (and was not used in any trigger in this analysis).

The ELB operated in either EVENT or CALIBRATION mode. The comparator thresholds were separately and automatically adjusted for each mode. In EVENT mode, the ELB was triggered externally. In CALIBRATION mode, the ELB generated an internal trigger from the coincidence of the S signal and an external enable gate pulse. At the end of a trigger cycle, a RESET or HB-RESET cleared the HITBITs and re-enabled the FSV circuitry.

Sum & Multiplex Board

The SMB performed four functions.

1. The 36 analog FAST-OUT pulses were linearly summed into an analog SUMOUT signal, corresponding to the total energy deposition in the plane.
2. Before and After switching pulses were made on the receipt of a trigger and sent to the amplifiers to provide gating for the sample-and-hold capacitors.
3. Trigger and RESET pulses were routed to the ELB.
4. The 36 SLOW-OUT pulse heights and 36 HITBITS were multiplexed on this board for digitization.

Interface Card

The IFC was a passive device providing RC and LC circuit filtering and diode protection for signals transmitted to and from the proportional plane. All low voltage electrical connections, analog signals, and logical level signals passed through this unit.

3.4.3 Off-board Proportional Plane Data Acquisition System

Running in EVENT mode, the SUMOUT and AM signals from each plane were discriminated and, along with the FSV, gated into CAMAC latches at each trigger. The discriminated SUMOUT rates were stored in CAMAC scalers. The discrimination of the SUMOUT signals was done after they had been divided in a 90%–10% split by a simple voltage divider, and was performed on the 90% section. The 10% sections of all the planes were summed in a sequence of linear electronic circuits. The outputs form two total detector energy signals called SUMSUM and SUMALL. SUMSUM leaves out signals from a few planes at the end of the detector to bias its effect towards the detectors' fiducial volume.

An apparatus called the SCANADC read out the SLOW-OUT pulse heights and HITBIT signals through a tiered multiplexing system involving the on-board SMBs. This readout occured after a delay of about 4 ms, to allow electrical noise broadcast from the flash chamber HV pulse to subside. For each channel, an address, a bit representing the HITBIT status, and the 12-bit digitized SLOW-OUT pulse height were packed into a 24-bit word in CAMAC-based Ultra-Fast Memory (UFM) units. After all channels have had their information stored, the data was transferred to the on-line data acquisition computer and a RESET was sent to all components in the proportional plane readout system.

3.5 Spectrometer Readout

The drift chamber readout system was similar to the proportional plane system, but with the addition of timing information for each channel. This information was provided by circuitry which counted the number of pulses from a 50 MHz clock signal between the detection of an anode wire hit and the receipt of a termination signal generated by either the toroid timing plane system or by a constant time delay from the initial trigger, whichever arrived first.

Other differences included:

- Pulse height was not important for track position determination (the spectrometer drift system's primary responsibility), so it was not recorded.
- There was one anode wire per channel instead of four. Even without ionization drift timing information, positions could be measured with the resolution provided by the 1 inch (2.54 cm) drift tube spacing (or better, if information from the staggered second layer was used). With timing information, resolution of about a millimeter was attainable.
- A simplified version of the proportional plane amplifier signal system provided the equivalents of the S and AM signals, from which the number of tracks in a plane could be quickly determined as 0, 1, or more than one. Some event trigger types used this information, which was latched in CAMAC.

The time-reference signal from the drift timing plane system was recorded via TDC circuitry, as was the trigger signal. The difference could be used in the course of analyzing the time signals in the drift chamber system or in tracking down problems in the readout system.

3.6 Event Triggers

A neutrino detector trigger system is required to distinguish energy deposition patterns corresponding to the characteristics of neutrino interactions from those which do not. Additional information may be used to further narrow the definition to particular classes of neutrino interactions, in order to bias the event sample towards or away from them.

The characteristics of the components of any detector impose restrictions on its trigger system. The Lab C Neutrino Detector was subject to several constraints.

- The flash chambers had no monitoring mode — they had to be triggered externally in order to see what was going on in them, and they could only flash once in a 5 second time period. The longer the flash cells had to wait between a particle's passing through and the receipt of the HV pulse, the longer the ionization trail had to recombine, reducing efficiency.
- The proportional planes' response to the ionization trail of a penetrating particle had to wait for the electrons to drift to the anode wire.
- In order for proper Before and After voltage levels to be measured, the SLOWOUT circuit on the proportional plane readout had to receive a trigger within 600 ns of the signal rise.

The strategy used for the design of the system was the adoption of a two-stage trigger based on proportional plane information. First, a pre-trigger which quickly responded to signs of energy deposition. Second, after a fixed delay to allow for electron drift and signal development, other conditions could be imposed.

The standard pre-trigger, called M, was a coincidence of any two SUMOUT signals above a common low threshold (typically 35 mV), representing simultaneous energy deposition in at least two proportional planes. The coincidence condition was imposed to avoid spurious pre-triggers due to electronic or electrical noise, the Cd^{109} calibration sources and low energy cosmic rays. Since a new pre-trigger could not be generated until a fixed 1 μs interval had elapsed, there was a small dead-time[7] introduced at this stage.

The second level of trigger conditions consisted primarily of information from the energy deposition and distribution signals from the proportional planes (and in some cases from the drift chambers), such as SUMSUM and various logic level signals derived from discriminating each plane's SUMOUT and AM signals individually.

The trigger used to collect the data for the present analysis was a *low bias* trigger called PTH. It made certain minimal assumptions about energy deposition in the detector, corresponding to a minimum energy of about 5 GeV. PTH-triggered events also had to extend for greater than one module in length (about 19 inches or 47 cm), so as to fulfill the pre-trigger SUMOUT coincidence requirement.

Higher bias triggers were also available, which imposed different and generally more restrictive conditions. The conditions required by each of the trigger types

---

[7] The present analysis is not sensitive to dead-time, so it is pointed out here that there were methods to measure and control for this and other dead-times, but they will not be described in detail.

used in the 1987–88 run are listed in Table 3.1.[8]

3.7 Online Data Acquisition

The Lab C Neutrino Detector was interfaced via CAMAC standard databus hardware to a DEC PDP-11/45 computer using the RSX-11 operating system. On-line data handling was controlled by the Fermilab program MULTI, with data structures designed for the experiment. Selected Fermilab beamline information was also made available to the computer via CAMAC, in addition to appearing on various monitors and a terminal in the control room. Incoming data was transferred from the CAMAC bus to disk and written to tape after each event. The MULTI system also made information available to local terminals for diagnostic evaluation. Certain automatic tests were performed by the computer (such as rate checks and run summaries) to alert the experimenters of equipment failure or beam status.

3.8 Offline Data Preparation

The original 1600-bps data tapes were the input for a *reformatting* procedure. The reformatted 6250-bps output tapes contained all events and run-condition records in a format readable by Fermilab's CDC Cyber computers running with the NOS operating system[9]. During the reformatting process, a small amount of event preprocessing was done. This mainly consisted of the elimination of duplicate flash

---

[8] In addition to the triggers listed in this table there was one called $PTor$, which was simply the logical OR of the PTH and low-y CC triggers.

[9] Software was later developed to read and process this event data format using DEC VAX computers running with the VMS operating system.

Table 3.1: E733 Triggers During 1987–88 Run.

M condition: at least 2 proportional planes with SUMOUT > 35 mV;
AM condition: at least 2 planes with AM signals showing at least 2 HITBITs.
All triggers also required "detector ready" status.

Trigger	**Gate**	**M**	**AM**	**SUMSUM**	**Other**
PTH	DBG	yes	yes	> 19 mV	$\overline{\text{veto}}$
Low-y CC	DBG	yes	no	< 75 mV	$\overline{\text{veto}}\cdot$STOP[a]
High Energy	DBG	yes	yes	> 300 mV	$\overline{\text{veto}}$
NH Beam (*"Test"*)	NH part of slow-spill	yes	no	*none*	$\overline{\text{Test veto}_N}$[b] and momentum-defining element coincidence
Cosmic Ray (*"Scint"*)	between beam spills	yes	no	< 75 mV[c]	proper coincidence from scintillator tanks and arrays in detector
Pulser	(various)[d]	no	no	*none*	*none*

[a] STOP is the coincidence signal from the Drift Timing Planes, indicating passage of a particle through the spectrometer.

[b] The *Test Veto* was TRUE if AM$\geq$2 in any of the first N prop planes. This allowed triggers only on hadrons which would survive in the detector long enough to leave a measurable track before interacting. N was usually 2 or 4. For *deep* hadron runs, $N \geq 6$.

[c] Scint trigger maximum energy was actually based on SUMALL.

[d] During normal data-taking runs, pulser triggers were taken immediately after DBGs in which no neutrino events occurred. In general, those preceding slow-spill periods were non-flashing pulser triggers, while those at the end of the entire spill were flashing pulser triggers (as there was then no danger of losing a real event due to the flash chambers' 4.5 s recharge time).

chamber hits in the central region of flash chambers where the readout systems at both ends of the magnetostrictive wires had overlapping coverage. Statistics used for determining the clock count coordinate system positions of the fiducial signals were also gathered to assist with the identification of these duplicate hits for removal, and to produce fiducial tables so that later analyses would not confuse fiducials with ionization hits.

Chapter 4

E733 Event Analysis Process

4.1 Basic Event Selection

Each of the events in the E733 data set went through a sequence of software routines which established its suitability for further analysis.

4.1.1 Triggers and trigger conditions

Each event's data record contained a number of pieces of information concerning the trigger as of the time when it occurred, including:

- the trigger type which caused the event to be recorded;
- which trigger conditions were valid at that time; and
- the status of various gates at the trigger time.

A simple consistency check on these was made in order to flag possible hardware problems. For example, standard low-bias PTH triggers required that the PTH trigger condition was true and that one of the neutrino beam gates was open. If a PTH trigger event's data record were to show that this was not the case, then some problem must have occurred during that event, and it was flagged as potentially unsuitable. This sort of error condition was rare, occurring only in a few thousand events, mainly near the beginning of the data-taking while the exact trigger timings and hardware logic designs were being established. These runs were excluded from the final data set anyway for the reason that triggers in them were not yet subject to standardization. Later runs in which hardware problems caused inconsistent triggers were also excluded from the final data set.

The other purpose for having the trigger and gate types checked was for the stripping of data from the initial reformatted data tapes to trigger-specific data tapes. There were sets of data tapes containing each of four main classes of data.

- Beam triggers included events taken in the neutrino beam gates. These should all have had PTH, HE, or CC triggers, and one or more of the corresponding trigger conditions. This set of stripped event tapes formed the basis for the final overall data set.
- SCINT triggers contained cosmic ray muon events recorded for alignment and calorimeter response studies.
- PULSER triggers, taken at random times outside the beam gates, represented the detector backgrounds, and were used for determining pedestals and noise patterns.
- TEST triggers contained events from calibration beam interactions.

The last two of these were further subdivided into flashing and non-flashing events, as there were data taken under both conditions.

4.1.2 Checking run quality

Early in the data processing, the run number of each event was checked against a list of runs with known problems or run conditions which would render their data unsuitable for use in the final data set. Reasons for exclusion by the CHEKRUN routine included hardware failure and non-standard trigger conditions. Trigger conditions may have been non-standard due to an error, or because the standard trigger conditions had not yet been defined (early in the run), or because certain tests were being run (*e.g.,* running with the toroidal magnets degaussed in order to measure drift chamber alignment and muon multiple scattering effects on spectrometer position resolution).

If a trigger had a legal configuration and occurred in a run not on the bad run list, it continued in the data analysis. Some non-standard triggers and bad run events did go on for further analysis for specific reasons, such as providing alignment information, but did not count in the neutrino or calibration beam data analyses.

4.1.3 Noise reduction, vertex finding and fiducial volume cuts

In an idealized calorimeter, in an idealized beam guaranteeing only one neutrino interaction (and no other sources of interactions) in the detector at a time, the extent of energy deposition would be clearly defined and measured. There would be an exact correspondence between energy deposition from the particles produced by the inelastic scattering process and the signals recorded by the detector. The site of the initial ν_μ interaction with the target, or *event vertex* would be at or very near to the hit signal registered furthest upstream. The shower length would be the distance in the detector from the first lit element to the last one associated with the shower.

A real calorimeter must account for numerous deviations from this idealized representation.

- Instrumental effects could masquerade as signs of ionization in the detector. These included pedestal fluctuations in the proportional plane system and noise hits in the flash chamber system, caused by electrical interference in the detector elements themselves or in their readout systems. Run 9355 event 73 in Figure 4.1(a) is an example of noise induced in the flash chamber readout system by a malfunctioning PFN spark gap.

- Other sources of ionization could appear in the calorimeter during the time of the neutrino interaction (*i.e.,* within the time period around the instant of the ν event when ionization would result in a signal). These included cosmic rays and debris reaching into the detector from neutrino interactions outside. A muon from a not-quite simultaneous interaction[1] upstream of the detector intrudes upon Run 9178 event 2234 in Figure 4.1(b).

- There were neutrino DIS interactions in the detector which for some reason did not satisfy the requirements of one of the neutrino event triggers. Such events could leave ionization behind them in detector elements which had not finished dissipating before a triggerable event occurred. These were called out-of-time events, and had more of an effect on the flash chamber calorimeter than on the proportional planes, mainly because the proportional planes provided the trigger, and thus set the timing.[2] An example of such an out-of-time event

---

[1] If it had been truly simultaneous, the Veto wall would have excluded this event entirely.

[2] The flash chambers' ionization latency time also appeared to be somewhat longer than that of

can be seen in Run 7577 event 1913 in Figure 4.2(a). From the proportional planes it can be seen that the larger shower is a "ghost" lingering on until the smaller event triggered the detector.[3]

- Sometimes, two neutrino interactions occurred in the detector within a very short time, close enough that both induced essentially full responses from all detector elements. Run 9294 event 2227 in Figure 4.2(b) is one such event.

The detector design minimized these effects as much as possible, as they would affect many aspects of the data analysis. Some of these design features (described in more detail in earlier sections) included:

- the adjustable comparator thresholds in the flash chamber readout system, to reduce the effects of electronic noise without losing signals;
- the veto wall, to reject intrusions from interactions outside the detector; and
- the signal integration times in the proportional plane readout system which maximized signal size while avoiding flash-induced electronic noise.

The remaining noise problems were handled in the analysis software. The first-line defense was the set of time-dependent proportional plane pedestal tables (a set for each type of event: flashing and non-flashing) and flash chamber noise-hit tables. These were generated from the data split tapes of pulser trigger events, which

---

the proportional planes — efficiency fell off fairly constantly at about 10% per microsecond, while the proportional planes' lower electric field resulted in a faster fall-off in response after the initial pulse.

[3] The question "why did the larger interaction *not* result in a trigger ?" may be answered in a number of ways; for example, there may have been another upstream interaction at about the same time which set off the Veto Wall but whose ionization had already faded by the time of this trigger. In this particular case, there was a *prescale* set on the PTH condition, allowing only every eleventh such trigger to be acted upon, and the unusual situation of a very small time difference between the tenth and eleventh trigger candidates is the most likely explanation.

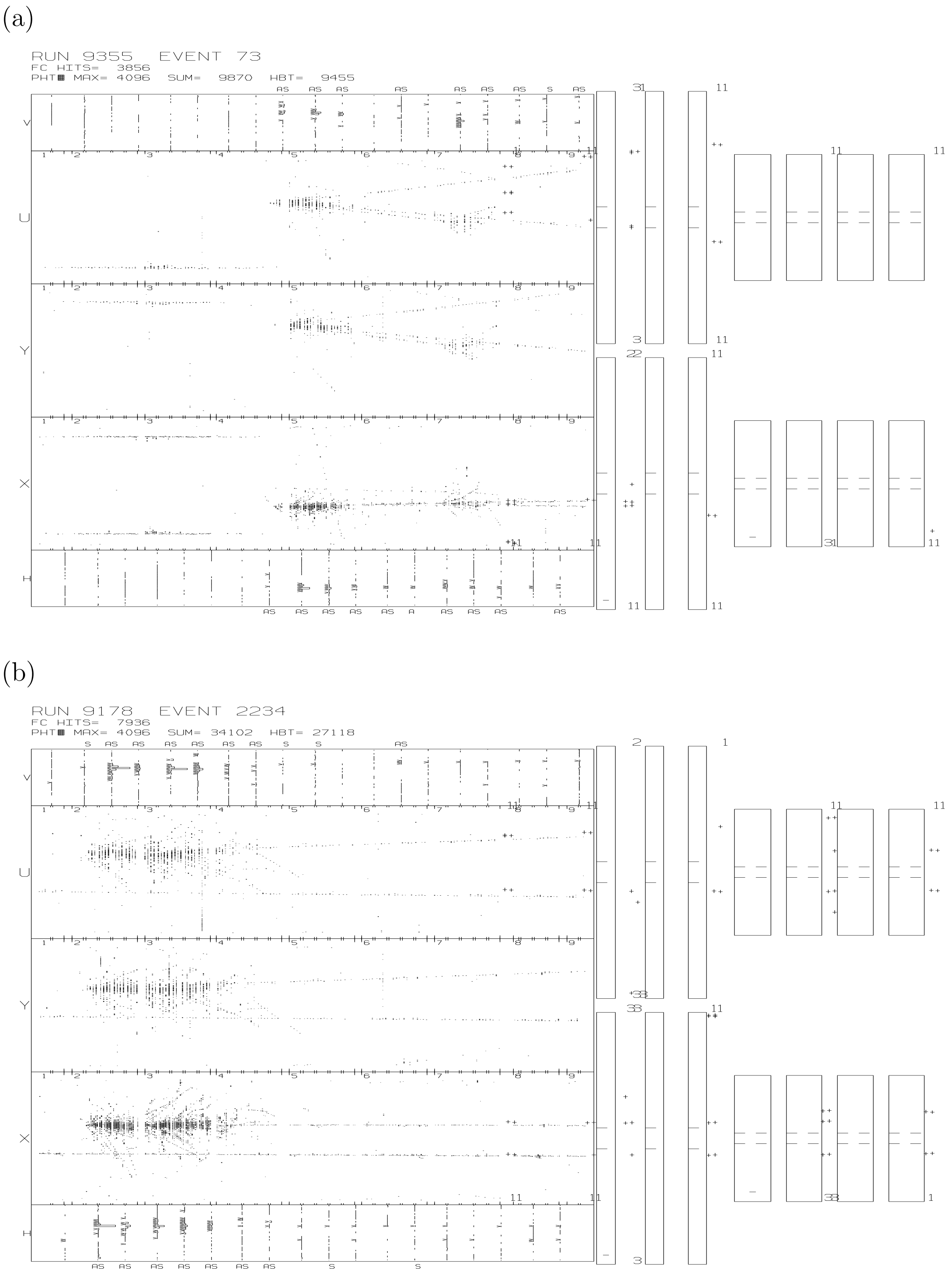

Figure 4.1: Examples of unwanted interference with neutrino interaction events by (a) instrumental noise, and (b) ionization sources from outside the detector.

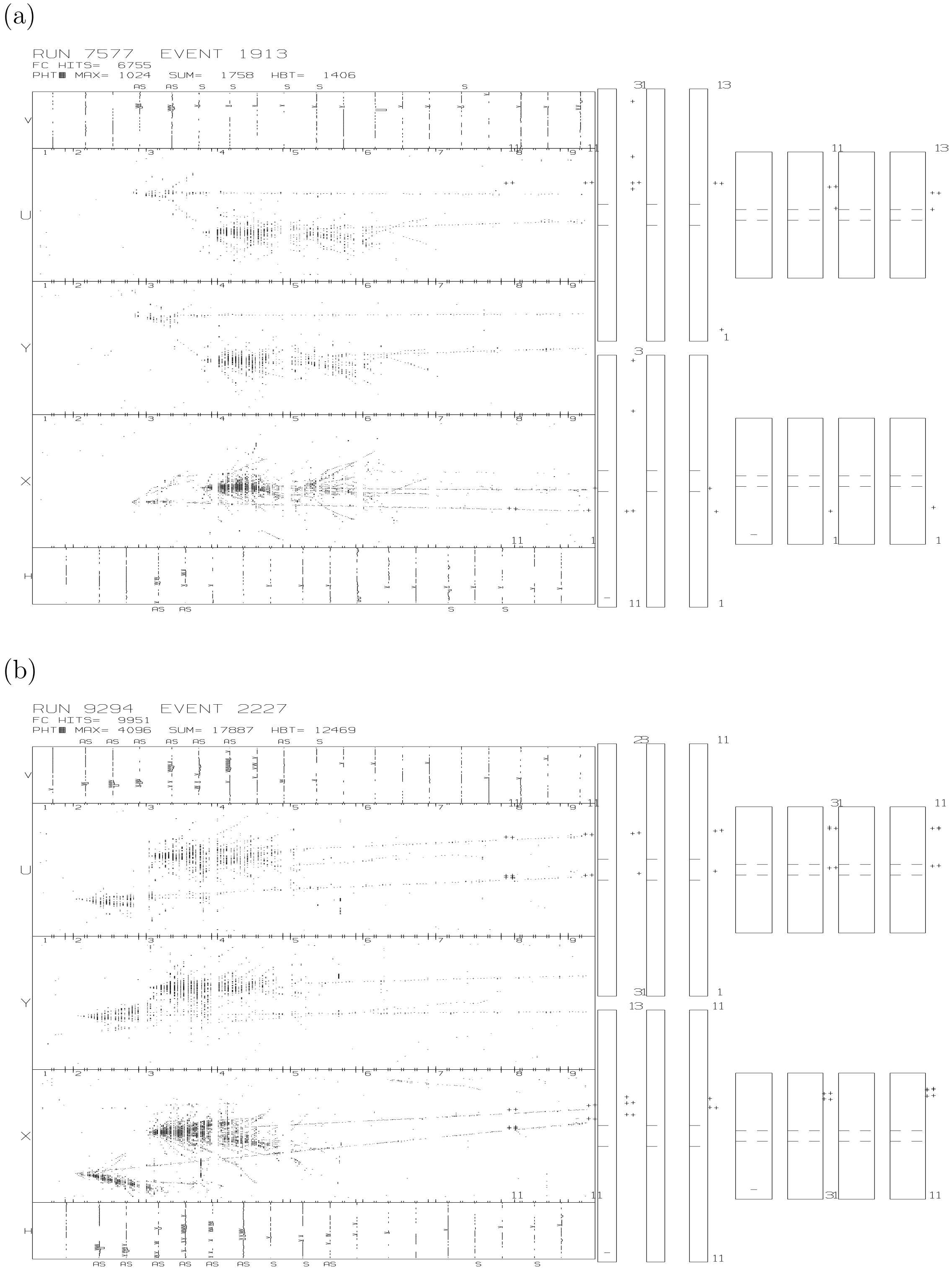

Figure 4.2: Examples of other neutrino interactions appearing in the same event as the interaction which caused the trigger: (a) out-of-time, and (b) in-time.

should have had no real signal in them; what they *did* contain could be considered a baseline for those events with ionization-based triggers. All proportional plane analysis routines used pedestal-subtracted information. The flash chamber noise-hit tables listed channels which appeared to be lit a substantial fraction ($\geq\sim$25%) of the time, with or without an interaction in the detector. These tables typically contained only 0.2% of the flash chamber channels. At the beginning of the data analysis process, each flashing event went through a filter which flagged flash hits appearing on the appropriate noise-hit list so that later analysis routines could ignore them.

The software routine which determined the position of the event vertex was called VRTDRV. Its basic strategy was to use the proportional plane with the furthest upstream hits recorded in the SUMOUT and AM latches as a first approximation in a search through the flash chambers for the position of the starting point of the hadronic shower. See Appendix A for a more detailed flowchart of how this is done.

The flash chamber which VRTDRV decided was closest to the longitudinal (z) position of the interaction site was called LVEST (and the z-position in centimeters was called ZVEST). The transverse position of the vertex was stored in an array, VV(3) holding the clock count coordinates of its projections in the three flash chamber orientations. Since most event analysis and display routines which dealt with flash chamber hits used the projection coordinates, this was the most convenient form for storing the transverse vertex information. It could be easily transformed to Cartesian coordinates when necessary.

To ensure that the analysis used an unbiased sample of fully reconstructed events, cuts were made on vertex positions which made certain that events were fully within the bounds of the detector. Events beginning too close to the end or sides of the detector might have had hadronic showers which extended beyond the active regions of the calorimeter. These would have resulted in inaccurate hadronic energy measurements, especially for those with higher shower energies. This would have introduced an energy-dependent bias into the sample. For charged current events, the muons may not have had enough room to separate from the hadronic showers or to be otherwise identifiable before exiting the detector. This would have introduced a classification bias into the sample. These vertex position cuts defined the *fiducial volume* of the detector, within which the reconstruction of events could be considered to be consistent.

The fiducial volume for neutrino interactions in this analysis included flash chambers 5 through 400, with transverse positions no closer than 300 clock counts ($\approx$ 75 cm) to the edge of any flash chamber's active area. Figure 4.3 is a representation of the distribution of events within the fiducial volume.

4.1.4 Hadronic Shower-length determination

The shower length routine SHRLEN used an algorithm which started at the vertex position established by VRTDRV and checked each detector element for hits, proceeding downstream until no substantial energy deposition was found, where it decided that the end of the shower had been reached.

If there was a muon associated with the event which out-traveled the hadronic debris (due to its small interaction cross section), adjustments were made in the simple procedure to avoid counting it as part of the hadronic shower during the shower-length determination.

This is a simplified picture of how SHRLEN operated (refer to Appendix A for

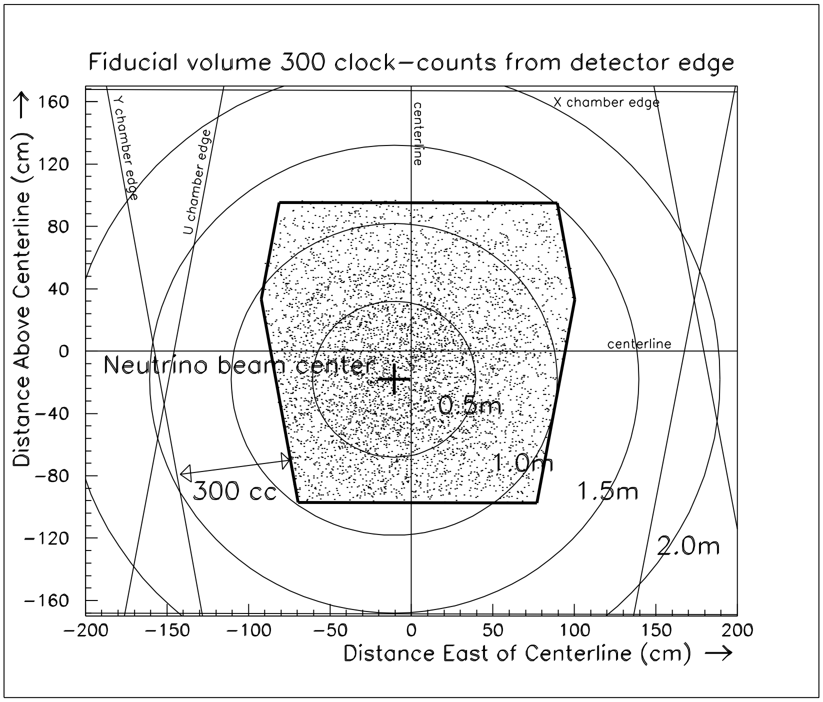

Figure 4.3: Distribution of events within the fiducial volume defined as the region more than 300 clock-counts from the edge of any flash chamber's active region

a more detailed schematic of the algorithm it used).

SHRLEN had three adjustable parameters which affected its determination of shower length by altering its definition of insufficient energy deposition.

1. A threshold was set for the number of hits per chamber which must be exceeded in order to consider a flash chamber as containing part of the hadronic shower.
2. A size was set for a window or buffer of contiguous flash chambers which were grouped together and tested to see how many had hits exceeding the threshold number.
3. A limit was set on the number of threshold-exceeding chambers a window must contain and still be considered as being in the hadronic shower.

The threshold value was set to 4 if the event had been classified as a neutral current interaction, and 5 if a muon track had been found in the calorimeter (allowing for an average of one extra hit per chamber induced by the muon). If the event turned out to have less than 2000 hits in threshold-exceeding flash chambers, these thresholds were reduced by one, reflecting the tendency of less energetic showers to also be less dense. The dependence of the threshold upon prior identification of the event classification meant that SHRLEN was run on events after the basic classification routines[4]. The standard settings for minimum filling of a window was 6 or more threshold-exceeding chambers in a window of 16 chambers.

SHRLEN returned three measures of the end of the hadronic shower:

JTAIL was the 80% containment limit, the flash chamber where

$$\sum_{i=\mathrm{LVEST}}^{\mathrm{JTAIL}} \mathrm{hits}_i \cdot \theta(\mathrm{hits}_i - \mathrm{THRESH}) = 0.8 * \sum_{i=\mathrm{LVEST}}^{\mathrm{ICHEND}} \mathrm{hits}_i \cdot \theta(\mathrm{hits}_i - \mathrm{THRESH})$$

where ICHEND was either the last flash chamber in the detector, or the last flash chamber in the sixth module downstream from the last proportional plane registering an AM latch, whichever came first.

JFINS was the sixth flash chamber downstream from JTAIL which failed to satisfy the threshold requirement.

JEND was most often used to designate the end of the hadronic shower. It was the flash chamber 16 chambers downstream of the last chamber satisfying the minimum window filling requirement.

---

[4] Since the NCCC classification routines required an estimate of shower length before deciding whether an event contained a muon track, SHRLEN was run both before (with a default NC classification) and afterwards (with the actual classification).

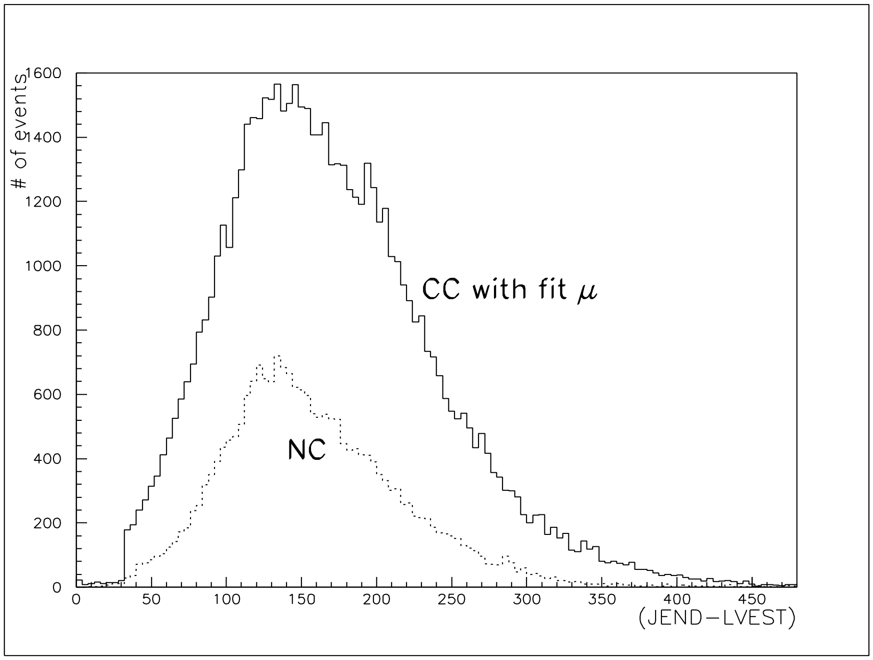

Figure 4.4: Distribution of shower lengths (JEND–LVEST) for NC and CC events.

Once the vertex and the end of the shower had been determined, the region over which flash chamber hits and proportional plane pulse heights were integrated for energy measurements was set. In practice, the summation was performed from a set distance upstream of the vertex to a set distance downstream of JEND, to be sure not to miss any energy deposition.

For proportional plane energy measurements, the summations were from the proportional plane immediately upstream of LVEST to the fifth plane downstream of JEND (or to the last plane in the detector if there were less than five proportional planes left beyond JEND).

For flash chamber energy measurements, the limits were LVEST–8 to JEND+80 (or the first and last chambers in the detector if they were reached first).

Figure 4.4 plots the distribution of the shower lengths determined by this method for events classified as NC and for those with a muon found and fit.

4.2 Hadronic Shower Measurements

4.2.1 Hadronic Shower Properties

A neutrino deep inelastic scattering interaction transfers energy and momentum to the struck parton, causing disruption of the nucleon in which it resides. A result of this disruption is the formation of a shower of hadronic debris which spreads out from the interaction site and scatters from target material downstream. Some of this scattering results in the further production of hadronic particles, which also scatter or decay in the calorimeter. The total energy available for these processes is determined by ν, the amount of energy transferred to the parton in the initial neutrino interaction. It should be noted that in the following discussion, the term E_H refers to the energy of the hadronic shower visible in the detector rather than to the energy component of the hadronic sector's momentum 4-vector. E_H should correspond roughly to ν.

Along their paths, the particles in the hadronic debris shower interact with the material in a calorimeter. As the bulk of a neutrino detector's calorimeter is target material, most of the interactions occur there. At regular intervals, however, there are active detector elements, which allow it to be used for calorimetry.

4.2.2 Calorimetry and Calibration

In the E733 neutrino detector, the target materials were mainly steel pellets and sand. The active elements were flash chambers and proportional planes, which were used for calorimetry, and scintillator devices used for other purposes.

Active calorimetric devices record the effects of the ionization of material within them as the hadronic shower particles pass through. As the ionization properties of relativistic charged particles are known, the total amount of energy contained in the debris of an interaction can be estimated from the part of that energy which went into ionization in the active elements, even though that part may not be a large fraction of the total. The process of extrapolating from the observed interaction effects to the total energy contained in the hadronic shower requires *calibration*.

The primary means of calibration in the E733 detector was the use of a calibration (or *test*) beam. This was a beam of hadronic particles at a known momentum, which entered the detector during times between neutrino beam spills, as described in Chapter 2. These hadrons interacted with the target material in the detector, releasing showers of hadronic debris much like those released in neutrino interactions. The energy available in the hadronic beam showers is determined by the momentum of the incoming hadronic beam particles, which is known. The measured properties of the ionized active detector element materials can thus be related to the total energy released into the detector in all active and inactive elements.

Once a basic calibration of the calorimeter was established using information from the hadron beam events, it could be fine-tuned by various methods using neutrino events, which were not subject to some of the restrictions of the hadron beam analysis.

- There were limitations on the physical positioning of calibration events within the detector. The hadron beam entered the detector in a narrow range of positions, and at a limited range of angles. The interactions of the hadrons in the calorimeter followed the expected vertex position distribution upon entering it, the number of interactions falling off exponentially with distance into the detector. Even with triggering strategies favoring deep interactions, calibration beam events with vertices in Bay 4 or beyond (over $8\Lambda_I$ into the detector) were very uncommon. Any systematic position-dependent variation of detector response might have affected the validity of the calibration.

- Hadronic particles produced ionization on their incoming tracks. Software procedures had to be developed to remove the effects of the incoming track signal, which may affect the energy measurement of some hadronic events. Neutrino interactions, of course, do not have detectable incoming tracks.

- The rate at which hadrons entered the detector caused the rate of in-time (or just-out-of-time) doubled-up events to be higher in the calibration beam than in the neutrino beam, especially at the higher energies. This is especially important since the hadron events all enter the detector at approximately the same position and angle, and so are often physically close together in the detector, whereas doubled-up neutrino events are randomly distributed throughout the calorimeter.

The analysis procedure *generally* assumed that such differences had little effect on the results of the $\mathrm{E_H}$ measurements. The method used to account for these small differences will be discussed in later sections.

4.2.3 Trigger efficiencies and the $\mathrm{E_H}$ cut

The importance of an accurate calibration for this analysis is due to the necessity and desirability of making cuts in the data sample based on hadronic energy. The detector triggered on neutrino events based on certain patterns and levels of ionization activity in the proportional plane detector elements. If these minimum activity levels were not seen, there was no trigger, and any neutrino interaction with insufficient hadronic energy to reach this level did not become part of the data set. Since the triggers were based on information from detector elements with a wide separation (55% of Λ_I) the geometry of the hadronic shower was important also, especially at low energies, where there were fewer debris particles. Random fluctuations in their trajectories could mean the difference between passing or failing the trigger criteria.

There was also a complication due to the muon produced in a charged current muon-neutrino interaction, which causes ionization in addition to that of the hadronic shower in the active detector elements. This effect made a difference between the probability of a charged current event's meeting the triggering criteria and that of a neutral current event with the same hadronic shower properties, but whose outgoing neutrino induced no ionization in the detector.

A solution to this potential bias is necessary, since the ratio between these numbers is the central goal of the present analysis. The solution used was to ignore events in the data set which were determined to have deposited less than a certain amount of hadronic energy in the detector. This $\mathrm{E_H}$ cut was set high enough (at a minimum of 10 GeV) that virtually all events which passed the cut also satisfied the initial trigger conditions, independent of the presence or absence of a muon. Since this was the case, there should have been no bias in the relative numbers of neutral current and charged current neutrino interaction events actually used in the analysis.

An E_H cut of 10 GeV also had the desirable side effect of almost completely eliminating from the data set several classes of events which were not caused by neutrino DIS interactions in the E733 detector. Among these were:

- neutrino interactions via quasielastic and inverse muon decay processes,
- muons in the detector generated by ν_μ interactions outside the detector, and
- most cosmic ray events.

Thus, the E_H cut not only helped to minimize biases in the NC/CC ratio due to triggering effects, it also served to filter out many sources of background events.

While this standard 10 GeV E_H cut is to be considered a minimum requirement for a successful analysis, there is also a reason for voluntarily raising the E_H cut to a higher value. Charm quark production in ν DIS processes is subject to an energy threshold. Below the threshold, there is insufficient available interaction energy to produce charmed particles. In the threshold region, however, the cross section for events depends on the effects of the mass and helicity of the charmed quark. These effects can be modeled (*e.g.,* the slow rescaling model). It can be shown that most of the model-dependence for this process goes away for conditions where E_H or y is high (as was discussed in section 1.3.8). This is reasonable: well above the energy threshold, charmed particles should be produced like any other particles of negligible mass.

Making a E_H cut higher than the minimum necessary to avoid trigger bias had the beneficial effect of requiring that the events surviving the cut were more likely to have a high enough E_H and/or y to avoid problems with charm production. The trade-off is that the overall hadronic energy spectrum is a steeply falling distribution, and higher E_H cuts lead to lower numbers of events and the consequent larger statistical uncertainties. In order to get a good measurement with a low uncertainty but high resistance to theoretical uncertainty (*i.e.,* model dependence), a choice of E_H cut must be made. In this analysis, this choice was 60 GeV; events passing this cut were either high-y pion band events or else they were events from the kaon band.

4.2.4 E_H-measuring Software

The minimization of bias in the NC/CC ratio by making an E_H cut does depend, however, on an accurate measurement of hadronic energy which is itself not biased by the presence or absence of a muon in the event.

The E733 data analysis used several procedures for determining the hadronic energy. Each had strengths and weaknesses and each had a different sensitivity to the presence of the muon produced by a charged current neutrino interaction.

4.2.5 Proportional Plane calorimetry: EHPROP

The most straightforward of the energy determination procedures was the method used for the information provided by the proportional plane system.

The proportional planes had several advantages for calorimetry.

- There was a wide dynamic range available for each channel, which aided in achieving linear response all the way up to very high hadronic shower energies,

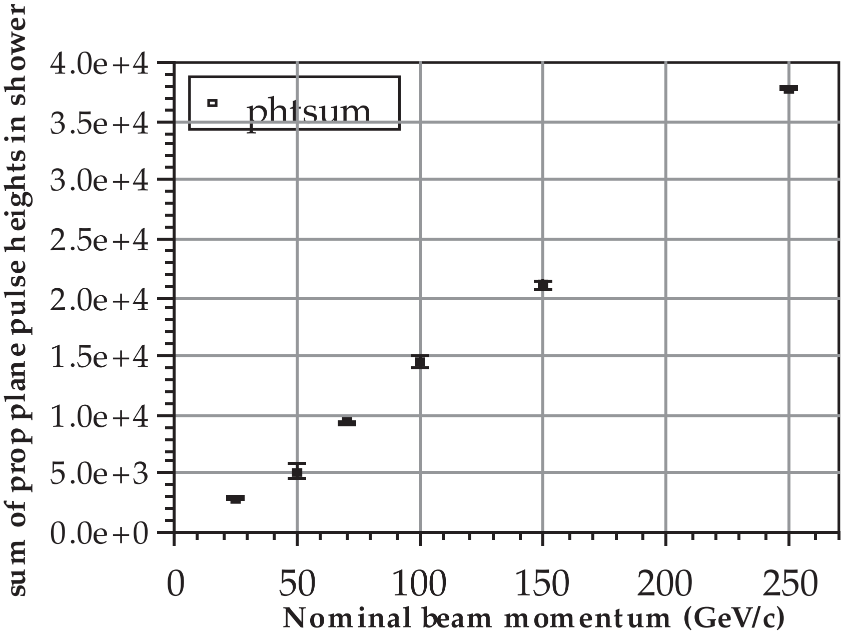

Figure 4.5: Proportional plane EH response: summed pulse heights for various calibration beam settings.

since saturated channels were rare. Figure 4.5 plots the summed pulse heights for the proportional planes *vs.* the nominal calibration beam momenta for several runs at different settings. It can be seen that it is very close to a linear relationship. With very little processing, this could be the basis of a linear E_H scale.

- The channel-by-channel energy response was fairly easily determinable. There was little fluctuation in energy response from channel to channel; most changes in response were global and thus readily measured. Figure 4.6 shows that a typical distribution of gains (excluding the effects of temperature and atmospheric pressure, which were accounted for separately) had an r.m.s. deviation of less than 20% of the mean value, and that the individual channels had a typical variation of less than 1% (with an r.m.s. deviation of about 8%) over a period of time of more than a month.

- Their pedestals were easily measurable (due to the frequent sampling of pulser triggers through the run), and were also quite stable over time. Figure 4.7 shows that the pedestal values for the proportional plane channels varied over a wide range of pulse height (in adc counts), but that they were very consistent (r.m.s. typically better than 5% of the typical pedestal, corresponding to less than 0.05 GeV, with means much better than that) on time scales of a month or so. Individual pedestal tables covered periods of 2 to 3 weeks each, to keep up with what small changes did occur.

The chief disadvantage was the coarseness of the granularity of coverage, allowing a spatial resolution of no better than about 10 cm transversely. Of more importance, the longitudinal sampling was only one plane per 18.5 inches (46.9 cm), or 55% of Λ_I) in the detector material. The former was chiefly a hindrance to procedures requiring pattern recognition, such as those used for event classification. The latter resulted in a poor resolution of the energies of small hadronic showers. A low energy yet triggerable shower might have spanned only two or three proportional planes. The biases from the random selection of which parts of the shower were sampled led to a large uncertainty in extrapolating back to the actual total energy dissipated in the calorimeter. A plot of fractional $\mathrm{E_H}$ resolution appears as Figure 4.8. It presents the resolution function used in this analysis, which was

$$\frac{\sigma(\mathrm{E_H})}{\mathrm{E_H}} = 0.001738 + \frac{1.3995}{\sqrt{\mathrm{E_H}}}$$

A secondary disadvantage to the sole use of the proportional planes for the

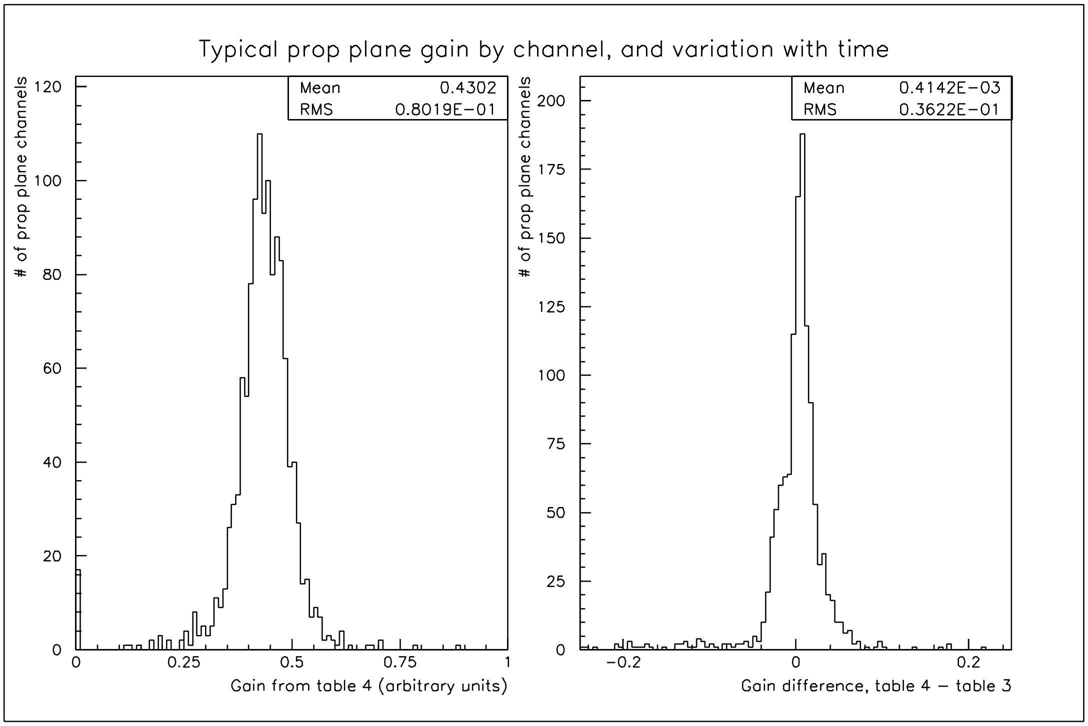

Figure 4.6: Proportional plane channel gain: distribution and variation with time.

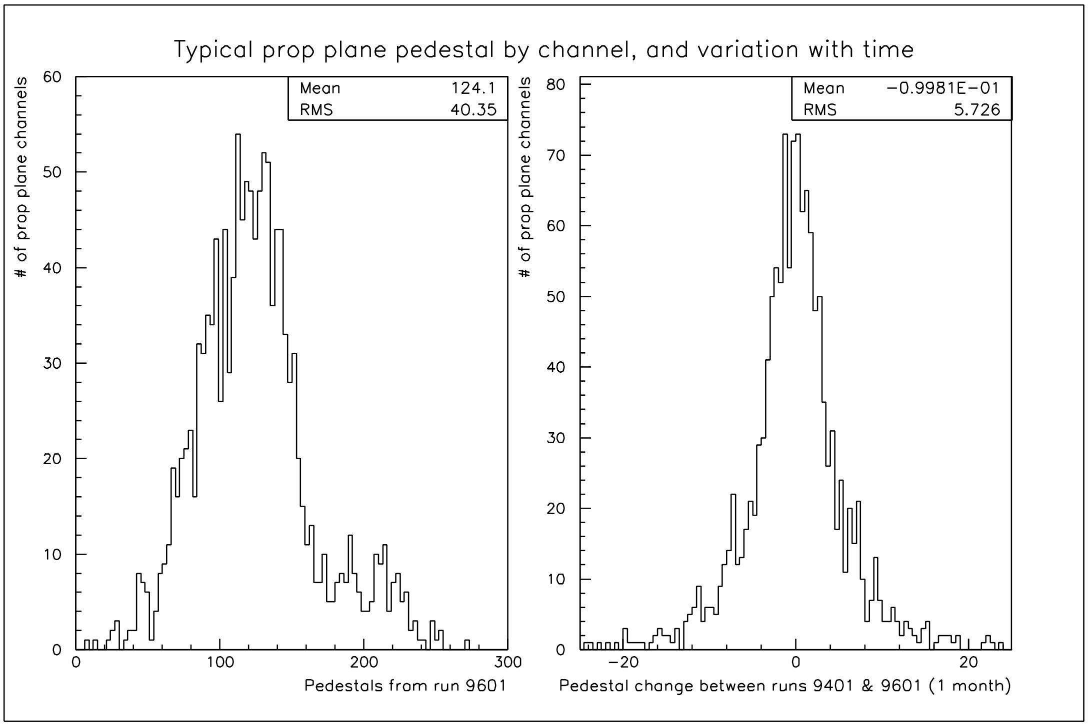

Figure 4.7: Proportional plane channel pedestals: distribution and variation with time. Units = ADC counts; roughly 150 ADC counts per GeV.

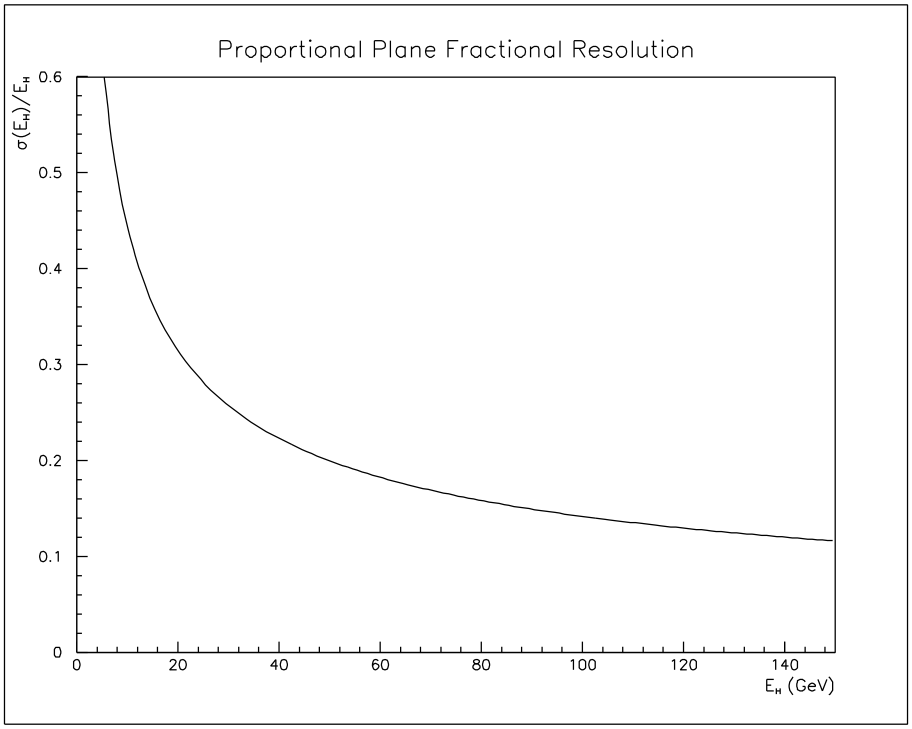

Figure 4.8: Fractional energy resolution for the proportional plane calorimeter as a function of shower energy.

determination of $\mathrm{E_H}$ would be that there was no practical way of sorting out the energy deposition of a muon in a charged current event from the energy deposited by the other particles in the shower. There was a way of making at least an approximate correction for this, which will be described below.

These were the basic equations for finding the energy of the hadronic shower from proportional plane information:

$$\mathrm{PH}^{\mathrm{corr}}_{\mathrm{total}} = \sum_{j=first}^{last} \left\{ \sum_{i=1}^{36} [k \cdot \mathrm{PH}_{ij} - \mathrm{PED}_{ij}(t)] * \mathrm{GAIN}_{ij}(t) * \mathrm{ENV}(T,P) \right\}$$

and

$$\mathrm{EHPROP} = f(\mathrm{PH}^{\mathrm{corr}}_{\mathrm{total}}).$$

In these equations:

i and j	represent channel number and proportional plane number, respectively. The *first* and *last* were the first and last proportional planes in the energy-summation region as described in the shower-length section.
PH_{ij}	was the 12-bit ADC reading for the SLOW-OUT measurement in a particular channel.
k	stood for a constant factor used in converting ADC integers to pulse height real numbers before processing them. For the 1987-88 run, $k = \frac{107}{64} = 1.6719$.
(t)	signifies quantities looked up in tables of time-dependent information. Time-dependence in these cases meant that the tables were divided into sections corresponding to ranges of data run numbers:
PED_{ij}	was the pedestal for a channel in this data run, expressed in converted ADC counts.
GAIN_{ij}	was the gain factor applicable to this data run. This included a time-dependent measurement for this particular channel, a global constant factor and a run-dependent correction factor for the gas quality of particular tankers of P-10 gas.
$\mathrm{ENV}(T,P)$	was the environmental correction, a function of the measured temperature and atmospheric pressure in the detector at the time of the event. These affected the density of the P-10 gas, which in turn affected the response of the proportional planes. This factor applied equally to all channels.

$f(x)$	was the function used to convert the corrected total pulse height, $\mathrm{PH}^{\mathrm{corr}}_{\mathrm{total}}$, into $\mathrm{E_H}$ (in GeV). For the 1987-88 run, this was a simple linear equation, $f(x) = 2.76 + 0.00632x$.
EHPROP	was the name given to this $\mathrm{E_H}$ measurement, using only proportional plane information.

An extra function, $X_{ij}(t)$, could have multiplied each of the elements to allow for such procedures as transverse position cuts or additional run-dependent parameters. In the present analysis, however, there were no such extra cuts or run dependencies. X would have been a constant equal to 1, and so was ignored.

4.2.6 The Rescaling Process

The result for each event gleaned from this basic procedure was then enhanced by performing a pass through an adjustment process where the basic $\mathrm{PH}^{\mathrm{corr}}_{\mathrm{total}}$-to-$\mathrm{E_H}$ conversion scale determined from the calibration beam is made to better match information gleaned from the analysis of the neutrino data.

The basic idea behind this adjustment process was that the y-distribution for charged current muon neutrino DIS interactions was well known. There was also a reliable model of the E_ν spectrum of the neutrino events expected to be seen in the E733 detector. The model predicted this spectrum as a function of radial distance from the central axis of the neutrino beam. Charged current neutrino events with daughter muons of known momenta (from fitting of the E733 detector's spectrometer information) yield measurements of both $\mathrm{E_H}$ and y. The residuals of measured *versus* predicted $\mathrm{E_H}$ could be minimized with some adjustment to the measured value. This adjustment was called *rescaling*, and was performed on all of the major hadronic energy determination procedures' results, not just EHPROP.

4.2.7 The Statistical Muon Correction

Another enhancement, or correction, to either the basic or the rescaled EHPROP is the *statistical muon correction*. There is no way of determining exactly how much pulse height is due to the ionization caused by a particular charged current event's muon. Leaving the muon-induced energy in EHPROP would clearly make it too large to accurately reflect the hadronic shower energy of the event. The standard procedure was the subtraction of an amount of energy *expected* to have been left by an *average* muon in the shower region of the detector.

This method reflected an assumption that not only were the proportional planes virtually linear in energy response for hadronic showers, but also for muons, and that the same scaling factors apply. There is little reason to believe that it did not, as the linear response region extends down to the low energy region where individual hadrons are not substantially different from muons in their interactions with the P10 gas. If the assumption held, then the energy observed in a charged current event was simply E_H plus the energy released by the muon in the shower region; that is, the translation from pulse height to energy is equally applicable to the muon as to the shower components.

For events with fully reconstructed muons, the correction was determined by summing up dE_μ/dx contributions along the measured path of the muon using the Bethe-Bloch formula and the measured final muon momentum in the spectrometer. This summation was the total expected energy loss in the calorimeter. It was then adjusted for the fraction of the muon's path through the calorimeter which was within the shower-energy summation bounds.

For events with muons found but not reconstructed in the spectrometer, the total expected energy loss in the detector was summed using the typical value (based on studies of the reconstructed muons) for muon energy deposition of 0.0083 GeV per flash chamber traversed.

4.2.8 Flash Chamber Calorimetry: General

There were advantages to using the flash chambers for calorimetry.

- The sampling was extremely fine-grained. The longitudinal spacing of 3% of Λ_I and transverse spacing of 5.8 mm guaranteed that each shower has many samples taken of its constituents' progress through the target material. (A rough approximation of the raw rate of hits recorded was 40 lit flash cells per GeV of hadronic shower energy).
- The identifiability of muon-associated hits in charged current neutrino interaction events raised the possibility of measuring the hadronic energy deposition separately from that of the muon.

There were also disadvantages to using the flash chambers for calorimetry.

- The binary nature of the information received from each flash chamber cell allowed the recognition only of the presence or absence of ionization, not of the quantity of ionization in the cell. The signature of one particle traversing a flash chamber cell was no different from that of many particles in the same

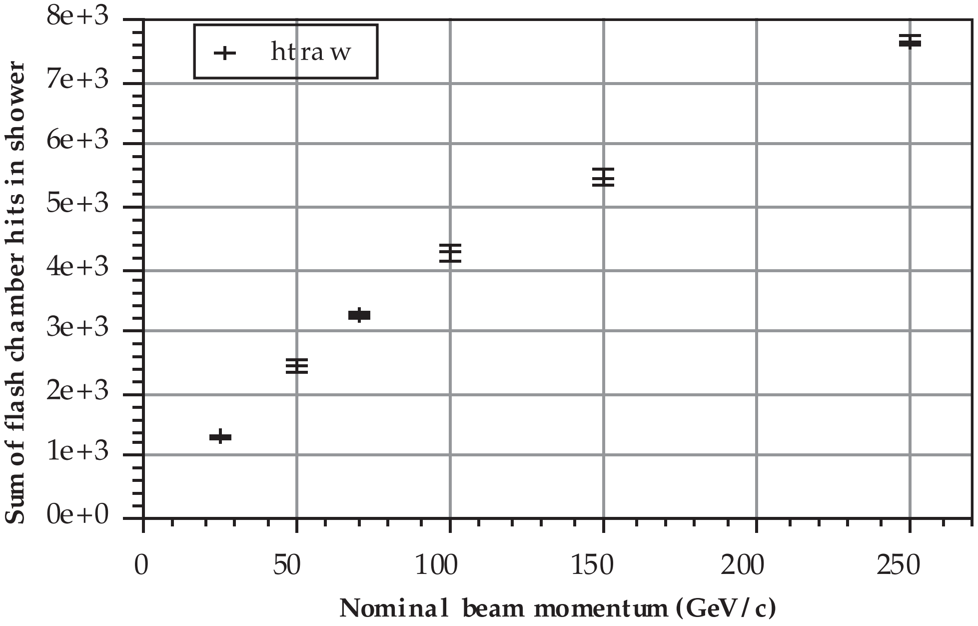

Figure 4.9: Raw flash chamber hits *vs* calibration beam momentum setting

cell. Therefore, hadronic showers with large numbers of constituent particles were likely to have instances where more than one pass through the same flash chamber cell, resulting in an effective undercount. This was a saturation effect, where additional deposited energy did not increase the observed number of hits in the detector. Figure 4.9 shows the total number of flash chamber hits in showers of various energies, demonstrating this saturation effect.

- The flash chamber response was sensitive to atmospheric conditions, especially the amount of water vapor in the air. These effects can be seen in Figure 4.10. The arbitrary units are such that they reflect a water vapor partial pressure of approximately 1 mmHg. Since there were other phenomena which also affected the hit density of tracks, and the effect of water vapor is not as strong as some of them, the results of this study are merely suggestive of the problem. In any case, during the 1987–88 run period, the climate-control system of Lab C was

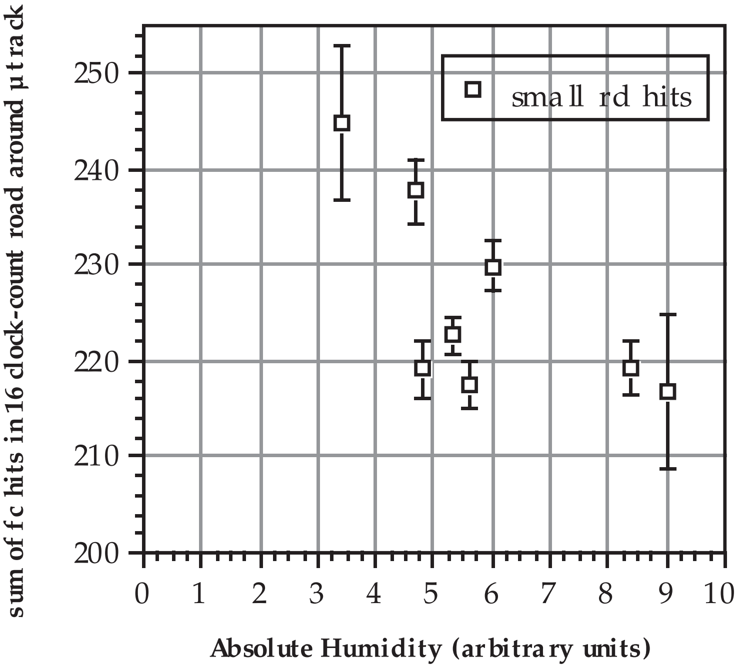

Figure 4.10: Flash chamber efficiency as a function of water vapor partial pressure.

enhanced in order to minimize such effects, restricting the absolute humidity to the lower end of the plotted range.

- The flash chamber response varied over a wide range from chamber to chamber and from cell to cell within a chamber, complicating the effort to establish a hits-to-energy conversion process. Figure 4.11 shows variation of efficiency and multiplicity within a single flash chamber, chosen at random.

4.2.9 Flash chamber calorimetry: the SHOWER routine

One method for determining hadronic shower energies from flash chamber information was via the software package called SHOWER. Its basic strategy was to correct for flash chamber response and shower geometry using statistical methods and thus

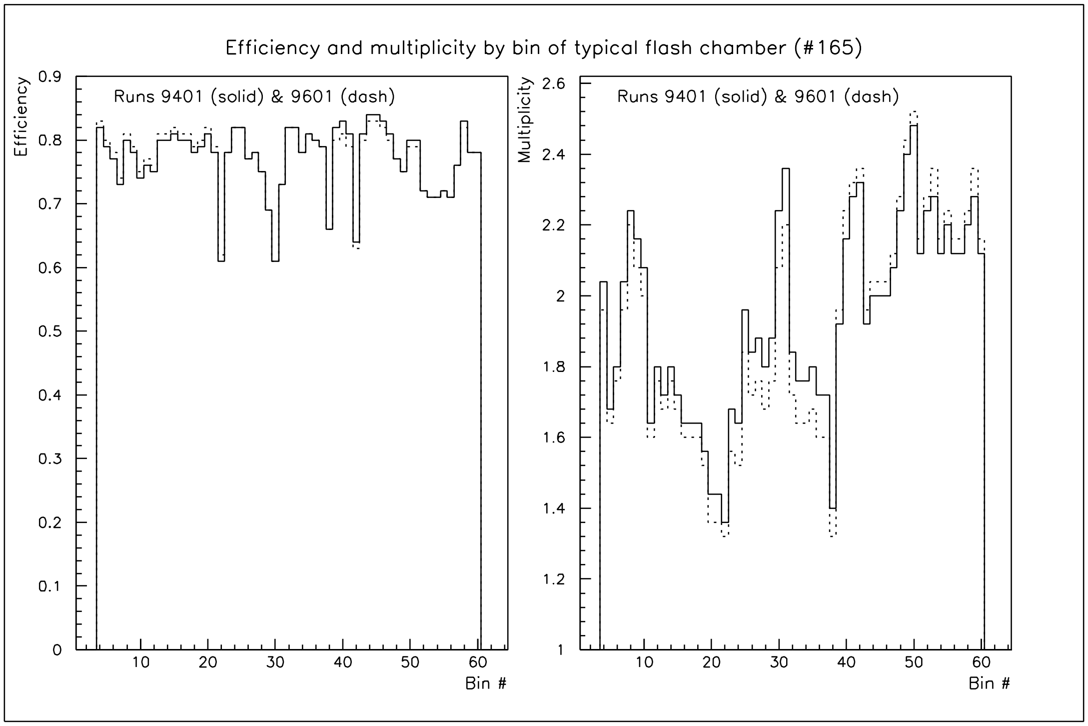

Figure 4.11: Efficiency and multiplicity for a typical flash chamber during two runs, separated by a month (*note: this chamber's multiplicity is on the high side of average*).

transform the raw number of lit cells in a shower into a number of corrected hits which was a simple function of E_H. Performing the corrections and executing this simple function yielded a result called, for historical reasons, *EHDOOM*.

4.2.10 Flash chamber response

The SHOWER routine started by considering each of the 592 flash chambers as being made up of a set of ten-cell regions (approximately 60 for each chamber, depending on its orientation). For each of these 10-cell regions, a characteristic response was determined based on data taken during the intervals between beam spills consisting of cosmic ray muons traversing the detector at low angles. Over the course of the run, tens of thousands of these events were accumulated, enough that nearly all of the ten-cell regions had a substantial number (hundreds) of muons crossing them. The muon tracks were fit, and relative responses for each of the ten-cell regions were determined according to whether any of the member cells contained a hit associated with the fit position of the muon's passage.

Once an overall response table was established, time dependent fluctuations were determined and a set of time-dependent ten-cell region response tables was generated. Physical reasons for such fluctuations from constant response included:

- water vapor contamination or other variations of gas quality in the flash chamber system, and
- damage, repairs or adjustments to the flash chambers over the course of the run.

These response tables were in the form of pairs of efficiency and multiplicity tables, taking into account different aspects of the ten-cell regions' response. The term response table will refer to this combination.

The procedure used to generate the efficiency and multiplicity tables has been described above in general terms. Some specific considerations are illustrated in Figure 4.12, which represents a section of the calorimeter containing several flash chambers of one orientation. The distance between chambers has been compressed to allow the flash chamber sections themselves to be drawn larger for clarity. The solid line represents the actual path taken through the section by a cosmic ray muon. The cells which are recorded as having lit up are shaded. The dashed line is the least-squares fit to the lit cell positions, such as the table-making procedure used. The ten-cell regions of interest are indicated (note that for the purposes of

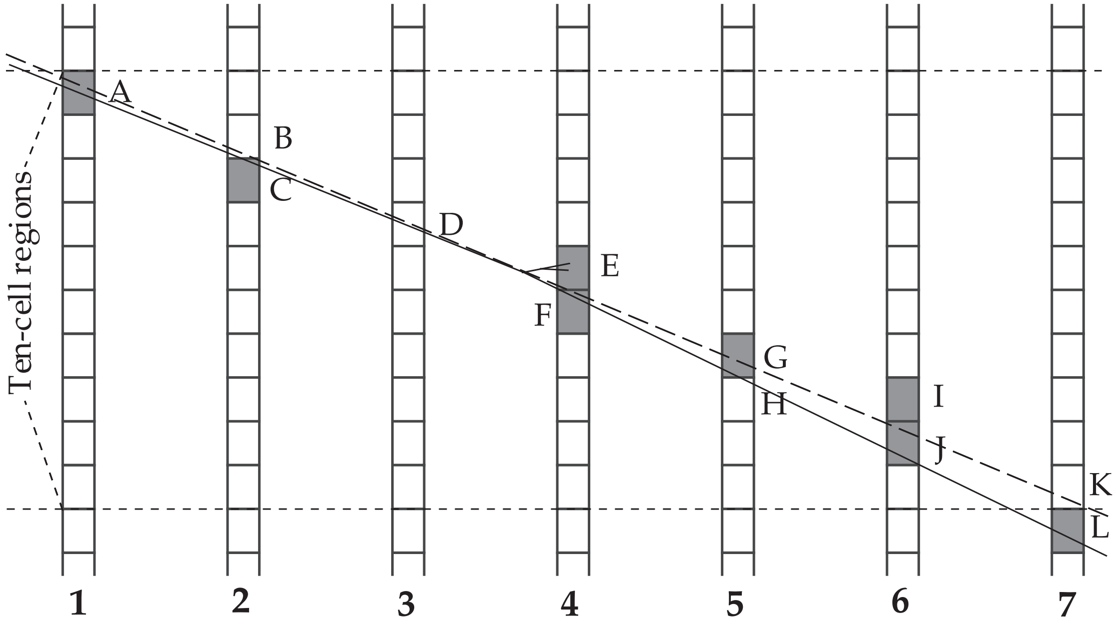

Figure 4.12: Illustration used in describing the efficiency and multiplicity calculation procedure (*see text*).

this simplified illustration, the alignment of the flash chambers is assumed to be perfect).

The most typical case seen was when the muon went through a cell, lit it up, and the fit to the muon's position was close to its actual postion (*e.g.,* cells A, C, G or J in Figure 4.12).

There were numerous other effects seen to occur.

- The muon, travelling at an angle to the flash chambers, passed through two cells in a single plane and lit both of them (there are no examples of this in the figure). This increased multiplicity.

- The muon passed through a cell, but only in the plastic part of it, so no gas was ionized to provide the seed for a glow discharge (*e.g.,* cell B in Figure

4.12). The plastic separating the cells varied from 0.01 to 0.02 inches (0.25–0.5 mm) in thickness of a total cell width of about 0.23 inches (5.8 mm), so this geometric acceptance effect on the efficiency was small.

- The muon passed through a cell, but for some reason, no hit was recorded (as in cell D in Figure 4.12). This was a common cause of inefficiency for most flash chambers. The reasons for not lighting up included gas composition problems, HV pulse problems, and irregularities in the readout system, among others. Most were probabilistic in nature—some muons would trigger the cell while others would not (apparently by chance with probabilities governed by Poisson statistics). There were a number of sections of the detector, however, which were completely dead for part or all of the data-taking due to hardware problems. Sometimes the lack of a hit was due mainly to the shortness of the muon's path-length in a cell, which limits the amount of ionization produced in the cell and increases the chances that it will have recombined by the time of the trigger (as in cell H in Figure 4.12).

- The muon could produce other ionizing particles via its interactions with the material in the calorimeter. These included high energy photons from bremsstrahlung and delta rays from pair production. These occasionally survived passage through enough target material to light up flash chamber cells of their own, usually near the muon's own trail of hit cells (*e.g.,* cell E in Figure 4.12). This resulted in an increase in multiplicity.

- The readout may register a hit in a cell which was not really lit up at all (cell I in Figure 4.12). Such occurences were generally random, with the probability dependent on the particular characteristics (such as the setting of the discriminator threshold) of the readout system of a given flash chamber, and were the primary cause of multiplicity in many flash chambers.

- Occasionally, the fit to the muon's path may be locally far enough away from its true path as to indicate its presence in a ten-cell region when in fact it really went through the chamber in another ten-cell region (*e.g.*, chamber 7 in Figure 4.12, where an inefficiency is reported for the ten-cell region containing cell K, since the actual hit in cell L does not count towards cell K's region's hit-reporting). The frequency of this type of problem was minimized by making cuts on the qualities of the cosmic ray muon tracks: tracks which were unusually curved or kinked were rejected from the study sample.

The results from hundreds of muons through each region of each chamber allowed the probabilistic effects to average out. A ten-cell region had N events where a muon track passed through it, of which H events showed at least one hit in the region, resulting in a total of H′ hits. The flash efficiency (ϵ) and multiplicity (μ) for that region were defined by

$$\epsilon \equiv \frac{\mathrm{H}}{\mathrm{N}} \quad \text{and} \quad \mu \equiv \frac{\mathrm{H}'}{\mathrm{H}}\,.$$

Typical efficiencies and multiplicities were $\epsilon = 0.74$ and $\mu = 1.30$.

In addition to showing the variation in efficiency and multiplicity between different ten-cell regions[5] of a typical flash chamber, Figure 4.11 also demonstrates the variation of these quantities with time. The example chamber's efficiency remained quite stable in the month between the two plotted curves, while the multiplicity was somewhat more variable.

Figure 4.13 depicts the distribution of efficiencies and multiplicities for all of the

---

[5] The bins at the high and low ends of these plots had insufficient muon statistics to establish ϵ and μ. These correspond to ten-cell regions well outside the fiducial volume, so this lack of information has virtually no effect on E_H measurement.

non-dead ten-cell regions (where *dead* is defined here as having a measured efficiency less than 0.05, or no measured efficiency at all). While the majority of efficiencies and multiplicities cluster around the typical values referred to above, there are long tails towards low efficiency and high multiplicity.

The stability of these distributions over time was good during the month interval between the two runs selected as examples. There was effectively no change in the average efficiency or multiplicity, and the r.m.s. of the distribution of individual bin efficiency changes was 4% and that of the distribution of bin multiplicity changes was 6.5%. This can be seen in Figure 4.14.

4.2.11 Response corrections to hadronic shower hits

Since each individual cell in a ten-cell region had a known chance (given by the response tables) of lighting up in response to a minimum ionizing particle's passage, the probability of seeing N out of ten cells lit due to the passage of M particles through the ten-cell region was calculable. Similarly, given that a ten-cell region with a known response character did see N hits, the most probable number of traversing particles could be calculated.

This principle could be extended to quantities of ionization energy if the assumption was made that a track causing twice as much ionization as some standard also would cause the flash chamber cell to behave as it would if two such standard tracks were to pass through. Since the assumption regarding tracking results relative to a standard was really based on amounts of ionization, this led to an estimate of *response-corrected hits* which should be proportional to the energy deposited in the ten-cell region.

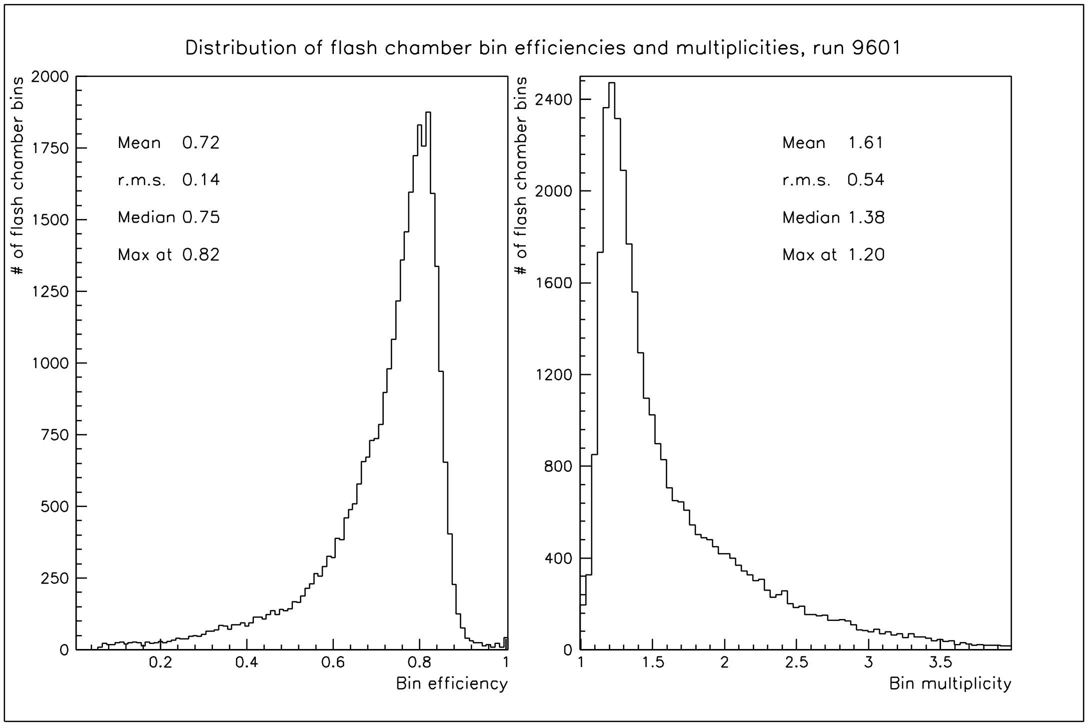

Figure 4.13: The distribution of efficiencies and multiplicities for all 10-cell regions with $\epsilon > 0.05$.

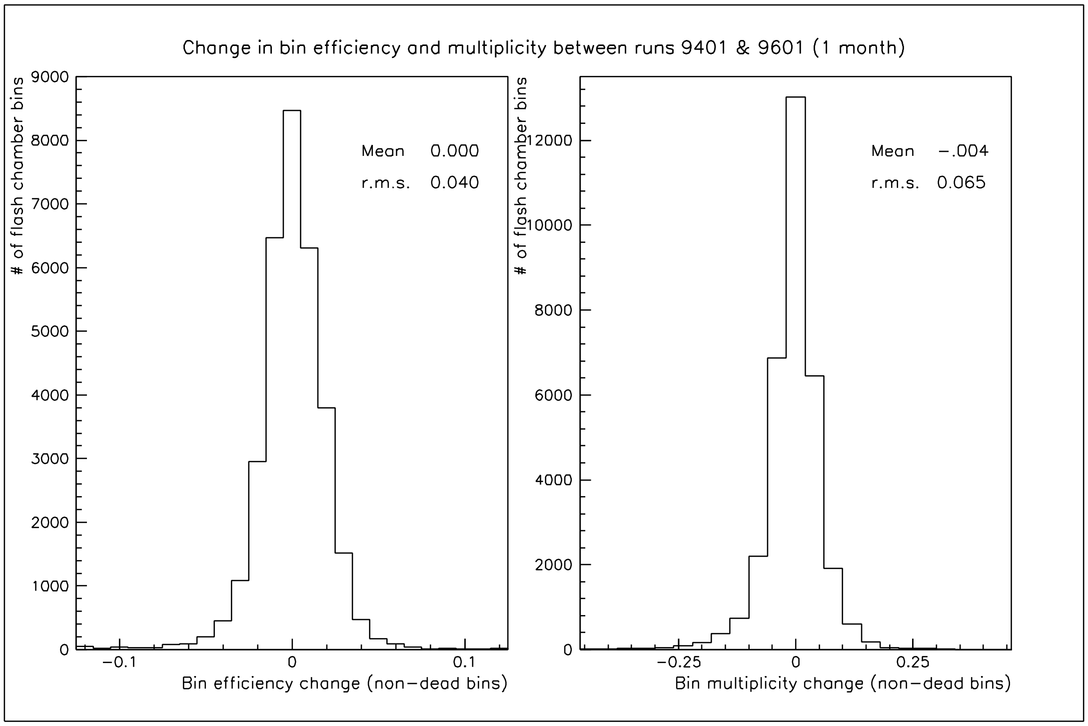

Figure 4.14: The distribution of changes in 10-cell region efficiency and multiplicity between runs 9401 and 9601 (an interval of one month).

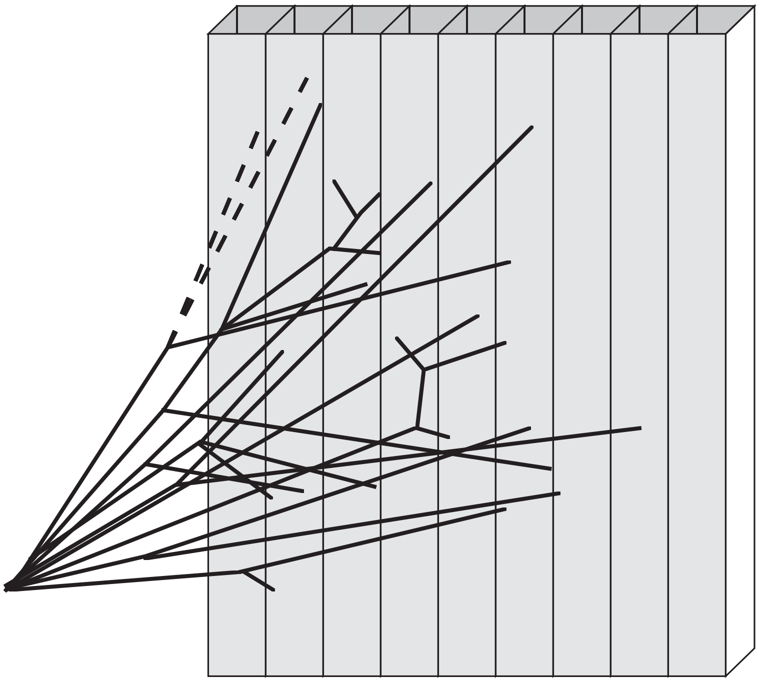

Figure 4.15: Hadronic shower interaction with flash chamber, illustrating the geometric enhancement effect.

This assumption was especially important, considering the three-dimensional nature of the hadronic showers. As the density of particles in a shower increased, so did the probability that a single cell will be struck by more than one particle somewhere along its length. Figure 4.15 depicts a shower interacting with a flash chamber, showing some of these 3-D effects.

Since the basic on/off measurement of a single cell could not properly report energy deposition from more than one particle at a time, information on the local shower density was used to make a *geometric correction* which took into account the probable multiplicity of hits in the direction along the length of a hit cell. Table 4.1 lists some typical values for the combined response and geometric correction factors applied to hits in regions with typical efficiencies and multiplicities.

Both the response and geometric corrections made use of ten-cell regions to better

Table 4.1: Typical enhancement factors for hit cells in 10 cell region (correction factors are dependent on efficiency and multiplicity; these assume typical values $\epsilon = 0.74$ and $\mu = 1.30$).

Raw Hits	**Corrected Hits**
1	1.1
2	2.4
3	3.9
4	5.6
5	7.8
6	10.7
7	14.6
8	20.8
9	35.3
10	57.6

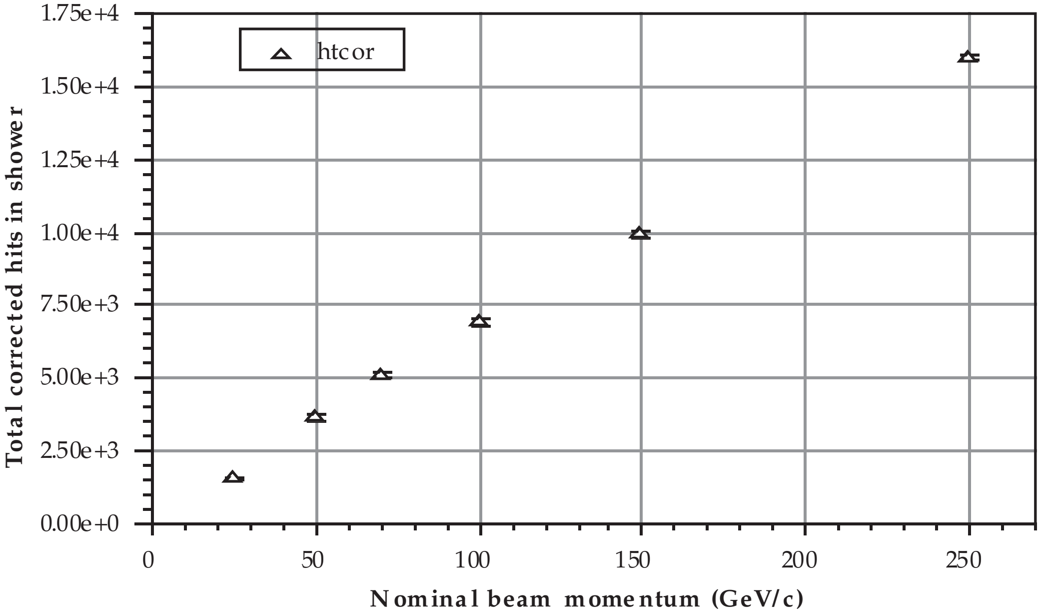

Figure 4.16: Corrected hits as a function of shower energy.

extrapolate from the simple binary single-cell response to the energy-deposition-sensitive response needed for calorimetry. A limitation to these methods appeared at hit densities approaching ten hits per ten cells. At such high densities, additional energy deposition is unlikely to result in higher hit densities. This saturation effect must be taken care of by other means. It is not as bad as the initial saturation seen in the case of the raw hit total, as can be seen in Figure 4.16.

Once the hits in the various ten-cell regions were processed for each flash chamber, the simple next step was to sum over the shower region. This resulted in an estimate for total shower energy in units of corrected hits.

This corrected-hit total was then associated with real units of energy by fitting procedures using data from the hadronic calibration beam and with such techniques as muon momentum / shower momentum balancing (after determining an angle for the shower vector). This quantitative result was called EHDOOM. It could then be adjusted using a rescaling process as described above. The conversion from corrected hits to EHDOOM was nonlinear, as would be expected for a system with saturation properties.

The fractional energy resolution achieved by EHDOOM is plotted in Figure 4.17 as

$$\frac{\sigma(\mathrm{E_H})}{\mathrm{E_H}} = \max\left[0.10, \left(0.04 + \frac{0.80}{\sqrt{\mathrm{E_H}}}\right)\right]$$

Compare this to the fractional resolution of EHPROP (Figure 4.8) and it can be seen that for the lower energy region depicted in the figures ($\mathrm{E_H} < 150$ GeV), EHDOOM provides better energy resolution. Above the range of the figures, EHDOOM's resolution continues effectively unchanged at the 10 % level, while EHPROP continues to improve its resolution as energy increases up to the highest shower energies likely to be measured in FNAL neutrino beam interactions.

4.2.12 Muon correction

The presence of a charged current interaction daughter muon within the hadronic shower posed a problem for the EHDOOM procedure. Due to the non-linearity of the correction for saturation effects in the shower energy calculation, the hit signatures of identical muons would be translated into different energies depending on the density of hadronic shower hits in their vicinities.

There were two effects which competed with one another in causing these differences.

- The number of corrected hits in a ten-cell region was a non-linear function of the number of actual hits observed; if a muon added one hit to a ten-cell

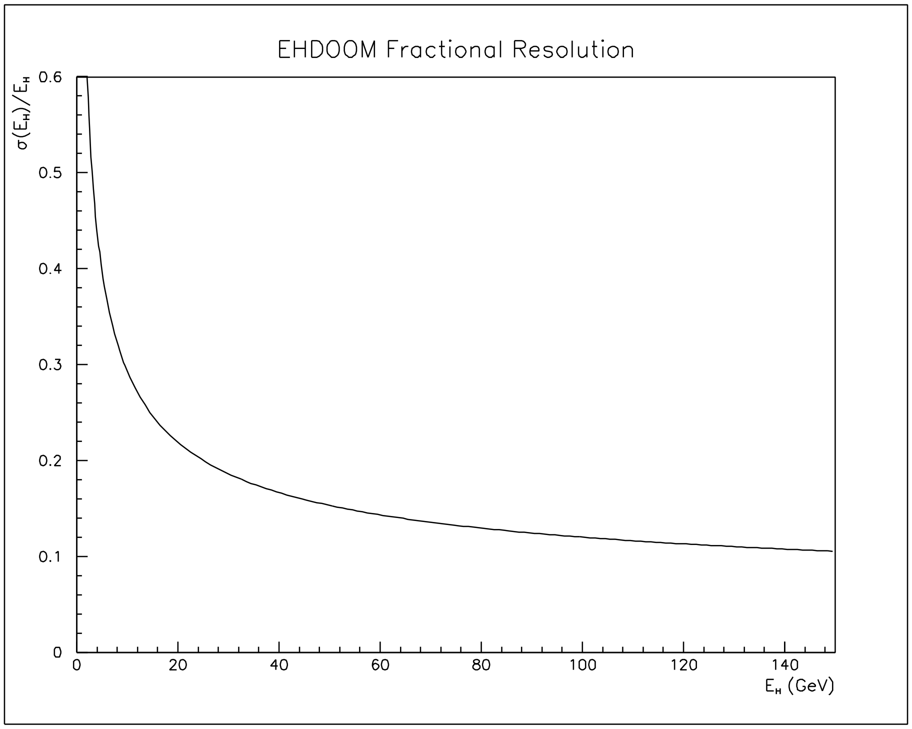

Figure 4.17: Fractional energy resolution of EHDOOM.

region which already had several hits in it, it would count as a greater energy deposition than the same muon adding one hit to a region with very few hadronic ionization tracks registered in it.

- If a ten-cell region already had most of its cells hit by particles in the hadronic shower, the probability rose that the cell lit up by the passage of the muon would have been lit up anyway. In this case, the *effective* energy deposition from the muon would have been zero.

The amount by which the first effect enhanced the muon's contribution to the measured shower energy and the second effect diminished it depended a great deal on the geometry of the hadronic shower. Several showers which contained the same amount of transferred interaction energy might have been recorded as having very different EHDOOMs depending on the position of the muon track relative to the various patterns of their energy deposition.

A related problem was the inherent inapplicability of the hadronic shower energy procedure to the determination of energy loss by muons. The calibration of the procedure was based on hadronic showers, which consisted of mixes of particles, each with a characteristic interaction and ionization cross section. In a purely hadronic shower, such as those produced by neutral current neutrino interactions or calibration beam events, the exact mix would vary. The calibration procedure integrated over these variations, however, and they were measured, along with other effects, as part of the hadronic shower energy resolution.

A muon would have had different interaction characteristics from the average shower's (which was one of the reasons why muons could be distinguished so readily in the E733 detector). It would be much more likely to cause a trail of consistent ionization strength (just over the minimum required for ionization to occur at all) and was much less likely to deposit a large fraction of its energy in a small region of the detector. The binary nature of the flash chamber cell readout did not allow a distinction between the type of trail left by the passing of a muon and the heavier ionization deposited by an otherwise similar hadronic particle track, as could be done in the proportional plane system. Taking a length of muon track and running this flash chamber-based energy procedure on it as if it were a hadronic shower would result in an EHDOOM. This EHDOOM, however, would be a poor match for the value of the energy truly deposited in the detector by that muon.

The combination of these effects made the simple subtraction of an easily calculable predicted contribution from a muon's ionization to the shower energy unfeasible. This was unlike the situation with proportional plane based shower energy measurements.

There was a solution to the problem of muon interference with hadronic shower energy measurements which took into account the primary advantages of using the flash chambers. The fine sampling not only allowed the easy detection of muons, but also made it possible in many cases to determine with a good degree of accuracy which hits in the detector were produced by the muon. The details of the track finding will be discussed in a later section. This ability to discriminate between muon-induced hits and shower-associated hits made possible a more accurate determination of the shower energy.

In regions where the muon track was clearly separated from any hadronic energy deposition, it was easy to flag the muon track hits. In regions where the hadronic shower was too dense to allow identification of muon hits, such identification is likely to be irrelevant anyway, since the cells in question would probably be lit regardless of the presence of the muon's track. In regions of intermediate shower energy density, an algorithm was used which took into account the probability that a hit along a muon track was due solely to the muon, in which case it was flagged. If there was a good chance it would have been there anyway, it was left alone. Then, the hits which had been flagged as muon-induced were ignored by the energy measuring routine. The resulting energy measurement was referred to as the *muon-eliminated* EHDOOM.

The settings determining the sensitivity of the algorithm were established by means of various tests, including the production of artificial muons in software and overlaying real shower-only events. Comparing the shower energies measured after the addition and subsequent elimination of "muon" hits to those found by measurements beforehand, settings were adjusted so that, on average, it would be expected neither to eliminate too many hits from consideration (thus removing hits which really belonged to the shower), nor to leave too many muon-induced hits unflagged (allowing the shower energy measurement to include muon energy as well). The exact pattern of energy deposition by the shower and muon affected how well this balance worked in a given event, as did the quality of the muon finding system's track fitting and hit selection. The settings used were an attempt to achieve a good balance for typical events.

The muon-eliminated EHDOOM could then undergo the rescaling process, as well, ensuring the best possible fit to the expected energy spectrum. The version of rescaling actually used was one which improved the results at low $\mathrm{E_H}$ relative to the globally-fit rescaled EHDOOM. This was referred to as the modified-rescaled EHDOOM. Its response at high energies was not very good. As the analysis depended on good response at low shower energies in order to make $\mathrm{E_H}$ cuts which the Monte Carlo program could model properly, this trade-off between accuracy at low $\mathrm{E_H}$ and a more accurate overall $\mathrm{E_H}$ measurement was made.

4.2.13 Flash chamber calorimetry: EHBILL

The energy method referred to as EHBILL was not used in this analysis, but will be described briefly as an alternate method for using the flash chambers as a calorimeter.

The main difference between EHBILL and the older EHDOOM was in the division of the detector into sub-segments. Rather than subdividing each flash chamber into a large number of very small regions and determining a time-dependent relative response for every one of them, as the SHOWER procedure did, the EHBILL method took the approach of grouping together flash chambers by module. The philosophy behind this was that response variations in small regions of the detector were mostly due to random fluctuations and would be washed out when integrated over a large section of the detector. The non-random variations due to true effects such as gas quality would tend to be more global in nature, and would be measurable at the module level more easily than at the ten-cell region level. These sorts of response changes went into a time-dependent response table.

The measurement method used events from the calibration beam and an analysis of their transition curves to start with, and was then extended through the entire detector by a similar analysis selected from the neutrino event data set in a narrow range of energy (as found with EHPROP). When relative response characteristics were determined for each module, a factor could be applied to the observed number of hits in a module to estimate a corrected hit count for that module. These were summed over the shower region, yielding a total corrected hit count which was then transformed into an energy measurement by equations generated by fits to calibration beam data. The combination of transition curve analysis and fitting to calibration beam data was the only emulation of a geometric effect or saturation correction attempted by the EHBILL method.

This method was less sensitive to random fluctuations in small regions of the detector, and to the large sensitivity in corrected hits observed in the SHOWER method to the presence or absence of a mere handful of hits. There were, however, no specific methods for dealing with shower geometry effects or saturation. While its hits *vs* energy plot was monotonic, and energies could be determined, the energy resolution suffered, especially at high energies. Muons could be accounted for by either performing the muon-elimination procedure before using the EHBILL procedure, or by a statistical muon correction similar to that used with EHPROP.

Due to the non-linearity in energy response, the latter may have been less reliable, but since the method was not so sensitive to single hits here and there, it was at least a more reasonable course of action than attempting a similar correction with in the SHOWER procedure. In cases where the muon track fit was not very good, potential problems with the selection of which muon hits were to be ignored were of less importance, as the method dealt with integrated numbers of hits rather than local densities of hits.

EHBILL was not used in this analysis because the calibration and rescaling procedures used in setting its energy scale were geared towards CC events. The results for NC events using this CC event-based scale did not result in good agreement with Monte Carlo simulations, whereas the CC event results were in satisfactory agreement. Further study would be required to establish the reasons for these discrepancies and find a solution which would enable the use of this method to achieve consistent results for both classes of ν events.

4.2.14 EHAVG and EHAVG2

In order to make best use of the available information, the final E_H was measured using both the proportional plane system and the flash chamber system.

Procedures were written to perform resolution-weighted averages of the rescaled EHPROP (with a statistical muon elimination for events classified as charged current) and EHBILL (called EHAVG) or the modified-rescaled EHDOOM (called EHAVG2, using the muon-eliminated shower for events where a muon was found).

Since the resolutions affecting the weights in these averaging procedures were themselves energy dependent, the procedures were iterative processes. The main

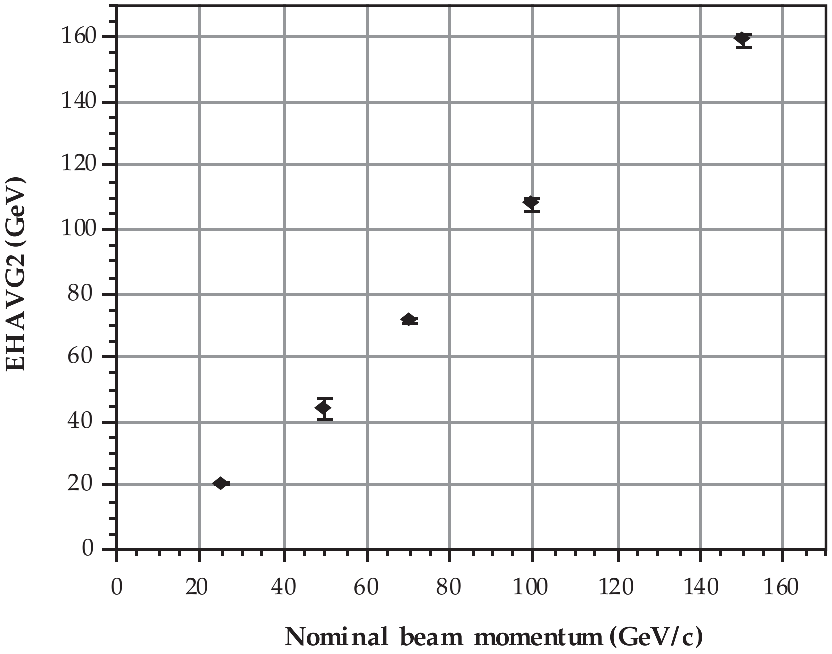

Figure 4.18: EHAVG2 measurement of calibration beam hadron showers.

assumption was that the result of each iteration was the true hadronic shower energy at which value the resolutions for the next iteration should be calculated. There was usually convergence by the end of the second iteration, but up to ten were allowed before the routines gave up trying to come any closer to the true weighted average.

This averaging scheme allowed the low energy measurements to be dominated by the flash chamber information, where frequent longitudinal sampling was a great advantage, and energy deposition densities had not yet reached the point of saturation. High energy measurements were dominated by the proportional plane information, which was less subject to saturation and geometric effects (or, for charged current ν_μ interactions, muon energy deposition in the shower) and therefore had better resolution at those energies.

This analysis used EHAVG2 as its standard E_H measurement procedure. The results of EHAVG2 measurements on a sample of calibration beam events can be seen in Figure 4.18. Note that the beam momenta used as the x-axis are the *nominal* momenta, the estimates used based on magnet currents in the NH beam line. They may be off by as much as 7 % from the actual central values of the momenta of the particles at those settings[6].

4.3 Event Classification: Muon Track Finding

The accurate classification of events as having resulted from either neutral current or charged current muon-neutrino interactions is the chief goal of this analysis. The key difference between the two is the presence of a muon among the primary products of the charged current interaction.

Muons interacted with the material in the calorimeter only via electroweak forces, unlike the hadronic particles in the debris shower, and with such a relatively small cross section that their range was very large in comparison. The paths they take were subject to less scattering, as well.

The signature of a charged current muon in the E733 calorimeter was a long, fairly straight track of energy deposition which pointed back to the vertex of the event. Generally, the track continued on into the spectrometer, where the muon's path was bent by a known magnetic field for the purpose of determining its momentum. Much could be learned from the study of these muons, but first they had to be found. Figure 4.19 demonstrates the contrast between the typical charged current

---

[6] The determination of actual beam momenta requires analysis based on the current-to-magnetic field curves for the particular beam line magnets and an accurate survey of the geometry of the momentum-selecting scintillator paddles, backed up by studies of the Čerenkov counter measurements made during the run. None of these studies has been finished yet for the 1987–88 run. The 7 % deviation figure is based on the results of these studies for the 1985 run period.

and neutral current interactions.

This identification procedure used information from the flash chamber detector elements, which were well suited to this task. The fine spacing of the flash chamber cells both transversely and longitudinally gave ample opportunity for determining the spatial position of energy deposition very precisely. This aided in the process of deciding whether a set of hits were consistent with having been produced by ionization along the path of a common particle. Since muon paths tended to be relatively straight in three-space, the projections of these paths onto the three orientations of viewing-planes of the flash chamber system will also be relatively straight lines, and thus suitable candidates for line-fitting procedures.

A simplistic procedure for muon track finding would have been to check the hits in the detector to see if they lined up. Subject to some criteria concerning how many hits forming how good of a fit to a straight line would be needed to call it a muon track, this would have been sufficient to find muons *if* they were the only producers of hits in the detector. Indeed, in parts of other analyses which look at muon-only events (such as spectrometer magnetic field mapping), this was essentially the method used.

In neutrino DIS events, however, the muon was not generally alone in the detector. The presence of the hadronic shower in close proximity to the origin point of the muon would have caused considerable difficulties for a very simple line-of-hits-fitting procedure. There were many more hits to consider which really did not have anything to do with the muon track. A simple fitting process would have no recourse but to consider them all as possible members of a proposed track. The result would have been a large number of spurious tracks. Even the real track could end up with a number of variants which fit any reasonable criteria, each based on a

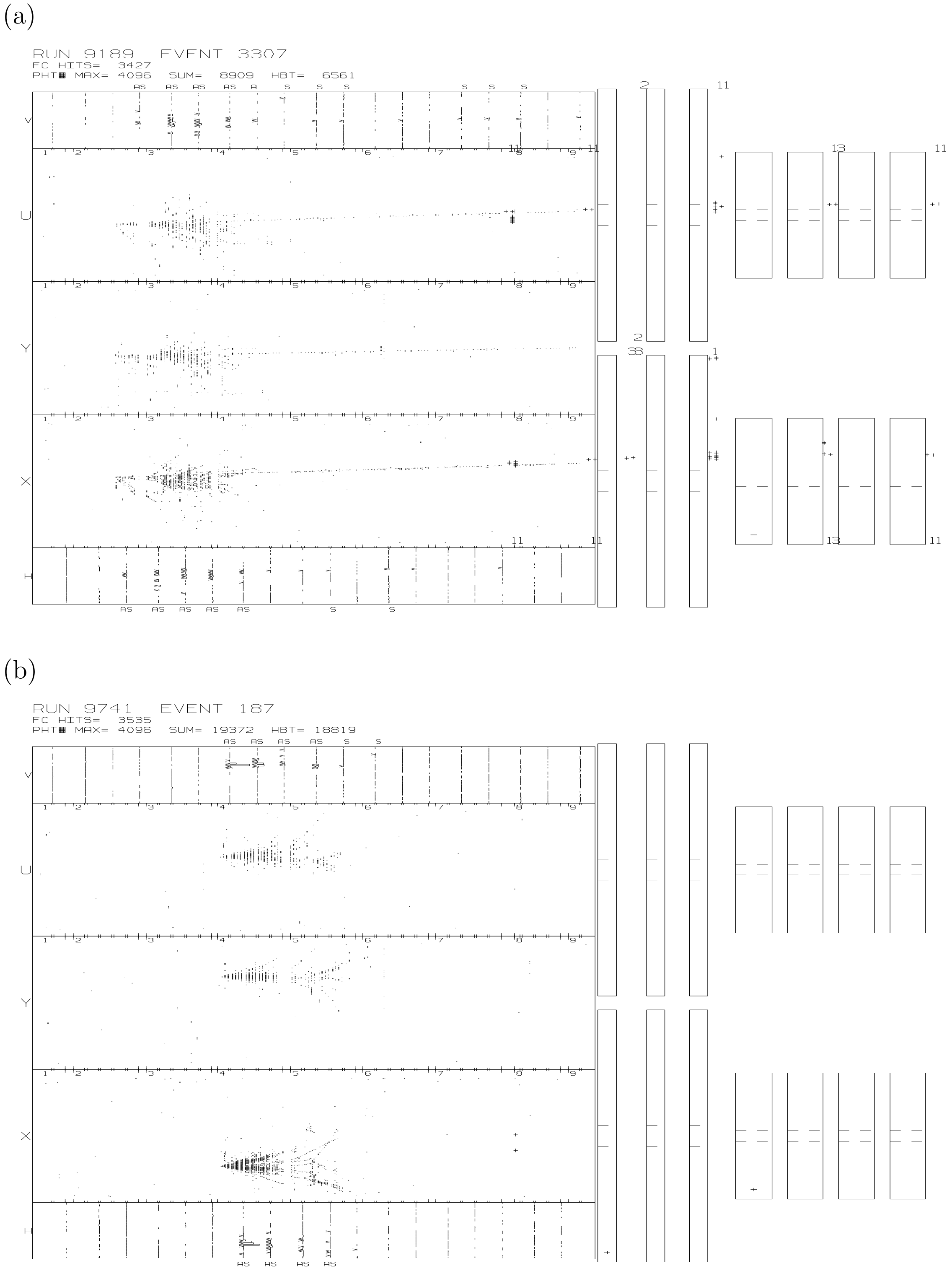

Figure 4.19: (a) Typical Charged Current ν_μ Interaction Event (b) Typical Neutral Current ν_μ Interaction Event

slightly different set of member hits. These real track variants might also have been simply incorrect, as shower-induced hits typically outnumbered muon-induced hits and would therefore unduly influence the linear fits.

The solution to these shower-induced complications used by the E733 Muon Track Finding (MTF) system was a preliminary selection mechanism which used pattern recognition algorithms geared towards the characteristics of real muon tracks. If a pattern of hits which had these basic characteristics had to be found before starting the fitting process, and only those hits fulfilling criteria consistent with being muon-induced were used in the fitting, then the result would be more trustworthy and time was not wasted attempting fits to sets of hits which bore no resemblance to muon tracks.

The system was designed and its parameters were adjusted to maximize the chance that the track of any real muon would be found (subject at most to cuts which would be easy to reproduce in a Monte Carlo simulation of the experiment). There would still be instances where a “muon track” was found which was not really due to a muon, but it would have to have had the same basic qualities as a real muon track to get that far along in the process. This restriction reduced the probability of such an occurrence. The frequency with which this misidentification occurred could be measured and accounted for in the final analysis.

There were two main phases in the MTF process. They were called Muon Hit Binning (MHB) and Muon Pattern Recognition (MPR).

4.3.1 Muon Hit Binning (MHB)

The Muon Hit Binning procedure made use of two properties of charged current interaction-produced muons.

- They were primary interaction products and so were present from the start, at the interaction site, and headed downstream from there.
- They tended to travel in reasonably straight lines through the detector which were preserved in two-dimensional projections such as the format of the flash chamber data.

These properties implied that if the detector were remapped to polar coordinates with the origin at the vertex site in each of the three projective views, a reasonable signature for a muon track in a view would have been a large number of hits at essentially the same angle, ranging all the way from very low to very high radius.

The basic steps of the approach which MHB took are outlined here.

1. MHB produced arrays representing each detector view transformed into polar coordinates with the event vertex at the origin; detector boundaries in this coordinate system were noted.
2. It looped over all the hits in the detector, filling the polar-coordinate array for each of the three views with information about hits within each bin. Figure 4.20 performs these operations on a sample CC event.
3. Array columns (representing angles) with a large fraction of radial bins filled were noted. For details of this process, see Appendix A for a flowchart of the subroutine MHBLEN. These were some of its features.

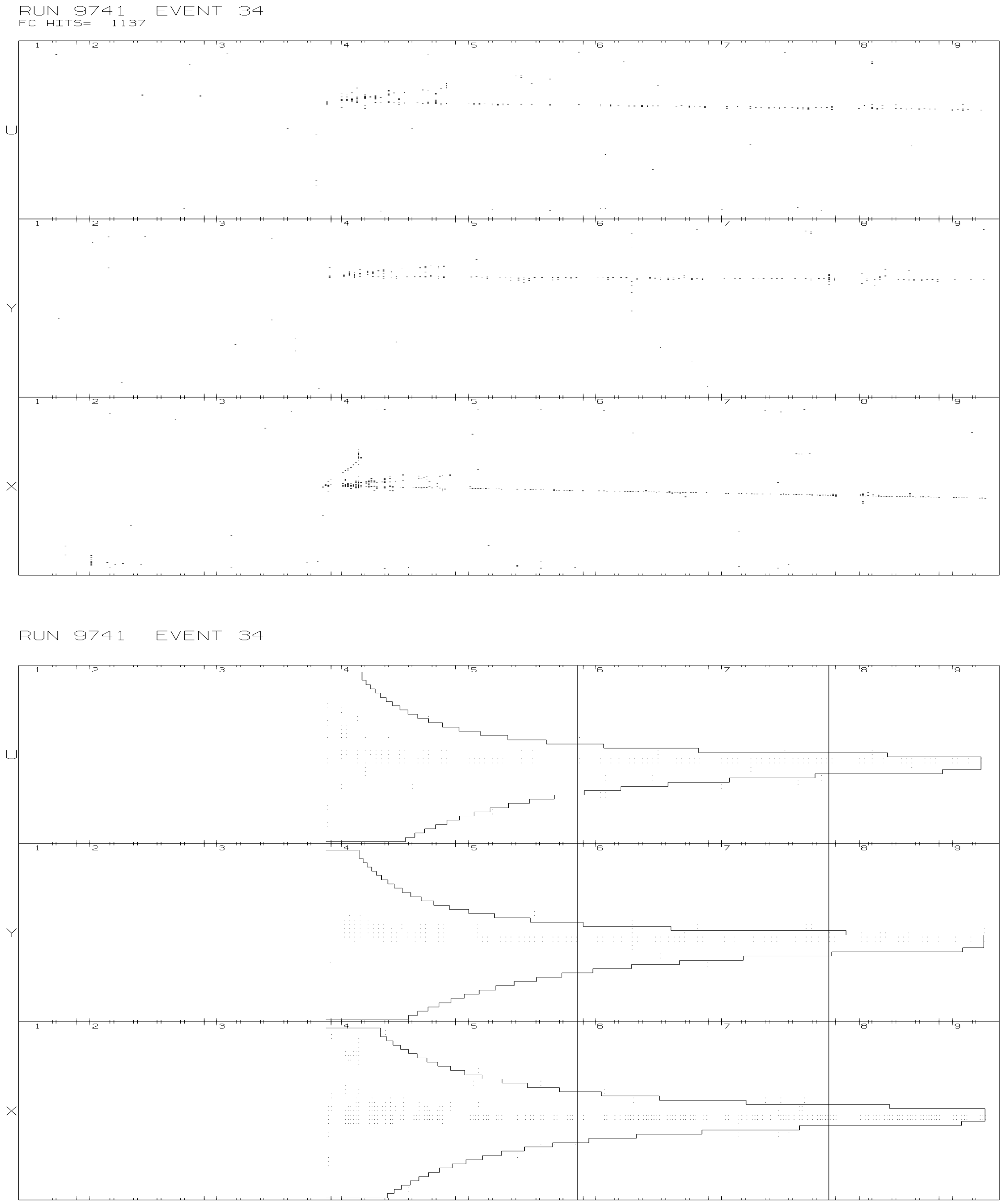

Figure 4.20: A demonstration of MHB's "searchlight"-style polar coordinate flash chamber hit array, used to identify muon track candidates. The vertical lines denote DZMIN and DZSUF.

- To account for tracks which might not have gone exactly straight, or instances where the vertex position determined by VRTDRV was a little bit off, skewing the angular distribution, MHB allowed a spill-over from columns on either side of a given column to count towards this and later requirements for the bins in that column.
- It also accounted for variations in detector response, not penalizing a bin for lacking a hit as much in less-efficient regions of the detector as in more-efficient regions.
- If a fraction of the radius bins in a column contained hits which was consistent with a muon track traversing the corresponding sections of the detector, out to either the detector edge radius bin or to a minimum longitudinal distance called DZSUF (set to 1000 cm in the E733 analysis), the column was flagged for further consideration. Consistency with muon behavior was based on a statistical test with a limit of 3.1 standard deviations between observed and expected hit densities.
- Candidates in columns where the detector edges were nearer to the vertex than a parameter called DZMIN (set to 500 cm in the E733 analysis) were also excluded for practical purposes. Hadronic particles were able to traverse distances up to the neighborhood of this length, while it was rare for a charged particle other than a muon to travel more than that distance downstream. Longitudinal distance was chosen as the parameter to ease calculation and Monte Carlo simulation. The value chosen for DZMIN was based on studies, and was equivalent to 5.9 $\pm 0.1 \Lambda_I$, at which distance 0.3 % of the primary shower hadrons were expected to have remained without interacting with the medium. Some larger fraction of secondary shower hadrons may also have still beem around. Some of the

less energetic or very high angle muons will fail this cut as well, which underlines the need for a cut conducive to a Monte Carlo simulation's replication ability.

4. When all three views had gone through the above procedures, and all of them had at least one candidate column, each combination of these candidates was checked to see if three-dimensional geometry would have allowed a real muon to have these projections.

If there were no such candidates, or if the only sets of three candidates were inconsistent with a common original three-dimensional track, the MTF package gave up at this point with a negative result.

4.3.2 Muon Pattern Recognition (MPR)

If there were candidates which fulfilled all of the requirements to this point, they were passed to the Muon Pattern Recognition (MPR) section of the MTF package. The main task of this section was to identify sets of hits associated with the candidate angular regions which had the characteristics of muon tracks.

These were the basic steps which MPR took in order to provide track-like sets of hits for the fitting packages to work with.

1. For each candidate angular region in each detector view, starting at the downstream end of the region, MPR looked for sets of hits which formed straight lines which pointed back towards the event vertex.
    - These restrictions (straightness and pointing back) were not stringent, as it was possible for a real muon track to have some curvature which causes

the instantaneous derivative of its projected path to point well away from its initial trajectory. The algorithm did try, however, to disallow abrupt kinks in track candidates, as they were not typical of muon tracks.

   - The qualities of straightness and continuity of these sets of tracks were subject to requirements set by adjustable parameters and also took into account the response table's information on each detector region.
   - As an example of an effect subject to one of these adjustable parameters, consider that a cluster of many hits close together contributed little to a line fit (since it conveyed only vague positional information due to the difficulty of determining which of the hits was the one left by the muon itself). It still, however, may have been considered for the continuity requirement.
   - The adjustable parameters in this case included a critical localized hit density for ignoring a hit's contribution to a linear fit (set to 4 hits in a region plus or minus 24 clock counts from a candidate hit), and the number of no-hit chambers MPR was to allow after seeing such a cluster before giving up its search of that particular trajectory (set to 15).

2. The result of the first step was that each candidate angular region may have had anywhere from zero to several sets of hits associated with it which satisfied the basic requirements of length, continuity, and localized straightness which pointed back to the general vicinity of the view's interaction vertex.

3. If there were no successful muon-like patterns in a region, it was dropped from consideration. If there were more than one, each was compared with the others to see if it was consistent with being a duplicate of another, better track, sharing some hits but not others. If such were the case, then the track

variant which was of least quality (shorter, more gaps, etc.) was dropped from the list.

4. After all this, there was a list of sets of hits consistent with muon tracks in each view. If one or more views had no candidate hit-sets, the MPR section reported to MTF that no muon patterns could be found. A muon seen only in one or two views was not considered to be good enough. True muons which left tracks like this would be excluded, and their expected number would be part of the Monte Carlo simulation. Similarly, if no combination of hit-sets in the three views was consistent with a three-dimensional muon track, a negative report was delivered.

5. Each combination of three hit-sets which was consistent with a muon track through three-dimensional space then underwent a final re-fit procedure which imposed constraints of three-dimensionality onto the fit weighting by incorporating the single-view uncertainties into an error matrix which accounted for correlations between the views' information while fitting. This yielded the best-fit line coefficients for the track as a whole, as well as additional fits biased towards the upstream end and towards the downstream end of the track.

    - The three separate fits were to account for curvature.
    - A track may have had a curve in it, but the upstream part of the track's path was of interest as the initial trajectory of the daughter muon, which was where the interaction physics played a role.
    - The downstream part of the track was also of interest, as it might more closely resemble the muon's actual behavior upon entering into the spectrometer. A more detailed knowledge of this behavior aided in the momentum fitting process, as it represented the straight line path the muon

was taking before it met the curvature-inducing toroidal magnetic field.

- For technical reasons (poor hit statistics in the smaller-region fits, mainly), in some events, the smaller-region fits were deemed of too poor a quality to be of use and were replaced by copies of the full track fit.

Events where MTF identified muon-track candidates which fulfilled all of the requirements and were fit in the calorimeter were classified as charged current (CC) interactions. Those where no track was found which survived all cuts were classified as neutral current (NC) interactions.

The CC events were then sent along to the muon spectrometer analysis package to see if their muon tracks corresponded to any hits in the spectrometer, and, if so, if it was possible to determine from them the magnitude of the muon momentum and the charge of the muon.

4.4 Muon spectrometer analysis package

The muon package attempted to determine the momentum and charge of a muon passing through the spectrometer of the Lab C detector used in E733. The toroidal magnetic field induced in the magnets would have bent a positively charged muon outward from its initial path, while a negatively charge muon would be bent inward from its initial path, towards the centerline of the toroidal magnets. The rate of this deflection is inversely proportional to the component of the muon momentum normal to the magnetic field lines; i.e., the z-component of the momentum. Combining this information with the angle of the trajectory, the total momentum can be determined.

Complications in this procedure stem from several sources.

- Inefficiencies in the drift chambers could allow muons to pass through unnoticed.

- Noise hits in the drift chambers, either associated with the muon (e.g., delta rays, collision debris from the iron in the toroids) or not (e.g., cosmic rays, debris from other events outside the calorimeter, electronic noise, punch-through debris from an unusually long hadronic shower over-reaching the the calorimeter and hitting the spectrometer planes), could make track identification and fitting more difficult.

- The toroidal magnets' inner and outer edges caused a fairly sharp discontinuity in the bending field, which had to be accounted for properly in order to get a trustworthy fit to the momentum.

- The muon itself was losing energy (and therefore altering its momentum) as it traveled through the spectrometer, and its path scattered randomly away from a predictable path via multiple scattering processes and catastrophic events (collisions with spectrometer material, elastic and inelastic).

The muon package accomplishes its task via the following sequence of steps. Some of the routines involved are described in more detail after the flowcharts in Appendix A.

1. The basic pertinent information for the event is loaded into the appropriate common blocks.

    - Calorimeter tracks were forwarded from MTF (or other muon-finding package), if any (if there were no calorimeter tracks, the process stopped here).

  - Drift chamber information was loaded: which wires were hit and what drift times were reported. If there were no hit wires in the drift chamber system, no fit could possibly be found, so the process would stop here with a null result.

  - The basic drift chamber information was processed by a package called MMCLUS, which grouped associated hits (such as back-to-back sets of hits in the bilayered drift chambers) and established their spatial positions. This helped to reduce fit complications due to delta rays or other physical interactions of the muons with spectrometer material, as very closely spaced hits would be counted in the same cluster. This saved the processing time of attempting to establish fits through more than one nearly identical hit position, most likely caused by the same passing muon anyway.

2. After there was a list of potential muon hits in the spectrometer, and the information concerning candidate tracks' initial trajectories at the point of entry had been established, the package entered the Muon Hit Selection (MHS) phase. MHS associated sets of spectrometer hits with the various incoming calorimeter tracks. It then decided on an initial estimate for the muon momenta which would have led muons with those calorimeter trajectories to cause the observed patterns of hits in the spectrometer drift chambers.

3. After the MHS process, each incoming track may have had an associated spectrometer track with an estimated momentum. If none could be found, that was the end of the trail for that particular incoming track. There was a slight detour here into a routine called MHSREDO, which flagged the set of hits associated with the best momentum fit, and then went through the

MHS iteration process one last time for all of the other tracks, instructing it to ignore the hit clusters flagged as being associated with the best fit. This eliminated some of the bias induced in the less-well-fit tracks due to having a better-fittable line of hits in the same field of view. While occasionally,[7] two real muon tracks may have shared hits in one cluster on one plane, it would have been very unusual for them to share them in more than one plane in a row (due to variations in incoming trajectory and momenta), so any fit which depended on duplicating the pathway of the best-fit track over the course of more than one drift station was now forced to re-adjust. Fits with only one cluster in common with the best-fit trajectory would have to change much less, unless that was the only hit-cluster in the predicted path. This might have caused more preliminary tracks to be rejected, but those which remained were much more likely to be due to the passage of real muons, and not mere mathematical constructs due to the passage of another track's muon through the general vicinity.

4. The final fit process was called MMDRV. Given the preliminary fits found by MHS, it used more refined fit procedures, as well as better drift information[8] yielding more precise position measurements. The MMDRV fit procedures used the same basic cluster quality weighting schemes and fit requirements as those in the MHS package. Several features are worth noting.

    - The quantity actually fit was (1/p), the inverse of the muon momentum, which is directly proportional to the magnitude of the deflection of a

---

[7] The rate of di-muon events from all sources is less than 2% of all CC events.

[8] Since the drift timing-to-position transformation was partially dependent on the angle of the muon path through the drift chamber cell, an initial trajectory had to be assumed in order to properly calculate it. The estimated muon trajectory from the MHS package provided the seed for the drift chamber position information available to MMDRV.

charged particle's path through a magnetic field such as the spectrometers'.

- MMDRV ended up with a matrix of information which was solved by inverting, which preserved possible correlations in the uncertainties predicted in the knowledge of cluster positions both in the data and in the theoretical fit projections (which had to account for such occurrences as multiple scattering and slow energy loss by the muon on its way through many centimeters of iron in the toroidal magnets, but had no way of knowing the specifics on an event-by-event basis).
- The solution of the matrix equation yielded a best fit momentum and track trajectory through the spectrometer.
- Essential information such as the amount of iron traversed and the spectrometer exit point of the track were recorded along with information on the fit process such as a quantity estimating the quality of the final fit, and the χ^2s minimized in the fit.
- The momentum determined was given as a signed quantity, such that a negatively charged muon (pulled towards the center of the toroidal magnetic field, given the usual field polarity) was assigned a negative-valued momentum, while positively charged muons (deflected outwards by the field) were assigned positive-valued momenta. Theoretically, a track which was deflected neither inwards nor outwards by the magnetic field had an undetermined charge and infinite momentum. For practical purposes, this would never happen exactly, though there were some very stiff muon paths which had very large best-fit momenta, reflecting their resistance to field-induced path-bending. These events could be considered as having some uncertainty in the muon charge found for them, as

well.

5. After a final fit was found for each track which had a final fit solution, there was one additional cut generally made in order to reduce the number of spurious muon fits. This cut, called MMGOOD, required that a fit contain hits in at least three drift chambers, at least one of which was in the chamber orientation complementary to that of the other two, and at least one of which is in a drift station different from that of the other two. This ensured that there was some real ability to measure its three-dimensional character, as both vertical and horizontal positions were recorded somewhere in the spectrometer. It also made sure that the muon had survived long enough to be recorded in at least two drift stations, giving enough lever arm to associate a particular deviation from the straight track projected into the magnetic field of the spectrometer from the calorimeter with a particular value of momentum and sign of muon charge.

Chapter 5

Determining R_ν from the Experimental Data

This is a description of the analysis procedure used in determining R_ν from the E733 data and the MSU Monte Carlo simulation program.

The basic assumption behind the analysis procedure is that the Monte Carlo program adequately describes the distribution of accepted states for a given true event. A second assumption, to which it is less sensitive, is that the Monte Carlo program is producing the true events in relative quantities equivalent to those produced in the neutrino beam's interaction with the detector. With these assumptions made, an extrapolation from the observed quantities to the original physical quantities which produced them can also be made.

This chapter will cover several topics.

- A summary will be presented of the relevant items of data and what corrections were made to them.

- The physicists' scan of randomly selected events will be described, as will its uses in providing corrections to the data.

- The MSU Monte Carlo program will be described, including the methods it used to simulate the data and what corrections were applied to this simulated data in the analysis procedure.

- There will be a discussion of the analysis procedure which uses this data and this simulated data to extract the value of R_ν which underlay the observed quantities and a measure of the uncertainties involved in the determination of this value.

- Potential systematic uncertainties will be discussed.

5.1 The Data

5.1.1 Neutrino-nucleon deep inelastic scattering

The data set contains events originating from several types of ν DIS interactions.

- ν_μ Neutral Current Events
- $\overline{\nu}_\mu$ Neutral Current Events
- ν_μ Charged Current Events
- $\overline{\nu}_\mu$ Charged Current Events
- ν_e Neutral Current Events
- $\overline{\nu}_e$ Neutral Current Events
- ν_e Charged Current Events
- $\overline{\nu}_e$ Charged Current Events

This list could be further subdivided, if desired, according to:

- the type of secondary-beam particles which decayed to form the neutrinos or anti-neutrinos in question;

- the type of nucleon target involved in the interaction; or

- whether the hadronic debris generated by the interaction spawned a decay muon or not.

These subdivisions are handled by the Monte Carlo, but need not be explicitly described in this part of the description of the analysis.

5.1.2 Background events

The design of the Quad Triplet neutrino beam line and the characteristics of the E733 detector require the use of deep inelastic ν_μ scattering interactions only to measure R_ν. This excludes ν_e, $\overline{\nu_e}$ and $\overline{\nu_\mu}$ DIS interactions, which become the major sources of background events.

Other background events due to non-DIS ν interactions include those from:

- ν elastic scattering from electrons;
- inverse muon decay ($\nu_\mu + e \rightarrow \nu_e + \mu$); and
- quasi-elastic (QE) νN scattering.

The cross sections for all of these are small relative to ν DIS scattering, and all but the electron scattering and $\nu_e N$ QE scattering deposit very little shower energy (typically less than 2 GeV of apparent energy) in the calorimeter and therefore do not meet the trigger criteria and fail the data $\mathrm{E_H}$ cut as well. In the current analysis procedure, the assumption is made that the contribution of these processes to the final data set is negligible, and such events are not modeled in the simulation software.

In addition to events due to neutrino interactions, the data set contains other beam-related events in two general categories, described earlier in section 4.1.3.

1. *Upstream* and *outside* events which avoid being rejected by the veto wall (due to the $\lesssim$1% veto wall inefficiency or because the outside event did not come in from the front of the detector at all). Most of these events fail the basic fiducial volume cuts — the vertex is found very close to the front or edge of the detector — but a few get through due to unusual geometry or other reasons.

2. *Out-of-time* events, which are mainly true ν interactions which have either caused a spurious trigger to occur in the detector long after the actual event happened or are still active enough to register some response in the detector when another actual event triggers it. These events are fairly easy to differentiate from normally-triggered events due to the nature of the detector — many components are very sensitive to the timing of energy deposition. The usual symptoms are a shower signal in the flash chambers (often a little sparse) and very little if any signal in the proportional planes and drift chambers.

There are also events in the non-beam-related category of *cosmic ray* events, most of which fail the basic energy deposition and fiducial volume cuts.

In some sense, misclassification of ν_μ DIS events by the data analysis software causes some fraction each of the varieties of those events to act as a background for each of the others. This is called *confusion*, and is dealt with by reassigning events from one classification to another, rather than eliminating them from the data set entirely, as is the case with true background events.

5.1.3 Information available for each event

As described in chapter 4, the basic data analysis process measures several quantities for each event.

- VRTDRV measures vertex location, which fiducial volume cuts are based on.
- MTF looks for muon track candidates. If any are found, the spectrometer analysis package attempts a fit. The results determine the placement of the event into one of four classifications:

  NC : no muon track found at all;

  CC0: at least one muon track found, but none result in a spectrometer fit;

  CC–: at least one muon track found, and a spectrometer fit to a μ^-;

  CC+: at least one muon track found, and a spectrometer fit to a μ^+;

  NC and **CC0** together form the **N0** class (no fit μ), while CC– and CC+ together may be referred to as the **CCfit** class.

- SHRLEN finds the limits of the hadronic shower.
- The shower energy routines measure the energy deposition within the shower limits. This analysis uses EHAVG2, which in turn makes use of EHPROP and EHDOOM. The $\mathrm{E_H}$ cut is then made on this quantity.

The result of this sequence is a data set within some region of the detector with some characteristic energy range and only four distinct kinds of events.

Referring back to the underlying composition of the data set, some generalizations can be made about the origins of the events in each of these classes. The primary constituents of the **CC−** class will be ν_μ charged current events, which are the only ones on the list which generally have a μ^- in the final state. Similarly, the **CC+** class will contain mostly $\overline{\nu}_\mu$ charged current events. All other kinds of events will tend to end up in the **N0** class. There will be some mixing between classes due to physics effects such as decay muons, instrumental effects, and the effects of the algorithms used in the classification process.

Part of the analysis involves determining the magnitude of each variety of misclassification, which leads to the next section.

5.2 Corrections to the Data

The only explicit exclusion of events from the data set is done in making fiducial volume and hadronic shower energy related cuts. This does not mean, however, that the numbers in each class for a given data set are completely fixed at this point. Three main types of correction are applied to these numbers. The first two types are based on the results of the *physicists' scan*, described in section 5.3.

5.2.1 Background subtraction

A statistical correction to the data is made based on the scan's determination of the rates of occurrence of the main types of non-neutrino events listed in the previous section — upstream, outside, out-of-time, and cosmic ray events. Nearly all of these events end up in class **N0**, so this can be seen as a reduction in the number of valid **N0** events in the data set.

5.2.2 Muon track finding software correction

There is a small correction made to the data set based on the results of the scan aimed at accounting for any slight variance from the basic rules of the standard MTF algorithm which may have occurred in the data analysis. This is important because the Monte Carlo assumes a very strict adherence to a set of basic rules in the decision of whether or not a track might count as a muon track. The software algorithm used on the data was designed with a certain amount of flexibility (mainly to avoid getting confused by noise hits), and did not always strictly abide by the underlying basic rules in making its decision.

The discrepancy rate was determined by the scanners and corrected for here. It took the form of a shift[1] of events from the **CCfit** classes into the **N0** class to account for events which had actual fit muons, but which would not have if the data analysis package followed its own basic rules more stringently.

An alternate method of achieving the goal of equivalence between the results of the data analysis software and the Monte Carlo simulation of the MTF process would have been to allow each to make its decision and then employ a more stringent cut which should apply equally to both processes. Rather than shifting a small number of events between the data's **CCfit** and **N0** classes, there would have been **CCfit→NC** shifts in both the data set and the Monte Carlo's simulated event set. This method was not used since the scan was necessary to measure the rates of the other types of backgrounds anyway, so the information for the rule-discrepancy method was available. The decision was made to minimize the number of shifted

---

[1] The amount of this shift can be found in Tables 5.2, 5.4 and 5.5. It is called the *NC→CC→NC Reprieve* correction. A similar shift is calculated and performed for events called CC0, but as this shift is just between two parts of the **N0** class, it plays no role in the final result of the analysis.

events to reduce overall uncertainty in making such shifts.

5.2.3 ν_e interaction correction

The last type of correction is the elimination of a number of events from each class corresponding to the predicted fraction of events originating from ν_e and $\overline{\nu}_e$ interactions. This correction is necessary mainly because ν_e and $\overline{\nu}_e$ events in the detector

- are indistinguishable from one another; and
- have almost no chance of differentiating their neutral current and charged current origins[2].

Because they have different physical properties (which in turn affect their observable characteristics, such as ability to avoid $\mathrm{E_H}$ cuts), they cannot simply be lumped in with the ν_μ and $\overline{\nu}_\mu$ events in the analysis, even though the underlying cross sections will have virtually the same NC/CC ratio. The response in this analysis was to make a correction (described later) to the data based on information received from the Monte Carlo simulation.

---

[2] The outgoing $e^{\pm}$s from the CC events form showers which are not easily separable from the hadronic showers which also emanate from the interaction vertex. They are denser than a hadronic shower of the same energy, but not sufficiently different from hadronic showers of higher energies to make a reliable event-by-event identification.

5.3 The Physicists' Scan

A random sample of 12061 events (over 10% of the total data set) was selected and run through the analysis procedure. Pictures of each of these events similar to the ones found in the figures in this dissertation were printed out. These pictures were scanned by physicists in the E733 group (in most cases by three scanners; in all cases by at least two).

The scanners' primary task was to classify each event as a member of one of six basic event types: **NC**, **CC0**, **CCfit**, cosmic ray, out-of-time, or upstream interaction. Other distinguishing features were also noted, but played no role in the final analysis.

The classification of events as **NC**, **CC0**, **CC–**, or **CC+** in the actual analysis was *not* determined by the physicists' scan. The computer algorithms used for this purpose were explicitly designed to be easily simulated. Because of random instrumental effects such as electronic noise or remnants of extraneous or out-of-time interactions, however, the algorithm appeared to "not follow its own rules" a small fraction of the time. The physicists' scan was primarily to determine that algorithmic failure rate.

The size of this failure rate is noted in Table 5.1 in the categories "CC→NC→CC reprieve" and "Extra CC→NC events". When properly combined, the result is that MTF failed 1.09±0.12 per cent of the time. As shown in Table 5.2, this is the largest contribution to the analysis from the scan.

The scanning instructions were very specific about the definitions to be used for the various classes. As described in section 5.2, the chief purposes of the scan were to establish rates of background events and to correct for deviations by the software from its design specifications. The physicists' interpretation of the underlying physical processes for the events was only a secondary notation in most cases. The goal was to provide a baseline equivalent to the data set which the Monte Carlo program would produce. Deviations from this baseline would result in corrections either to the Monte Carlo or to the experimental data[3].

Any events which contained disagreements among the scanners' classifications were scrutinized carefully by a committee of physicists which made the final classification decision. In the special case of out-of-time events, the scanners' opinions were supplemented by a software routine which flagged large discrepancies between the energies recorded by the proportional plane system and th flash chamber calorimeter. These events were also specially scrutinized by the committee. This also acted as a check on the scanners' attentiveness: several such events went unnoticed by one or more scanners. Very few slipped by *all* of the scanners before the software routine pointed them out, however, demonstrating the value of parallel scanning by more than one physicist.

Table 5.1 lists the final outcome of the physicists' scan with the standard fiducial volume cuts and a 10 GeV E_H cut. It can be seen that the great majority of events in the fiducial volume were classified in the same way by the analysis software and by the consensus of the scanners.

The events where the scanners disagreed with the analysis software were further reviewed and a decision was made as to the reason for the disagreement. In some cases, events bypassed the basic underlying rules of the software for reasons which parts of the Monte Carlo analysis accounted for (*e.g.,* the simulation of **CC0** events

---

[3] The application of these corrections is displayed quantitatively step by step through the analysis process in Appendix C.

based on the $2^{nd}\mu$ study, to be described in section 5.4.5), and would therefore not be counted in the same correction factor as those which violated the basic rules in other ways. Based on this assessment, the disagreement groups were sub-divided, and the final correction factors were based on the appropriate combinations of these sub-groups.

Background correction factors are simply the fraction of the accepted data which was in the background group in question. Misclassification correction factors, involving a shift from one class to another are generally the fraction of the affected original class which is to be removed and placed into another class.

Table 5.2 lists these final corrections factors and their uncertainties, which are based on the statistical significance of the scan sampling, and the assumption that the various backgrounds and misclassifications obey Poisson or binomial statistics, whichever is applicable.

5.4 The MSU Monte Carlo

The Monte Carlo program used in this analysis was called the *MSU Monte Carlo*, distinguishing it from the other similar programs in use by the E733 group. It simulates the muon and electron ν and $\overline{\nu}$ interactions seen in the data, predicting in which of the observed classes each event will end up.

The MSU Monte Carlo generated events in a certain sequence of steps.

Table 5.1: Results of the physicists' event scan for the standard fiducial volume (>300 clock-counts from any edge) and E_H cut of 10 GeV.

Scan/Software class	**# events**
Total scan set	**12061**
Fail vertex cuts	1637
Fail E_H cut	199
Pass cuts	**10225**
Out-of-time events	
called **NC**	12
called **CC0**	18
Upstream/outside events	
called **NC**	3
called **CC0**	1
called **CC–**	2
called **CC+**	1
Scan and Software agree	
NC	2296
CC0	598
CCfit	6963
(software class) (CC–)	*5984*
(CC+)	*1069*
Cosmic rays (*called* **NC**)	11

Scan/Software class	**# events**
Scan **CCfit**, Software **CC0**	
μ in toroid hole (no $\vec{B}$)	19
bad calorimeter μ track fit	13
unknown failure to fit μ	4
Scan **NC**, Software **CC0**	
processes known to MC	106
"CC→NC→CC0 reprieve"	22
Scan **NC**, Software **CCfit**	
processes known to MC	*(CC–)* 4
(software class)	*(CC+)* 2
"CC→NC→CCfit reprieve"	*(CC–)* 1
(software class)	*(CC+)* 0
Scan **CC0**, Software **NC**	
probable true NC	35
processes known to MC	11
"extra" CC0→NC events	84
Scan **CC0**, Software **CCfit**	*(CC–)* 12
(software class)	*(CC+)* 2
Scan **CCfit**, Software **NC**	
"extra" CCfit→NC events	5

Table 5.2: Correction factors based on the physicists' scan, standard fiducial volume (>300 clock-counts from any edge) and E_H cut of 10 GeV.

correction factor	**value**	**description**[a]
`cosmics_nc`	0.00108 ± 0.00032	fraction called *cosmics*
`outtime_nc`	0.00117 ± 0.00034	fraction called *out-of-time* **NC**
`outtime_cc0`	0.00176 ± 0.00041	fraction called *out-of-time* **CC0**
`upstream_nc`	0.00029 ± 0.00017	fraction called *upstream*[b] **NC**
`upstream_cc0`	0.00010 ± 0.00010	fraction called *upstream*[b] **CC0**
`upstream_cc-`	0.00020 ± 0.00014	fraction called *upstream*[b] **CC−**
`upstream_cc+`	0.00010 ± 0.00010	fraction called *upstream*[b] **CC+**
`reprieve_cc0`	0.00284 ± 0.00061	data correction *(see section 5.2.2)*
`reprieve_ccfit`	0.00013 ± 0.00013	data correction *(see section 5.2.2)*
`extra_cc0nc`	0.01086 ± 0.00118	MC correction *(see section 5.5)*
`extra_ccfitnc`	0.00065 ± 0.00029	MC correction *(see section 5.5)*

[a] "fraction" *refers to fraction of accepted events.*
[b] *Any interaction originating outside the detector.*

5.4.1 Selection of candidate neutrinos

Interaction candidates were selected from the *beam files* (databases of νs and $\overline{\nu}$s), each entry of which has

- an E_ν;
- a transverse position (x,y) at the longitudinal position (z) of the Lab C detector; and
- the type of parent particle ($\pi^\pm_;$ $K^\pm_;$ or K^0_L) which produced it.

The distributions used to generate these beam files were based on the Malensek parameterization[15] of the Atherton spectrum[16] scaled to the Fermilab neutrino line plus a simulation of the affects of the transport of the secondary particles through the beamline components downstream of the target, and the physics of their ν-producing decays. Selection of interaction candidates alternated from the neutrino beam files to the anti-neutrino beam files with relative selection rates proportional to the results of a simple calculation of what this ratio should be.

There were separate neutrino and anti-neutrino beam files for the K^0_L-produced neutrinos, which were sampled at a rate calculated as appropriate to the actual predicted neutrino flux.

5.4.2 Random x and y, rejection method based on cross sections

Given an interaction candidate, a rejection method procedure was performed to establish a final selection of events with the proper distributions consistent with our current knowledge of neutrino physics. The linear dependence of the cross sections on neutrino energy was enforced, and an event was randomly assigned (half-and-half) to the NC or CC interaction group. x and y were thrown randomly from a normalized distribution which had the advantages of being easily integrable and having a shape fairly similar to, but always overlying, the functional form of the ν and $\overline{\nu}$ cross sections. For x, this was $2(1-x)$; for y, this was $\frac{2}{3}(2-y)$. Then the rejection method was performed using the actual cross section appropriate to the kind of neutrino interaction represented.

5.4.3 Adjustments by reweighting events

Later in the analysis, the Monte Carlo $\overline{\nu}/\nu$ ratio was readjusted in accordance with information from the data by reweighting the $\overline{\nu}$ events. A weighting scheme was also used to adjust the number of events where the parent particle of the incoming beam ν or $\overline{\nu}$ was a kaon. The best Data-MC E_ν spectrum fits indicated that the number of kaon-parent ν interactions in the data was about 10% larger than that predicted by the basic Atherton model.

5.4.4 Analysis of simulated events

Events which survived so far were treated as simulated data, and went through the MSU Monte Carlo's versions of the data analysis, as outlined here.

Vertex position

It is assumed that the found vertex will be essentially the same as the true interaction vertex of the generated event.

Muon track finding

Just as the data analysis looks for potential muon tracks, the Monte Carlo must determine if an event would contain anything which the data analysis would have called a muon track candidate. As the calorimeter simulation is of a strictly four-vector nature[4], this is not a trivial procedure.

- Charged current ν_μ and $\overline{\nu}_\mu$ events have a real muon in the final state. Based on its actual characteristics (range, starting and stopping or exiting positions), a decision is made whether it would have been counted as a muon candidate according to the identification rules underlying the algorithm used in the data analysis. If it is acceptable here, the analysis continues to the spectrometer phase, which, unlike the calorimeter phase, has a hit-by-hit simulation and is analyzed with virtually the same software routines as the data analysis uses. This will determine whether a spectrometer fit is possible and what its properties are.

- All neutral current events, ν_e events, and charged current events for which it has been decided that no muon would have been fit in the spectrometer are given a chance to see if they might still end up in one of the **CCfit** classes due to the presence of a decay muon. Neutral currents, ν_e events, and charged current

---

[4] *i.e.*, the hits and pulse-heights seen in the data are not simulated in any way. only the true four-vectors associated with the components of the interaction are known.

events for which the true muon would not have satisfied the basic muon track requirements are given a chance to see if they might end up in the **CC0** class. This doesn't matter as much, since the final analysis makes no distinction between such events and events where no muon candidates are found at all; both are in class **N0**. It is done mostly to attempt a more complete simulation of the data. These chances are given via a rejection method procedure based on a table of $\mathrm{E_H}$- and detector position-dependent probabilities derived from the $2^{nd}\mu$ study described in section 5.4.5, as is the momentum spectrum of the second-chance found-and-fit muons.

- At this point, each Monte Carlo event is in one of the same four classes as the data (**NC**, **CC0**, **CC–**, or **CC+**).

Shower length and energy

A shower end is determined, dependent on $\mathrm{E_H}$, based on a study of shower lengths in a sample of the data. This is done mainly for consistency with the data, as the current analysis doesn't use this information.

Found shower energies are determined, based on the true $\mathrm{E_H}$ and the resolution functions for each of the main shower energy algorithms used in the data analysis, as determined by various studies using the neutrino data and the calibration beam (as shown in Figures 4.8 and 4.17). The contribution of the primary final state electron or positron to the overall flash chamber shower energy of ν_e and $\overline{\nu}_e$ charged current interactions was determined from its true energy and a detector channel-saturation formula derived from a study of Monte Carlo ν_e events generated using the GEANT full detector simulation program (otherwise not utilized in this analysis).

Fiducial volume and E_H cuts

The same fiducial volume and shower energy cuts are made on the Monte Carlo event set as on the data set at this point. Plots comparing various quantities as the MSU Monte Carlo predicts they would be measured with those quantities as measured in the data may be found in Appendix B.

5.4.5 The $2^{nd}\mu$ study

Because the rate and distribution of muons emanating from hadronic showers originating from the decay of hadrons in those showers is difficult to predict from a theoretical basis, difficult to model without a full detector simulation, and difficult to measure due to the limitations of the hadronic calibration beam, an empirical procedure was developed to estimate the properties of these muons. This was called the $2^{nd}\mu$ study.

The general principle of this study was that a charged current ν_μ DIS interaction's hadronic shower appears to be identical to a neutral current ν_μ DIS interaction's hadronic shower *except for its μ track*. The large available sample of CC events has essentially the same distribution of detector positions, shower energies, and underlying kinematics as the NC event sample. To measure the rate and distribution of decay muons among NC events, their rate and distribution among CC events was measured.

While an event with one muon track found may be a CC event or an NC event with a decay μ, the decay rate is low enough that events with *two* muons found are virtually all CC events with 2^{nd} muons. The characteristics of decay muons from NC events' hadronic showers should match those of the secondary muons in CC events with two muons. Similarly, if restricted to just the part of the detector where the hadronic calibration beam lay, the predicted number of excess **CC** events should be a reasonable match to the number observed in the analysis of the calibration beam's hadronic showers[5].

An advantage of using the $2^{nd}\mu$ study for this measurement is that its use of data provides a mechanism for including potential backgrounds and misclassifications in the obtained rates with no additional effort. This may be contrasted with, for example, doing calculations based on fragmentation functions, decay rates and interaction probabilities. Such a procedure would leave undone difficult-to-measure items such as detector acceptances and the effects of noise hits and the presence of the hadronic shower on the track-finding and spectrometer fit routines. As there is no reason why the applicable backgrounds for NC and CC events should be different, the $2^{nd}\mu$ rate for CC events should be a good approximation to the single-μ rate for NC events, *including* background effects and misclassifications. Most of the extra misclassifications result in "muons" which are found but not fit, changing the event from **NC** to **CC0** and so end up staying in the **N0** class and having no effect on the outcome of the analysis. Backgrounds which result in a found *and* fit μ track are rare, but are accounted for by this method.

The rates of finding and of fitting $2^{nd}\mu$ tracks were measured in bins of fiducial volume location and hadronic shower energy, so that the Monte Carlo could use this information when deciding whether an event will have its classification modified by the presence of a decay muon.

---

[5] This match may not be absolute, as the calibration beam's kinematics force a particular invariant mass for the debris shower, while neutrino interaction kinematics allows a spread in the hadronic showers' invariant mass.

One complication in the procedure used is that a $2^{nd}\mu$ in a CC event may be due to a hadronic decay in the shower, or it may be due to the prompt decay of a charm quark produced in a flavor-changing CC process. The rate of the charm decay component could be estimated by studying the distribution of the momenta and the minimum distances from the found tracks and the interaction vertex position. Secondary muons derived from charm decay nearly all have a charge opposite to that of the primary CC-interaction muon and effectively originate at the interaction vertex. Secondary muons derived from hadronic particle decays are of both charges and originate throughout the shower. The excess number of events with charm decay characteristics could be discerned above the background of hadronic decay events, and could be accounted for by the Monte Carlo analysis software as a *charm correction*, as described in section 5.5.2 below.

5.5 Corrections to the MSU MC output

The MSU Monte Carlo event set is now in a condition analogous to that of the data set before corrections are made. At his stage, it undergoes a set of Monte Carlo-specific corrections. Most of these corrections involve a relatively small number of simulated events. For an example, see the output listing in Appendix C, which gives the values used in the 10 GeV E_H cut, standard fiducial volume procedure.

5.5.1 Rearrange decay muons

The found-and-fit decay muons are rearranged. This is done mainly due to the very low statistics involved: these events are generated by the Monte Carlo in such low numbers that the number of class **CC−** events and the number of class **CC+** events are subject to large statistical fluctuations. This regrouping also allows us to choose a value for the relative acceptance of decay muon **CC−** events and **CC+** events and its uncertainty independent of the Monte Carlo statistical error in the individual numbers (leaving only the statistical error in the sum of the two).

5.5.2 Charm correction to decay muon quantity

A *charm correction* is made, which moves some of the decay muon **CCfit** events back into the **N0** class (and some from the **CC0** subclass to the **NC** subclass within class **N0**). This corrects for a systematic error due to the nature of the second-muon study described in section 5.4.5.

5.5.3 $2^{nd}\mu$ study correction

A *second-muon study* correction is made to account for changes in the energy dependence of the confusion probabilities found by that study using different energy scales. This involves the shift of a number of MC-simulated events from one category to another in cases where the energy scale used in the analysis differs from that used to originally calculate the probabilities of decay muon production. Since these energy scale differences are generally small (generally $< 10\%$), and the decay muon production probability function varies slowly with shower energy, these shifts are generally small (fewer than 1% of the events are shifted in most classes).

5.5.4 Extra CC→NC correction

An adjustment is made, based on the scan results, for events in the "Extra CC→NC", or MTF failure category. Some fraction of all true CC events in the data simply failed to have their muons found by the muon track finding algorithm, even though, according to the scanners, they really fulfilled the basic criteria for legal muon tracks. Since the Monte Carlo assumes that all true muons which satisfy these criteria will in fact be found, an adjustment is made to reflect the reality that they are not.

5.5.5 $\overline{\nu}_\mu$ reweighting

At this stage, the numbers of events in the **CC−** and **CC+** classes are compared with the equivalent numbers in those classes in the data, and the $\overline{\nu}_\mu$ re-normalization factor described above is calculated and applied. Note that this implies that the *shape* of the true $\overline{\nu}_\mu$ spectrum matches that of the model, so that re-weighting all $\overline{\nu}_\mu$ events by the same factor is a valid procedure.

5.5.6 ν_e and $\overline{\nu_e}$ subtraction

By this time, the MSU Monte Carlo events are fully corrected. Using the numbers of accepted ν_e and $\overline{\nu}_e$ events relative to the total number of accepted events of all parentages in each "observed" class, the final correction factors used to remove the ν_e and $\overline{\nu}_e$ events from the data set are calculated now and applied to the data, as described above.

The result of this process to this point is a set of numbers representing fully corrected MSU Monte Carlo events and the fully corrected data which is simulated by that Monte Carlo.

5.6 Processing the Data and MSU MC to get $\mathbf{R}_\nu$

5.6.1 Status of Data and MSU MC Simulated Data

At this stage, there are two sets of corrected numbers available to work with.

From the DATA: `Data_NO`, `Data_CC-`, and `Data_CC+`.

The MSU Monte Carlo has full information available about each event's generated and accepted classification. This can be seen as a matrix[6], depicted in Table 5.3. The individual elements of the matrix have been labelled for later reference, as have the sums of the columns and rows. The *cut* column in Table 5.3 contains events which fail cuts which are to be compensated for in some way; *i.e.*, the Monte Carlo is trusted to represent what's really going on below the cut, and the analysis equations take the cut into account.

A procedure is used which makes no assumptions on the accuracy of the Monte Carlo simulation below the cut (aside from accounting for the fact that the cuts are generally on observed quantities, so that such a cut is not absolutely applicable to true quantities, due to resolution effects). In effect, it is assumed that the simulation is to be trusted *at least* insofar as representing the observed events which pass the

---

[6] an equivalent matrix is available for ν_e and $\overline{\nu}_e$ events and it will not be explicitly listed here; it was used in generating the correction factors which were used in adjusting the *data* numbers to represent ν_{mu} and $\overline{\nu}_{mu}$ events only. For details, see Appendix C

Table 5.3: Matrix of generated *vs* accepted classifications for MSU MC simulated events.

```
accepted in class -->  N0      CC-      CC+      cut        totals

generated as          ----    -----    -----    -----       ------

 muon neutrino NC   nN_N0    nN_C-    nN_C+    nN_cut  ->  nN_tot

 muon neutrino CC   nC_N0    nC_C-    nC_C+    nC_cut  ->  nC_tot

 muon anti-neu NC   aN_N0    aN_C-    aN_C+    aN_cut  ->  aN_tot

 muon anti-neu CC   aC_N0    aC_C-    aC_C+    aC_cut  ->  aC_tot

                    -------  -------  -------  ---------

 observed totals -> obs_N0   obs_CC-  obs_CC+  total cut
```

cuts in question. How well the Monte Carlo handles events which fail the cuts is made unimportant. As a procedural matter, the numbers under the *cut* heading were set to zero. The totals of the generated categories were reset to ignore the cut events. Once this was done, the same equations could be used as were used in the more general procedure.

5.6.2 Basic R_ν extraction procedure

The theoretical basis of the procedure

Given this information, it is possible to extract the R_ν which must underlie the data in order that the observed numbers result from the processes which are known to be occurring (and have modelled with the Monte Carlo program). There are several ways of doing this[7], and the focus will be on the one actually used, a variant of the procedure described in E733 Memo #87-13.

The procedure used is constructed as a sequence of corrections to an initial "observed R-nu" = `Data_NO` / `Data_CC-`, leading to an expression for the number which is consistent with the data's underlying true R_ν. The idea behind this sequence comes from the observation that the Monte Carlo also has an underlying true R_ν (simply `nN_tot` / `nC_tot`) and an "observed" R-nu (`obs_NO` / `obs_CC-`), and that given the information derived from the Monte Carlo of all of the values in the acceptance matrix, one should be able to formulate a transformation from one to the other.

The practical aspects of the procedure

The standard method takes information from the matrix, forms a set of acceptance and confusion factors from them, which are strictly applicable to the Monte Carlo results, and then applies them to the numbers observed in the data. If the Monte Carlo has appropriately simulated the processes, cross sections, and distributions underlying the data, then the *observed* → *true* transformation which works exactly for the Monte Carlo numbers should also work for the data numbers (along with reliable estimates of the uncertainties introduced by the process – additional uncertainties will have to be determined for the effects of the assumption of appropriate simulation inherent in this statement).

Since the MSU Monte Carlo does an adequate job of reproducing the observed

---

[7] Many of these are roughly equivalent from a mathematical standpoint, differing mainly in the degree of difficulty in extracting useful information on uncertainties, and on their sensitivities to some of the underlying assumptions.

distributions of many of the measurable quantities in the data (as may be seen in Appendix B), the systematic uncertainty in making this assumption is small. It will be seen that of all the quantities which are assumed by the MSU MC as representing the real state of affairs, the hadronic energy scale has the largest effect on the final result. By comparison, most of the other uncertainties will be seen to be so dwarfed by this uncertainty as to become negligible.

Acceptance factors

The following are the definitions of the acceptance factors (and their representations from the matrix).

$\mathbf{a}_N$ fraction of generated ν_μ NC events lost to cuts

$a_N =$ `nN_cut` / `nN_tot`

$\mathbf{a}_\nu$ fraction of generated ν_μ CC events lost to cuts

$a_\nu =$ `nC_cut` / `nC_tot`

$\mathbf{a}_{\overline{N}}$ fraction of generated $\overline{\nu}_\mu$ NC events lost to cuts

$a_{\overline{N}} =$ `aN_cut` / `aN_tot`

$\mathbf{a}_{\overline{\nu}}$ fraction of generated $\overline{\nu}_\mu$ CC events lost to cuts

$a_{\overline{\nu}} =$ `aC_cut` / `aC_tot`

For the version of the R_ν determination method which was used, which ignores cut events, these all become exactly zero.

Confusion factors

The following are the definitions of the confusion factors (and their representations from the matrix in Table 5.3):

$\boldsymbol{\Delta}_{\nu}$ net fractional loss in ν_μ CC events due to misclassification between the **CC–** and **N0** classes (both directions)

$\Delta_\nu = (\texttt{nC\_N0} - \texttt{nN\_C-} - \texttt{aN\_C-})\ /\ \texttt{nC\_tot}$

$\boldsymbol{\Delta}_{\overline{\nu}}$ net fractional loss in $\overline{\nu}_\mu$ CC events due to misclassification between the **CC+** and **N0** classes (both directions)

$\Delta_{\overline{\nu}} = (\texttt{aC\_N0} - \texttt{nN\_C+} - \texttt{aN\_C+})\ /\ \texttt{aC\_tot}$

$\mathbf{e}_{\nu}$ net fractional gain in ν_μ CC events due to misclassification between the **CC–** and **CC+** classes (both directions)

$e_\nu = (\ \texttt{aC\_C-} - \texttt{nC\_C+}\ )\ /\ \texttt{nC\_tot}$

$\mathbf{e}_{\overline{\nu}}$ net fractional gain in $\overline{\nu}_\mu$ CC events due to misclassification between the **CC–** and **CC+** classes (both directions)

$e_{\overline{\nu}} = (\ \texttt{nC\_C+} - \texttt{aC\_C-}\ )\ /\ \texttt{aC\_tot}$

Application to MSU MC quantities

Using these definitions and looking at the matrix, it can be can see that the relations between the observed Monte Carlo quantities and the true Monte Carlo quantities can be expressed as follows.

$$\texttt{obs\_N0} = \texttt{nN\_tot} * (1 - a_N) + \texttt{aN\_tot} * (1 - a_{\overline{N}}) + \texttt{nC\_tot} * \Delta_\nu + \texttt{aC\_tot} * \Delta_{\overline{\nu}}$$

$$\texttt{obs\_CC}- = \texttt{nC\_tot} * (1 - \Delta_\nu + e_\nu - a_\nu)$$

$$\texttt{obs\_CC}+ = \texttt{aC\_tot} * (1 - \Delta_{\overline{\nu}} + e_{\overline{\nu}} - a_{\overline{\nu}})$$

Recall that for the Monte Carlo, $R_\nu = \texttt{nN\_tot}/\texttt{nC\_tot}$ and $R_{\overline{\nu}} = \texttt{aN\_tot}/\texttt{aC\_tot}$.

We identify the three observable quantities from the data with their counterparts in the MSU Monte Carlo program.

$$\mathbf{N0} = \texttt{obs\_N0}, \qquad \mathbf{CC-} = \texttt{obs\_CC}-, \qquad \mathbf{CC+} = \texttt{obs\_CC}+$$

Algebraic manipulation of these simple relations yields the equation

$$R_\nu = \frac{1}{(1-a_N)}\Bigg\{\frac{\mathbf{N0}}{\mathbf{CC-}}(1-\Delta_\nu+e_\nu-a_\nu)-\Delta_\nu - \frac{\mathbf{CC+}}{\mathbf{CC-}}\frac{(1-\Delta_\nu+e_\nu-a_\nu)}{(1-\Delta_{\bar{\nu}}+e_{\bar{\nu}}-a_{\bar{\nu}})}\left[\Delta_{\bar{\nu}}+R_{\bar{\nu}}\,(1-a_{\bar{N}})\right]\Bigg\} \tag{5.1}$$

This is an identity. The $\texttt{Data\_}x$ numbers can then be substituted for the **NC, CC–,** and **CC+** in the equation, and the result is a determination of the value of R_ν consistent with the data and the assumptions which have been made in the generation and analysis of the MSU Monte Carlo program.

In the variant of the procedure which ignores all events which fail cuts, the a factors are all identically zero, and this equation simplifies to

$$R_\nu = \frac{\mathbf{N0}}{\mathbf{CC-}}(1-\Delta_\nu+e_\nu)-\Delta_\nu-\left(\frac{\mathbf{CC+}}{\mathbf{CC-}}\right)\frac{(1-\Delta_\nu+e_\nu)}{(1-\Delta_{\bar{\nu}}+e_{\bar{\nu}})}\left[\Delta_{\bar{\nu}}+R_{\bar{\nu}}\right]. \tag{5.2}$$

Ideally, one should be able to express R_ν in terms of a ratio of neutral current to charged current events, corrected for detector effects, backgrounds, confusions, and so on. These *corrected NC* and *CC* values can be seen as related to this form of the equation using the following sequence of definitions.

Looking back at the original Monte Carlo generated→accepted event matrix and the definitions of the confusion factors (the acceptance factors are all zero), it can be seen that the transformation from the original sample of ν_μ CC events to the observed sample (**CC–**) involved only two corrections:

- a net loss due to confusion with the NC class, measured by the factor Δ_ν, and
- a net gain[8] due to confusion with $\overline{\nu}_\mu$ CC events, measured by the factor e_ν.

Since **CC–** is simply `nC_tot`$\cdot(1-\Delta_\nu+e_\nu)$, applying the principle that the Monte Carlo generated→accepted event matrix reflects the underlying physics and the detector's actual characteristics, a *corrected* CC_ν event total may be defined as

$$CC^*_\nu \;=\; \frac{\mathbf{CC-}}{(1-\Delta_\nu+e_\nu)}.$$

Similarly,

$$CC^*_{\overline{\nu}} \;=\; \frac{\mathbf{CC+}}{(1-\Delta_{\overline{\nu}}+e_{\overline{\nu}})}.$$

This does not appear explicitly in the expression $R_\nu = NC^*_\nu/CC^*_\nu$, but it is nevertheless important in the appropriate handling of the neutral current sample.

The case of the neutral current events is more difficult than that of the charged current events, since the identical appearance of NC ν_μ and $\overline{\nu}_\mu$ events adds a major background to the observed sample. The confusion factors actually are simplified by

---

[8] These confusion factors may be positive or negative; the characterization of one as a loss and the other as a gain is merely a convention reflecting the sign arbitrarily chosen when defining the original equations.

the lack of distinction between NC$_\nu$ and NC$_{\overline{\nu}}$ events, as only the NC↔CC confusion moves events into or out of the **N0** category. Accepting the results of the Monte Carlo program for the true ratio of NC to CC events among the anti-neutrinos (as this ratio is relatively insensitive to the relevant physical parameters such as $\sin^2\theta_W$ and the charm quark mass), the true number of NC$_{\overline{\nu}}$ events is $(R_{\overline{\nu}}CC^*_{\overline{\nu}})$. The importance of having a way of determining $CC^*_{\overline{\nu}}$ may now be seen. This $NC_{\overline{\nu}}$ number must be modified by the number of events gained or lost due to NC→CC confusion, just as the original number of NC_ν events must.

The observed members of class **N0** are thus seen as the following blend of events, which can be solved for the corrected number of NC_ν events:

$$\begin{aligned}
\mathbf{N0} &= NC^*_\nu + \Delta_\nu CC^*_\nu + NC^*_{\overline{\nu}} + \Delta_{\overline{\nu}}CC^*_{\overline{\nu}} \\
NC^*_\nu &= \mathbf{N0} - \Delta_\nu CC^*_\nu - (NC^*_{\overline{\nu}} + \Delta_{\overline{\nu}}CC^*_{\overline{\nu}}) \\
&= \mathbf{N0} - \Delta_\nu CC^*_\nu - (R_{\overline{\nu}} + \Delta_{\overline{\nu}})CC^*_{\overline{\nu}}
\end{aligned}$$

A definition of measured R_ν as the ratio of the corrected NC^*_ν and CC^*_ν values just defined will generate an equation identical to (5.2) above. A similar (but clearly much more complicated) sequence of definitions would reproduce equation (5.1) in the case of non-zero acceptance cuts. Table 5.4 is a summary of the main steps taken in going from the original data sample to the corrected values for NC^*_ν and CC^*_ν. Refer to Appendix C for an even more detailed description of the procedure.

Table 5.4: Sequence of Data Corrections in R_ν Derivation, 10 GeV E_H Cut

Status	**NC**	**CC0**	**N0**	**CC–**	**CC+**
Initial Data Events	19397 ± *139*	6156 ± *78*	25553 ± *160*	45137 ± *212*	8043 ± *90*
Δ Cosmics	− 85 ± *25*	0 ± *0*	− 85 ± *25*	0 ± *0*	0 ± *0*
Δ Out-of-Time	− 92 ± *27*	−139 ± *32*	−231 ± *42*	0 ± *0*	0 ± *0*
Δ Upstream	− 23 ± *13*	− 8 ± *8*	− 31 ± *16*	− 16 ± *11*	− 8 ± *8*
Δ CC→NC→CC repr.	+176 ± *37*	−169 ± *36*	+ 8 ± *8*	− 7 ± *7*	− 1 ± *1*
Subtotal	19373 ± *149*	5841 ± *93*	25214 ± *168*	45115 ± *213*	8034 ± *90*
Δ ν_e Events	−1322 ± *25*	−243 ± *11*	−1586 ± *22*	− 12 ± *3*	− 7 ± *2*
Subtotal	18051 ± *141*	5598 ± *89*	23629 ± *159*	45103 ± *213*	8027 ± *90*
Δ N0 ↔ CC± conf.			−5280 ± *71*	+4796 ± *60*	+484 ± *38*
Δ CC+ ↔ CC– conf.			0 ± *0*	+155 ± *11*	− 155 ± *11*
Δ $\overline{\nu}_\mu$ N0 events			−3128 ± *113*	0 ± *0*	0 ± *0*
Corrected Events			15220 ± *207*	50055 ± *244*	8356 ± *102*

Table 5.5: Sequence of Data Corrections in R_ν Derivation, 60 GeV E_H Cut

Status	**NC**	**CC0**	**N0**	**CC–**	**CC+**
Initial Data Events	8617 ±*93*	4026 ± *63*	12643 ±*112*	20966 ±*145*	2270 ±*48*
Δ Cosmics	− 8 ± *8*	0 ± *0*	− 8 ± *8*	0 ± *0*	0 ± *0*
Δ Out-of-Time	− 8 ± *8*	–139 ± *32*	− 8 ± *11*	0 ± *0*	0 ± *0*
Δ Upstream	− 0 ± *8*	− 8 ± *8*	− 8 ± *11*	− 8 ± *11*	− 8 ± *8*
Δ CC→NC→CC repr.	+ 92 ±*27*	− 85 ± *26*	+ 8 ± *8*	− 7 ± *7*	− 1 ± *1*
Subtotal	8694 ±*98*	3933 ± *69*	12627 ±*114*	20951 ±*145*	2269 ±*48*
Δ ν_e Events	–1144 ±*26*	–221 ± *11*	–1393 ± *21*	− 10 ± *3*	− 5 ± *2*
Subtotal	7549 ±*88*	3712 ± *66*	11234 ±*103*	20942 ±*145*	2264 ±*48*
Δ N0 ↔ CC± conf.			–3059 ± *53*	+2827 ± *46*	+232 ±*26*
Δ CC+ ↔ CC– conf.			0 ± *0*	+109 ± *8*	− 109 ± *8*
Δ $\overline{\nu}_\mu$ N0 events			− 927 ± *49*	0 ± *0*	0 ± *0*
Corrected Events			7248 ±*126*	23878 ±*172*	2387 ±*58*

5.6.3 The measured value of R_ν

Using either the long equation or the equivalent corrected events procedure, the result for this analysis was

$$\begin{aligned} R_\nu &= 0.30408 \text{ with a 10 GeV } \mathrm{E_H} \text{ cut, and} \\ &= 0.30354 \text{ with a 60 GeV } \mathrm{E_H} \text{ cut.} \end{aligned}$$

5.7 Uncertainty determination

5.7.1 Basic uncertainties

Each of the quantities in this equation has an associated uncertainty due to the Monte Carlo simulation process and subsequent corrections (and in many cases, also includes uncertainty information from the processes used to determine the parameters used by the Monte Carlo). Standard error analysis methods are used to determine the overall uncertainty in R-nu from these sources. These standard methods assume Gaussian-distributed independent uncertainties in each of the quantities used in the equation, and Poisson uncertainties in the data numbers. For the most part, there should be no reason to doubt this assumption. Uncertainties from other sources will have to be dealt with by other means. The standard analysis methods lead to the following expressions for the uncertainty in the measurement of R_ν.

The boldfaced quantities are the values measured as data and the others are the acceptance and confusion factors as described above. $R_{\overline{\nu}}$ is the value of the *true* ratio of NC to CC $\overline{\nu}_\mu$ events as determined by the MSU MC for the given fiducial volume and $\mathrm{E_H}$ cuts. Its uncertainty is based on the statistical uncertainty of the MSU MC plus an added uncertainty to account for the theoretical uncertainty due to the assumptions made in the model (charm quark mass and estimate of $\sin^2\theta_W$).

The initial definition from which the specific expression is derived is:

$$\begin{aligned}
\delta {R_\nu}^2 \;=\;& \Big(\frac{\partial R_\nu}{\partial \mathbf{N0}}\delta\mathbf{N0}\Big)^2 + \Big(\frac{\partial R_\nu}{\partial \mathbf{CC-}}\delta\mathbf{CC-}\Big)^2 + \Big(\frac{\partial R_\nu}{\partial \mathbf{CC+}}\delta\mathbf{CC+}\Big)^2 + \Big(\frac{\partial R_\nu}{\partial R_{\overline{\nu}}}\delta R_{\overline{\nu}}\Big)^2 + \\
& \Big(\frac{\partial R_\nu}{\partial \Delta_\nu}\delta\Delta_\nu\Big)^2 + \Big(\frac{\partial R_\nu}{\partial \Delta_{\overline{\nu}}}\delta\Delta_{\overline{\nu}}\Big)^2 + \Big(\frac{\partial R_\nu}{\partial e_\nu}\delta e_\nu\Big)^2 + \Big(\frac{\partial R_\nu}{\partial e_{\overline{\nu}}}\delta e_{\overline{\nu}}\Big)^2 + \\
& \Big(\frac{\partial R_\nu}{\partial a_\nu}\delta a_\nu\Big)^2 + \Big(\frac{\partial R_\nu}{\partial a_{\overline{\nu}}}\delta a_{\overline{\nu}}\Big)^2 + \Big(\frac{\partial R_\nu}{\partial a_N}\delta a_N\Big)^2 + \Big(\frac{\partial R_\nu}{\partial a_{\overline{N}}}\delta a_{\overline{N}}\Big)^2.
\end{aligned}$$

Evaluating the partial derivatives, the expression becomes[9]:

$$\begin{aligned}
\delta {R_\nu}^2 \;=\;& \frac{1}{(1-a_N)^2}\Bigg\{\Big[\frac{1-\Delta_\nu+e_\nu-a_\nu}{\mathbf{CC-}}\Big]^2\Big[\delta\mathbf{N0}^2 + \Big(\frac{\mathbf{N0}}{\mathbf{CC-}}\delta\mathbf{CC-}\Big)^2 + \\
& \Big[\frac{R_{\overline{\nu}}(1-a_{\overline{N}})+\Delta_{\overline{\nu}}}{1-\Delta_{\overline{\nu}}+e_{\overline{\nu}}-a_{\overline{\nu}}}\Big]^2\Big[\Big(\frac{\mathbf{CC+}}{\mathbf{CC-}}\delta\mathbf{CC-}\Big)^2 + \delta\mathbf{CC+}^2\Big]\Big] + \\
& \Big[\Big(\frac{\mathbf{CC+}}{\mathbf{CC-}}\Big)\Big(\frac{1-\Delta_\nu+e_\nu-a_\nu}{1-\Delta_{\overline{\nu}}+e_{\overline{\nu}}-a_{\overline{\nu}}}\Big)\Big]^2\Big[\Big((1-a_{\overline{N}})\delta R_{\overline{\nu}}\Big)^2 + \Big(R_{\overline{\nu}}\delta a_{\overline{N}}\Big)^2\Big] + \\
& \Big[1 + \Big(\frac{\mathbf{NC}}{\mathbf{CC-}}\Big) - \Big(\frac{\mathbf{CC+}}{\mathbf{CC-}}\Big)\Big(\frac{R_{\overline{\nu}}(1-a_{\overline{N}})+\Delta_{\overline{\nu}}}{1-\Delta_{\overline{\nu}}+e_{\overline{\nu}}-a_{\overline{\nu}}}\Big)\Big]^2\delta{\Delta_\nu}^2 + \Big(R_\nu\delta a_N\Big)^2 + \\
& \Big[\Big(\frac{\mathbf{CC+}}{\mathbf{CC-}}\Big)\frac{(1-\Delta_\nu+e_\nu-a_\nu)[1+e_{\overline{\nu}}-a_{\overline{\nu}}+R_{\overline{\nu}}(1-a_{\overline{N}})]}{(1-\Delta_{\overline{\nu}}+e_{\overline{\nu}}-a_{\overline{\nu}})^2}\delta\Delta_{\overline{\nu}}\Big]^2 + \\
& \Big[\Big(\frac{\mathbf{N0}}{\mathbf{CC-}}\Big) - \Big(\frac{\mathbf{CC+}}{\mathbf{CC-}}\Big)\Big(\frac{R_{\overline{\nu}}(1-a_{\overline{N}})+\Delta_{\overline{\nu}}}{1-\Delta_{\overline{\nu}}+e_{\overline{\nu}}-a_{\overline{\nu}}}\Big)\Big]^2\Big(\delta{e_\nu}^2 + \delta{a_\nu}^2\Big) + \\
& \Big[\Big(\frac{\mathbf{CC+}}{\mathbf{CC-}}\Big)\frac{(1-\Delta_\nu+e_\nu-a_\nu)[R_{\overline{\nu}}(1-a_{\overline{N}})+\Delta_{\overline{\nu}}]}{(1-\Delta_{\overline{\nu}}+e_{\overline{\nu}}-a_{\overline{\nu}})^2}\Big]^2\Big(\delta{e_{\overline{\nu}}}^2 + \delta{a_{\overline{\nu}}}^2\Big)\Bigg\}
\end{aligned}$$

---

[9] R_ν in the fourth line is the calculated R_ν, as defined in section 5.6.2

In practice, this was simplified by using a variant of the R_ν-finding procedure for which all of the a factors were defined to be zero (which effectively zeroed their uncertainties as well).

The first term, dependent on the uncertainties in the values of the data numbers **N0**, **CC–**, and **CC+**, may be considered to be the statistical uncertainty of R_ν, while the rest of the equation is the basic component of the systematic uncertainty.

For a graphical depiction of how the value of R_ν and its uncertainty depends on the various constituents of this equation, see Appendix E.

5.7.2 The calculated value of the basic R_ν uncertainties

Using this uncertainty equation, the result for this analysis with a 10 GeV $\mathrm{E_H}$ cut was

$$\begin{aligned} R_\nu &= 0.30408 \\ \delta R_\nu &= 0.00490\,\textit{total}, \\ &\ 0.00397\,\textit{statistical}, \\ &\ 0.00287\,\textit{basic systematic}. \end{aligned}$$

For a 60 GeV $\mathrm{E_H}$ cut,

$$\begin{aligned} R_\nu &= 0.30354 \\ \delta R_\nu &= 0.00656\,\textit{total}, \\ &\ 0.00551\,\textit{statistical}, \\ &\ 0.00356\,\textit{basic systematic}. \end{aligned}$$

5.7.3 Additional systematic uncertainties

Certain systematic uncertainties arise due to inputs to or assumptions made by the Monte Carlo program. The basic uncertainty contains information on the uncertainties due to the Monte Carlo's statistics and many sources of measurement uncertainty which are accounted for in the analysis procedure. Other uncertainties, however, require re-running the analysis procedure many times while varying the relevant parameters. Making reasonable assumptions about the probabilities of such variances, one can relate them to the changes in the measured R_ν value they induce.

The additional systematic uncertainties determined for R_ν can be found in Table 5.6. When taken together with the other uncertainties, these additional uncertainties bring the δR_ν result up to this new value at a 10 GeV $\mathrm{E_H}$ cut:

$$\delta R_\nu = 0.00582\, total.$$

For a 60 GeV $\mathrm{E_H}$ cut,

$$\delta R_\nu = 0.00783\, total.$$

5.7.4 Comparison with other experiments

With the appropriate rounding off, the measurement which is the topic of this dissertation is

$$R_\nu = 0.304 \pm 0.006 \qquad \textit{[0.004 stat., 0.004 syst.]} \qquad (10\text{ GeV } \mathrm{E_H} \text{ cut});$$

$$R_\nu = 0.304 \pm 0.008 \qquad \textit{[0.006 stat., 0.006 syst.]} \qquad (60\text{ GeV } \mathrm{E_H} \text{ cut}).$$

Table 5.6: Additional systematic uncertainties

One standard deviation effect	ΔR_ν 10 GeV cut	ΔR_ν 60 GeV cut
1/3 change in radiative correction	0.00010	0.00005
0.25 GeV/c^2 change in charm quark mass	0.00062	0.00009
0.010 change in $\sin^2\theta_W$ used in MC	0.00012	0.00080
5% change in event rate from kaon-parent νs	0.00072	0.00206
25% change in event rate from K_L^0-parent νs	0.00123	0.00228
2.5% change in overall $\mathrm{E_H}$ scale	0.00057	0.00090
2.5% change in $\mathrm{E_H}$ scale for **N0** relative to **CC**	0.00034	0.00221
1 GeV offset in overall $\mathrm{E_H}$ scale	0.00230	0.00054
1 GeV offset in $\mathrm{E_H}$ scale for **N0** relative to **CC**	0.00130	0.00148
Sum in quadrature	0.00314	0.00427

The CHARM collaboration has reported[17] a value of

$$R_\nu = 0.3093 \pm 0.0031\,(4\text{ GeV E}_\text{H}\text{ cut});\;\; R_\nu = 0.3052 \pm 0.0033\,(9\text{ GeV E}_\text{H}\text{ cut}).$$

The CDHS collaboration has reported[18] a value of

$$R_\nu = 0.3072 \pm 0.0025(stat.) \pm 0.0020(syst.)\;(10\text{ GeV E}_\text{H}\text{ cut}).$$

Both of these groups' measurements agree with the current measurement within the uncertainty limits quoted.

5.8 Progress towards measuring $\sin^2\theta_W$

5.8.1 General

The measurement of R_ν is a good first step towards the measurement of $\sin^2\theta_W$, as was discussed in Chapter 1.

In order to advance a credible value for $\sin^2\theta_W$ and its measurement uncertainty, some further study is required. This is chiefly on the theoretical side of the issue, though there are some studies which should be done to perhaps narrow the range of certain sources of systematic errors. Several of the items in Table 5.6 could be reduced even further with careful study of the effect in question. The uncertainties quoted there tend to be on the conservative side.

The theoretical concerns include the adoption of one of the more recently developed next-to-leading-order QCD models for our cross sections and for the parton distribution functions which go along with them. The MSU Monte Carlo was run with the standard parton model cross section, but used the HMRS-BCDMS parton distribution functions, which were meant to be used with a more sophisticated cross section model. Appendix B shows that we achieve considerable agreement between data and Monte Carlo, nevertheless, which is perhaps a demonstration that for ordinary processes at the high interaction energies achieved in the E733 neutrino experiment there is relatively little happening which cannot be modelled simply. The primary need, then, for a more consistent and reliable theoretical framework is in studying the effects of cuts to the data, where a limited deviation from theoretical simplicity may cause the presence or absence of a relatively large sample of events. The effects of measurement resolution in moving data to or from regions of phase space still under dispute by the theoreticians makes the experimentalists' jobs more difficult and the need for better models more clear.

5.8.2 Specific

The presumption is made that the MSU Monte Carlo generates event types in the proper ratios and handles resolutions and acceptances reasonably well (as evidenced by the good match to data distributions for most observable quantities). As a result, when the various cuts are made, Monte Carlo "events" remain which have a particular ratio of generated NC and CC events. This is not the same as the observable classes which these events represent. It also does not have a significant effect on the value determined as the data's underlying R_ν (the results of which have just been presented).

On the other hand, if the two numbers *do* happen to be the same, then the idea that the Monte Carlo is properly simulating reality from the start is reinforced. If it is believed that the acceptance and resolution effects are handled properly and that its physics model is being used appropriately, then one may use the Monte Carlo's internal R_ν generation to work backwards to extract information on the $\sin^2\theta_W$ underlying the data.

By running the MSU Monte Carlo a number of times with a range of input $\sin^2\theta_W$, one can see when the generated NC/CC ratio (which is sensitive to this change in input parameter) matches the R_ν calculated for the data (which is supposed to be dependent only on the true value in nature, and in fact, *is* relatively insensitive to changes in this Monte Carlo input parameter – see Table 5.6).

Figure 5.1 shows the results of one such preliminary study. Some warnings must be given before taking this too seriously.

The uncertainty analysis of plot of this type is complicated by the fact that the various $\mathrm{E_H}$ cut data-points are not independent measurements, in that a high energy event will be found in all data sets, while a low energy one will only appear in those up to the point where it was cut. Uncertainty analysis is further hampered by the fact that the measurement uncertainties in any one of the plotted points are fairly large on the scale of the deviations shown in the plot.

It can be seen that the more consistent matches between the data and Monte Carlo appear when the $\sin^2\theta_W$ used in the cross section formulas which generate the Monte Carlo events is towards the upper range of $\sin^2\theta_W$ plotted. The 10 GeV $\mathrm{E_H}$ cut data points (not differentiated from the others in this figure) tend to a best match for $\sin^2\theta_W$ between 0.238 and 0.243, as do the 60 GeV $\mathrm{E_H}$ cut data points. The value used for the charm quark mass in the slow rescaling part of the cross section also has an effect on the point at which the $\sin^2\theta_W$ input matches the data's quantity. Allowing a value for m_c which is less than 1.5 GeV/c^2 causes the crossover to move to lower values of $\sin^2\theta_W$. This mass effect will definitely have to be studied.

The work on this measurement is far from complete, but it would not be unreasonable to say that *at this time*, a supportable value for $\sin^2\theta_W$ would be 0.24 with an uncertainty of about 0.01. Work continues towards refining this value.

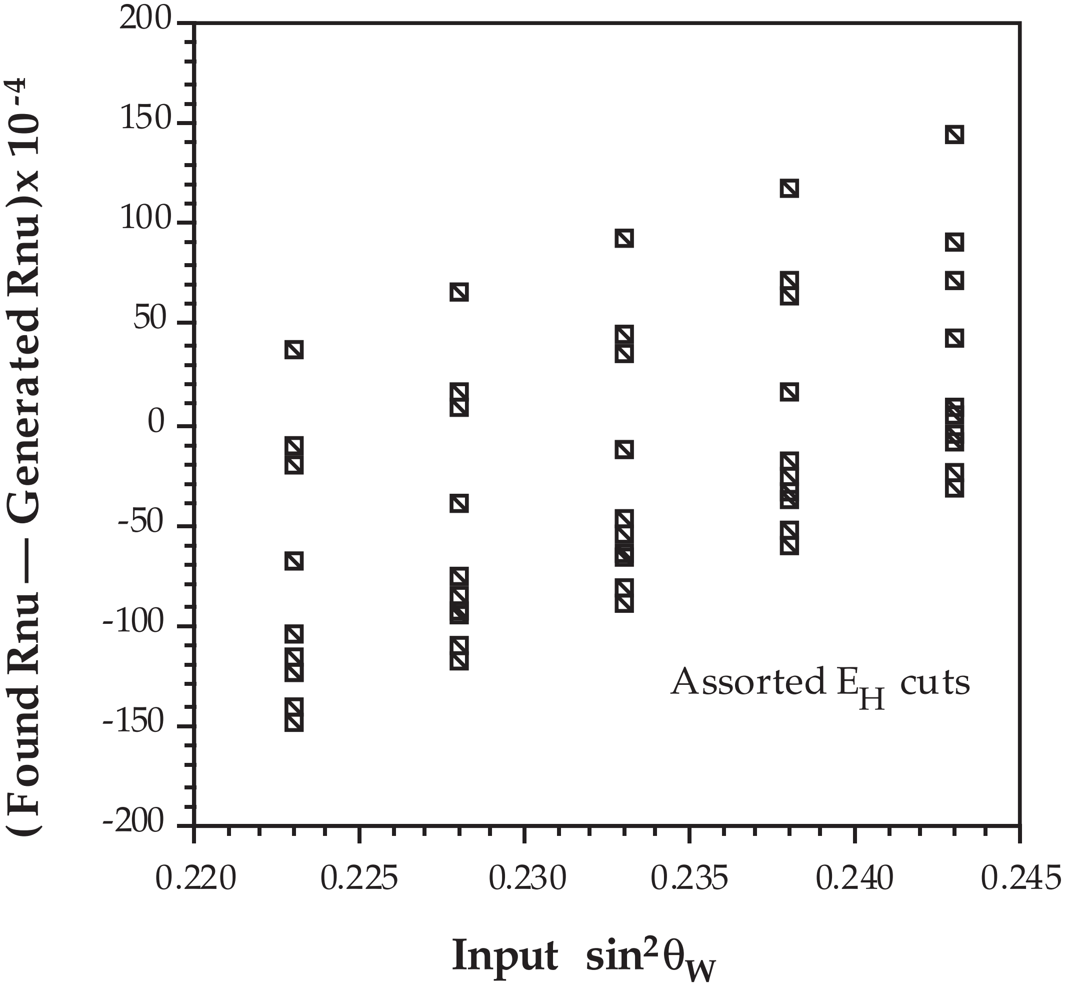

Figure 5.1: Results of a *very* preliminary study for determining $\sin^2\theta_W$ by varying the $\sin^2\theta_W$ input to the MSU Monte Carlo program.

Appendices

Appendix A

Flowcharts of selected data analysis routines

Several of the standard analysis routines are flowcharted here in this Appendix. Additionally, the Muon Hit Selection (MHS) part of the spectrometer package is outlined in greater detail than it was in the body of the dissertation (though not in flowchart format).

VRTDRV – INTERACTION VERTEX FINDER

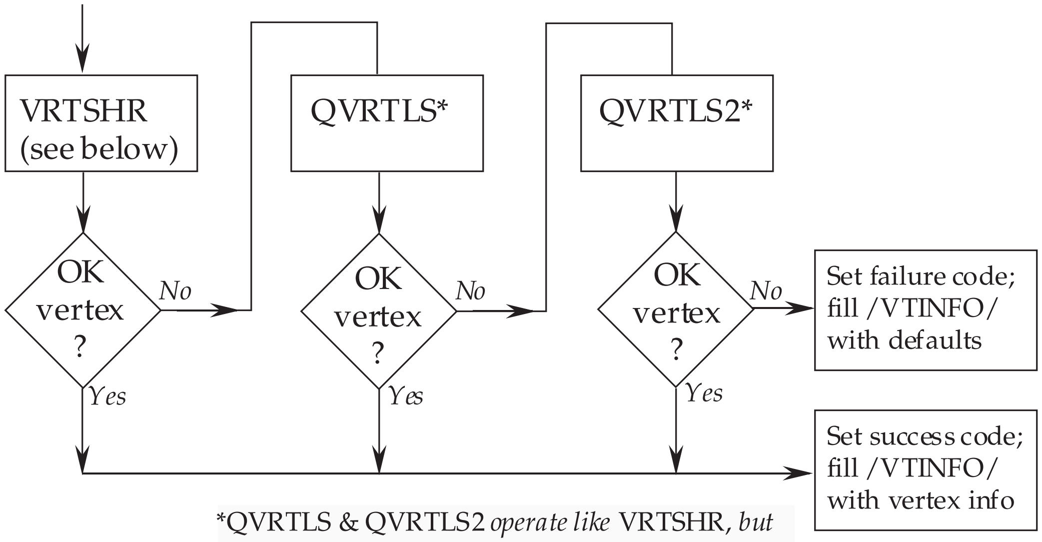

Set failure code; fill /VTINFO/ with defaults

Set success code; fill /VTINFO/ with vertex info

*QVRTLS & QVRTLS2 *operate like* VRTSHR, *but with parameters re-adjusted for very sparse showers*

VRTSHR

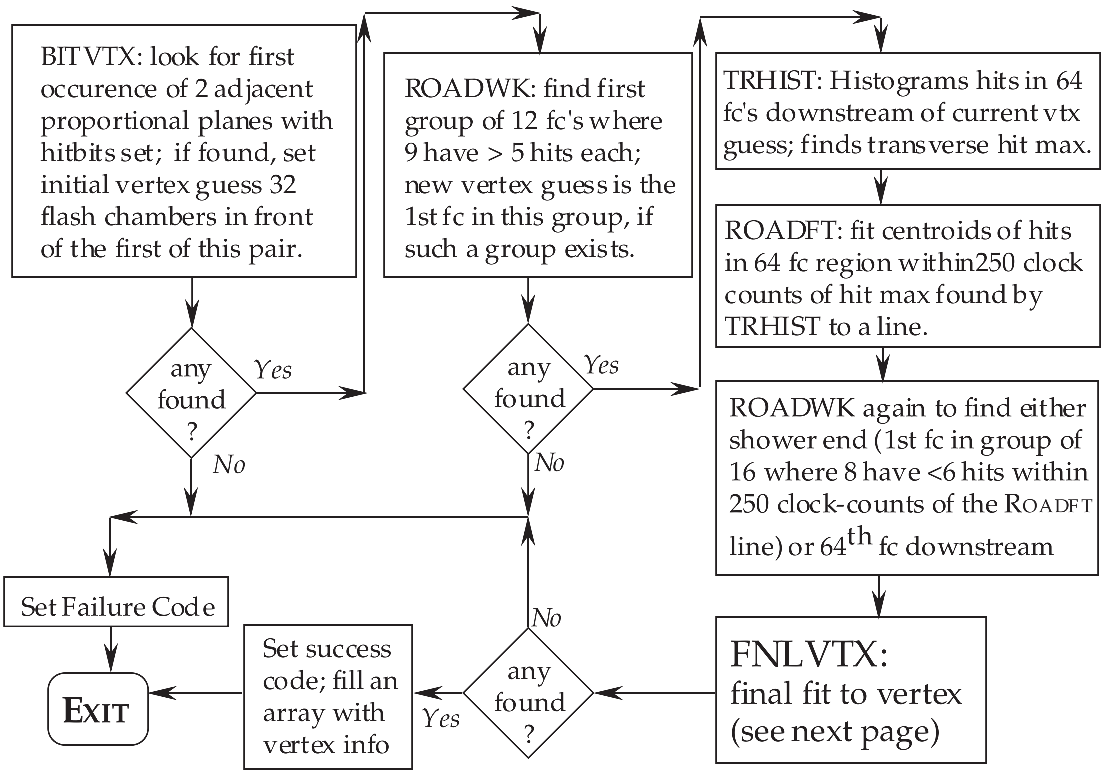

BITVTX: look for first occurence of 2 adjacent proportional planes with hitbits set; if found, set initial vertex guess 32 flash chambers in front of the first of this pair.

ROADWK: find first group of 12 fc's where 9 have > 5 hits each; new vertex guess is the 1st fc in this group, if such a group exists.

TRHIST: Histograms hits in 64 fc's downstream of current vtx guess; finds transverse hit max.

ROADFT: fit centroids of hits in 64 fc region within250 clock counts of hit max found by TRHIST to a line.

ROADWK again to find either shower end (1st fc in group of 16 where 8 have <6 hits within 250 clock-counts of the ROADFT line) or 64th fc downstream

FNLVTX: final fit to vertex (see next page)

Set success code; fill an array with vertex info

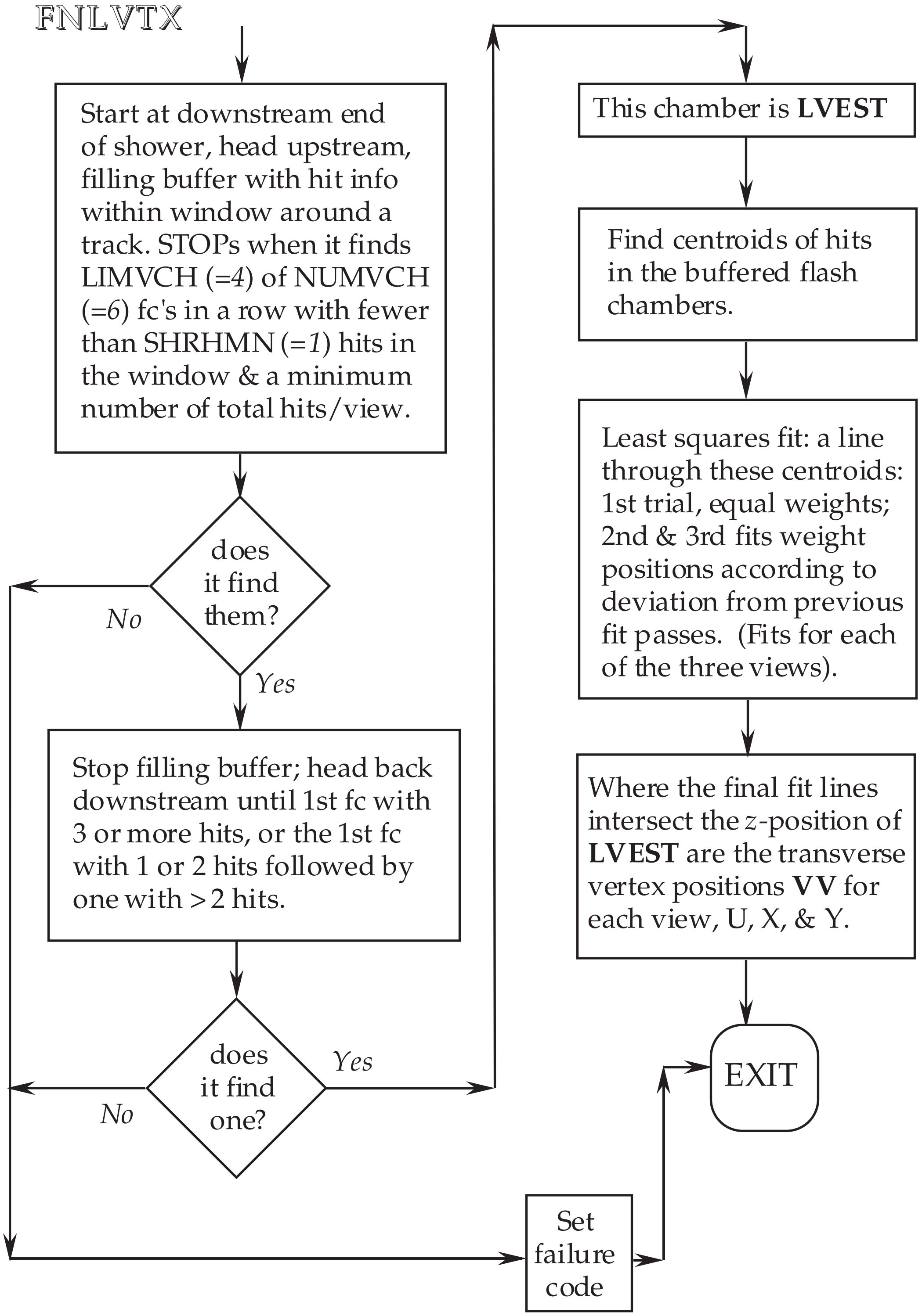
FNLVTX
Start at downstream end of shower, head upstream, filling buffer with hit info within window around a track. STOPs when it finds LIMVCH (=4) of NUMVCH (=6) fc's in a row with fewer than SHRHMN (=1) hits in the window & a minimum number of total hits/view.
does it find them?
No
Yes
Stop filling buffer; head back downstream until 1st fc with 3 or more hits, or the 1st fc with 1 or 2 hits followed by one with >2 hits.
does it find one?
Yes
No
This chamber is LVEST
Find centroids of hits in the buffered flash chambers.
Least squares fit: a line through these centroids: 1st trial, equal weights; 2nd & 3rd fits weight positions according to deviation from previous fit passes. (Fits for each of the three views).
Where the final fit lines intersect the z-position of LVEST are the transverse vertex positions VV for each view, U, X, & Y.
EXIT
Set failure code

SHRLEN: determination of length of hadronic shower

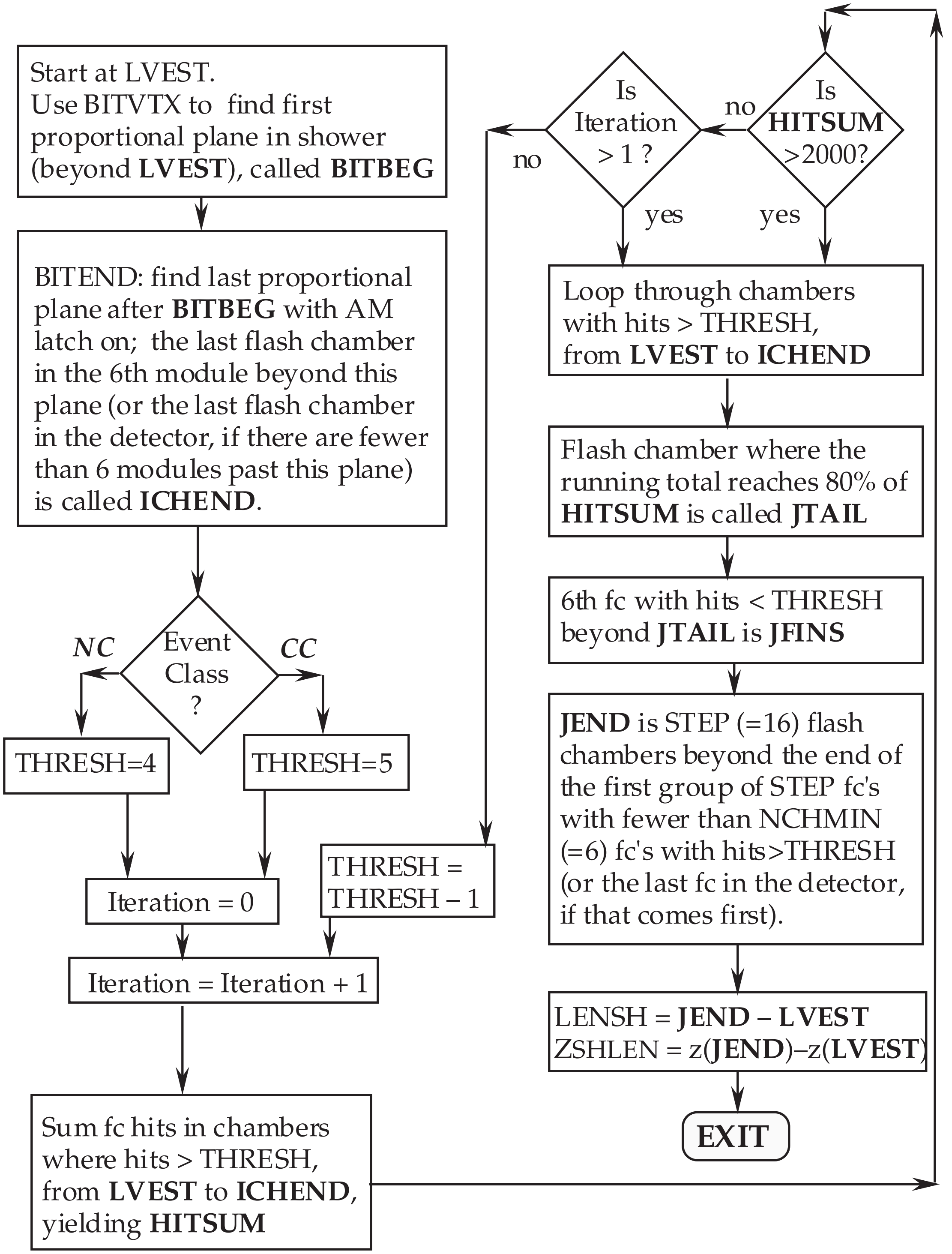

MHBLEN

The following procedure is repeated for each of the three flash chamber orientations independently, and for each of the forty angular bins into which they were divided, except those which *cannot* geometrically satisfy the requirements for a μ track .

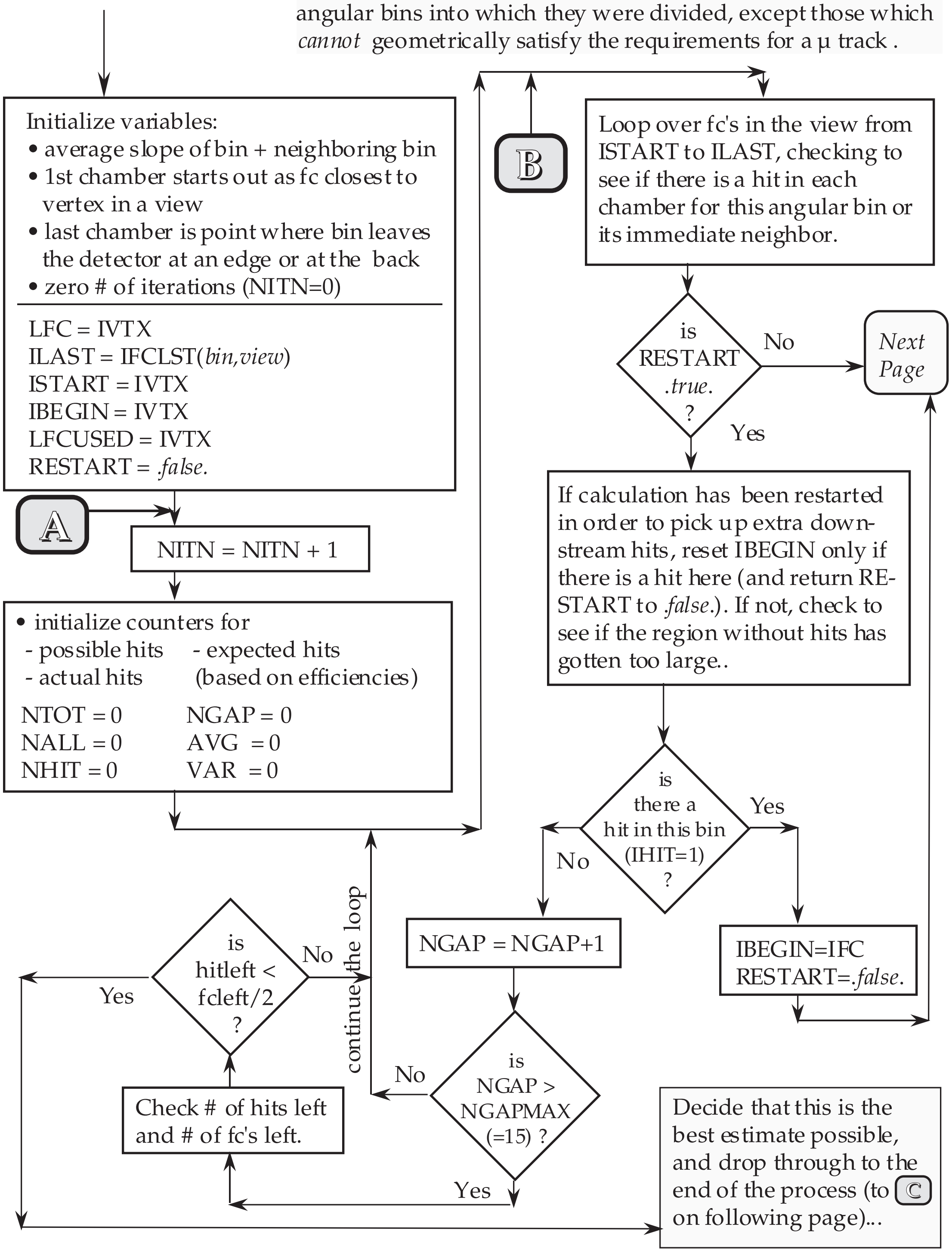

MHBLEN
(continued)

The following procedure is repeated for each of the three flash chamber orientations independently, and for each of the forty angular bins into which they were divided, except those which *cannot* geometrically satisfy the requirements for a μ track .

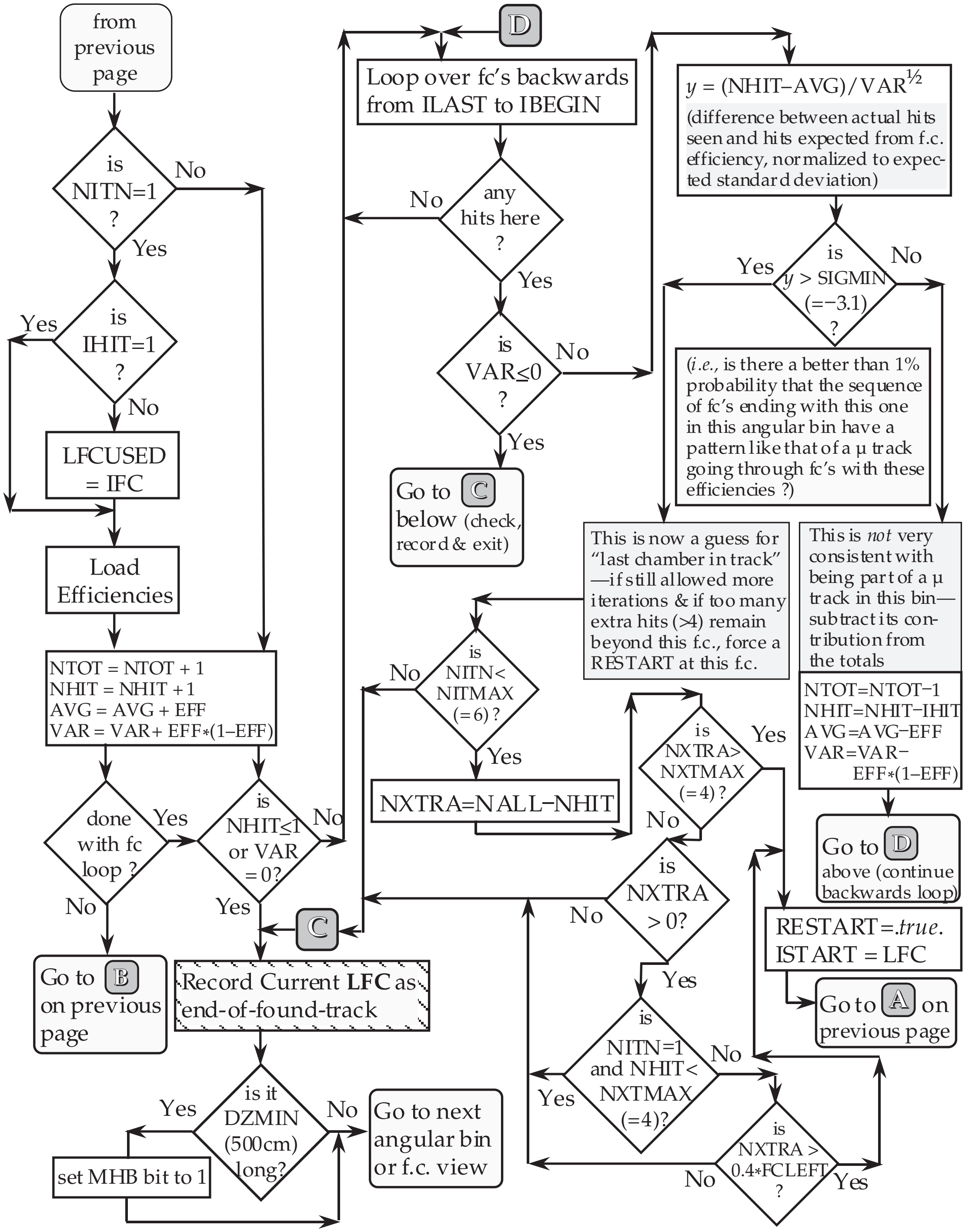

Muon Hit Selection (MHS) Basic Algorithm

The *M*uon *H*it *S*election (MHS) was referred to briefly in section 4.4 as the process by which the initial selection of sets of spectrometer hits was provided to the more sophisticated MMDRV fit procedure for the final momentum fit. The basic algorithm which MHS used for its preliminary fits is presented here in more detail.

For a given incoming track, with a calorimeter fit provided by MTFDRV or some other track-fitting package, the following steps were taken in the analysis of the spectrometer's output.

1. Starting with the incoming track, a family of spectrometer trajectories was calculated for a set of predetermined momenta and their intersections with each of the drift planes was recorded. These momentum "benchmarks" were set to correspond to
    - negatively charged muons with momenta = 5, 8, 10, 12, 15, 20, 25, 40, and 100 GeV/c;
    - positively charged muons with momenta = 5, 8, 10, 12, 15, 20, 25, 40, and 100 GeV/c; and
    - a hypothetical infinite-momentum particle, *i.e.,* a particle undergoing no net deflection by the magnetic fields of the toroids.
2. Starting at the downstream end of the spectrometer, the hits in a given plane were checked against the predicted trajectories' positions in that plane. By determining that a hit fell between the projected paths of muons of two momenta, it was assumed that it was caused by the passage of a muon with a momentum between the two of them. An interpolated momentum could usually be determined, or on occasion, an extrapolated one, if the hit position had

fallen in a region of the detector outside the predicted range of muons with momenta on the list.

3. This interpolation/extrapolation gave a starting point for a fit. Chambers upstream were checked to see if they might contain hits in some road around a trajectory based on this momentum.

4. If it was found that other chambers did have hits which may have been caused by a muon of this momentum, these hits were flagged, and a better estimate for the originating muon momentum was made. This was based on information from all hits along the road – residual distances from the projected path, with weights for the hit-clusters based on the quality of each. A precise back-to-back hit pair counted more than a hit recorded in only one of the two faces of the drift chamber, for example, and also more than a cluster consisting of several hits side-by-side, any one of which may have been due to the true muon passage, with the rest due to electronic noise, bremsstrahlung debris or delta rays.

5. This re-fitting procedure took into account the preference for using more hits to define a track, rather than minimizing some chi-squared by fitting one hit exactly and rejecting all of the other hits in the track on the basis of increased chi-squared. It also took into account the likelihood of having missed whatever chambers contribute no hits to the fit, based on measurements of the various drift chambers' recording efficiencies and geometric considerations. This reduced the chance of achieving a spurious fit to some momentum in which the fitter chose a path far out of its way just to pick up a random hit (noise, or belonging to another track) far downstream, with nothing in between.

6. The re-fitting procedure went through a number of iterations as long as the fit continued to improve each time more than some calculated amount of uncertainty in the fit inverse-momentum[1], or until five passes had been made.

After this stage, the MHS procedure goes into the MHSREDO stage described in section 4.4 and then is finished, passing the final measurement duty to the MMDRV process.

---

[1] Specifically, the iteration process was to keep going through all iterations unless the actual fit inverse-momentum matched the preceding best guess to within 1% of the uncertainty in the fit.

Appendix B

Monte Carlo – Data Comparison Plots

This Appendix consists of a number of plots comparing distributions of physical and derived quantities in the E733 data and the MSU Monte Carlo simulated data.

The standard comparison layout is as follows.

- In the upper left corner, the Data set is represented by horizontal marks with Poisson-statistical vertical error bars. The Monte Carlo sample has been area-normalized to the number of events in the data sample and has been drawn as a solid line. It also has statistical errors, but these are not explicitly shown. Their size relative to those on the data points may be estimated by the square root of the ratio of total numbers of events in the plot, which is listed below the plot.

- In the upper right corner, the same comparison is made, but the vertical scale is now logarithmic. For some comparisons, it is useful to see the details of the sparsely filled bins.

- The lower left corner is a difference plot, Data minus Monte Carlo. The scale is linear.

- The lower right plot is a ratio plot, Data divided by Monte Carlo, bin by bin. The scale is logarithmic.
- There is also information on the statistical significance found in comparing the two distributions using the χ^2 technique and also from a simple comparison of means and deviations.

The measurable quantities compared include, for **CC** events, p_μ, E_ν, θ_μ, $\mathrm{E_H}$ and the amounts of iron and hole which the muon crossed on its way through the toroidal spectrometer. The quantities derived from these values are Q^2, x, and y. For **N0** events, only $\mathrm{E_H}$ is available. Since the majority of muons pass through no part of the toroids' holes, an 8 GeV cut was imposed only on the "hole" plot in order to see the structure of the rest of the distribution better. All plots have a 10 GeV $\mathrm{E_H}$ cut and the standard fiducial volume cut imposed upon them.

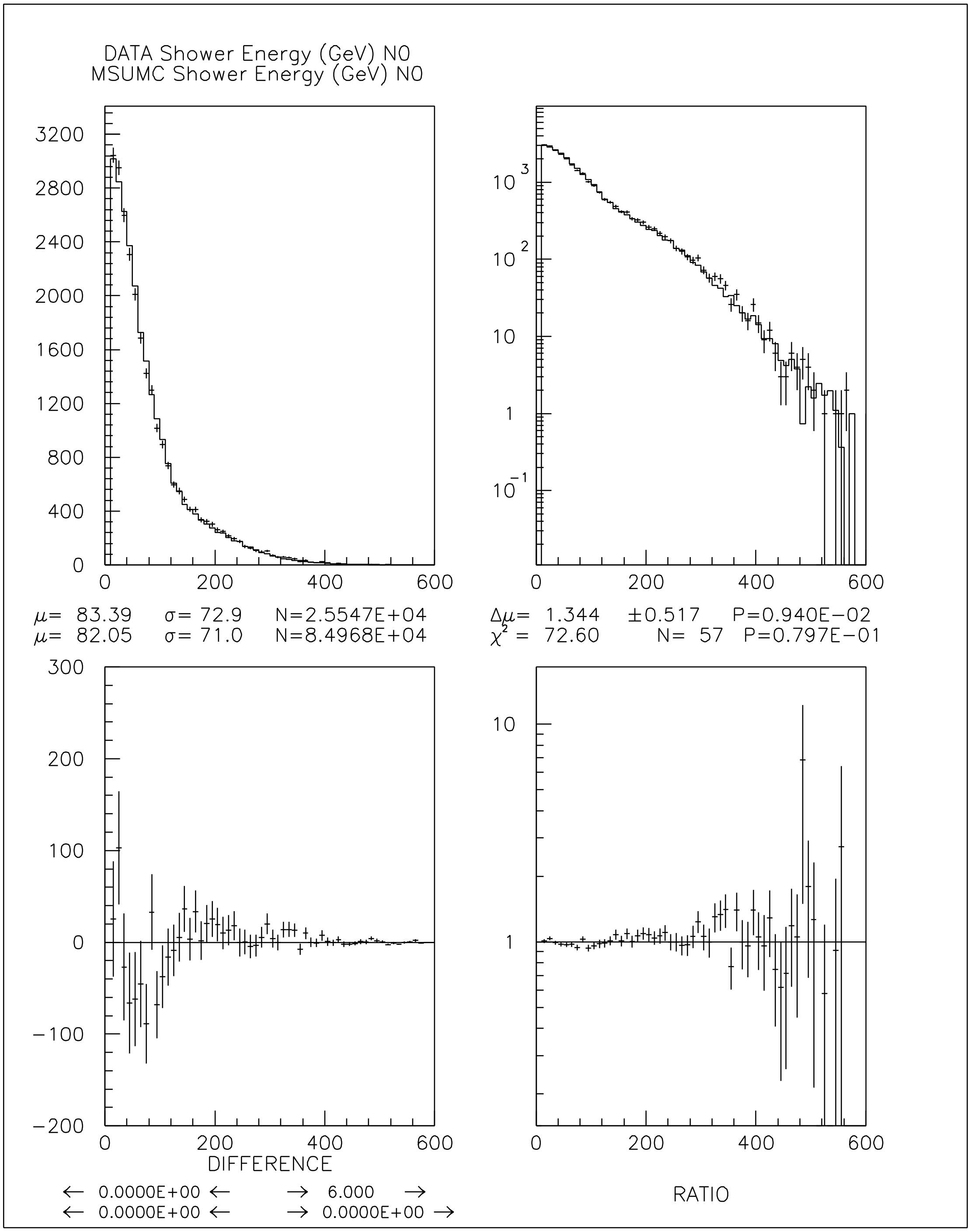

Figure B.1: Comparison of Data and Monte Carlo — E_H for class **N0**

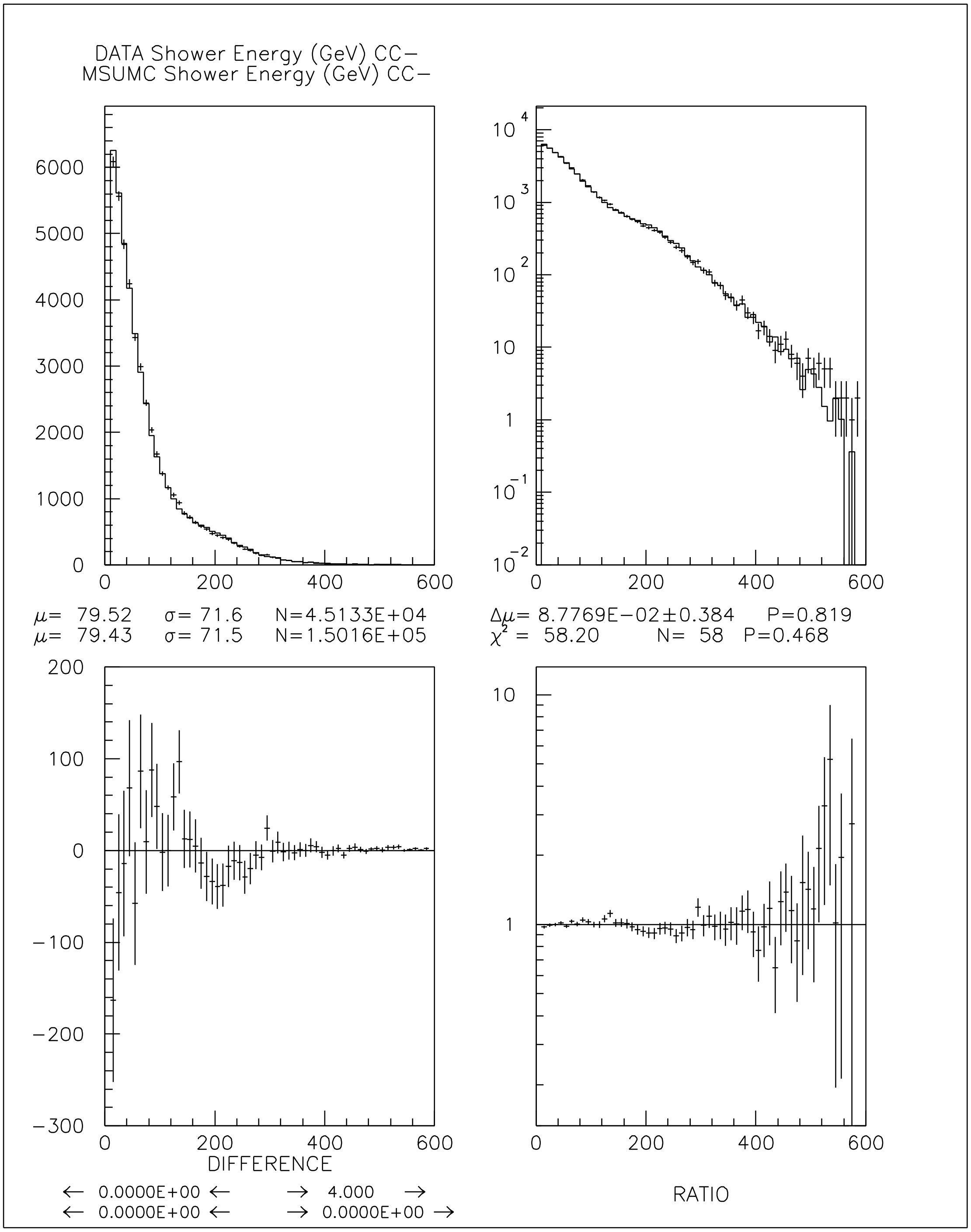

Figure B.2: Comparison of Data and Monte Carlo — E_H for class **CC–**

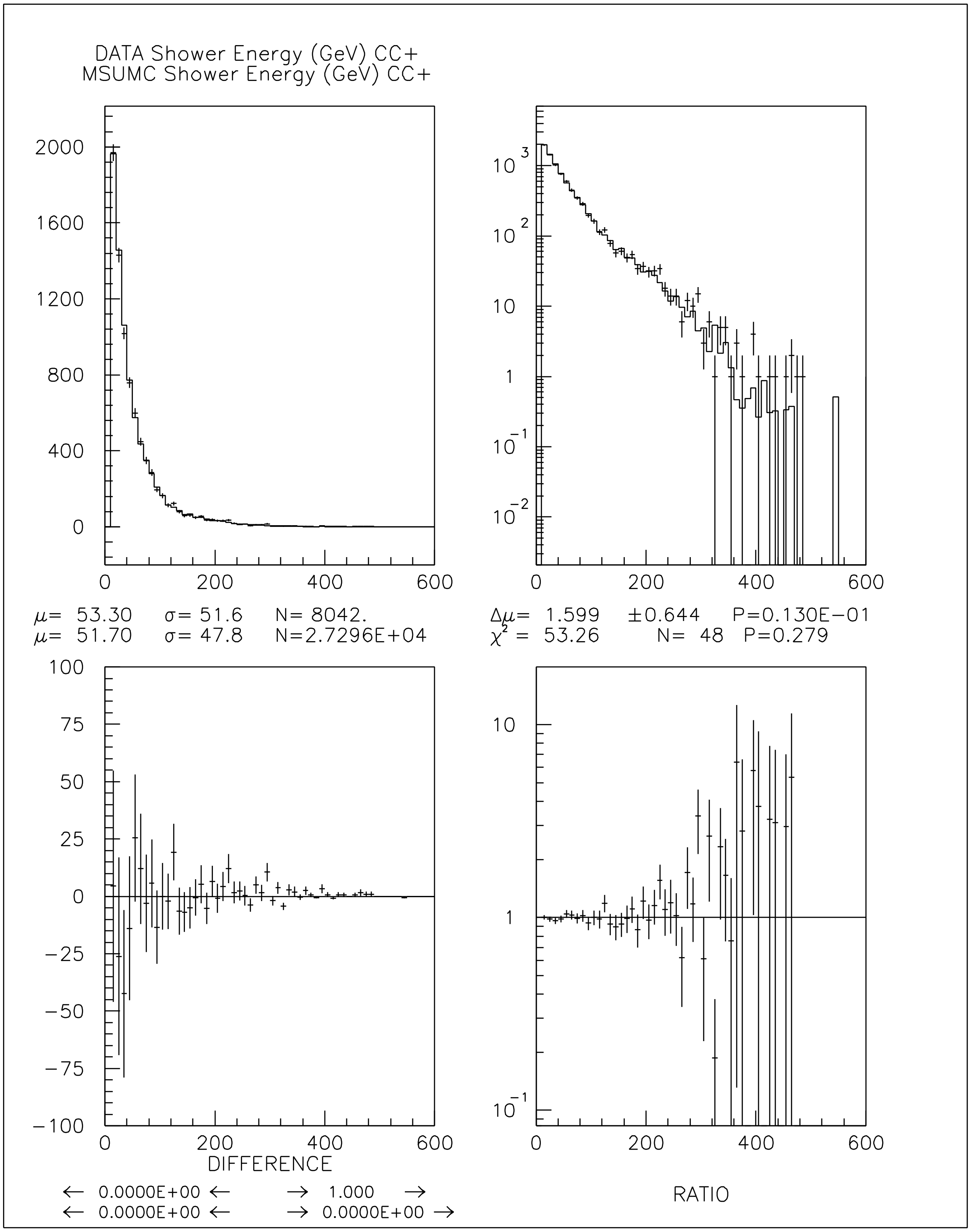

Figure B.3: Comparison of Data and Monte Carlo — E_H for class **CC+**

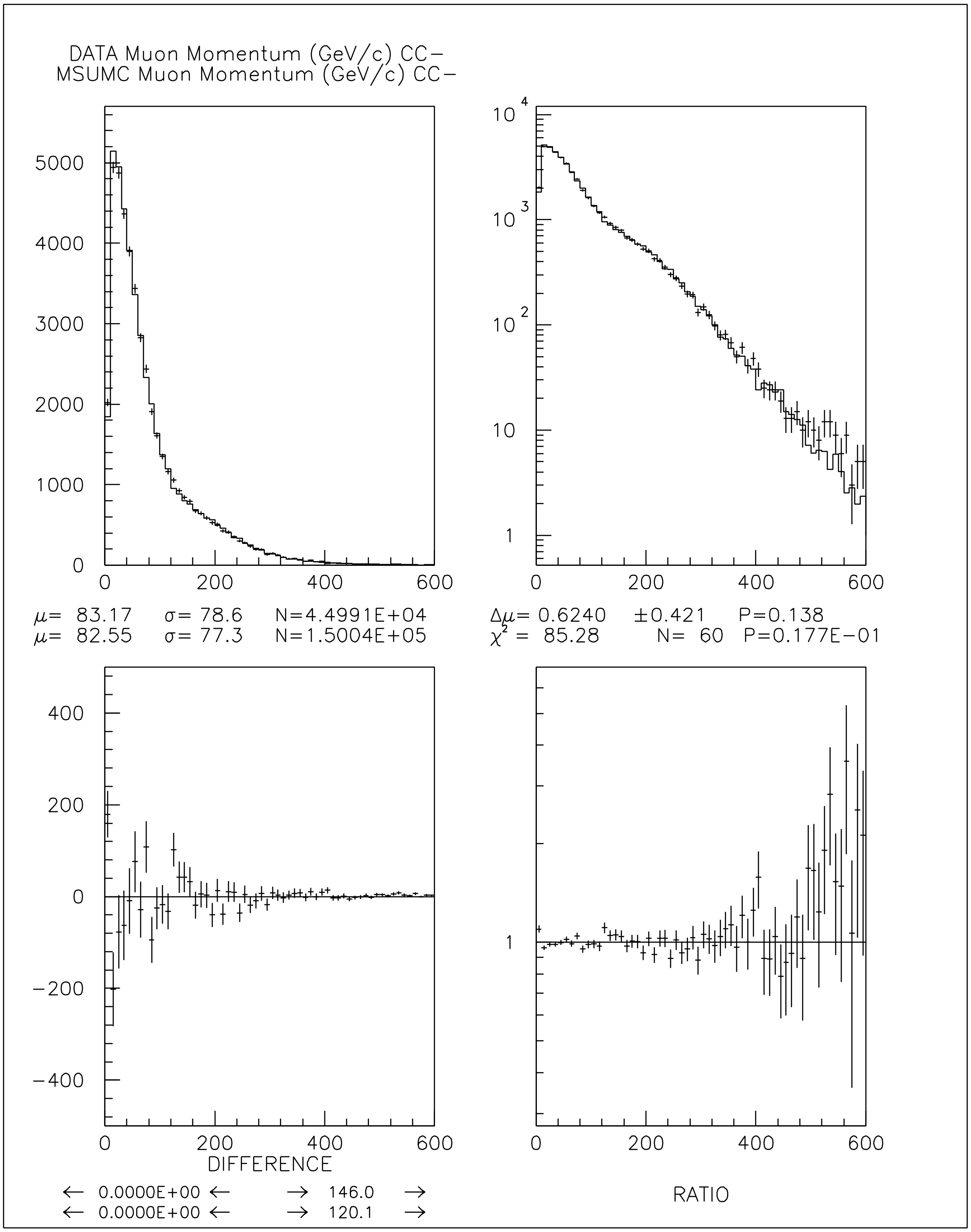

Figure B.4: Comparison of Data and Monte Carlo — E_μ for class **CC−**

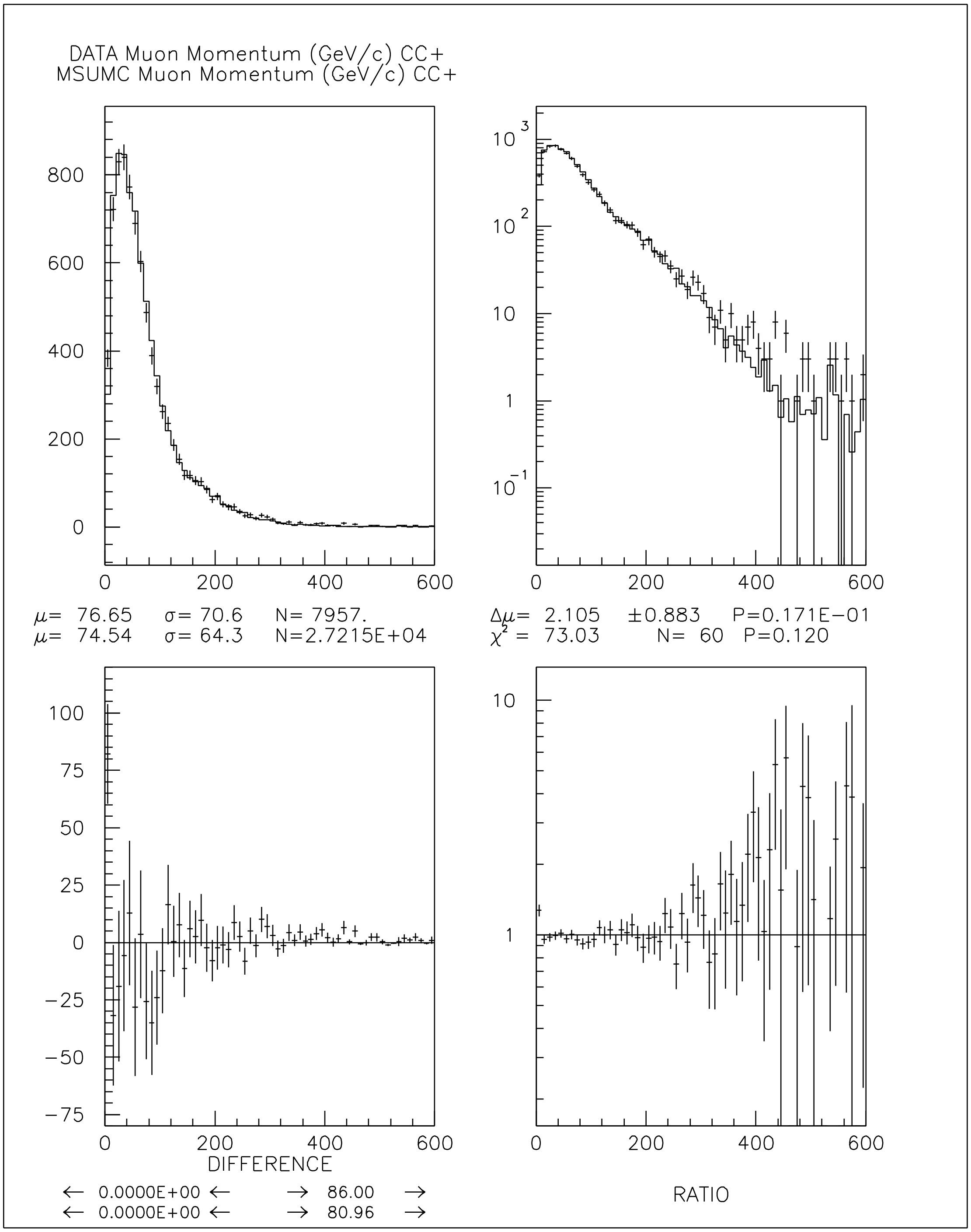

Figure B.5: Comparison of Data and Monte Carlo — E_μ for class **CC+**

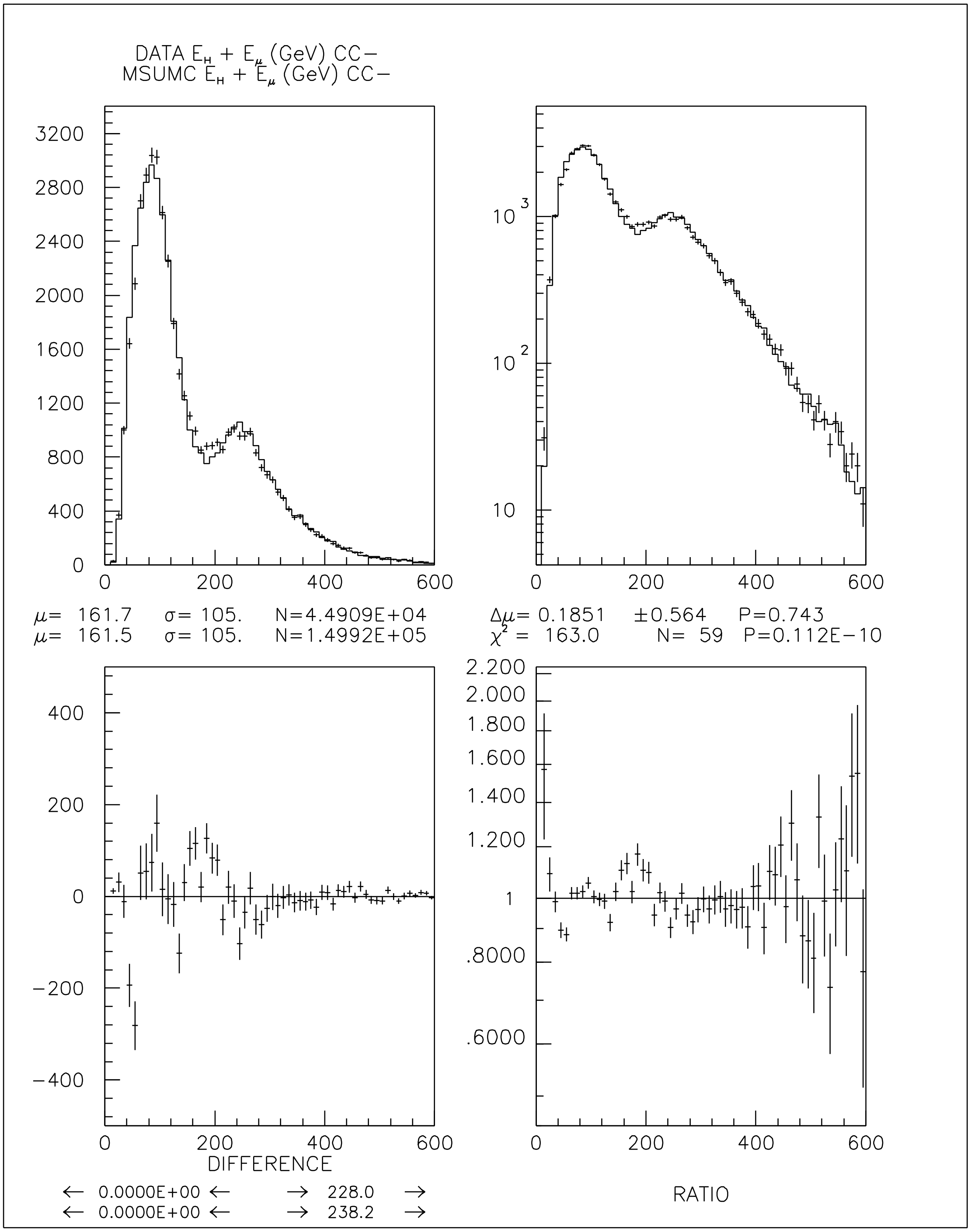

Figure B.6: Comparison of Data and Monte Carlo — E_ν for class **CC−**

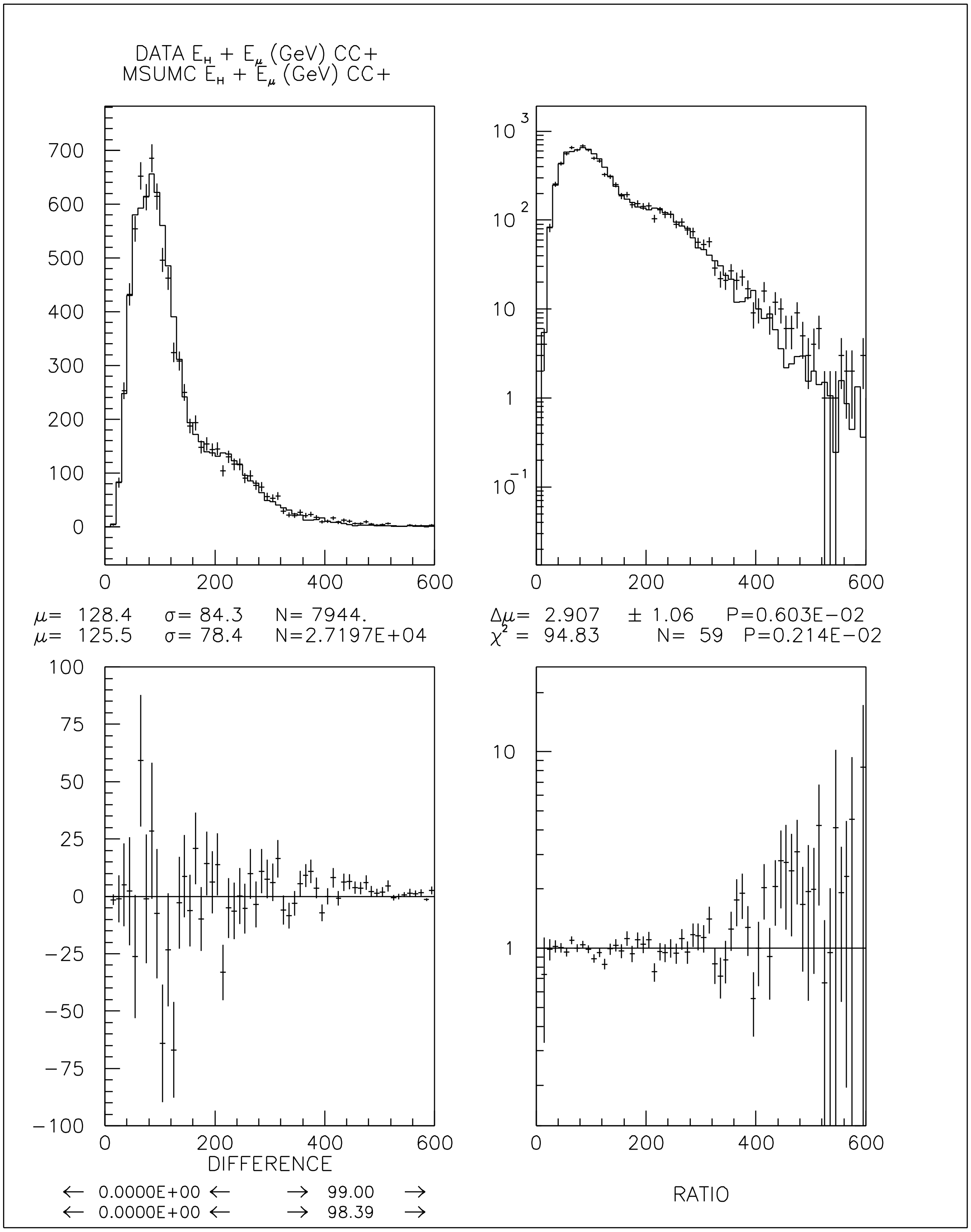

Figure B.7: Comparison of Data and Monte Carlo — E_ν for class **CC+**

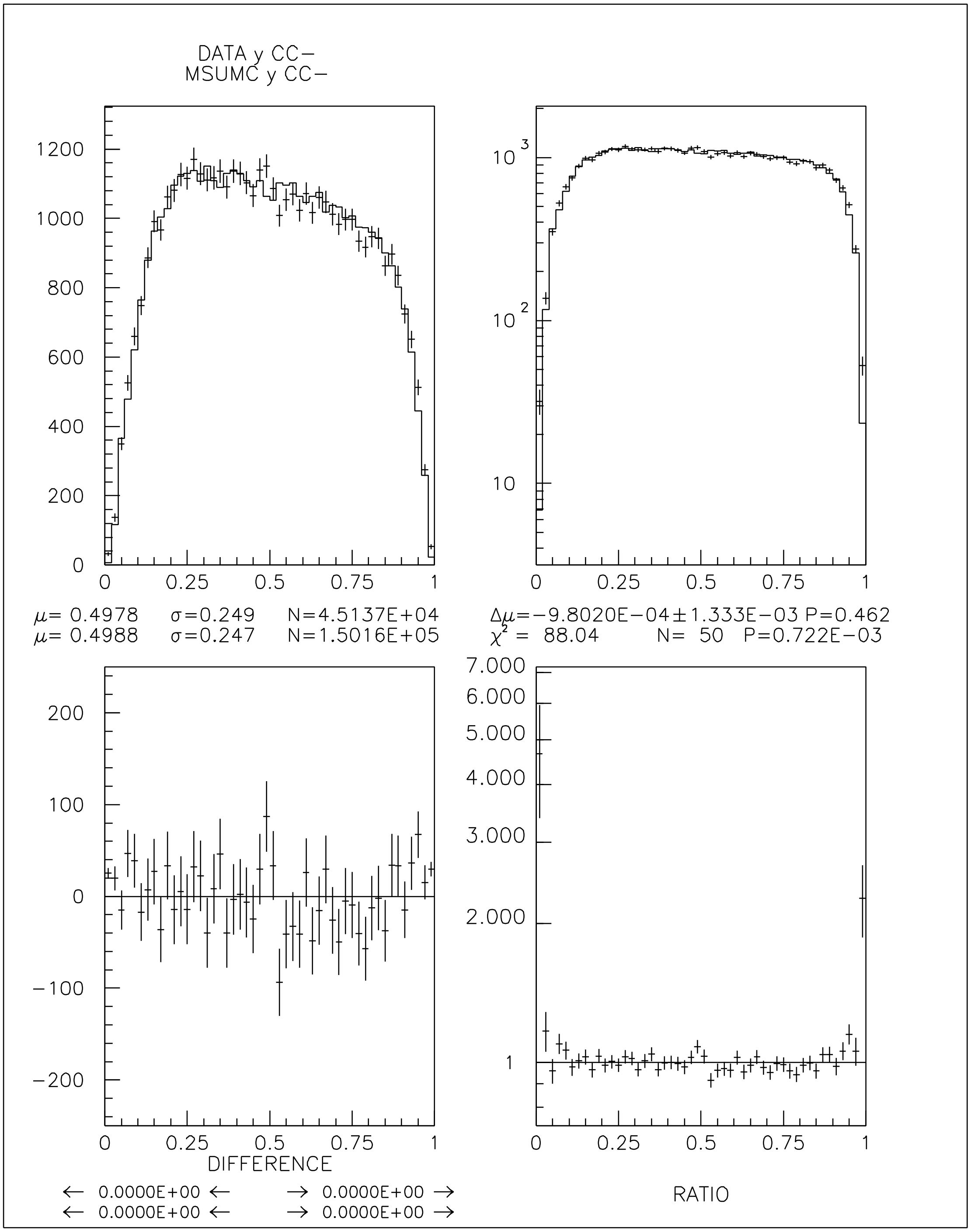

Figure B.8: Comparison of Data and Monte Carlo — y for class **CC−**

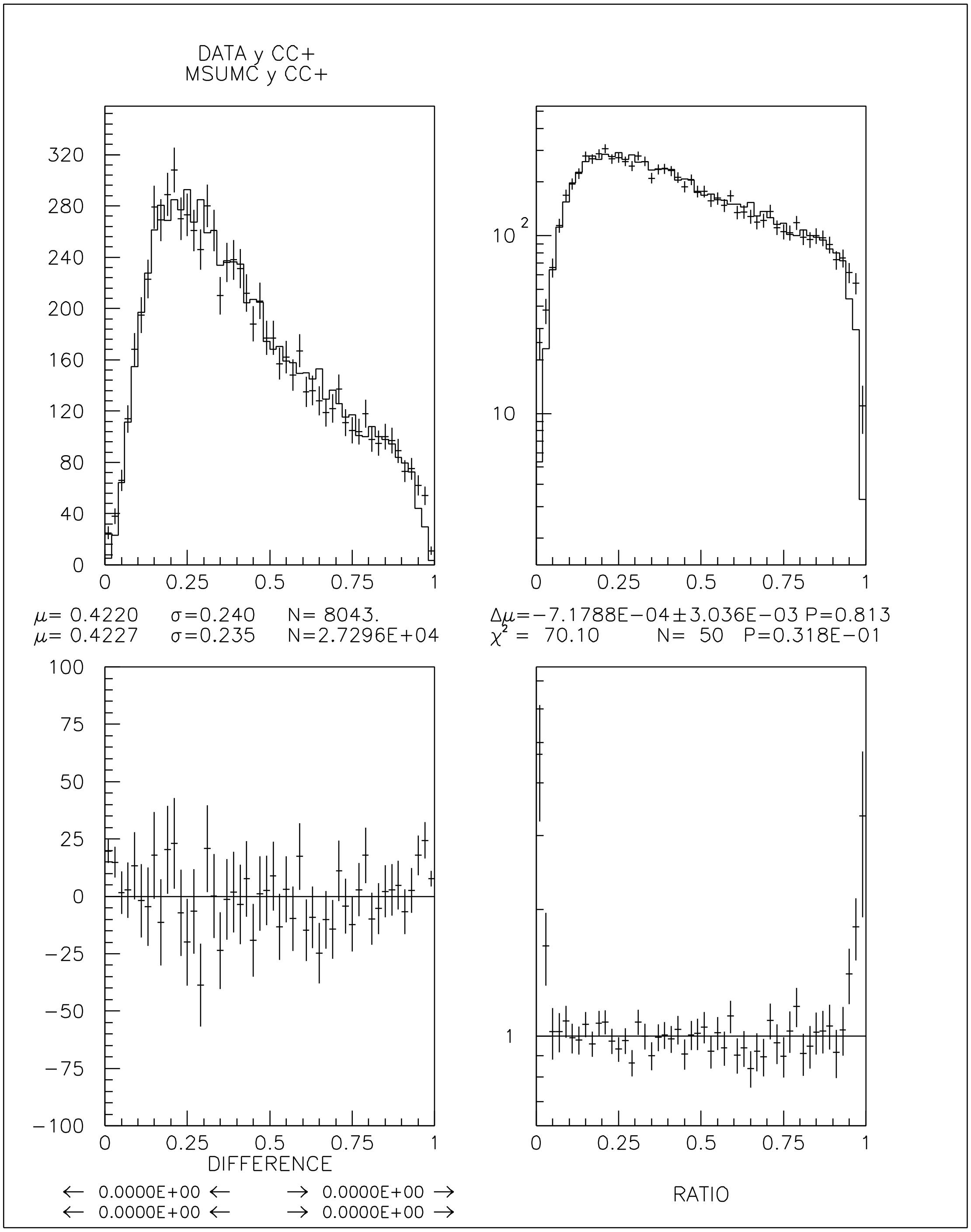

Figure B.9: Comparison of Data and Monte Carlo — y for class **CC+**

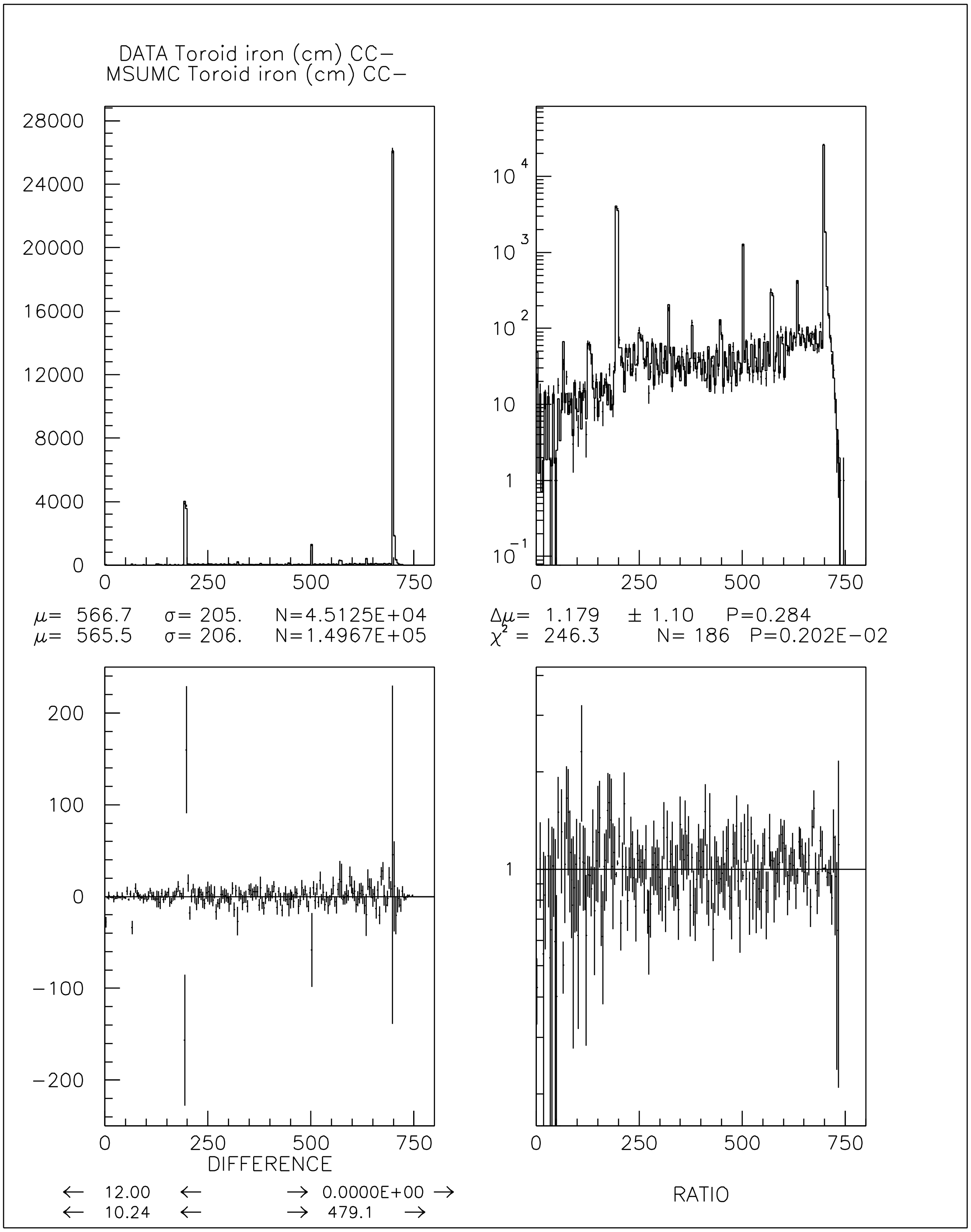

Figure B.10: Comparison of Data and Monte Carlo — Toroid iron traversed for class **CC–**

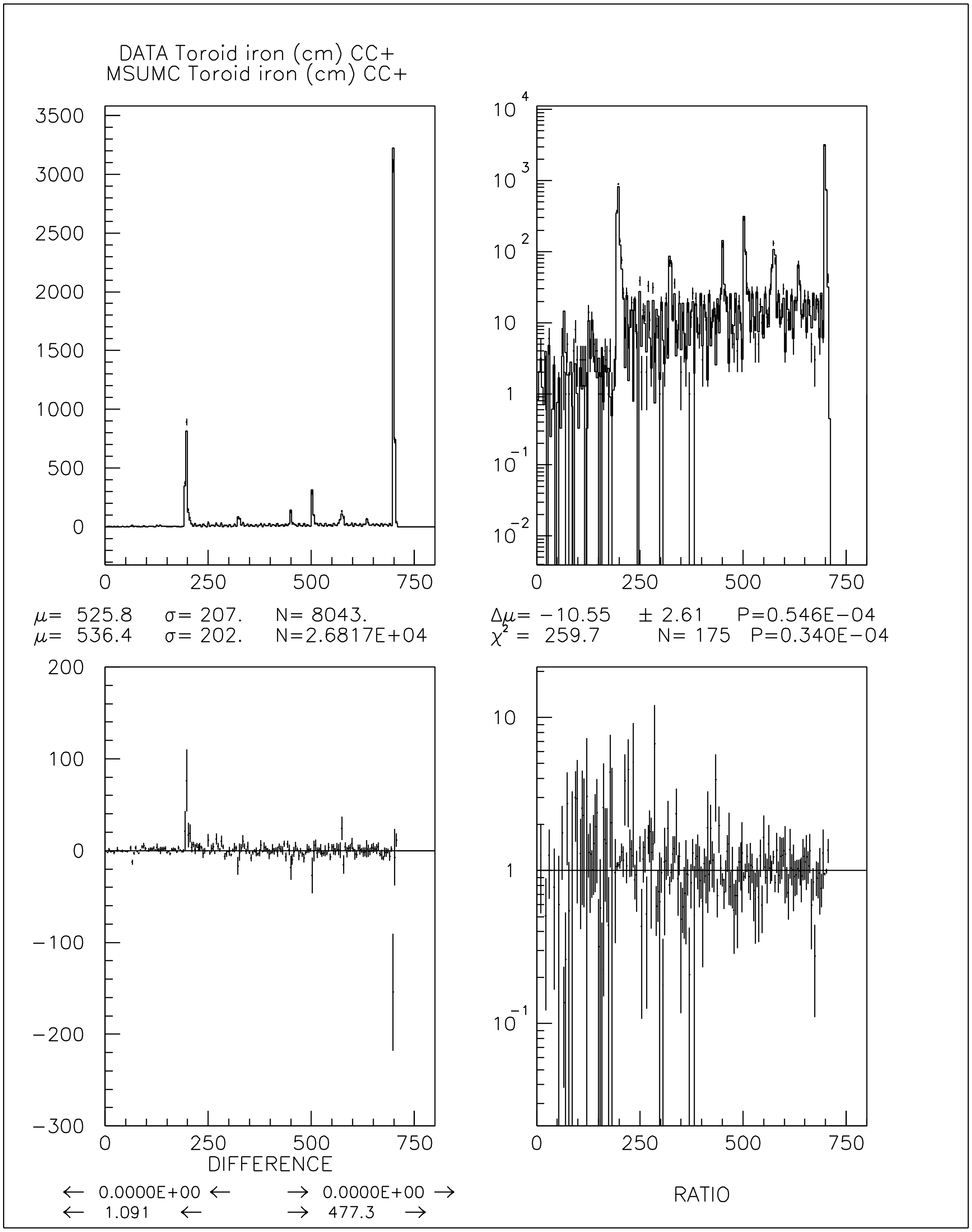

Figure B.11: Comparison of Data and Monte Carlo — Toroid iron traversed for class **CC+**

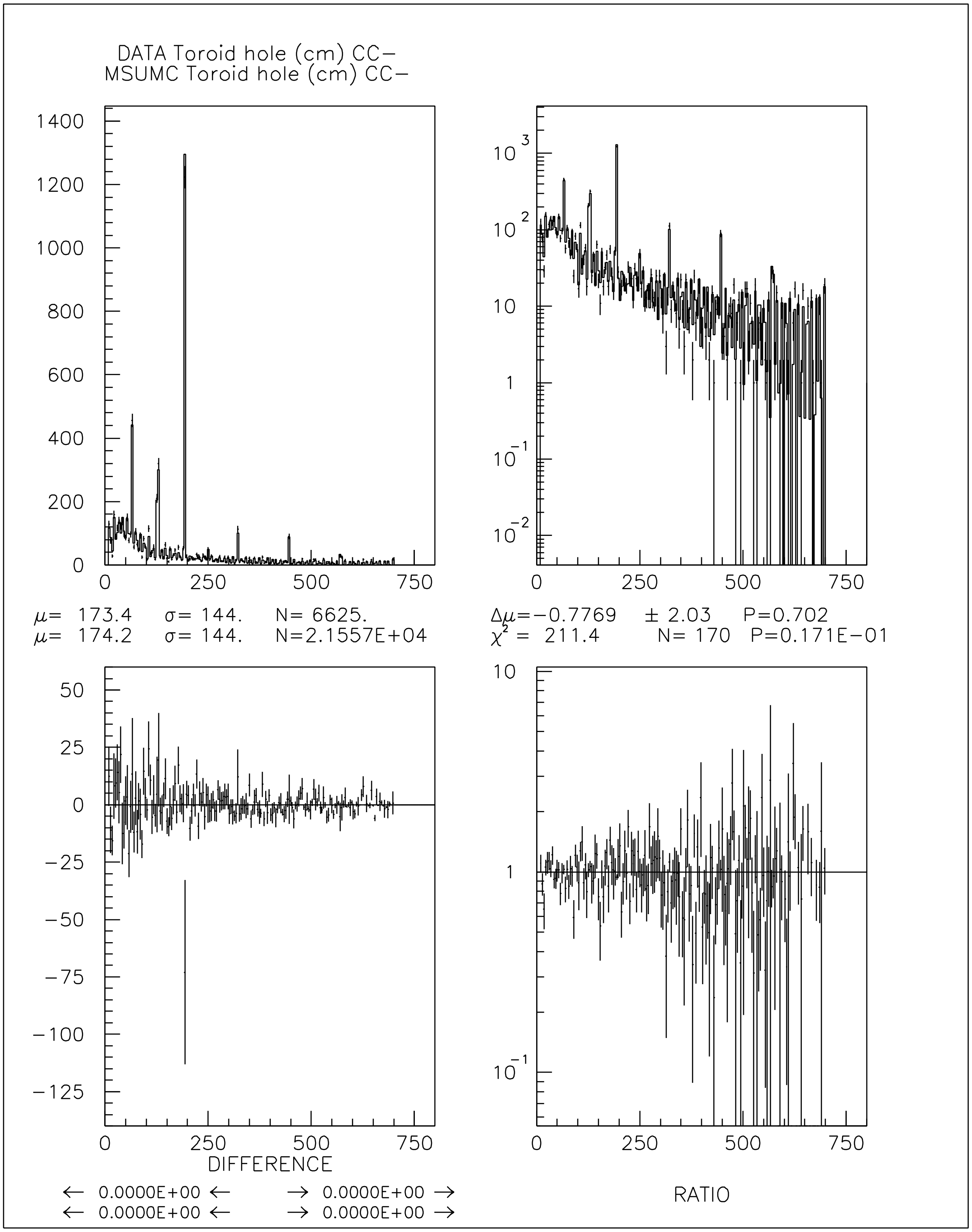

Figure B.12: Comparison of Data and Monte Carlo — Toroid hole traversed for class **CC–** (hole > 8 cm)

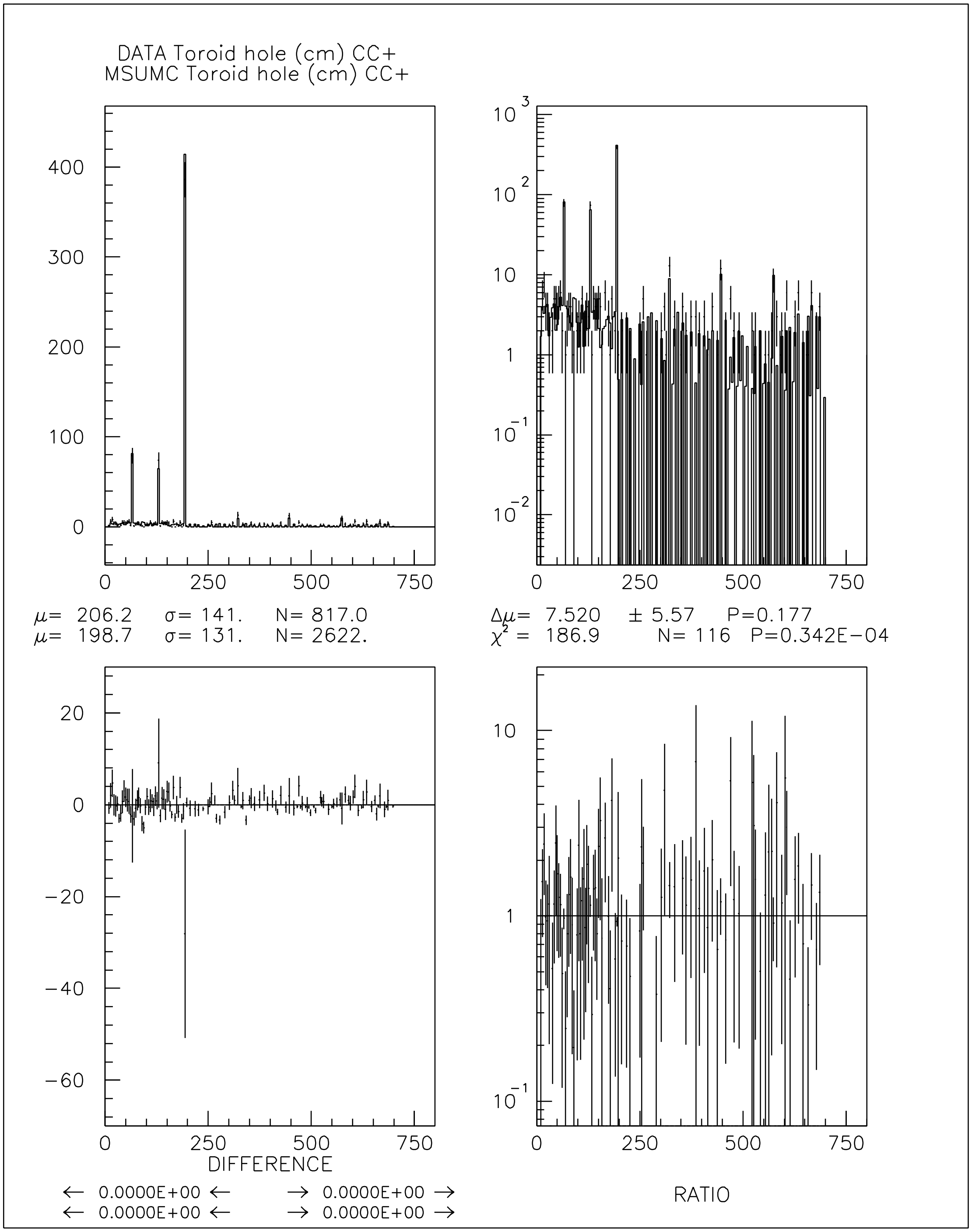

Figure B.13: Comparison of Data and Monte Carlo — Toroid hole traversed for class **CC+** (hole > 8 cm)

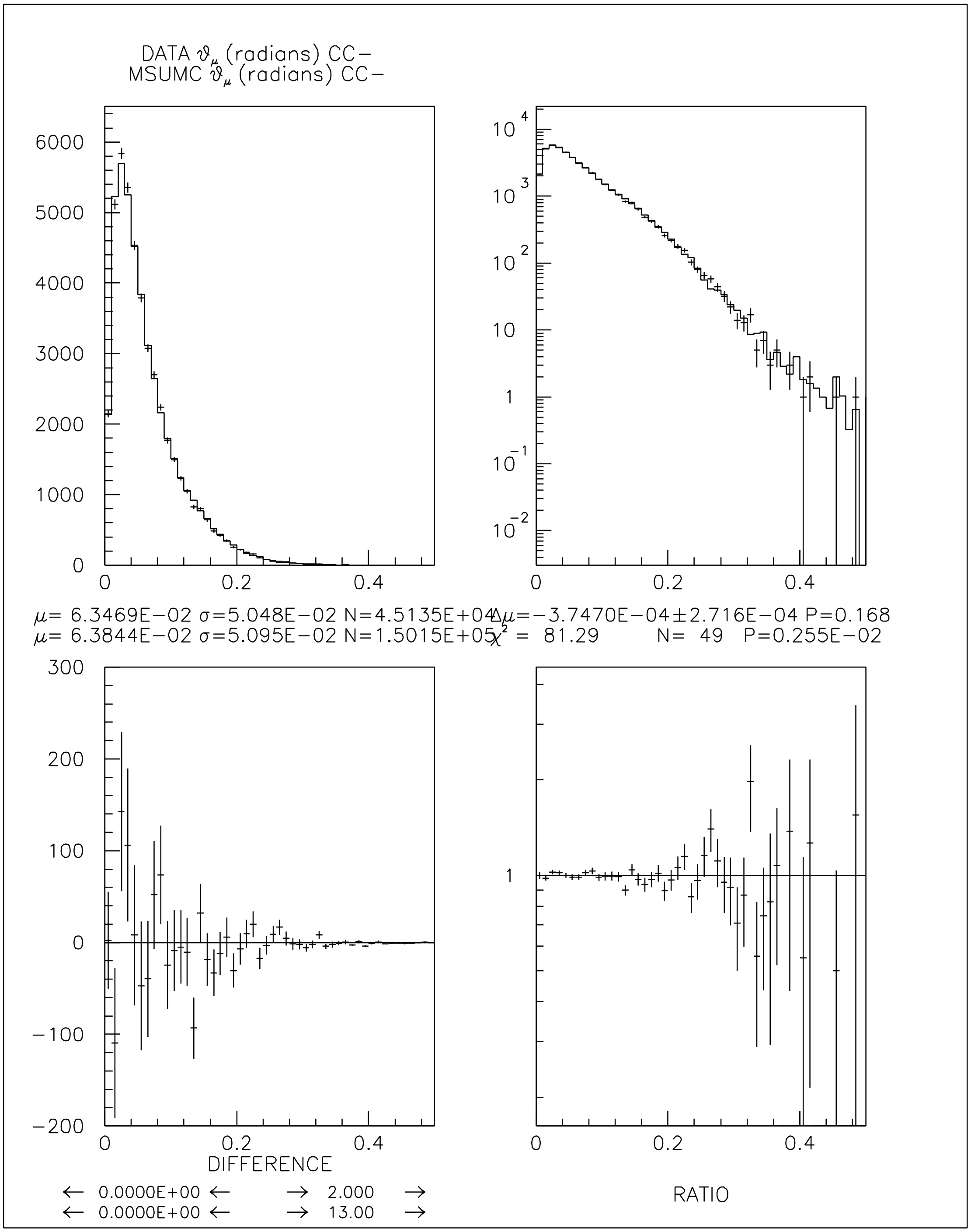

Figure B.14: Comparison of Data and Monte Carlo — θ_μ for class **CC–**

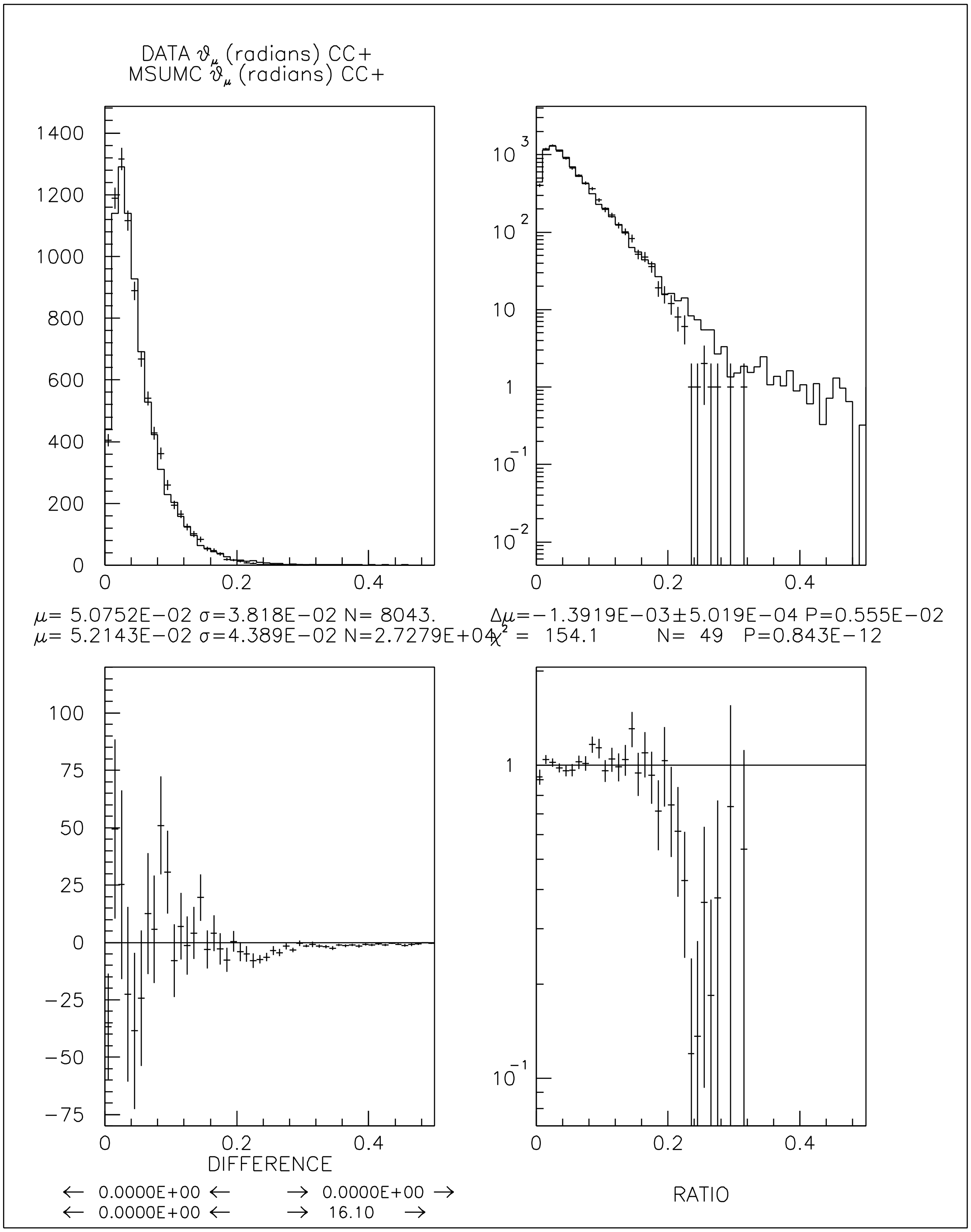

Figure B.15: Comparison of Data and Monte Carlo — θ_μ for class **CC+**

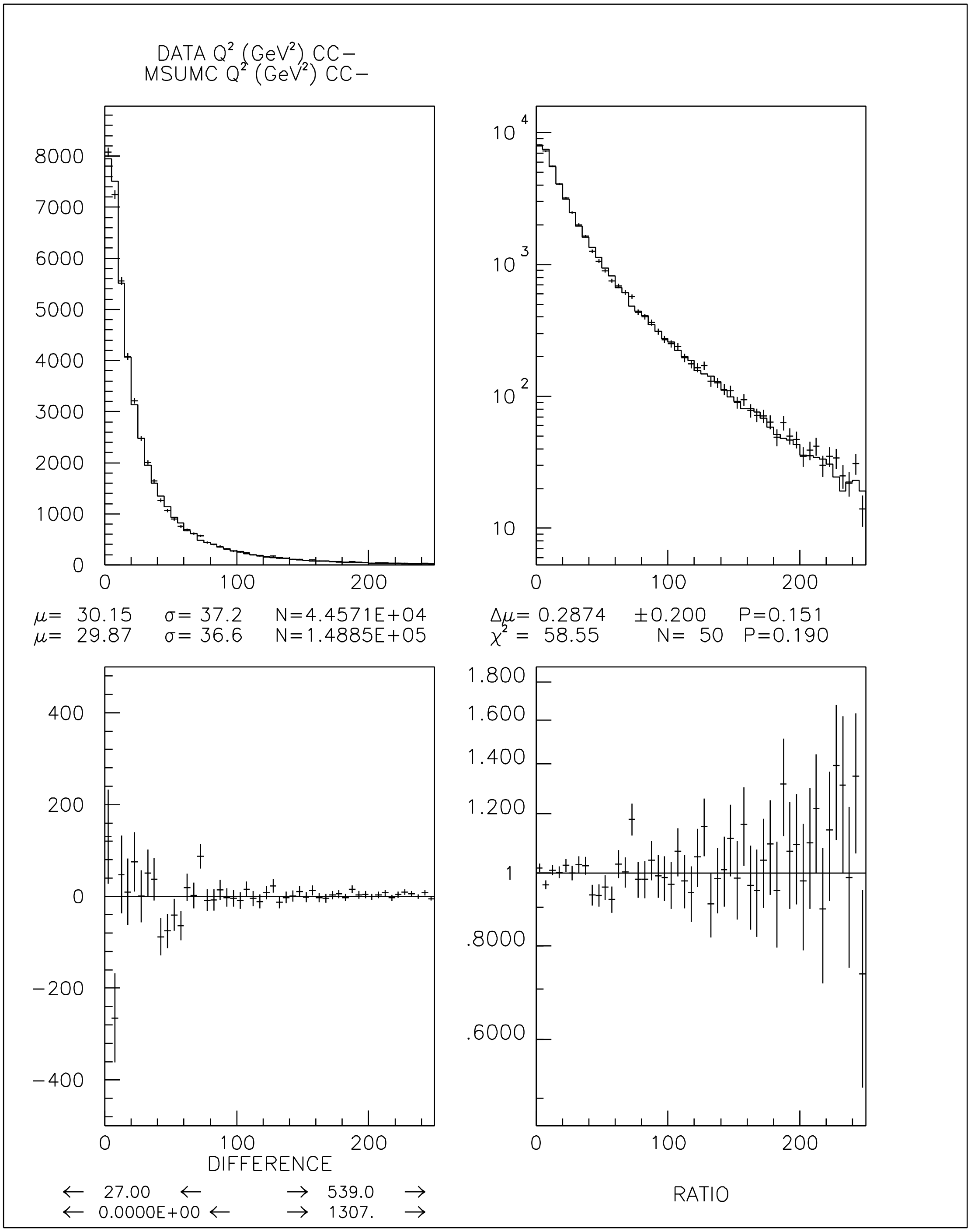

Figure B.16: Comparison of Data and Monte Carlo — Q^2 for class **CC−**

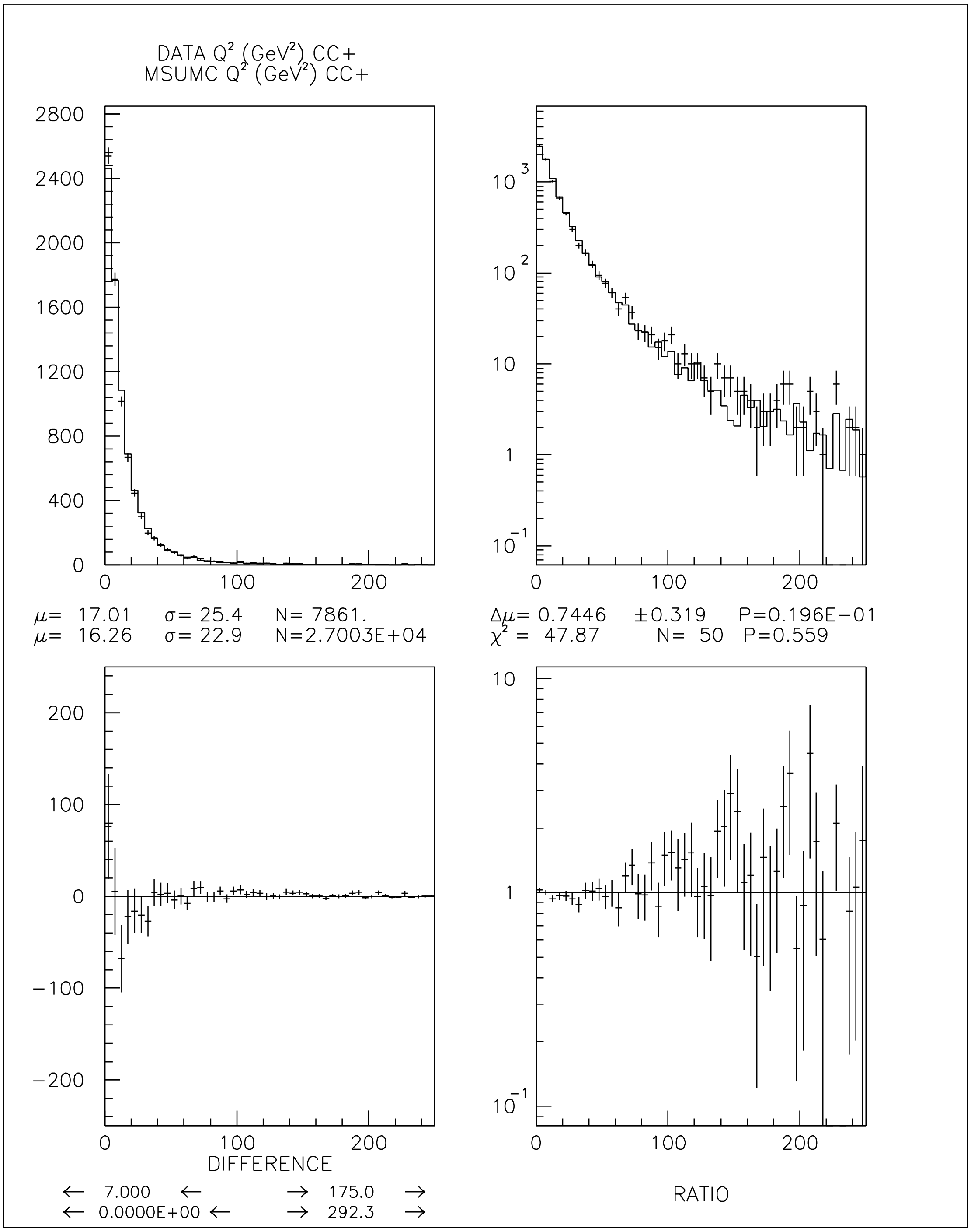

Figure B.17: Comparison of Data and Monte Carlo — Q^2 for class **CC+**

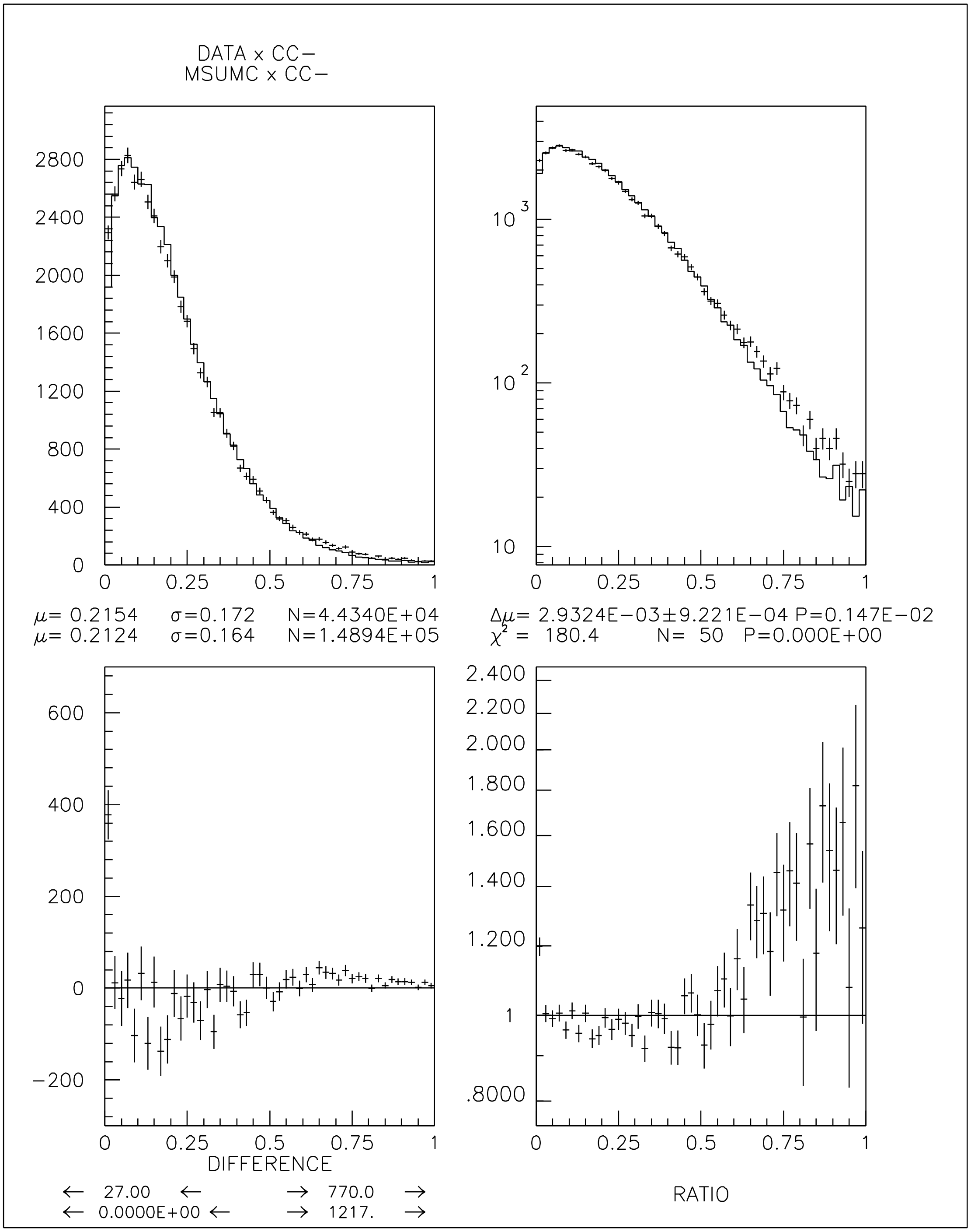

Figure B.18: Comparison of Data and Monte Carlo — x for class **CC–**

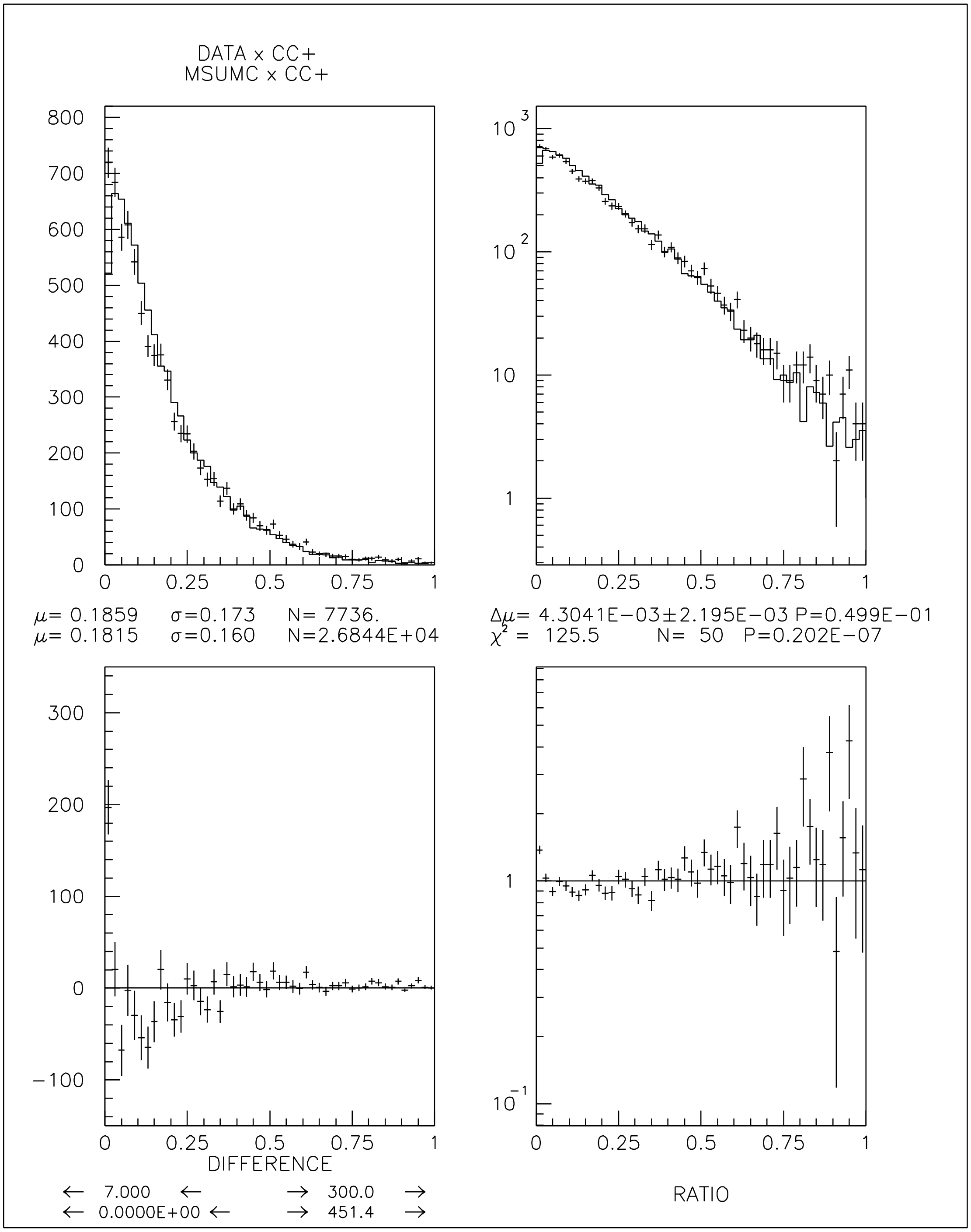

Figure B.19: Comparison of Data and Monte Carlo — x for class **CC–**

Appendix C

Computer printout of R_ν analysis, step-by-step

These two computer printouts are the output of the final R_ν analysis package as described in Chapter 5. They are for runs in the standard fiducial volume with E_H cuts of 10 GeV and 60 GeV, respectively.

The procedure is explained in Chapter 5, and the results are summarized in Tables 5.4 and 5.5. These outputs are provided to display quantitatively what the correction process involved, step-by-step.

Note: the *prime* label on some of the variable names indicates the particular procedure used (absolute acceptance cuts; treat **NC** and **CC0** together as the **N0** class).

C.1 10 GeV $\mathrm{E_H}$ cut

```
 Data   GJPG2A:G2ADAT_4_BCD_AM10.NL
 MC Neu GJPG2A:G2AMCN_5P15_BCD_AME5_10_87.NL
 MC Ant GJPG2A:G2AMCA_5P15_BCD_AME5_10_87.NL
 Scan   GJPG2A:G2ASCF_5_BCD_AM10.NL
 MC 2Mu GJPG2A:G2A2MC_5P15_BCD_AME5_10_87.NL
 Ch cor GJPG2A:G2ACHC_5P15_BCD_AME5_10_87.NL
 Process mode = BATCH
Extra_Rnubar_unc logical sets extra_R_nu_bar_unc = 0.01170
 Opening namelist files...  Reading namelist files...
$DATAIN
DATA_TOT_NC     =   19397.00    ,
DATA_TOT_CCO    =   6156.000    ,
DATA_TOT_CCM    =   45137.00    ,
DATA_TOT_CCP    =   8043.000
$END
$MCNEUIN
GNC_TOT_N       =   60540.63    ,    TNC_TOT_N       =   55793.00    ,
GNC_ANC_N       =   44609.66    ,    TNC_ANC_N       =   41346.00    ,
GNC_ACCO_N      =   6594.516    ,    TNC_ACCO_N      =   5986.000    ,
GNC_ACCM_N      =   331.1472    ,    TNC_ACCM_N      =   303.0000    ,
GNC_ACCP_N      =   337.2605    ,    TNC_ACCP_N      =   306.0000    ,
GNC_EHCUT_N     =   7490.471    ,    TNC_EHCUT_N     =   6835.000    ,
GNC_OTHCUT_N    =  0.0000000E+00,    TNC_OTHCUT_N    =  0.0000000E+00,
GNC_ELNC_N      =   907.8909    ,    TNC_ELNC_N      =   788.0000    ,
GNC_ELCCO_N     =   141.6375    ,    TNC_ELCCO_N     =   123.0000    ,
GNC_ELCCM_N     =   4.608100    ,    TNC_ELCCM_N     =   4.000000    ,
GNC_ELCCP_N     =   8.184700    ,    TNC_ELCCP_N     =   7.000000    ,
GNC_ELEHC_N     =   115.2471    ,    TNC_ELEHC_N     =   95.00000    ,
GNC_ELOC_N      =  0.0000000E+00,    TNC_ELOC_N      =  0.0000000E+00,
GCC_TOT_N       =   191786.8    ,    TCC_TOT_N       =   176046.0    ,
GCC_ANC_N       =   7001.567    ,    TCC_ANC_N       =   6904.000    ,
GCC_ACCO_N      =   9165.950    ,    TCC_ACCO_N      =   8773.000    ,
GCC_ACCM_N      =   149423.2    ,    TCC_ACCM_N      =   135932.0    ,
GCC_ACCP_N      =   834.4239    ,    TCC_ACCP_N      =   788.0000    ,
GCC_EHCUT_N     =   21785.45    ,    TCC_EHCUT_N     =   20567.00    ,
GCC_OTHCUT_N    =  0.0000000E+00,    TCC_OTHCUT_N    =  0.0000000E+00,
GCC_ELNC_N      =   3033.241    ,    TCC_ELNC_N      =   2607.000    ,
GCC_ELCCO_N     =   500.0763    ,    TCC_ELCCO_N     =   437.0000    ,
GCC_ELCCM_N     =   18.91340    ,    TCC_ELCCM_N     =   17.00000    ,
GCC_ELCCP_N     =   23.99680    ,    TCC_ELCCP_N     =   21.00000    ,
GCC_ELEHC_N     =  0.0000000E+00,    TCC_ELEHC_N     =  0.0000000E+00,
GCC_ELOC_N      =  0.0000000E+00,    TCC_ELOC_N      =  0.0000000E+00
$END


$MCANTIN
GNC_TOT_A       =   11755.41    ,    TNC_TOT_A       =   10429.00    ,
GNC_ANC_A       =   8120.443    ,    TNC_ANC_A       =   7191.000    ,
GNC_ACCO_A      =   653.1902    ,    TNC_ACCO_A      =   563.0000    ,
GNC_ACCM_A      =   48.74890    ,    TNC_ACCM_A      =   43.00000    ,
```

```
GNC_ACCP_A      =   35.45110    ,    TNC_ACCP_A      =   30.00000    ,
GNC_EHCUT_A     =   2693.208    ,    TNC_EHCUT_A     =   2434.000    ,
GNC_OTHCUT_A    =  0.0000000E+00,    TNC_OTHCUT_A    =  0.0000000E+00,
GNC_ELNC_A      =   148.2288    ,    TNC_ELNC_A      =   123.0000    ,
GNC_ELCC0_A     =   12.78700    ,    TNC_ELCC0_A     =   10.00000    ,
GNC_ELCCM_A     =  0.0000000E+00,    TNC_ELCCM_A     =  0.0000000E+00,
GNC_ELCCP_A     =   2.362100    ,    TNC_ELCCP_A     =   2.000000    ,
GNC_ELEHC_A     =   40.99040    ,    TNC_ELEHC_A     =   33.00000    ,
GNC_ELOC_A      =  0.0000000E+00,    TNC_ELOC_A      =  0.0000000E+00,
GCC_TOT_A       =   31977.79    ,    TCC_TOT_A       =   28195.00    ,
GCC_ANC_A       =   439.0644    ,    TCC_ANC_A       =   361.0000    ,
GCC_ACC0_A      =   1064.083    ,    TCC_ACC0_A      =   887.0000    ,
GCC_ACCM_A      =   271.3635    ,    TCC_ACCM_A      =   228.0000    ,
GCC_ACCP_A      =   21886.61    ,    TCC_ACCP_A      =   18981.00    ,
GCC_EHCUT_A     =   7815.659    ,    TCC_EHCUT_A     =   7329.000    ,
GCC_OTHCUT_A    =  0.0000000E+00,    TCC_OTHCUT_A    =  0.0000000E+00,
GCC_ELNC_A      =   448.2307    ,    TCC_ELNC_A      =   369.0000    ,
GCC_ELCC0_A     =   49.94390    ,    TCC_ELCC0_A     =   38.00000    ,
GCC_ELCCM_A     =   1.469700    ,    TCC_ELCCM_A     =   1.000000    ,
GCC_ELCCP_A     =   1.366100    ,    TCC_ELCCP_A     =   1.000000    ,
GCC_ELEHC_A     =  0.0000000E+00,    TCC_ELEHC_A     =  0.0000000E+00,
GCC_ELOC_A      =  0.0000000E+00,    TCC_ELOC_A      =  0.0000000E+00
$END
$MUCORIN
GNC_2MC_CC0_A   =  -98.99800    ,
GNC_2MC_CC0_A_UNC = 33.86800    ,
TNC_2MC_CC0_A   =  -108.8726    ,
GNC_2MC_CCF_A   =  -4.775700    ,
GNC_2MC_CCF_A_UNC = 12.38020    ,
TNC_2MC_CCF_A   =  -4.371500    ,
GCC_2MC_CC0_A   =  -73.94140    ,
GCC_2MC_CC0_A_UNC = 13.86790    ,
TCC_2MC_CC0_A   =  -87.97610    ,
GCC_2MC_CCF_A   =  -4.622300    ,
GCC_2MC_CCF_A_UNC = 4.510600    ,
TCC_2MC_CCF_A   =  -4.603400    ,
GNC_2MC_CC0_N   =  -256.2842    ,
GNC_2MC_CC0_N_UNC = 104.3136    ,
TNC_2MC_CC0_N   =  -280.8750    ,
GNC_2MC_CCF_N   =  -26.86790    ,
GNC_2MC_CCF_N_UNC = 35.36150    ,
TNC_2MC_CCF_N   =  -26.31120    ,
GCC_2MC_CC0_N   =  -525.3037    ,
GCC_2MC_CC0_N_UNC = 55.72660    ,
TCC_2MC_CC0_N   =  -608.4191    ,
GCC_2MC_CCF_N   =  -42.16680    ,
GCC_2MC_CCF_N_UNC = 18.30060    ,
TCC_2MC_CCF_N   =  -48.35420
$END
$CORFACIN
COSMICS_NC_COR   =  1.0800000E-03,   COSMICS_NC_COR_UNC   =  3.1999999E-04,
OUTTIME_NC_COR   =  1.1699999E-03,   OUTTIME_NC_COR_UNC   =  3.4000000E-04,
```

```
OUTTIME_CC0_COR  =  1.7600000E-03,   OUTTIME_CC0_COR_UNC  =  4.1000001E-04,
UPSTREAM_NC_COR  =  2.9000000E-04,   UPSTREAM_NC_COR_UNC  =  1.7000000E-04,
UPSTREAM_CC0_COR =  9.9999997E-05,   UPSTREAM_CC0_COR_UNC =  9.9999997E-05,
UPSTREAM_CCM_COR =  1.9999999E-04,   UPSTREAM_CCM_COR_UNC =  1.4000000E-04,
UPSTREAM_CCP_COR =  9.9999997E-05,   UPSTREAM_CCP_COR_UNC =  9.9999997E-05,
REPRIEVE_CC0_COR =  2.8400000E-03,   REPRIEVE_CC0_COR_UNC =  6.0999999E-04,
REPRIEVE_CCF_COR =  1.3000000E-04,   REPRIEVE_CCF_COR_UNC =  1.3000000E-04,
EXTRA_CC0NC_COR  =  1.0860000E-02,   EXTRA_CC0NC_UNC      =  1.1800000E-03,
EXTRA_CCFNC_COR  =  6.5000000E-04,   EXTRA_CCFNC_UNC      =  2.9000000E-04
$END
$CHCORIN
GNC_CHC_CC0     =   128.5950    ,
GNC_CHC_CC0_UNC =   28.10800    ,
TNC_CHC_CC0     =   141.0760    ,
GNC_CHC_CCF     =   257.1852    ,
GNC_CHC_CCF_UNC =   53.87910    ,
TNC_CHC_CCF     =   282.1518    ,
GCC_CHC_CC0     =   37.77420    ,
GCC_CHC_CC0_UNC =   9.739100    ,
TCC_CHC_CC0     =   40.98740    ,
GCC_CHC_CCF     =   75.54760    ,
GCC_CHC_CCF_UNC =   17.43120    ,
TCC_CHC_CCF     =   81.97510
$END


 Initial MC event numbers

          Acc NC   Acc CC0  Acc CC-  Acc CC+  EH cut  Other cut  |
Neut NC :  44609.7   6594.5    331.1    337.3   7490.5      0.0  |
Neut CC :   7001.6   9166.0 149423.2    834.4  21785.5      0.0  |
Anti NC :   8120.4    653.2     48.7     35.5   2693.2      0.0  |
Anti CC :    439.1   1064.1    271.4  21886.6   7815.7      0.0  |
                                                                 |
          elec NC elec CC0 elec CC- elec CC+ elecEHcut e othcut  |
Neut NC :    907.9    141.6      4.6      8.2    115.2      0.0  |
Neut CC :   3033.2    500.1     18.9     24.0      0.0      0.0  |
Anti NC :    148.2     12.8      0.0      2.4     41.0      0.0  |
Anti CC :    448.2     49.9      1.5      1.4      0.0      0.0  |


 Adjust MC to make EH cut absolute

          Acc NC   Acc CC0  Acc CC-  Acc CC+  EH cut  Other cut  |
Neut NC :  44609.7   6594.5    331.1    337.3      0.0      0.0  |
Neut CC :   7001.6   9166.0 149423.2    834.4      0.0      0.0  |
Anti NC :   8120.4    653.2     48.7     35.5      0.0      0.0  |
Anti CC :    439.1   1064.1    271.4  21886.6      0.0      0.0  |
                                                                 |
          elec NC elec CC0 elec CC- elec CC+ elecEHcut e othcut  |
Neut NC :    907.9    141.6      4.6      8.2      0.0      0.0  |
Neut CC :   3033.2    500.1     18.9     24.0      0.0      0.0  |
Anti NC :    148.2     12.8      0.0      2.4      0.0      0.0  |
```

```
Anti CC :    448.2     49.9      1.5      1.4      0.0      0.0  |

 Adjust MC to make other cuts absolute

          Acc NC   Acc CC0  Acc CC-  Acc CC+  EH cut  Other cut  |
Neut NC :  44609.7   6594.5    331.1    337.3      0.0      0.0  |
Neut CC :   7001.6   9166.0 149423.2    834.4      0.0      0.0  |
Anti NC :   8120.4    653.2     48.7     35.5      0.0      0.0  |
Anti CC :    439.1   1064.1    271.4  21886.6      0.0      0.0  |
                                                                 |
          elec NC elec CC0 elec CC- elec CC+ elecEHcut e othcut  |
Neut NC :    907.9    141.6      4.6      8.2      0.0      0.0  |
Neut CC :   3033.2    500.1     18.9     24.0      0.0      0.0  |
Anti NC :    148.2     12.8      0.0      2.4      0.0      0.0  |
Anti CC :    448.2     49.9      1.5      1.4      0.0      0.0  |

 Initial found_cc_ratio =  0.1781908     +/-   2.1566723E-03

Initial Data Events   NC          CC0         N0          CC-         CC+
                   19397+-139   6156+- 78  25553+-160  45137+-212   8043+- 90

First corrections to data based on Scan:
 Cosmics (all NC) =   85.0, Out-of-time (NC,CC0) =   92.1,   138.6
 Upstream (NC,CC0,CC-,CC+) =   22.8,     7.9,    15.7,     7.9

Table lines 2-4       NC          CC0         N0          CC-         CC+
 Delta COSMICS       -85+- 25      0+-  0    -85+- 25      0+-  0      0+-  0
 Delta OUT-OF-TIME   -92+- 27   -139+- 32   -231+- 42      0+-  0      0+-  0
 Delta UPSTREAM      -23+- 13     -8+-  8    -31+- 16    -16+- 11     -8+-  8

 After corrections for cosmics, upstream and OT events:

DATA :
NC  =  19197.0, CC0 =   6009.6, N0  =  25206.6, CC- =  45121.3, CC+ =   8035.1
  +/-    144.7           85.2           167.9           212.7           90.0

 Adjusted found_cc_ratio =  0.1780785     +/-   2.1647022E-03

Table line 5          NC          CC0         N0          CC-         CC+
 Delta REPRIEVES     176+- 37   -169+- 36      8+-  8     -7+-  7     -1+-  1

 After corrections for CC>NC>CC reprieve events:

DATA :
NC  =  19373.2, CC0 =   5841.0, N0  =  25214.3, CC- =  45114.7, CC+ =   8034.0
  +/-    149.3           92.6           168.1           212.8           90.0

Table line 6          NC          CC0         N0          CC-         CC+
Subtotal           19373+-149   5841+- 93  25214+-168  45115+-213   8034+- 90


 Adjustment to MC to rearrange fit decay mus
```

```
          Acc NC   Acc CC0  Acc CC-  Acc CC+  EH cut  Other cut  |
Neut NC :      0.0      0.0    103.3   -103.3      0.0      0.0  |
Neut CC :      0.0      0.0      0.0      0.0      0.0      0.0  |
Anti NC :      0.0      0.0      6.0     -6.0      0.0      0.0  |
Anti CC :      0.0      0.0      0.0      0.0      0.0      0.0  |
                                                                 |
          elec NC elec CC0 elec CC- elec CC+ elecEHcut e othcut  |
Neut NC :      0.0      0.0      3.7     -3.7      0.0      0.0  |
Neut CC :      0.0      0.0      9.0     -9.0      0.0      0.0  |
Anti NC :      0.0      0.0      1.5     -1.5      0.0      0.0  |
Anti CC :      0.0      0.0      0.4     -0.4      0.0      0.0  |

 After fit decay muon readjustment

          Acc NC   Acc CC0  Acc CC-  Acc CC+  EH cut  Other cut  |
Neut NC :  44609.7   6594.5    434.5    233.9      0.0      0.0  |
Neut CC :   7001.6   9166.0 149423.2    834.4      0.0      0.0  |
Anti NC :   8120.4    653.2     54.7     29.5      0.0      0.0  |
Anti CC :    439.1   1064.1    271.4  21886.6      0.0      0.0  |
                                                                 |
          elec NC elec CC0 elec CC- elec CC+ elecEHcut e othcut  |
Neut NC :    907.9    141.6      8.3      4.5      0.0      0.0  |
Neut CC :   3033.2    500.1     27.9     15.0      0.0      0.0  |
Anti NC :    148.2     12.8      1.5      0.8      0.0      0.0  |
Anti CC :    448.2     49.9      1.8      1.0      0.0      0.0  |

 Make the following 2nd muon study corrections to MC

          Acc NC   Acc CC0  Acc CC-  Acc CC+  EH cut  Other cut  |
Neut NC :   -283.2    256.3     17.5      9.4      0.0      0.0  |
Neut CC :   -567.5    525.3     27.4     14.8      0.0      0.0  |
Anti NC :   -103.8     99.0      3.1      1.7      0.0      0.0  |
Anti CC :    -78.6     73.9      3.0      1.6      0.0      0.0  |
                                                                 |
          elec NC elec CC0 elec CC- elec CC+ elecEHcut e othcut  |
Neut NC :      0.0      0.0      0.0      0.0      0.0      0.0  |
Neut CC :      0.0      0.0      0.0      0.0      0.0      0.0  |
Anti NC :      0.0      0.0      0.0      0.0      0.0      0.0  |
Anti CC :      0.0      0.0      0.0      0.0      0.0      0.0  |

 After 2nd muon study corrections to MC

          Acc NC   Acc CC0  Acc CC-  Acc CC+  EH cut  Other cut  |
Neut NC :  44326.5   6850.8    451.9    243.3      0.0      0.0  |
Neut CC :   6434.1   9691.3 149450.6    849.2      0.0      0.0  |
Anti NC :   8016.7    752.2     57.8     31.1      0.0      0.0  |
Anti CC :    360.5   1138.0    274.4  21888.2      0.0      0.0  |
                                                                 |
          elec NC elec CC0 elec CC- elec CC+ elecEHcut e othcut  |
Neut NC :    907.9    141.6      8.3      4.5      0.0      0.0  |
Neut CC :   3033.2    500.1     27.9     15.0      0.0      0.0  |
```

```
Anti NC :    148.2     12.8      1.5      0.8      0.0      0.0  |
Anti CC :    448.2     49.9      1.8      1.0      0.0      0.0  |

 Make the following Charm corrections to MC

          Acc NC   Acc CC0  Acc CC-  Acc CC+  EH cut  Other cut  |
Neut NC :    308.6   -102.9   -133.7    -72.0      0.0      0.0  |
Neut CC :     90.7    -30.2    -39.3    -21.2      0.0      0.0  |
Anti NC :     77.2    -25.7    -33.4    -18.0      0.0      0.0  |
Anti CC :     22.7     -7.6     -9.8     -5.3      0.0      0.0  |
                                                                 |
          elec NC elec CC0 elec CC- elec CC+ elecEHcut e othcut  |
Neut NC :      0.0      0.0      0.0      0.0      0.0      0.0  |
Neut CC :      0.0      0.0      0.0      0.0      0.0      0.0  |
Anti NC :      0.0      0.0      0.0      0.0      0.0      0.0  |
Anti CC :      0.0      0.0      0.0      0.0      0.0      0.0  |

 After Charm corrections to MC

          Acc NC   Acc CC0  Acc CC-  Acc CC+  EH cut  Other cut  |
Neut NC :  44635.1   6747.9    318.2    171.3      0.0      0.0  |
Neut CC :   6524.8   9661.0 149411.3    828.0      0.0      0.0  |
Anti NC :   8093.8    726.5     24.4     13.1      0.0      0.0  |
Anti CC :    383.2   1130.5    264.5  21882.9      0.0      0.0  |
                                                                 |
          elec NC elec CC0 elec CC- elec CC+ elecEHcut e othcut  |
Neut NC :    907.9    141.6      8.3      4.5      0.0      0.0  |
Neut CC :   3033.2    500.1     27.9     15.0      0.0      0.0  |
Anti NC :    148.2     12.8      1.5      0.8      0.0      0.0  |
Anti CC :    448.2     49.9      1.8      1.0      0.0      0.0  |

 Adjust MC for scan "Extra CC->NC" events

          Acc NC   Acc CC0  Acc CC-  Acc CC+  EH cut  Other cut  |
Neut NC :      0.0      0.0      0.0      0.0      0.0      0.0  |
Neut CC :   1918.3  -1809.9   -108.3      0.0      0.0      0.0  |
Anti NC :      0.0      0.0      0.0      0.0      0.0      0.0  |
Anti CC :    276.1   -260.5      0.0    -15.6      0.0      0.0  |
                                                                 |
          elec NC elec CC0 elec CC- elec CC+ elecEHcut e othcut  |
Neut NC :      0.0      0.0      0.0      0.0      0.0      0.0  |
Neut CC :      0.0      0.0      0.0      0.0      0.0      0.0  |
Anti NC :      0.0      0.0      0.0      0.0      0.0      0.0  |
Anti CC :      0.0      0.0      0.0      0.0      0.0      0.0  |

 After adjusting MC for scan "Extra CC->NC" events:

          Acc NC   Acc CC0  Acc CC-  Acc CC+  EH cut  Other cut  |
Neut NC :  44635.1   6747.9    318.2    171.3      0.0      0.0  |
Neut CC :   8443.0   7851.1 149303.0    828.0      0.0      0.0  |
Anti NC :   8093.8    726.5     24.4     13.1      0.0      0.0  |
Anti CC :    659.2    870.0    264.5  21867.3      0.0      0.0  |
```

```
                                                                 |
          elec NC elec CC0 elec CC- elec CC+ elecEHcut e othcut  |
Neut NC :    907.9    141.6      8.3      4.5      0.0      0.0  |
Neut CC :   3033.2    500.1     27.9     15.0      0.0      0.0  |
Anti NC :    148.2     12.8      1.5      0.8      0.0      0.0  |
Anti CC :    448.2     49.9      1.8      1.0      0.0      0.0  |


 Monte Carlo event totals heading into nubar/nu normalization

Total gen neut NC =  Total NC nu-mu   + Total NC nu-e
        52934.91           51872.59          1062.32
Total gen neut CC =  Total CC nu-mu   + Total CC nu-e
       170001.36          166425.13          3576.23
Total gen anti NC =  Tot NC nu-mu-bar + Tot NC nu-e-bar
         9021.21            8857.83           163.38
Total gen anti CC =  Tot CC nu-mu-bar + Tot CC nu-e-bar
        24162.13           23661.12           501.01

 Monte Carlo event totals after nubar/nu normalization of    1.174146

Total gen neut NC =  Total NC nu-mu   + Total NC nu-e
        52934.91           51872.59          1062.32
Total gen neut CC =  Total CC nu-mu   + Total CC nu-e
       170001.36          166425.13          3576.23
Total gen anti NC =  Tot NC nu-mu-bar + Tot NC nu-e-bar
        10592.22           10400.39           191.83
Total gen anti CC =  Tot CC nu-mu-bar + Tot CC nu-e-bar
        28369.87           27781.62           588.26

MC elements of electron neutrino correction

nu-e(&-bar) Evts accepted / Tot Evts accepted = elec fraction
NC  :            4641.46           67997.00      0.06826
CC0 :             715.37           17188.86      0.04162
N0  :            5356.83           85185.86      0.06288
CC- :              40.17          150000.63      0.00027
CC+ :              21.63           26711.89      0.00081
-----------------------------------------------------------------------
From current values of

DATA :
NC  =  19373.2, CC0 =   5841.0, N0  =  25214.3, CC- =  45114.7, CC+ =   8034.0
  +/-    149.3            92.6           168.1           212.8            90.0

Subtract electron-neutrino quantities:

DATA :
NC  =   1322.4, CC0 =    243.1, N0  =   1585.6, CC- =     12.1, CC+ =      6.5
  +/-     24.7            11.2            21.7             3.0             2.4

To get final values of
```

```
DATA :
NC  =  18050.8, CC0 =   5597.9, N0  =  23628.7, CC- =  45102.6, CC+ =   8027.5
  +/-    140.9            89.3           158.6           212.8           90.0

-----------------------------------------------------------------------
 Final cc+/cc- ratio =   0.1779820     +/-  2.1648211E-03

Table lines 7 & 8     NC          CC0         N0          CC-         CC+
 Delta NU_E EVENTS   1322+- 25    243+- 11   1586+- 22     12+-  3      7+-  2
 Subtotal           18051+-141   5598+- 89  23629+-159  45103+-213   8027+- 90

 ------------------------------------------------------------------------------

Table lines 9-12      NC          CC0         N0          CC-         CC+
 Delta N0<>CCFIT    ----------  ----------  -5280+- 71   4796+- 60    484+- 38
 Delta CC-<>CC+     ----------  ----------      0+-  0    155+- 11   -155+- 11
 Delta NUBAR N0     ----------  ----------  -3128+-113      0+-  0      0+-  0
CORRECTED EVENTS    ----------  ----------  15220+-207  50055+-244   8356+-102

TABLE yields Corrected NC/CC = 0.30408 +/- 0.00440
 ------------------------------------------------------------------------------

      "Found" CC+/- =        0.17798

      "Obs N0/CC-"  =        0.52389

       MC anti norm =        1.17415     +/- 0.01143

       e_nu         =       -0.00311     +/- 0.00023
       e_nu_bar     =        0.01862     +/- 0.00138

       True_R_nu_bar=        0.37436     +/- 0.01275
       R_nu_MC      =        0.31169     +/- 0.00167

       a_nu_prime   =        0.00000     +/- 0.00000
       a_nu_bar_prim=        0.00000     +/- 0.00000
       a_N_prime    =        0.00000     +/- 0.00000
       a_N_bar_prime=        0.00000     +/- 0.00000

       Delta_nu_prim=        0.09582     +/- 0.00110
       Delta_nu_b_pr=        0.05791     +/- 0.00444

       R_nu_prime   =        0.30408     +/- 0.00490    St/Sy 0.00397 / 0.00287
```

C.2 60 GeV $\mathrm{E_H}$ cut

```
 Data   GJPG2A:G2ADAT_4_BCD_AM60.NL
 MC Neu GJPG2A:G2AMCN_5P15_BCD_AME5_60_87.NL
 MC Ant GJPG2A:G2AMCA_5P15_BCD_AME5_60_87.NL
 Scan   GJPG2A:G2ASCF_5_BCD_AM60.NL
 MC 2Mu GJPG2A:G2A2MC_5P15_BCD_AME5_60_87.NL
 Ch cor GJPG2A:G2ACHC_5P15_BCD_AME5_60_87.NL
 Process mode = BATCH
Extra_Rnubar_unc logical sets extra_R_nu_bar_unc = 0.01500
 Opening namelist files...  Reading namelist files...
$DATAIN
DATA_TOT_NC     =   8617.000    ,
DATA_TOT_CC0    =   4026.000    ,
DATA_TOT_CCM    =   20966.00    ,
DATA_TOT_CCP    =   2270.000
$END
$MCNEUIN
GNC_TOT_N       =   60540.63    ,    TNC_TOT_N       =   55793.00    ,
GNC_ANC_N       =   18818.93    ,    TNC_ANC_N       =   17300.00    ,
GNC_ACC0_N      =   5175.628    ,    TNC_ACC0_N      =   4649.000    ,
GNC_ACCM_N      =   223.4711    ,    TNC_ACCM_N      =   202.0000    ,
GNC_ACCP_N      =   223.8473    ,    TNC_ACCP_N      =   202.0000    ,
GNC_EHCUT_N     =   34921.19    ,    TNC_EHCUT_N     =   32423.00    ,
GNC_OTHCUT_N    =  0.0000000E+00,    TNC_OTHCUT_N    =  0.0000000E+00,
GNC_ELNC_N      =   512.2939    ,    TNC_ELNC_N      =   448.0000    ,
GNC_ELCC0_N     =   110.5279    ,    TNC_ELCC0_N     =   96.00000    ,
GNC_ELCCM_N     =   2.411500    ,    TNC_ELCCM_N     =   2.000000    ,
GNC_ELCCP_N     =   4.707300    ,    TNC_ELCCP_N     =   4.000000    ,
GNC_ELEHC_N     =   547.6273    ,    TNC_ELEHC_N     =   467.0000    ,
GNC_ELOC_N      =  0.0000000E+00,    TNC_ELOC_N      =  0.0000000E+00,
GCC_TOT_N       =   191786.8    ,    TCC_TOT_N       =   176046.0    ,
GCC_ANC_N       =   3951.162    ,    TCC_ANC_N       =   3858.000    ,
GCC_ACC0_N      =   5512.367    ,    TCC_ACC0_N      =   5256.000    ,
GCC_ACCM_N      =   68697.36    ,    TCC_ACCM_N      =   61778.00    ,
GCC_ACCP_N      =   423.9253    ,    TCC_ACCP_N      =   394.0000    ,
GCC_EHCUT_N     =   109625.7    ,    TCC_EHCUT_N     =   101678.0    ,
GCC_OTHCUT_N    =  0.0000000E+00,    TCC_OTHCUT_N    =  0.0000000E+00,
GCC_ELNC_N      =   2929.076    ,    TCC_ELNC_N      =   2520.000    ,
GCC_ELCC0_N     =   493.0229    ,    TCC_ELCC0_N     =   431.0000    ,
GCC_ELCCM_N     =   17.71030    ,    TCC_ELCCM_N     =   16.00000    ,
GCC_ELCCP_N     =   19.36590    ,    TCC_ELCCP_N     =   17.00000    ,
GCC_ELEHC_N     =   117.0520    ,    TCC_ELEHC_N     =   98.00000    ,
GCC_ELOC_N      =  0.0000000E+00,    TCC_ELOC_N      =  0.0000000E+00
$END
$MCANTIN
GNC_TOT_A       =   11755.42    ,    TNC_TOT_A       =   10429.00    ,
GNC_ANC_A       =   2091.687    ,    TNC_ANC_A       =   1820.000    ,
GNC_ACC0_A      =   404.1015    ,    TNC_ACC0_A      =   342.0000    ,
GNC_ACCM_A      =   19.88610    ,    TNC_ACCM_A      =   17.00000    ,
GNC_ACCP_A      =   15.82090    ,    TNC_ACCP_A      =   13.00000    ,
```

```
GNC_EHCUT_A     =   9019.554    ,    TNC_EHCUT_A     =   8069.000    ,
GNC_OTHCUT_A    =  0.0000000E+00,    TNC_OTHCUT_A    =  0.0000000E+00,
GNC_ELNC_A      =   50.18930    ,    TNC_ELNC_A      =   41.00000    ,
GNC_ELCC0_A     =   10.33130    ,    TNC_ELCC0_A     =   8.000000    ,
GNC_ELCCM_A     =  0.0000000E+00,    TNC_ELCCM_A     =  0.0000000E+00,
GNC_ELCCP_A     =   1.212400    ,    TNC_ELCCP_A     =   1.000000    ,
GNC_ELEHC_A     =   142.6353    ,    TNC_ELEHC_A     =   118.0000    ,
GNC_ELOC_A      =  0.0000000E+00,    TNC_ELOC_A      =  0.0000000E+00,
GCC_TOT_A       =   31977.80    ,    TCC_TOT_A       =   28195.00    ,
GCC_ANC_A       =   239.7708    ,    TCC_ANC_A       =   197.0000    ,
GCC_ACC0_A      =   484.6784    ,    TCC_ACC0_A      =   404.0000    ,
GCC_ACCM_A      =   56.73330    ,    TCC_ACCM_A      =   48.00000    ,
GCC_ACCP_A      =   5738.936    ,    TCC_ACCP_A      =   4821.000    ,
GCC_EHCUT_A     =   24956.67    ,    TCC_EHCUT_A     =   22316.00    ,
GCC_OTHCUT_A    =  0.0000000E+00,    TCC_OTHCUT_A    =  0.0000000E+00,
GCC_ELNC_A      =   401.0966    ,    TCC_ELNC_A      =   333.0000    ,
GCC_ELCC0_A     =   46.56900    ,    TCC_ELCC0_A     =   36.00000    ,
GCC_ELCCM_A     =   1.469700    ,    TCC_ELCCM_A     =   1.000000    ,
GCC_ELCCP_A     =   1.366100    ,    TCC_ELCCP_A     =   1.000000    ,
GCC_ELEHC_A     =   50.50900    ,    TCC_ELEHC_A     =   38.00000    ,
GCC_ELOC_A      =  0.0000000E+00,    TCC_ELOC_A      =  0.0000000E+00
$END
$MUCORIN
GNC_2MC_CC0_A   =  -49.37130    ,
GNC_2MC_CC0_A_UNC = 24.97180    ,
TNC_2MC_CC0_A   =  -53.27490    ,
GNC_2MC_CCF_A   =  -7.824000    ,
GNC_2MC_CCF_A_UNC = 8.289900    ,
TNC_2MC_CCF_A   =  -8.123800    ,
GCC_2MC_CC0_A   =  -74.16600    ,
GCC_2MC_CC0_A_UNC = 12.59770    ,
TCC_2MC_CC0_A   =  -87.29670    ,
GCC_2MC_CCF_A   =  -7.713600    ,
GCC_2MC_CCF_A_UNC = 3.674600    ,
TCC_2MC_CCF_A   =  -8.882800    ,
GNC_2MC_CC0_N   =  -284.8940    ,
GNC_2MC_CC0_N_UNC = 87.67660    ,
TNC_2MC_CC0_N   =  -302.1162    ,
GNC_2MC_CCF_N   =  -39.92770    ,
GNC_2MC_CCF_N_UNC = 29.04740    ,
TNC_2MC_CCF_N   =  -42.92010    ,
GCC_2MC_CC0_N   =  -507.7756    ,
GCC_2MC_CC0_N_UNC = 50.76700    ,
TCC_2MC_CC0_N   =  -589.4847    ,
GCC_2MC_CCF_N   =  -55.29660    ,
GCC_2MC_CCF_N_UNC = 16.32150    ,
TCC_2MC_CCF_N   =  -61.93020
$END
$CORFACIN
COSMICS_NC_COR   =  2.2000000E-04,   COSMICS_NC_COR_UNC   =  2.2000000E-04,
OUTTIME_NC_COR   =  2.2000000E-04,   OUTTIME_NC_COR_UNC   =  2.2000000E-04,
OUTTIME_CC0_COR  =  0.0000000E+00,   OUTTIME_CC0_COR_UNC  =  2.2000000E-04,
```

```
UPSTREAM_NC_COR  =  0.0000000E+00,   UPSTREAM_NC_COR_UNC  =  2.2000000E-04,
UPSTREAM_CC0_COR =  2.2000000E-04,   UPSTREAM_CC0_COR_UNC =  2.2000000E-04,
UPSTREAM_CCM_COR =  2.2000000E-04,   UPSTREAM_CCM_COR_UNC =  2.2000000E-04,
UPSTREAM_CCP_COR =  0.0000000E+00,   UPSTREAM_CCP_COR_UNC =  2.2000000E-04,
REPRIEVE_CC0_COR =  3.1099999E-03,   REPRIEVE_CC0_COR_UNC =  9.4000000E-04,
REPRIEVE_CCF_COR =  2.8000001E-04,   REPRIEVE_CCF_COR_UNC =  2.8000001E-04,
EXTRA_CC0NC_COR  =  1.4690000E-02,   EXTRA_CC0NC_UNC      =  2.0200000E-03,
EXTRA_CCFNC_COR  =  8.5000001E-04,   EXTRA_CCFNC_UNC      =  4.9000001E-04
$END
$CHCORIN
GNC_CHC_CC0     =   93.19430    ,
GNC_CHC_CC0_UNC =   20.99050    ,
TNC_CHC_CC0     =   102.9664    ,
GNC_CHC_CCF     =   186.3836    ,
GNC_CHC_CCF_UNC =   39.69810    ,
TNC_CHC_CCF     =   205.9326    ,
GCC_CHC_CC0     =   32.35010    ,
GCC_CHC_CC0_UNC =   8.614600    ,
TCC_CHC_CC0     =   35.43520    ,
GCC_CHC_CCF     =   64.69930    ,
GCC_CHC_CCF_UNC =   15.23610    ,
TCC_CHC_CCF     =   70.87060
$END


 Initial MC event numbers

          Acc NC   Acc CC0  Acc CC-  Acc CC+  EH cut  Other cut  |
Neut NC :  18818.9   5175.6    223.5    223.8  34921.2      0.0  |
Neut CC :   3951.2   5512.4  68697.4    423.9 109625.7      0.0  |
Anti NC :   2091.7    404.1     19.9     15.8   9019.6      0.0  |
Anti CC :    239.8    484.7     56.7   5738.9  24956.7      0.0  |
                                                                 |
          elec NC elec CC0 elec CC- elec CC+ elecEHcut e othcut  |
Neut NC :    512.3    110.5      2.4      4.7    547.6      0.0  |
Neut CC :   2929.1    493.0     17.7     19.4    117.1      0.0  |
Anti NC :     50.2     10.3      0.0      1.2    142.6      0.0  |
Anti CC :    401.1     46.6      1.5      1.4     50.5      0.0  |

 Adjust MC to make EH cut absolute

          Acc NC   Acc CC0  Acc CC-  Acc CC+  EH cut  Other cut  |
Neut NC :  18818.9   5175.6    223.5    223.8      0.0      0.0  |
Neut CC :   3951.2   5512.4  68697.4    423.9      0.0      0.0  |
Anti NC :   2091.7    404.1     19.9     15.8      0.0      0.0  |
Anti CC :    239.8    484.7     56.7   5738.9      0.0      0.0  |
                                                                 |
          elec NC elec CC0 elec CC- elec CC+ elecEHcut e othcut  |
Neut NC :    512.3    110.5      2.4      4.7      0.0      0.0  |
Neut CC :   2929.1    493.0     17.7     19.4      0.0      0.0  |
Anti NC :     50.2     10.3      0.0      1.2      0.0      0.0  |
Anti CC :    401.1     46.6      1.5      1.4      0.0      0.0  |
```

```
 Adjust MC to make other cuts absolute

          Acc NC   Acc CC0  Acc CC-  Acc CC+  EH cut  Other cut  |
Neut NC :  18818.9    5175.6   223.5    223.8      0.0      0.0  |
Neut CC :   3951.2    5512.4 68697.4    423.9      0.0      0.0  |
Anti NC :   2091.7     404.1    19.9     15.8      0.0      0.0  |
Anti CC :    239.8     484.7    56.7   5738.9      0.0      0.0  |
                                                                 |
          elec NC elec CC0 elec CC- elec CC+ elecEHcut e othcut  |
Neut NC :    512.3     110.5     2.4      4.7      0.0      0.0  |
Neut CC :   2929.1     493.0    17.7     19.4      0.0      0.0  |
Anti NC :     50.2      10.3     0.0      1.2      0.0      0.0  |
Anti CC :    401.1      46.6     1.5      1.4      0.0      0.0  |

 Initial found_cc_ratio =  0.1082705     +/-   2.3923253E-03

Initial Data Events   NC          CC0         N0          CC-         CC+
                    8617+- 93   4026+- 63  12643+-112  20966+-145   2270+- 48


First corrections to data based on Scan:
 Cosmics (all NC) =    7.9, Out-of-time (NC,CC0) =    7.9,     0.0
 Upstream (NC,CC0,CC-,CC+) =    0.0,     7.9,     7.9,     0.0

Table lines 2-4       NC          CC0         N0          CC-         CC+
 Delta COSMICS        -8+-  8      0+-  0     -8+-  8      0+-  0      0+-  0
 Delta OUT-OF-TIME    -8+-  8      0+-  8     -8+- 11      0+-  0      0+-  0
 Delta UPSTREAM        0+-  8     -8+-  8     -8+- 11     -8+-  8      0+-  8

 After corrections for cosmics, upstream and OT events:

DATA :
NC  =   8601.2, CC0 =   4018.1, N0  =  12619.3, CC- =  20958.1, CC+ =   2270.0
  +/-     93.8            64.4           113.8           145.0            48.3

 Adjusted found_cc_ratio =  0.1083113     +/-   2.4231104E-03

Table line 5          NC          CC0         N0          CC-         CC+
 Delta REPRIEVES      92+- 27    -85+- 26      8+-  8     -7+-  7     -1+-  1

 After corrections for CC>NC>CC reprieve events:

DATA :
NC  =   8693.6, CC0 =   3933.3, N0  =  12627.0, CC- =  20951.2, CC+ =   2269.3
  +/-     97.6            69.3           114.1           145.2            48.3


Table line 6          NC          CC0         N0          CC-         CC+
Subtotal            8694+- 98   3933+- 69  12627+-114  20951+-145   2269+- 48

 Adjustment to MC to rearrange fit decay mus

          Acc NC   Acc CC0  Acc CC-  Acc CC+  EH cut  Other cut  |
```

```
Neut NC :      0.0      0.0     67.3    -67.3      0.0      0.0  |
Neut CC :      0.0      0.0      0.0      0.0      0.0      0.0  |
Anti NC :      0.0      0.0      3.3     -3.3      0.0      0.0  |
Anti CC :      0.0      0.0      0.0      0.0      0.0      0.0  |
                                                                 |
          elec NC elec CC0 elec CC- elec CC+ elecEHcut e othcut  |
Neut NC :      0.0      0.0      2.2     -2.2      0.0      0.0  |
Neut CC :      0.0      0.0      6.4     -6.4      0.0      0.0  |
Anti NC :      0.0      0.0      0.8     -0.8      0.0      0.0  |
Anti CC :      0.0      0.0      0.4     -0.4      0.0      0.0  |

 After fit decay muon readjustment

          Acc NC   Acc CC0  Acc CC-  Acc CC+  EH cut  Other cut  |
Neut NC :  18818.9   5175.6    290.8    156.6      0.0      0.0  |
Neut CC :   3951.2   5512.4  68697.4    423.9      0.0      0.0  |
Anti NC :   2091.7    404.1     23.2     12.5      0.0      0.0  |
Anti CC :    239.8    484.7     56.7   5738.9      0.0      0.0  |
                                                                 |
          elec NC elec CC0 elec CC- elec CC+ elecEHcut e othcut  |
Neut NC :    512.3    110.5      4.6      2.5      0.0      0.0  |
Neut CC :   2929.1    493.0     24.1     13.0      0.0      0.0  |
Anti NC :     50.2     10.3      0.8      0.4      0.0      0.0  |
Anti CC :    401.1     46.6      1.8      1.0      0.0      0.0  |

 Make the following 2nd muon study corrections to MC

          Acc NC   Acc CC0  Acc CC-  Acc CC+  EH cut  Other cut  |
Neut NC :   -324.8    284.9     26.0     14.0      0.0      0.0  |
Neut CC :   -563.1    507.8     35.9     19.4      0.0      0.0  |
Anti NC :    -57.2     49.4      5.1      2.7      0.0      0.0  |
Anti CC :    -81.9     74.2      5.0      2.7      0.0      0.0  |
                                                                 |
          elec NC elec CC0 elec CC- elec CC+ elecEHcut e othcut  |
Neut NC :      0.0      0.0      0.0      0.0      0.0      0.0  |
Neut CC :      0.0      0.0      0.0      0.0      0.0      0.0  |
Anti NC :      0.0      0.0      0.0      0.0      0.0      0.0  |
Anti CC :      0.0      0.0      0.0      0.0      0.0      0.0  |

 After 2nd muon study corrections to MC

          Acc NC   Acc CC0  Acc CC-  Acc CC+  EH cut  Other cut  |
Neut NC :  18494.1   5460.5    316.7    170.5      0.0      0.0  |
Neut CC :   3388.1   6020.1  68733.3    443.3      0.0      0.0  |
Anti NC :   2034.5    453.5     28.3     15.2      0.0      0.0  |
Anti CC :    157.9    558.8     61.7   5741.6      0.0      0.0  |
                                                                 |
          elec NC elec CC0 elec CC- elec CC+ elecEHcut e othcut  |
Neut NC :    512.3    110.5      4.6      2.5      0.0      0.0  |
Neut CC :   2929.1    493.0     24.1     13.0      0.0      0.0  |
Anti NC :     50.2     10.3      0.8      0.4      0.0      0.0  |
Anti CC :    401.1     46.6      1.8      1.0      0.0      0.0  |
```

```
 Make the following Charm corrections to MC

          Acc NC   Acc CC0  Acc CC-  Acc CC+  EH cut  Other cut  |
Neut NC :    223.7    -74.6    -96.9    -52.2      0.0      0.0  |
Neut CC :     77.6    -25.9    -33.6    -18.1      0.0      0.0  |
Anti NC :     55.9    -18.6    -24.2    -13.0      0.0      0.0  |
Anti CC :     19.4     -6.5     -8.4     -4.5      0.0      0.0  |
                                                                 |
          elec NC elec CC0 elec CC- elec CC+ elecEHcut e othcut  |
Neut NC :      0.0      0.0      0.0      0.0      0.0      0.0  |
Neut CC :      0.0      0.0      0.0      0.0      0.0      0.0  |
Anti NC :      0.0      0.0      0.0      0.0      0.0      0.0  |
Anti CC :      0.0      0.0      0.0      0.0      0.0      0.0  |

 After Charm corrections to MC

          Acc NC   Acc CC0  Acc CC-  Acc CC+  EH cut  Other cut  |
Neut NC :  18717.8   5386.0    219.8    118.3      0.0      0.0  |
Neut CC :   3465.7   5994.3  68699.7    425.2      0.0      0.0  |
Anti NC :   2090.4    434.8      4.1      2.2      0.0      0.0  |
Anti CC :    177.3    552.4     53.3   5737.1      0.0      0.0  |
                                                                 |
          elec NC elec CC0 elec CC- elec CC+ elecEHcut e othcut  |
Neut NC :    512.3    110.5      4.6      2.5      0.0      0.0  |
Neut CC :   2929.1    493.0     24.1     13.0      0.0      0.0  |
Anti NC :     50.2     10.3      0.8      0.4      0.0      0.0  |
Anti CC :    401.1     46.6      1.8      1.0      0.0      0.0  |

 Adjust MC for scan "Extra CC->NC" events

          Acc NC   Acc CC0  Acc CC-  Acc CC+  EH cut  Other cut  |
Neut NC :      0.0      0.0      0.0      0.0      0.0      0.0  |
Neut CC :   1248.8  -1180.5    -68.3      0.0      0.0      0.0  |
Anti NC :      0.0      0.0      0.0      0.0      0.0      0.0  |
Anti CC :    104.5    -98.7      0.0     -5.7      0.0      0.0  |
                                                                 |
          elec NC elec CC0 elec CC- elec CC+ elecEHcut e othcut  |
Neut NC :      0.0      0.0      0.0      0.0      0.0      0.0  |
Neut CC :      0.0      0.0      0.0      0.0      0.0      0.0  |
Anti NC :      0.0      0.0      0.0      0.0      0.0      0.0  |
Anti CC :      0.0      0.0      0.0      0.0      0.0      0.0  |

 After adjusting MC for scan "Extra CC->NC" events:

          Acc NC   Acc CC0  Acc CC-  Acc CC+  EH cut  Other cut  |
Neut NC :  18717.8   5386.0    219.8    118.3      0.0      0.0  |
Neut CC :   4714.5   4813.8  68631.4    425.2      0.0      0.0  |
Anti NC :   2090.4    434.8      4.1      2.2      0.0      0.0  |
Anti CC :    281.8    453.6     53.3   5731.4      0.0      0.0  |
                                                                 |
          elec NC elec CC0 elec CC- elec CC+ elecEHcut e othcut  |
```

```
Neut NC :    512.3    110.5      4.6      2.5      0.0      0.0  |
Neut CC :   2929.1    493.0     24.1     13.0      0.0      0.0  |
Anti NC :     50.2     10.3      0.8      0.4      0.0      0.0  |
Anti CC :    401.1     46.6      1.8      1.0      0.0      0.0  |



 Monte Carlo event totals heading into nubar/nu normalization

Total gen neut NC =  Total NC nu-mu   + Total NC nu-e
        25071.82           24441.88           629.94
Total gen neut CC =  Total CC nu-mu   + Total CC nu-e
        82043.97           78584.80          3459.18
Total gen anti NC =  Tot NC nu-mu-bar + Tot NC nu-e-bar
         2593.23            2531.50            61.73
Total gen anti CC =  Tot CC nu-mu-bar + Tot CC nu-e-bar
         6970.62            6520.12           450.50

 Monte Carlo event totals after nubar/nu normalization of    1.204764

Total gen neut NC =  Total NC nu-mu   + Total NC nu-e
        25071.82           24441.88           629.94
Total gen neut CC =  Total CC nu-mu   + Total CC nu-e
        82043.97           78584.80          3459.18
Total gen anti NC =  Tot NC nu-mu-bar + Tot NC nu-e-bar
         3124.23            3049.85            74.37
Total gen anti CC =  Tot CC nu-mu-bar + Tot CC nu-e-bar
         8397.95            7855.20           542.75

MC elements of electron neutrino correction

nu-e(&-bar) Evts accepted / Tot Evts accepted = elec fraction
NC  :             3985.06           30275.22      0.13163
CC0 :              672.10           11942.27      0.05628
N0  :             4657.16           42217.49      0.11031
CC- :               31.90           68952.20      0.00046
CC+ :               17.18            7468.30      0.00230
-----------------------------------------------------------------------
From current values of

DATA :
NC  =   8693.6, CC0 =   3933.3, N0  =  12627.0, CC- =  20951.2, CC+ =   2269.3
  +/-     97.6            69.3           114.1          145.2            48.3

Subtract electron-neutrino quantities:

DATA :
NC  =   1144.3, CC0 =    221.4, N0  =   1392.9, CC- =      9.7, CC+ =      5.2
  +/-     25.8            10.8            20.7            2.7             2.1

To get final values of

DATA :
```

```
NC  =   7549.3, CC0 =   3712.0, N0  =  11234.0, CC- =  20941.5, CC+ =   2264.0
  +/-     87.6            66.2           102.8           145.1            48.2

-----------------------------------------------------------------------
 Final cc+/cc- ratio =   0.1081122     +/-  2.4220312E-03

Table lines 7 & 8      NC          CC0         N0          CC-         CC+
 Delta NU_E EVENTS  1144+- 26    221+- 11   1393+- 21     10+-  3      5+-  2
 Subtotal           7549+- 88   3712+- 66  11234+-103  20942+-145   2264+- 48

 ------------------------------------------------------------------------------

Table lines 9-12      NC          CC0         N0          CC-         CC+
 Delta N0<>CCFIT    ----------  ----------  -3059+- 53   2827+- 46    232+- 26
 Delta CC-<>CC+     ----------  ----------      0+-  0    109+-  8   -109+-  8
 Delta NUBAR N0     ----------  ----------   -927+- 49      0+-  0      0+-  0
CORRECTED EVENTS    ----------  ----------   7248+-126  23878+-172   2387+- 58

TABLE yields Corrected NC/CC = 0.30354 +/- 0.00570
 ------------------------------------------------------------------------------

      "Found" CC+/- =        0.10811

      "Obs N0/CC-"  =        0.53645

       MC anti norm =        1.20476     +/- 0.02558

       e_nu         =       -0.00459     +/- 0.00032
       e_nu_bar     =        0.04594     +/- 0.00341

       True_R_nu_bar=        0.38826     +/- 0.01813
       R_nu_MC      =        0.31103     +/- 0.00246

       a_nu_prime   =        0.00000     +/- 0.00000
       a_nu_bar_prim=        0.00000     +/- 0.00000
       a_N_prime    =        0.00000     +/- 0.00000
       a_N_bar_prime=        0.00000     +/- 0.00000

       Delta_nu_prim=        0.11839     +/- 0.00174
       Delta_nu_b_pr=        0.09739     +/- 0.01080

       R_nu_prime   =        0.30354     +/- 0.00656   St/Sy 0.00551 / 0.00356
```

Appendix D

Results of the $2^{nd}\mu$ Study

The second-muon study explained in section 5.4.5 yielded information on the rate of NC→CC misclassification due to the detection of muons from the decay of particles in hadronic showers and other background sources. The plots on the next page show the magnitude of this effect and its distribution with regard to shower energy and detector position.

It can be seen that the rate of *finding* muons is much higher than that of achieving a fit to their momenta in the spectrometer. It is also clear that higher energy showers are more apt to generate muons, and also more apt to generate tracks which are identified as muons whether they are or not. The rate of muon-finding also increases with flash chamber number, as the further downstream the interaction takes place, the wider the angle of acceptance of the spectrometer is.

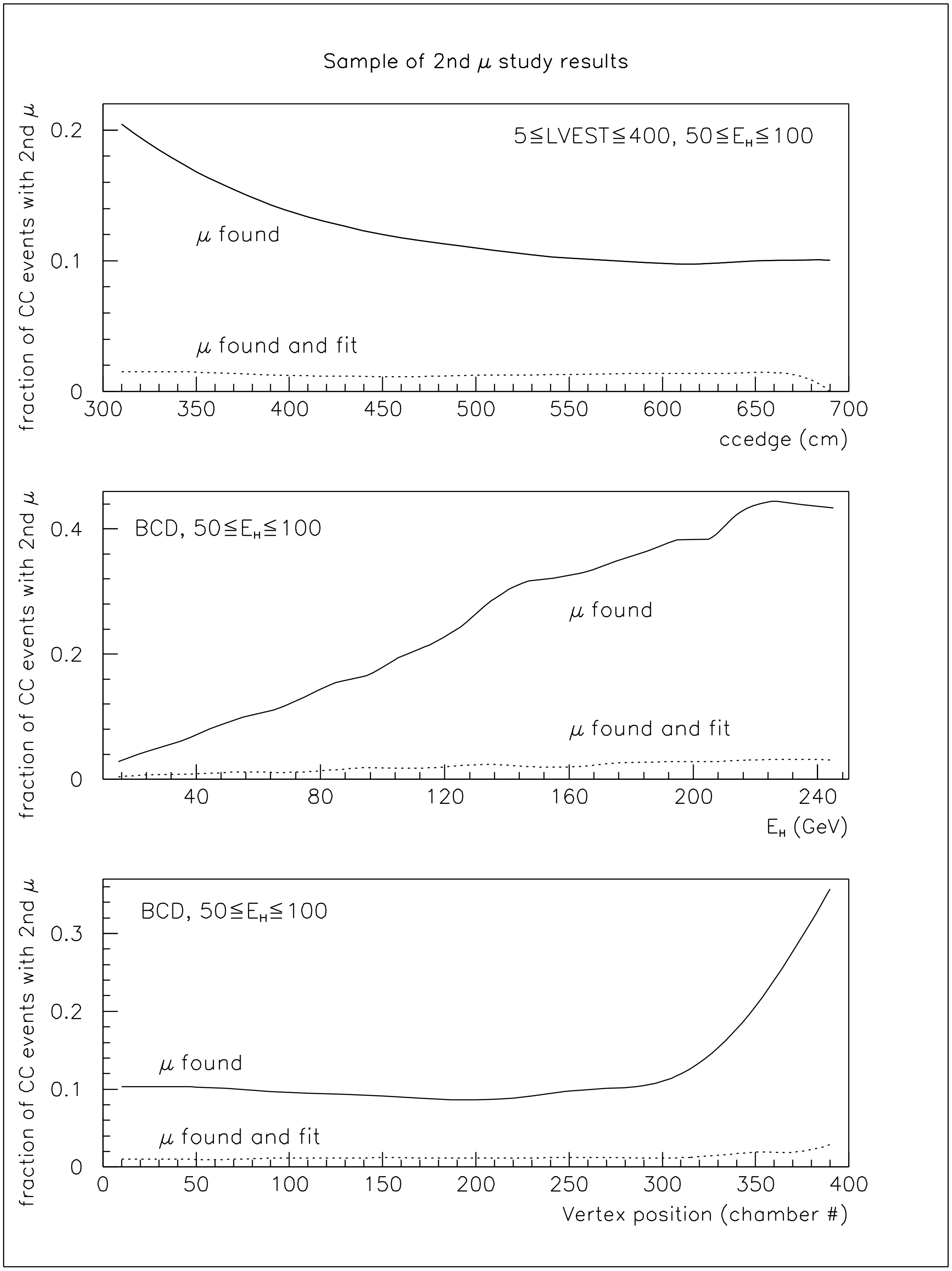

Figure D.1: Dependence of $2^{nd}\mu$ probability on detector position and hadronic shower energy

Appendix E

Graphical Depiction of the Sensitivity of R_ν and its Uncertainty to Various Quantities

This is a set of figures demonstrating the effect on R_ν and δR_ν which varying some of the quantities which go into its measurement would induce. In these figures, the effect shown is that of varying a single quantity while all other quantities remain fixed.

The vertical error bars on the first two pages of figures represent the actual uncertainty determined for R_ν. Horizontal error bars, if any, represent the uncertainty in the featured quantity.

The first page shows the effect of the values of

- $R_{\overline{\nu}}$ used in the analysis,
- the actual number of **CC−** events in the data set,
- the fraction of this number which were found in class **N0**, and
- the fraction of this number which were found in class **CC+**.

It can be seen that R_ν is fairly insensitive to $R_{\overline{\nu}}$ and the measured ratio of **CC+/CC–**, and (as should be expected) doesn't depend at all on the actual value of **CC–**. It does (again, as expected) depend on the found ratio of **N0/CC–**, with a slope virtually equal to 1.0 (the vertical scale has been stretched so as to show the less sensitive dependencies on other quantities more clearly).

The second figure page shows the effects of the confusion factors defined in section 5.6.2. (Since the procedure used sets the acceptance factors to zero, they do not contribute to the measurement of R_ν, and are not plotted here). While R_ν is very sensitive to Δ_ν, it is significantly less sensitive to the other confusion factors. This is in part due to the fact that a **CC–** event which is misclassified will not only subtract from the number of **CC–** events, but also add to the number of **N0** events, thus exaggerating the effect of such confusion. The other categories involve switching between classes which are subtracted as backgrounds or otherwise suppressed, and thus avoid such double-counting.

The third and fourth pages show the effects of the quantities from the first two pages on the *uncertainty* in the final value of R_ν. The fifth and sixth pages show the effects of the uncertainties in various quantities upon the uncertainty in R_ν. In these figures,

- the solid line represents the total uncertainty;
- the diamond shows the actual values of the total uncertainty and of the quantity being plotted;
- the dotted line represents the statistical uncertainty due to the data sample's size;
- the dashed line represents the MSUMC systematic uncertainty; and

- the dot-dash line (on the fifth and sixth figure pages) represents that part of the systematic uncertainty which is due solely to the particular uncertainty being plotted.

The sensitivity of R_ν to Δ_ν noted above may be seen on the fifth page, which shows that a large fraction of the entire systematic uncertainty is caused by the $\delta\Delta_\nu$ term. A glance at the fourth page shows that the uncertainty in R_ν is affected very little by the actual value of Δ_ν; if the goal is a precise measurement of R_ν, then it is not the actual value of Δ_ν which is so important, but the precision with which that value is known.

Another point to notice is in Figure E.3, where the expected dependence of the statistical uncertainty upon the number of events in the data sample is visible.

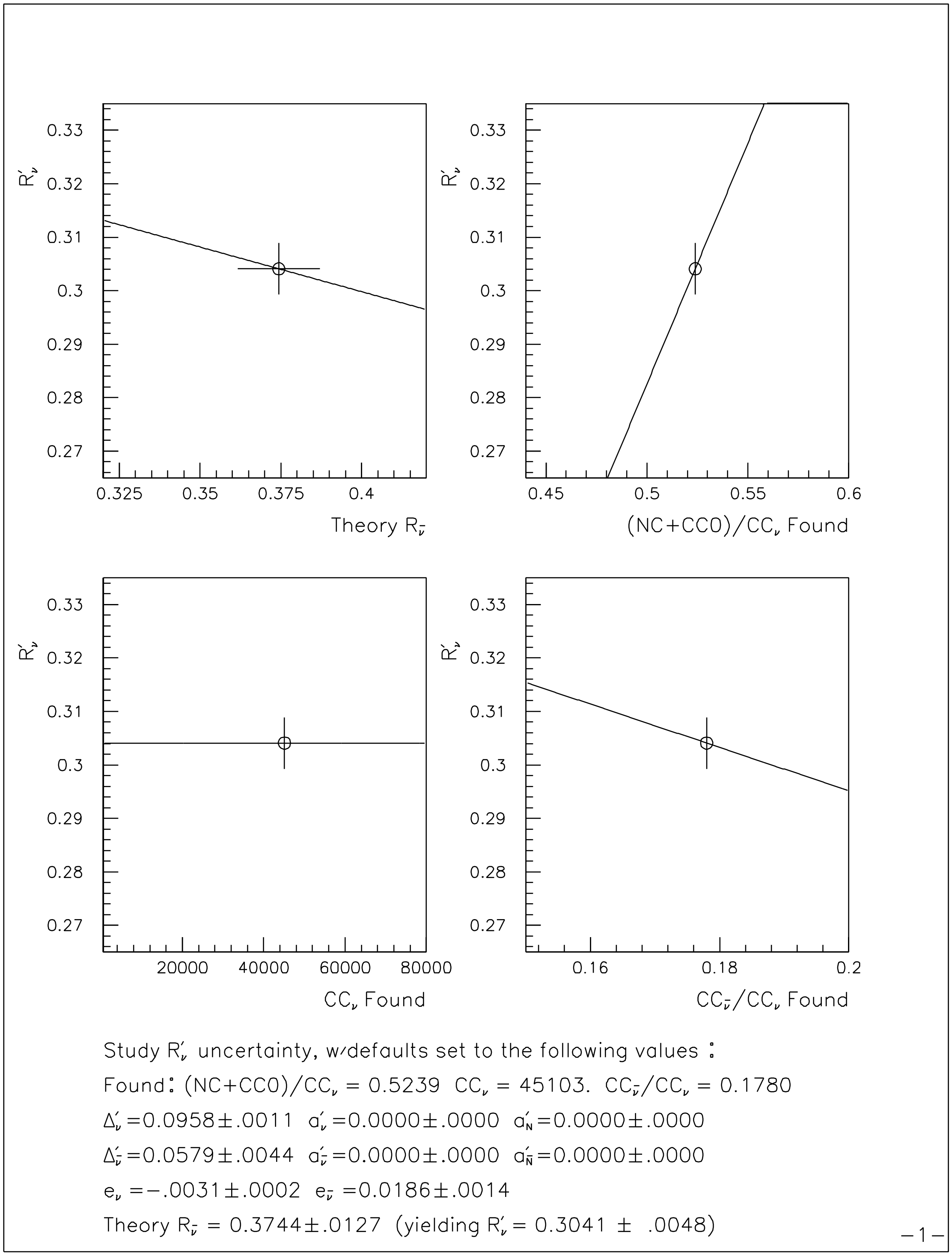

Study R'_ν uncertainty, w/defaults set to the following values :

Found: (NC+CC0)/CC$_\nu$ = 0.5239 CC$_\nu$ = 45103. CC$_{\bar\nu}$/CC$_\nu$ = 0.1780

Δ'_ν=0.0958±.0011 a'_ν=0.0000±.0000 a'_N=0.0000±.0000

$\Delta'_{\bar\nu}$=0.0579±.0044 $a'_{\bar\nu}$=0.0000±.0000 $a'_{\bar N}$=0.0000±.0000

e_ν =−.0031±.0002 $e_{\bar\nu}$ =0.0186±.0014

Theory $R_{\bar\nu}$ = 0.3744±.0127 (yielding R'_ν = 0.3041 ± .0048)

Figure E.1: The effect upon R_ν of several quantities used in its measurement; 10 GeV E_H cut, standard fiducial volume.

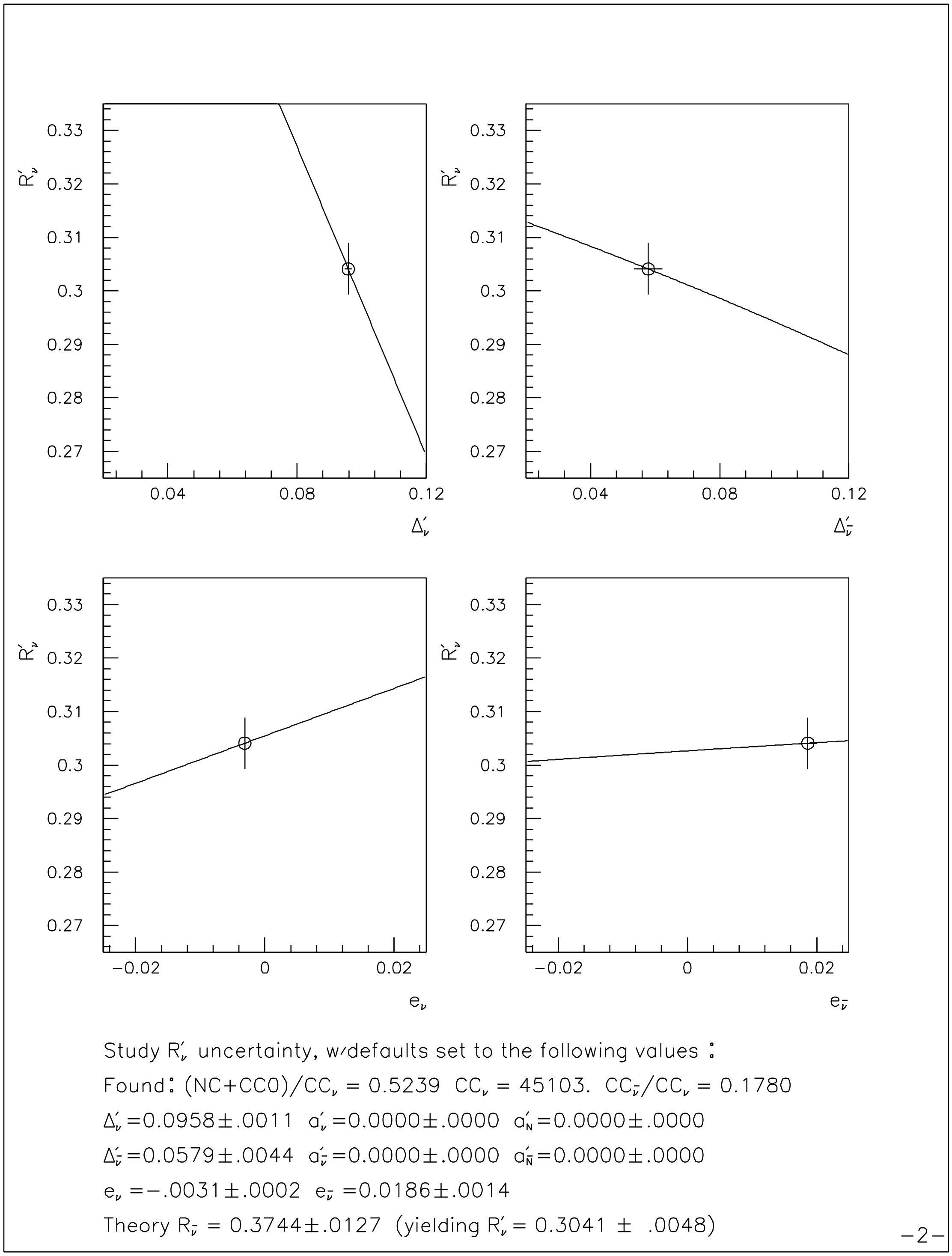

Study R'_ν uncertainty, w/defaults set to the following values :

Found: $(NC+CC0)/CC_\nu = 0.5239$ $CC_\nu = 45103.$ $CC_{\bar\nu}/CC_\nu = 0.1780$

$\Delta'_\nu = 0.0958 \pm .0011$ $\alpha'_\nu = 0.0000 \pm .0000$ $\alpha'_N = 0.0000 \pm .0000$

$\Delta'_{\bar\nu} = 0.0579 \pm .0044$ $\alpha'_{\bar\nu} = 0.0000 \pm .0000$ $\alpha'_{\bar N} = 0.0000 \pm .0000$

$e_\nu = -.0031 \pm .0002$ $e_{\bar\nu} = 0.0186 \pm .0014$

Theory $R_{\bar\nu} = 0.3744 \pm .0127$ (yielding $R'_\nu = 0.3041 \pm .0048$)

Figure E.2: The effect upon R_ν of the confusion factors from section 5.6.2.

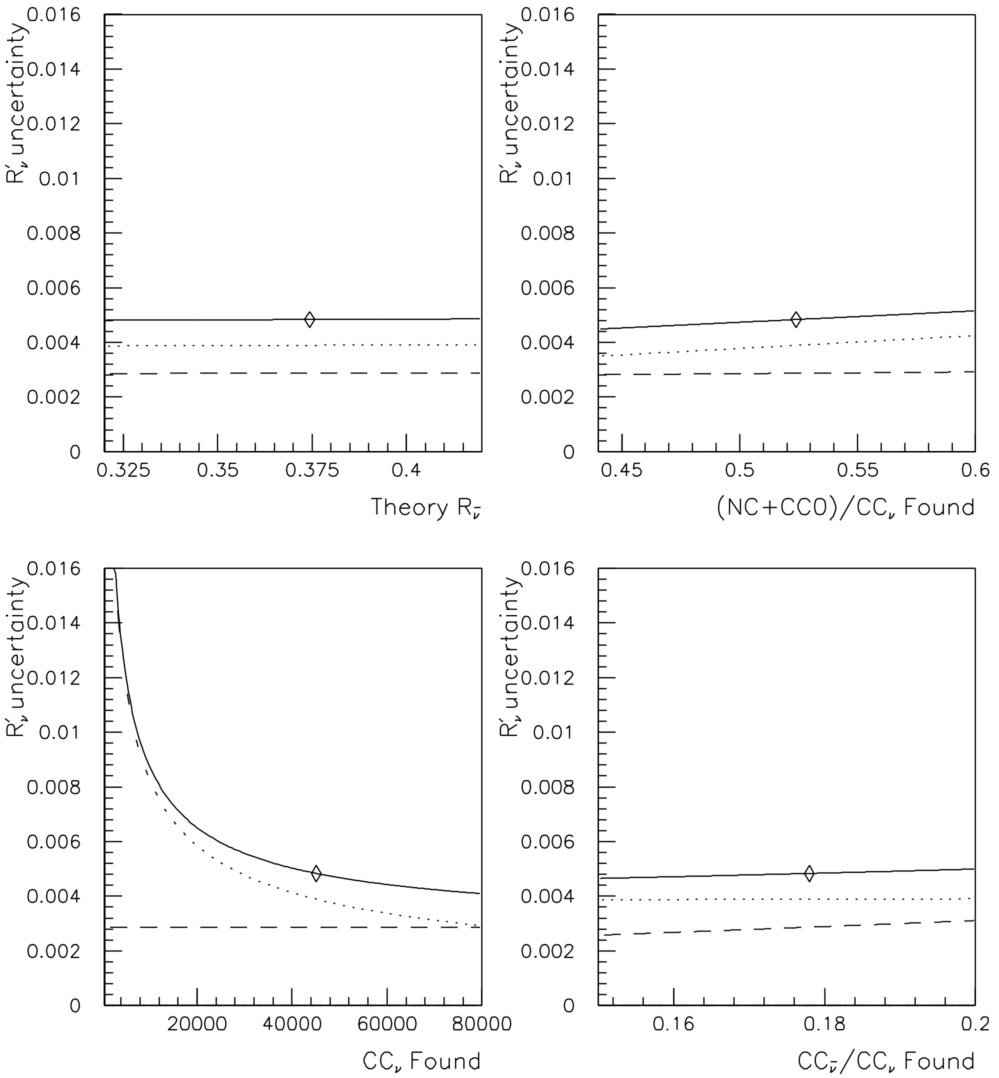

Study R'_ν uncertainty, w/defaults set to the following values :

Found: (NC+CC0)/CC$_\nu$ = 0.5239 CC$_\nu$ = 45103. CC$_{\bar\nu}$/CC$_\nu$ = 0.1780

Δ'_ν=0.0958±.0011 a'_ν=0.0000±.0000 a'_N=0.0000±.0000

$\Delta'_{\bar\nu}$=0.0579±.0044 $a'_{\bar\nu}$=0.0000±.0000 $a'_{\bar N}$=0.0000±.0000

e_ν =−.0031±.0002 $e_{\bar\nu}$ =0.0186±.0014

Theory $R_{\bar\nu}$ = 0.3744±.0127 (yielding R'_ν = 0.3041 ± .0048)

−3−

Figure E.3: The effect upon the uncertainty in R_ν of several quantities used in its measurement; 10 GeV $\mathrm{E_H}$ cut, standard fiducial volume.

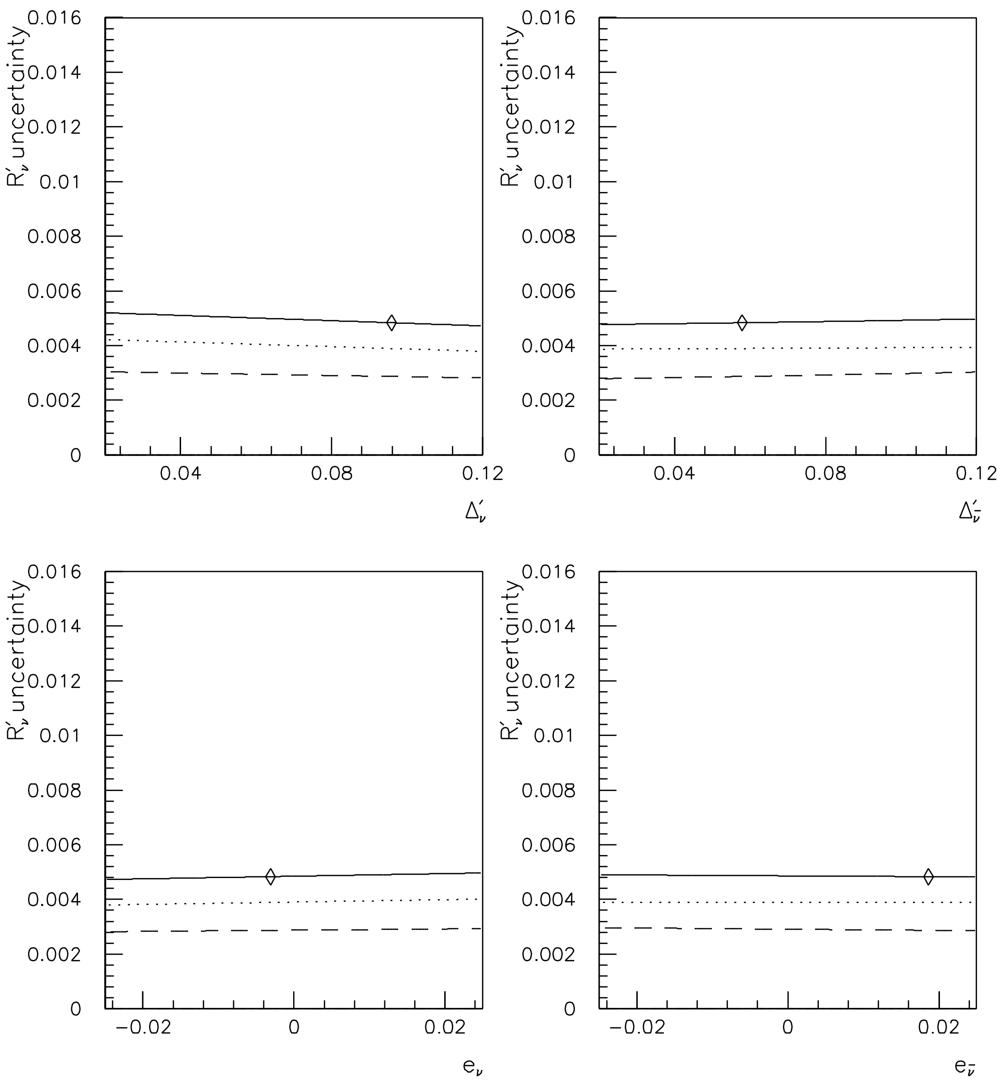

Study R'_ν uncertainty, w/defaults set to the following values :
Found: (NC+CC0)/CC$_\nu$ = 0.5239 CC$_\nu$ = 45103. CC$_{\bar\nu}$/CC$_\nu$ = 0.1780
Δ'_ν=0.0958±.0011 a'_ν=0.0000±.0000 a'_N=0.0000±.0000
$\Delta'_{\bar\nu}$=0.0579±.0044 $a'_{\bar\nu}$=0.0000±.0000 $a'_{\bar N}$=0.0000±.0000
e_ν =−.0031±.0002 $e_{\bar\nu}$ =0.0186±.0014
Theory $R_{\bar\nu}$ = 0.3744±.0127 (yielding R'_ν = 0.3041 ± .0048)

Figure E.4: The effect upon the uncertainty in R_ν of the confusion factors from section 5.6.2.

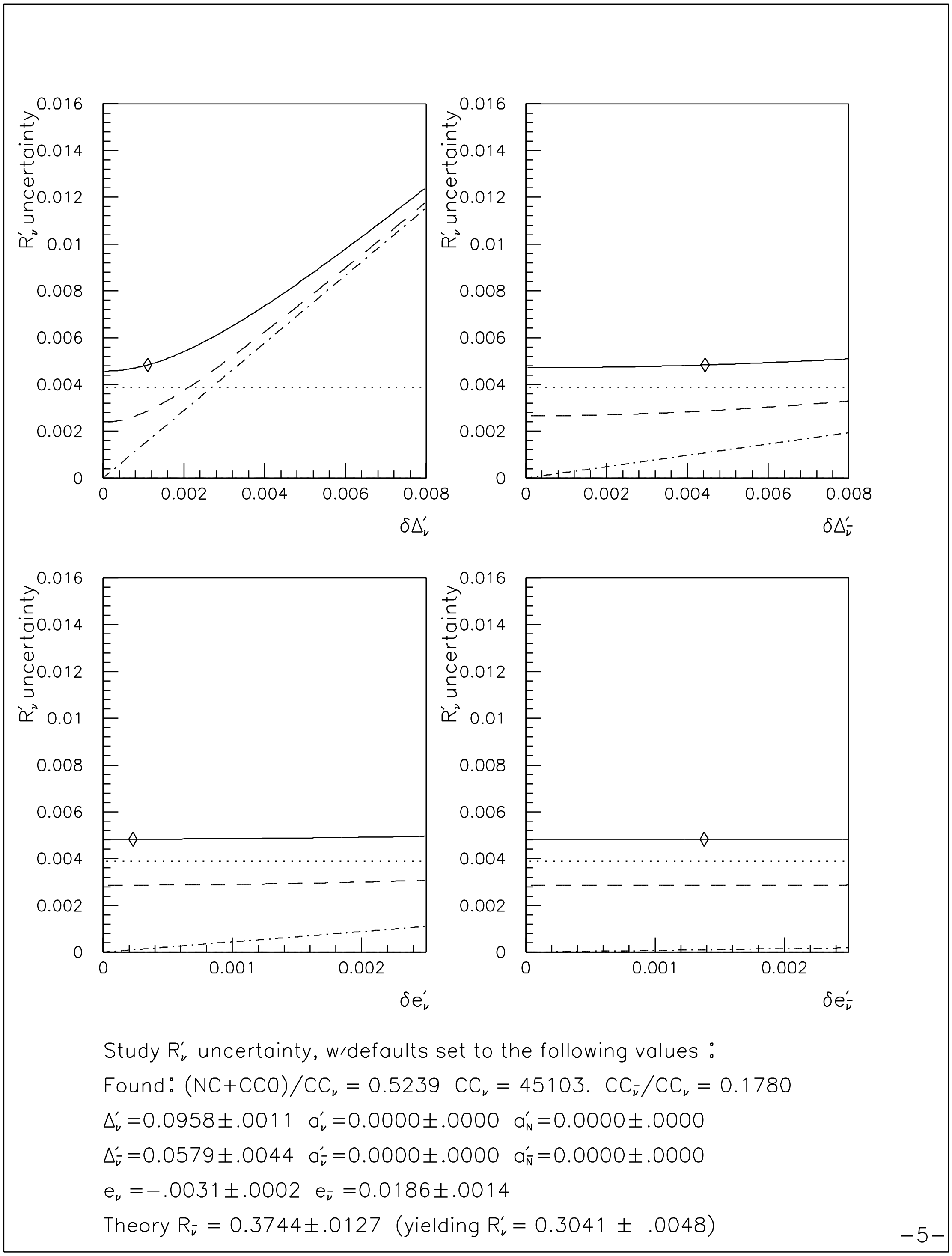

Study R'_ν uncertainty, w/defaults set to the following values :

Found: (NC+CC0)/CC$_\nu$ = 0.5239 CC$_\nu$ = 45103. CC$_{\bar\nu}$/CC$_\nu$ = 0.1780

Δ'_ν=0.0958±.0011 a'_ν=0.0000±.0000 a'_N=0.0000±.0000

$\Delta'_{\bar\nu}$=0.0579±.0044 $a'_{\bar\nu}$=0.0000±.0000 $a'_{\bar N}$=0.0000±.0000

e_ν =−.0031±.0002 $e_{\bar\nu}$ =0.0186±.0014

Theory $R_{\bar\nu}$ = 0.3744±.0127 (yielding R'_ν = 0.3041 ± .0048)

Figure E.5: The effect upon the uncertainty in R_ν of the uncertainties in the confusion factors from section 5.6.2.

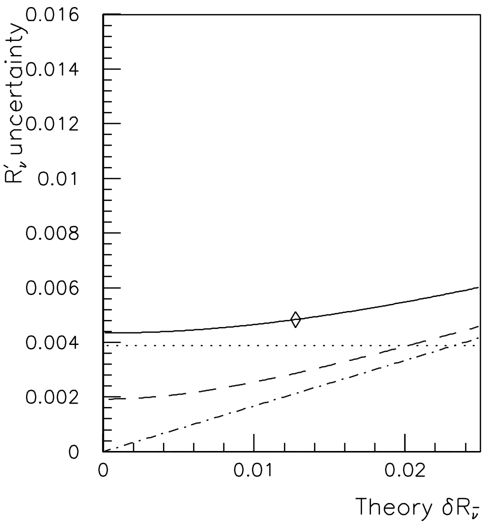

Study R'_ν uncertainty, w/defaults set to the following values :

Found: (NC+CC0)/CC_ν = 0.5239 CC_ν = 45103. $CC_{\bar\nu}/CC_\nu$ = 0.1780

Δ'_ν=0.0958±.0011 α'_ν=0.0000±.0000 α'_N=0.0000±.0000

$\Delta'_{\bar\nu}$=0.0579±.0044 $\alpha'_{\bar\nu}$=0.0000±.0000 $\alpha'_{\bar N}$=0.0000±.0000

e_ν =−.0031±.0002 $e_{\bar\nu}$ =0.0186±.0014

Theory $R_{\bar\nu}$ = 0.3744±.0127 (yielding R'_ν= 0.3041 ± .0048)

−6−

Figure E.6: The effect upon the uncertainty in R_ν of the uncertainty in the value of $R_{\bar\nu}$ used in the analysis.

Appendix F

Fermilab Experiment 733 / The FMMF Collaboration

The following physicists worked on Fermilab E733, designing, building, preparing, maintaining, testing, and running the experimental apparatus and beamline devices before and during the 1985 and 1987–88 runs.

M. Abolins, R. L. Brock, W. G. Cobau, E. Gallas, R. W. Hatcher, B. Johnston,
M. D. Morrow, D. Owen, G. J. Perkins, M. A. Tartaglia, H. Weerts
Michigan State University, East Lansing, MI

D. Bogert, S. C. Fuess, G. Koizumi, L. Stutte
Fermi National Accelerator Laboratory, Batavia, IL

J. I. Friedman, H. W. Kendall, V. Kistiakowsky, L. S. Osborne, R. E. Pitt,
L. Rosenson, U. Schneekloth, B. Strongin, F. E. Taylor
Massachusetts Institute of Technology, Cambridge, MA

J. K. Walker, A. White, J. Womersley
University of Florida, Gainesville, FL

Bibliography

Bibliography

[1] S. Weinberg. A model of leptons. *Phys. Rev. Lett.*, 19(21):1264–1266, 20 November 1967.

[2] A. Salam. Weak and electromagnetic interactions. In N. Svartholm, editor, *Elementary Particle Theory: Relativistic Groups and Analyticity, Proceedings of the 8th Nobel Symposium, Aspenasgarden, Sweden*, pages 367–377. Almquist and Wiksells; John Wiley, 19-25 May 1968.

[3] S.L. Glashow, J. Iliopoulos, and L. Maiani. Weak interactions with lepton-hadron symmetry. *Phys. Rev. D*, 2(7):1285–1292, 1 October 1970.

[4] The Particle Data Group. Review of particle properties. *Phys. Rev. D*, 45 (Part II)(11), 1 June 1992.

[5] Wu-Ki Tung, J.G. Morfin, H. Schellman, S. Kunori, A. Caldwell, and F. Olness. Structure functions and parton distributions. In *Snowmass 1988*, pages 305–330, 1988.

[6] P.N. Harriman, A.D. Martin, W.J. Stirling, and R.G. Roberts. Parton distributions extracted from data on deep inelastic scattering, prompt photon production and the drell-yan process. preprint, Durham/Rutherford, Jan. 1990. DTP/90/04; RAL/90/007.

[7] C.G. Callan, Jr. and D.J. Gross. High-energy electroproduction and the constitution of the electric current. *Phys. Rev. Lett.*, 22(4):156–159, 27 January 1969.

[8] William Gilbert Cobau. *Nucleon Structure Functions from Deep Inelastic Charged Current Neutrino Scattering.* PhD thesis, Michigan State University, East Lansing, MI, 1992. not yet in print.

[9] CDHS: H. Abramowicz et al. A measurement of the ratio of longitudinal and transverse structure functions in neutrino interactions between 30-GeV and 200-GeV. *Phys. Lett.*, 107B:141–144, December 1981.

[10] Raymond L. Brock, Jr. *An Experimental and Theoretical Study of Charmed and Strange Hadron Production in* $\overline{\nu}$ *and* ν *Charged Current Interactions at High Energies.* PhD thesis, Carnegie-Mellon University, Pittsburgh, Pennsylvania, 1980.

[11] C.H. Llewellyn Smith and J.F. Wheater. Electroweak radiative corrections and the value of $\sin^2\theta_w$. *Phys. Lett.*, 105B(6):486–488, 22 Oct. 1981.

[12] J.F. Wheater and C.H. Llewellyn Smith. Electroweak radiative corrections to neutrino and electron scattering and the value of $\sin^2\theta_w$. *Nuc. Phys.*, B208:27–76, 1982.

[13] J.F. Wheater and C.H. Llewellyn Smith. Errata: Electroweak radiative corrections to neutrino and electron scattering and the value of $\sin^2\theta_w$. *Nuc. Phys.*, B226:547, 1983.

[14] Michael Albert Tartaglia. *A Measurement of the Elastic Scattering Cross Section,* $\nu_\mu + e^- \rightarrow \nu_\mu + e^-$. PhD thesis, Massachusetts Institute of Technology, 1984. Submitted July. 6, 1984.

[15] A.J. Malensek. Empirical formula for thick target particle production. Technical report, FNAL, 12 October 1981. Fermilab Internal Note: FN-341.

[16] H.W. Atherton et al. Precise measurements of particle production by 400 GeV/c protons on beryllium targets. Technical report, CERN, 22 August 1980. CERN Report 80-7.

[17] CHARM Collaboration: J.V. Allaby et al. A precise determination of the electroweak mixing angle from semileptonic neutrino scattering. *Z. Phys.*, C(36):611, 1987.

[18] CDHS: H. Abramowicz et al. Precision measurement of $\sin^2\theta_w$ from semileptonic neutrino scattering. *Phys. Rev. Lett.*, 57(3):298–301, 21 July 1986.